Fourier-gebaseerd modelleren van hogesnelheidsmachines
met permanente magneten

Fourier-Based Modeling of Permanent-Magnet Synchronous Machines
Operating at High Speed

Bert Hannon

Promotoren: prof. dr. ir. L. Dupré, prof. dr. ir. P. Sergeant
Proefschrift ingediend tot het behalen van de graad van
Doctor in de ingenieurswetenschappen: werktuigkunde-elektrotechniek

UNIVERSITEIT
GENT

Vakgroep Elektrische Energie, Metalen, Mechanische Constructies en Systemen
Voorzitter: prof. dr. ir. L. Dupré
Faculteit Ingenieurswetenschappen en Architectuur
Academiejaar 2017 - 2018

ISBN 978-94-6355-073-4
NUR 959
Wettelijk depot: D/2017/10.500/108

Fourier-based modeling of permanent-magnet synchronous machines operating at high speed

Bert Hannon

Dissertation submitted to obtain the academic degree of
Doctor of Electromechanical Engineering

Supervisors:
Prof. dr. ir. Luc Dupré
Prof. dr. ir. Peter Sergeant
Department of Electrical Energy, Metals, Mechanical Constructions and Systems (EEMMeCS)
Faculty of Engineering and Architecture
Ghent University
Tech Lane Ghent Science Park 913
B-9052 Zwijnaarde, Belgium
http://www.ugent.be/ea/eemmecs/en

Members of the examining board:

Em. prof. dr. ir. Daniël De Zutter (chairman)	Ghent University
Prof. dr. ir. Lieven Vandevelde (secretary)	Ghent University
Prof. dr. ir. Peter Sergeant (supervisor)	Ghent University
Prof. dr. ir. Luc Dupré (supervisor)	Ghent University
Prof. dr. ir. An Ghysels	Ghent University
Prof. dr. Marc Vanhaelst	Ghent University
Prof. dr. Elena Lomonova	Technische Universiteit Eindhoven
Prof. dr. Thierry Lubin	Université de Lorraine

FACULTY OF ENGINEERING AND ARCHITECTURE

GHENT UNIVERSITY

Preface

With evermore strict demands on the performance of electric machines, the importance of optimizations during early design stages is growing. Typically, such optimizations have a vast initial design space. In order to limit the associated computational burden, fast machine models are required.
One class of electric machines that has gained special attention lately, is the class of high-speed machines. The main reason for this popularity is that such machines allow to power high-speed applications, e.g. distributed power generation or gas compression, in a direct-drive configuration. As this implies omitting the gear box, it increases the system's efficiency while decreasing its size and maintenance cost. However, operating electric machines at high speeds introduces problems that are not present in traditional machines. To understand these problems, a good insight in the physics of high-speed electric machines is paramount.
In light of the above-described needs for fast and accurate modeling tools on the one hand and a better understanding of high-speed electric machines on the other, prof. dr. ir. Peter Sergeant and prof. dr. ir. Luc Dupré requested, and received, a PhD position at Ghent University in 2012. This work presents the results of the research that has been performed in the scope of that PhD.

During my time as a PhD student at Ghent University, I received help from a lot of people. In the first place from my promotors, prof. dr. ir. Peter Sergeant and prof. dr. ir. Luc Dupré, whom I would like to thank for giving me the opportunity to start a PhD and for providing me with all the support I asked for. I would also like to thank my fellow PhD students, especially dr. ing. Bart Scheerlinck, dr. eng. Ahmed Hemeida, eng. Mohamed Nabil and ing. Jan De Bisschop, from whom I received a lot of interesting feedback. Another group of people I would like to thank are my colleagues from Campus Schoonmeersen, they made working at Ghent University a real pleasure.
Finally, I would also like to thank my parents and my entire family, whose unconditional support means a lot to me. In particular Iphigeneia, to whom I would like to dedicate this work. Your love was, and continues to be, my largest motivation.

Bert Hannon, August 2017

Contents

Summary

Two trends dominate the design of modern electric machines; a commitment to higher energy-efficiencies on the one hand and a tendency towards more dedicated drives on the other. As a result, the importance of rigorous optimizations during the design process of electric machines is at an all-time high. This, in turn, has sparked the interest for modeling tools that combine accuracy and a low computational time. The latter is especially important during the earliest phases of the machine's design, when the design space is still very large.
Another result of the above-described trends is the emerging of new electric machine types. Especially high-speed electric machines have gained a lot of attention over the past decade. Indeed, the dedicated design of such machines enables a direct-drive configuration of high-speed systems. This doesn't only allow to omit the gearbox, resulting in a higher efficiency and reliability, it also reduces the system's weight and size. In addition to the importance of optimization procedures, the need to gain more insight in emerging machine types is another incentive to develop comprehensible models for these machines.
The aforementioned needs for fast and accurate modeling tools and a better insight in emerging machine types form the motivation for this work. Because of their relative importance in the segment of high-speed machine, the focus is on surface-mounted permanent-magnet synchronous machines with a shielding cylinder. In the first place, the aim of this work is to study and improve the existing modeling techniques for high-speed synchronous machines with permanent magnets. Secondly, this work wants to provide the foundation for a better understanding of these machines. Especially regarding the physical processes through which the shielding cylinder affects the machine's performance.

The first part of this work discusses the modeling of permanent-magnet synchronous machines, with a focus on machines that operate at high speeds.
That discussion starts with an evaluation of the existing modeling techniques. Based on that evaluation, it was chosen to concentrate on the so-called Fourier-based modeling technique. This type of models combines the subdomain technique, i.e. dividing the studied machine topology in a number of subdomains, with the separation of variables technique to calculate the machine's magnetic field.
Next, the physical background and implementation of Fourier-based models is

described.
The term Fourier-based modeling actually covers a wide range of different techniques. There are, for example, different possibilities to account for slotting and even the initial physical formulation of the problem can be based on two different magnetic potentials. Therefore, the next step is to use the previous discussion on Fourier-based modeling as a basis to evaluate the different techniques within Fourier-based modeling. By coupling that evaluation to an overview of the existing literature, this work presents a comprehensible selection guide that can be used by anyone who wants to build a Fourier-based model.

The second part of this work concentrates on how the existing Fourier-based models can be improved.
The first improvement has been to further reduce the computational times of Fourier-based models, even though they are already inherently low. It was found that this can be done by simplifying the studied geometry and by performing a preliminary analysis of the machine's harmonic content. Especially the latter results in spectacular computational-time reductions up to 99% without affecting the model's accuracy.
Another contribution of this work to the Fourier-based modeling technique has been to account for voltage sources, as opposed to the current-density sources that are traditionally used. Although this does add to the model's complexity, it may greatly improve its value, especially when the modeled machine is to be powered with a voltage source.

Whereas the first two parts of this work focus on the calculation of the machine's magnetic field, the third part focuses on the electromagnetic quantities that can be obtained from that magnetic field.
Firstly the postprocessing itself, i.e. the actual calculation of the electromagnetic quantities is discussed. Four quantities in particular are considered; the magnetic flux density, the back electromotive force, the torque and the eddy-current losses. This work contributed to the existing literature by introducing a division of the torque in two components, one that is related to the shielding cylinder and one that is related to the magnets.
Secondly, the test setup that has been built in the scope of this PhD is introduced and used to validate the calculation of the back electromotive force and the currents that are obtained when imposing a voltage. Note that all other calculations have been validated with a finite-element model.
Finally, a number of parameter studies are performed to investigate the shielding cylinder's effect on the torque and the eddy-current losses. By evaluating the effect of the shielding cylinder's conductivity and its thickness while applying various current and voltage sources, a number of interesting observations have been made. It was for example noted that the torque related to the shielding cylinder behaves similarly to the torque that is produced in an induction machine. Another observation is that, unlike expected, the synchronous harmonic content of the machine is affected by the shielding cylinder's conductivity. Although it is difficult to ex-

trapolate the results to other machine topologies, the observations from these parameter studies clearly add to the understanding of high-speed permanent-magnet synchronous machines.

Combined, the three individual parts of this work meet the initial goals of this PhD. The first part provides an elaborate study of the existing Fourier-based modeling techniques. The second part makes these models even more attractive for research and optimization purposes by reducing the computational time and accounting for voltage sources. The last part applies Fourier-based modeling to gain a better understanding of high-speed permanent-magnet synchronous machines.

Samenvatting

Een streven naar betere efficiënties enerzijds en een tendens naar meer gespecialiseerde elektrische aandrijvingen anderzijds, domineren momenteel de evolutie van elektrische machines. Het gevolg daarvan is dat het belang van doorgedreven optimalisaties tijdens het ontwerp van elektrische machines sterk stijgt, wat op zijn beurt weer zorgt voor een toegenomen interesse in wiskundige modellen die zowel nauwkeurig als snel zijn. Dat laatste is bijzonder belangrijk tijdens de eerste fases van het ontwerpproces, als de ontwerpruimte nog zeer groot is.
Een ander gevolg van het streven naar efficiëntere en meer gespecialiseerde machines is dat er nieuwe types elektrische machines ontworpen worden. In het licht daarvan zijn hogesnelheidsmachines erg populair geworden tijdens de afgelopen tien jaar. Inderdaad, indien dergelijke machines specifiek ontworpen worden voor één bepaalde hogesnelheidstoepassing, is het mogelijk die toepassing aan te drijven zonder tussenkomst van een tandwielkast. Dit zorgt er niet enkel voor dat de efficiëntie en duurzaamheid verbeteren, het resulteert ook in een lichter en compacter systeem. Om een nieuwe machine te ontwerpen is er echter een goed inzicht in die machine nodig. In dit doctoraat bijvoorbeeld, ligt de focus op hogesnelheidsmachines met permanente magneten. Dergelijke machines worden vaak uitgerust met een beschermende cilinder rond de magneten. Het doel van die cilinder is de magneten op hun plaats te houden en/of de rotorverliezen te verminderen. Een goed inzicht in de fysische processen die zo'n beschermende cilinder teweegbrengt is belangrijk. Als aanvulling op het belang van optimalisatie procedures, is de behoefte naar meer inzicht in nieuwe types machines een extra reden om wiskundige modellen voor dergelijke machines te ontwerpen.
De behoefte naar zowel snelle en nauwkeurige wiskundige modellen én een beter inzicht in nieuwe types elektrische machines vormen de motivatie voor dit doctoraat. In de eerste plaats is het doel de bestaande wiskundige modellen voor permanentmagneetbekrachtigde synchrone machines te bestuderen en te verbeteren. Ten tweede wilt dit werk de basis leggen voor een beter inzicht in dergelijke machines.

In het eerste deel van dit werk wordt de wiskundige modellering van permanentmagneetbekrachtigde synchrone machines besproken, met een focus op machines die ontworpen zijn voor grote omwentelingssnelheden.
In een eerste stap worden de bestaande modelingstechnieken vergeleken. Op basis van die vergelijking werd er gekozen voor de Fourier-gebaseerde modellerings-

techniek. Deze techniek combineert de zogenaamde deelgebiedenmethode, die het bestudeerde probleem in kleinere delen opdeelt, met scheiding der veranderlijken om het magnetisch veld in de machine te berekenen.
In een tweede stap wordt de fysische achtergrond en de implementatie van Fourier-gebaseerde modellen besproken.
De term Fourier-gebaseerd modelleren dekt eigenlijk een brede waaier aan verschillende technieken. Er zijn bijvoorbeeld meerdere methodes om het gleufeffect in rekening te brengen. Zelfs de fysische formulering van het probleem kan gebaseerd zijn op verschillende magnetisch potentialen. Daarom is de volgende stap om, op basis van de voorgaande discussie, de verschillende technieken binnen Fourier-gebaseerd modelleren te evalueren. Door die evaluatie te koppelen aan een overzicht van de bestaande literatuur, slaagt dit werk erin een keuzehulp aan te bieden voor toekomstige onderzoekers die een dergelijk model willen maken.

Het tweede deel van dit werk tracht de bestaande Fourier-gebaseerde modellen te verbeteren.
Een eerste verbetering werd gerealiseerd door de rekentijd van Fourier-gebaseerde modellen te verlagen. Dit werd enerzijds gedaan door de bestudeerde geometrie te vereenvoudigen en anderzijds door een kwalitatieve studie van de harmonsiche inhoud van het magnetisch veld in de machine te gebruiken. Vooral die laatste methode levert een spectaculaire rekentijdreductie tot wel 99% op, zonder de nauwkeurigheid van het model te verminderen.
Een tweede bijdrage van dit werk is het in rekening brengen van spanningsbronnen, dit in tegenstelling tot het opdringen van stroomdichtheden. Ondanks het feit dat dit de complexiteit van het model vergroot, kan het een grote meerwaarde zijn. Zeker indien de te modelleren machine aangedreven wordt met een spanningsbron.

Waar de eerste twee delen van dit werk focussen op de berekening van het magnetisch veld, ligt de focus van het derde deel op de elektromagnetische grootheden. In een eerste stap word de berekening van vier elektromagnetische grootheden besproken; de magnetische flux dichtheid, de tegen elektromotorische kracht, het koppel en de wervelstroomverliezen. Dit doctoraat draagt bij aan de bestaande literatuur door de opdeling van het koppel in twee componenten te introduceren; een component gerelateerd aan de beschermende cilinder en een component gerelateerd aan de magneten.
In een tweede stap wordt de testopstelling, die gebouwd werd in het kader van dit doctoraat, kort voorgesteld. Vervolgens wordt ze gebruikt om de berekening van de tegen elektromotorische kracht en de stromen in de machine te onderzoeken. Merk op dat alle andere berekeningen eerder al gevalideerd werden met een eindige-elementen model.
Ten slotte werden er verschillende parameterstudies uitgevoerd om het effect van de beschermende cilinder op het koppel en de wervelstroomverliezen te valideren. Door het effect van de geleidbaarheid en de dikte van de cilinder te bestuderen bij verschillende stroom- en spanningsbronnen, kunnen een aantal interessante observaties gedaan worden. Zo werd er bijvoorbeeld vastgesteld dat de koppelcom-

ponent die gerelateerd is aan de beschermende cilinder dezelfde eigenschappen vertoond als het koppel in een inductiemachine. Verder werd er ook vastgesteld dat, tegen de verwachtingen in, de synchrone harmonische inhoud van de machine beïnvloed wordt door de geleidbaarheid van de beschermende cilinder. Ondanks het feit dat het moeilijk is de resultaten te extrapoleren naar andere machines, dragen de inzichten die voortkomen uit deze parameter studies zeker bij aan een beter begrip van permanentmagneetbekrachtigde hogesnelheidsmachines.

Samen komen bovenstaande delen van het werk tegemoet aan de initiële doelstellingen van dit doctoraat. Het eerste deel bevat een uitgebreide studie van de technieken binnen Fourier-gebaseerd modelleren. In het tweede deel worden twee verbeteringen van de bestaande techniek voorgesteld die Fourier-gebaseerd modeleren nog aantrekkelijker maakt voor onderzoeks- en optimalisatiedoeleinden. Het laatste deel van dit werk gebruikt Fourier-gebaseerd modeleren om een beter inzicht te krijgen in permanentmagneetbekrachtigde hogesnelheidsmachines.

List of Abbreviations

AG	air gap
AR	armature reaction
BLDC	brushless DC
CHP	combined heath and power
EMF	electromotive force
ESP	electric scalar potential
FB	Fourier-based
FE	finite element
FOC	field-oriented control
LVTTL	low voltage transistor-transistor logic
MEC	magnetic equivalent circuit
MMF	magnetomotive force
MQS	magneto-quasi static
MSP	magnetic scalar potential
MVP	magnetic vector potential
NL	no load
PAM	pulse-amplitude modulation
PDE	partial differential equation
PM	permanent magnet
PMSM	permanent-magnet synchronous machine
PWM	pulse-width modulation
RY	rotor yoke
SC	shielding cylinder
SL	slot
SM	surface mounted
SO	slot opening
SoS	star of slots
SY	stator yoke
TAD	total asynchronous distortion
THD	total harmonic distortion

List of Symbols

The following is a list of the most important symbols that have been used in this dissertation.

$\mathbf{A}$	magnetic vector potential (MVP) $\left[\frac{\mathrm{Vs}}{\mathrm{m}}\right]$
$\mathbf{B}$	magnetic flux density [T]
$\mathbf{B}_0$	residual magnetic flux density [T]
B_m	peak value of the residual magnetic flux density [T]
d	percentage RMS deviation [%]
$\mathbf{D}$	electric flux density $\left[\frac{\mathrm{C}}{\mathrm{m}^2}\right]$
$\mathbf{E}$	electric field $\left[\frac{\mathrm{V}}{\mathrm{m}}\right]$
f	frequency [Hz]
$\mathbf{H}$	magnetic field $\left[\frac{\mathrm{A}}{\mathrm{m}}\right]$
I_x	modified Bessel function of the first kind and x^{th} order
$\mathbf{J}$	current density $\left[\frac{\mathrm{A}}{\mathrm{m}^2}\right]$
$\mathbf{J}_{ext}$	externally imposed current density $\left[\frac{\mathrm{A}}{\mathrm{m}^2}\right]$
$\mathbf{J}_s$	boundary surface current density $\left[\frac{\mathrm{A}}{\mathrm{m}^2}\right]$
k	spatial-harmonic order
k_c	Carter's factor
K_x	modified Bessel function of the second kind and x^{th} order
l_s	stack length
L_{ew}	inductance of the coils' end windings [H]
m	number of phases
$\mathbf{M}$	magnetization $\left[\frac{\mathrm{A}}{\mathrm{m}}\right]$
$\mathbf{M}_0$	residual magnetization $\left[\frac{\mathrm{A}}{\mathrm{m}}\right]$
$\mathbf{M}_E$	induced magnetization $\left[\frac{\mathrm{A}}{\mathrm{m}}\right]$
n	time-harmonic order
n_r	rotational speed [rpm]
N	number of windings per slot
N_{bc}	number of boundary condtions
N_c	number of coils
N_g	number of slots per slot group
N_s	number of slots
N_ν	number of subdomains

$N^{(c,i_{N_s})}$	oriented amount of conducts that coil c has in slot i_{N_s}
p	number of pole pairs
P_m	mechanical power [W]
$\mathbf{P}$	polarization $\left[\frac{\mathrm{C}}{\mathrm{m}^2}\right]$
$\mathbf{P}_0$	residual polarization $\left[\frac{\mathrm{C}}{\mathrm{m}^2}\right]$
$\mathbf{P}_E$	induced polarization $\left[\frac{\mathrm{C}}{\mathrm{m}^2}\right]$
r	radial coordinate, cylindrical coordinate system [m]
r_0	Radius of the RY - external boundary [m]
r_1	Radius of the RY - PM boundary [m]
r_2	Radius of the PM - SC boundary [m]
r_3	Radius of the SC - AG boundary [m]
r_4	Radius of the AG - SO boundary [m]
r_5	Radius of the SO - SL boundary [m]
r_6	Radius of the SL - SY boundary [m]
r_7	Radius of the SY external boundary [m]
R	ohmic resistance of the coils $[\Omega]$
R_{SC}	ohmic resistance of the SC $[\Omega]$
S	surface $\left[\mathrm{m}^2\right]$
t	time [s]
t_{AG}	radial thickness of the AG [m]
$t_{AG,eff}$	effective radial thickness of the AG [m]
t_{ec}	radial thickness of the SC's part in which the eddy currents flow [m]
t_{SC}	radial thickness of the SC [m]
t_δ	penetration depth of the dominant asynchronous harmonic combinations [m]
T	torque [Nm]
$T^{(2)}$	torque in the magnets [Nm]
$T^{(3)}$	torque in the shielding cylinder [Nm]
T	torque [Nm]
T_s	spatial periodicity (mechanical) [rad]
T_t	time periodicity (mechanical) [s]
$\mathbf{v}$	speed $\left[\frac{\mathrm{m}}{\mathrm{s}}\right]$
V	electric scalar potential [V]
α_ν	angular position of subdomain ν [rad]
$\alpha^{(i_{N_s})}$	average MVP in slot i_{N_s} $\left[\frac{\mathrm{Vs}}{\mathrm{m}}\right]$
β_ν	angular span of subdomain ν [rad]
$\mathbf{\Gamma}$	Maxwell's stress tensor $\left[\frac{\mathrm{N}}{\mathrm{m}^2}\right]$
δ	Opening angle of the slot openings [rad]
$\delta_{n,k}$	penetration depth [m]
ϵ	Opening angle of the slots [rad]
ε	electric permittivity $\left[\frac{\mathrm{F}}{\mathrm{m}}\right]$
μ	magnetic permeability $\left[\frac{\mathrm{H}}{\mathrm{m}}\right]$

ν	subdomain number
σ	electric conductivity $\left[\frac{\mathrm{S}}{\mathrm{m}}\right]$
τ	machine period
υ	machine constant ($\upsilon = 1$ or 2)
ϕ	stator angular coordinate, cylindrical coordinate system [rad]
ϕ_0	angular shift between two coordinate systems [rad]
ϕ_m	angular span of a magnet [rad]
φ	magnetic scalar potential (MSP) [A]
ψ	coupled magnetic flux [Wb]
$\psi^{(c)}$	magnetic flux coupled with the active part of coil c [Wb]
ω	mechanical rotational speed $\left[\frac{\mathrm{rad}}{\mathrm{s}}\right]$

The following is a list of sub- and superscripts that are commonly used in this dissertation.

$X_{n,k}$	harmonic component with time-harmonic order n and spatial harmonic order k
$X_{n,s}$	harmonic component with time-harmonic order $n + s$
$X_{\lvert n,k\rvert}$	sum of conjugate time- and spatial-harmonic components, i.e. $X_{n,k} + X_{-n,-k}$
$X_{\lvert n,s\rvert}$	sum of conjugate time-harmonic components, i.e. $X_{n,s} + X_{-n,-s}$
$X^{(\nu)}$	indicates a relation to subdomain ν

Chapter 1

Introduction

In this first section, the work performed in the scope of this PhD is introduced. The context that motivates the interest of the work is sketched in Section 1.1 and a motivation of the adopted approach is formulated in Sections 1.2 and 1.3. Section 1.4 summarizes the scientific goals of this work. Section 1.5 gives an outline of this thesis. Finally, Section 1.6 lists the scientific publications that were made in the scope of this PhD.

1.1 High-speed electric machines

Three tendencies in both society and industry have sparked the interest for high-speed electric drives; a commitment to more cost- and energy-efficient solutions, a desire to reduce the volume of a wide range of applications and, finally, a demand to increase the reliability on a system-level.
Indeed, high-speed electric machines allow for a direct-drive configuration of applications that operate at high speeds, such as turbo compressors, milling tools, medical equipment, combined heath and power (CHP) units, etc. As a direct-drive configuration implies omitting the gear box, it also implies higher efficiency, lower volume and a higher reliability. Moreover, increasing the speed of an electric machine results in a higher power density. This doesn't only further reduce the volume, it also reduce the required amount of material. This is especially interesting for machine topologies that require expensive materials, such as rare-earth magnets.
However, designing high-speed electric machines is significantly more complicated than designing traditional machines. Indeed, machines operating at high speed require a rigorous mechanical, thermal and electromagnetic design. Moreover, not only the machine design is a complicated task, designing the inverter and implementing a high-speed control algorithm is a challenge as well.
Before continuing this discussion, a definition of the term high-speed machine is required. Such a definition cannot solely be expressed in terms of the machine's rotational speed; the challenges of operating a 10 kW machine at 100.000 rpm are much larger than the challenges of operating a 50 W machine at that same speed. Literature presents different definitions of high-speed machines, but mostly the one introduced by Binder *et al.* in [1] is used. According to this definition, only machines with rotational speeds that exceed the threshold speed, as defined in (1.1), are high-speed machines.

$$\log n_r = 4.27 - 0.275 \log(P_m) \tag{1.1}$$

where n_r is the machine's speed in revolutions per second and P_m is its mechanical power in Watt.
Binder's criterion is illustrated in Figure 1.1 together with a number of both industrial and academic high-speed applications [2–26].
The applications presented in Figure 1.1 illustrate the validity of Binder's criterion. As already mentioned, the development of high-speed electric drives is a significant challenge. It is therefore no wonder that a lot of research on high-speed electric machines has been, and continues to be, performed. Designing high-speed machines is a multi-physical challenge: not only electromagnetic aspects, such as eddy-current and iron losses, [14, 15, 19, 27–30] are important, the mechanical design of the rotor [4,8,12,18–20,27,29–32] and a thermal study [18,19,21,27,32,33] are critical as well. Apart from designing the machine, control architectures for high-speed drives have been developed as well [7, 16, 19, 23–25, 29, 34–37].

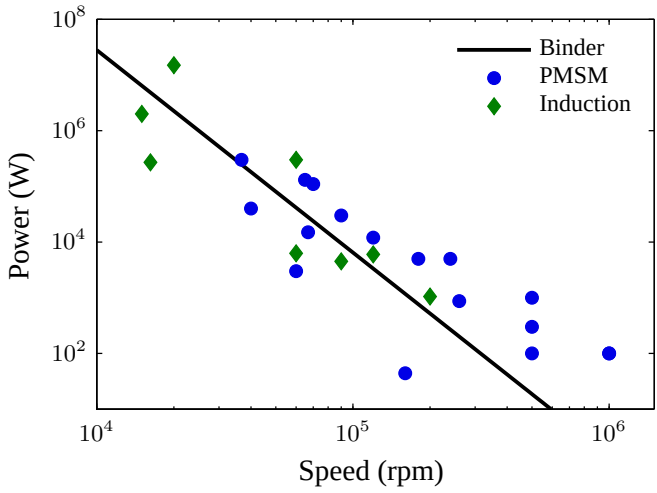

Figure 1.1: Binder's criterion for high-speed machines and real-life applications

One important question is which machine topology is best suited for high-speed drives. Figure 1.1 already indicated that two machine types, i.e. induction machines and permanent-magnet synchronous machines (PMSMs), are predominantly represented in the field of high-speed machines. For machines with a very high power, i.e. more than 500 kW, there is a tendency to use induction machines. The reason is that in these applications, induction machines are often superior from an economical point-of-view. When decreasing the power and increasing the rotational speed, the poor electromagnetic performance of induction motors favors PMSMs. Especially because at very high rotational speeds, the rotor's surface speed is too high for classical squirel cage induction machines [38]. This means that solid rotor induction machines have to be used, which further reduces the electromagnetic performance. Therefore, nowadays the focus is on PMSMs [4, 39]. More specifically, radial-flux surface-mounted (SM) PMSMs with a retaining sleeve are commonly used [20, 40]. The reason to prefer SM PMSMs is that rotor structures with interior magnets cannot withstand very high rotational speeds.

Note that various authors have proposed using a shielding cylinder (SC) [41–43]. This conductive cylinder is placed around the magnets. Its goal is to reduce the overall rotor losses, thereby limiting the risk of overheating the magnets. Indeed, asynchronous harmonics in the field will induce eddy-currents in the SC. These eddy currents counteract their origin, thereby shielding the magnets. By shifting the eddy-currents from the poorly conductive magnets to the highly conductive SC, the rotor's eddy-current losses can be reduced. Note, however, that the SC has

to be carefully designed to avoid it from increasing the eddy-current losses instead of decreasing them.
One aspect that recurs in the vast majority of the above-mentioned research is the need for adequate electromagnetic modeling tools. Such models should be able to accurately account for phenomena that are important in high-speed machines, like the slotting effect and the eddy-current reaction field. The latter is especially important for high-speed SM PMSMs, where the effect of eddy currents in the retaining sleeve and/or the SC is non-negligible. Apart from accurate, the modeling tools also have to be fast and flexible and have to give the user an insight in the physics of the studied machine. Despite the enormous amount of research on high-speed machines, there is still a lot of progress to be made in the field of models that match the above description. Therefore, this work aims at studying and developing electromagnetic modeling tools for high-speed machines. More specifically, the focus is on models that satisfy the following needs:

- capable of accounting for phenomena that relate to high-speed operation
- fast and flexible enough to be used for optimization purposes
- provide insight in the physics of the machine

1.2 Modeling techniques

Literature describes a large variety of electromagnetic models for electric machines, ranging from very simple 1D models to highly sophisticated models that account for complex physical phenomena in three dimensions. The goal of this section is to review some of the most widely used modeling techniques and to select the one that is best suited for our needs.

1.2.1 Finite-element models

Finite-element (FE) modeling is probably one of the most generic modeling techniques. FE models are capable of accurately accounting for complex geometries, non-linear materials and virtually every physical phenomenon. Moreover, electromagnetic FE models can easily be coupled with electric circuits and models of other physical domains, such as thermal or mechanical studies.
The underlying idea of FE modeling is to first mesh the studied geometry, i.e. divide it in a large, but finite, number of elements. These elements have to be sufficiently small to allow assuming that the magnetic field in each of them can be described with a polynomial. The coefficients of these polynomials are then obtained by minimizing the total (co-)energy of the problem while also accounting for boundary conditions at the boundaries between neighboring elements.
The implementation of a FE model is quite complex. However, there is a large number of FE software packages available that provide easy-to-use user interfaces.

For that reason, and because of the previously mentioned advantages, FE models are the most commonly used models, especially in industry.
The major downfall of FE models is their need to mesh the geometry. First of all, efficient meshing requires a preliminary knowledge of the problem's magnetic field, this reduces the flexibility of the technique with respect to parameter variations. Moreover, some effects, such as the eddy-current reaction field, may require mesh sizes that are very small when compared to the total size of the problem. This increases the computational time and may even result in numerical problems. Moreover, FE models give only very little insight in the machine's physics.
As a conclusion, it can be stated that FE models are capable of accounting for phenomena that relate to high-speed operation, but are not fast, nor flexible enough and do not provide the desired insight in the machine's physics. For these reasons, FE modeling will only be used as a validation tool in this PhD.

1.2.2 Magnetic equivalent circuits

Much like FE models divide the geometry in a number of mesh elements, the technique of magnetic equivalent circuits (MEC) divides the geometry in flux tubes. The magnetic flux is assumed to have a spatially constant value and direction in each of these tubes. The field is then calculated by accounting for magnetomotive force (MMF) sources and the permeances of the flux tubes in an equivalent circuit [44, 45]. The technique is very effective at accounting for slotting and saturation of soft-magnetic materials. As shown by Hemeida *et al.* [46], MEC models can account for eddy-current reaction field by introducing inductances in addition to the resistive permeances. MEC modeling further owes its popularity to a low computational time and a relatively simple implementation. It may therefore provide a faster, yet simplified, alternative for FE modeling.
On the downside, like FE models, MEC models require a form of meshing. As mentioned, this is a drawback in the light of parameter studies. Due to the importance of leakage fluxes, the meshing is especially problematic in machines with a large air gap, like SM PMSMs. Moreover, although [46] illustrated the possibility, MEC models are not very efficient at accounting for eddy-current reaction field. This is mainly because it is not evident to predict the eddy-current path. For these reasons, MEC is not the best-suited modeling technique for this PhD.

1.2.3 Charge and current modeling

Using Green's functions, charge and current models provide direct solutions for the magnetic potential formulation of Maxwell's equations. The latter will be discussed in more detail in Chapter 2. For charge models, which use the magnetic scalar potential (φ) and account for permanent magnet sources through equivalent

magnetic volume (ρ_m) and surface (σ_m) charges, this solution is [47]:

$$\varphi(\mathbf{x}) = \frac{1}{4\pi}\int_V \frac{\rho_m(\mathbf{x}')}{|\mathbf{x}-\mathbf{x}'|}\,\mathrm{d}v' + \frac{1}{4\pi}\int_S \frac{\sigma_m(\mathbf{x}')}{|\mathbf{x}-\mathbf{x}'|}\,\mathrm{d}s' \tag{1.2}$$

where $\mathbf{x}$ is the position vector and $\mathbf{x}'$ is the observation point.
For current models, which use the magnetic vector potential $(\mathbf{A})$ and account for source terms through equivalent volume $(\mathbf{J}_m)$ and surface $(\mathbf{j}_m)$ current densities, the solution for Maxwell's equations is [48]:

$$\mathbf{A}(\mathbf{x}) = \frac{\mu_0}{4\pi}\int_V \frac{\mathbf{J}_m(\mathbf{x}')}{|\mathbf{x}-\mathbf{x}'|}\,\mathrm{d}v' + \frac{\mu_0}{4\pi}\int_S \frac{\mathbf{j}_m(\mathbf{x}')}{|\mathbf{x}-\mathbf{x}'|}\,\mathrm{d}s' \tag{1.3}$$

where μ_0 is the magnetic permeability of vacuum.
Charge and current modeling are very effective techniques to calculate the magnetic field in three dimensional problems with a uniform magnetic permeability [47, 48]. Their very straightforward approach also implies that they provide a good insight in the machine's physics. However, charge nor current models are very efficient at accounting for problems with multiple materials. They then require more complex techniques [49]. This makes them less suited for this PhD, where material-dependent effects, such as the slotting effect and eddy-current reaction field, have to be accounted for.

1.2.4 Fourier-based models

Similar to charge and current models, Fourier-based (FB) models use a magnetic potential formulation of Maxwell's equations. However, instead of Green's functions, separation of variables is used to solve Maxwell's equations. This allows to divide the problem in a number of regions, called subdomains. As a result, Maxwell's equations do not have to be solved in the entire problem domain, instead every subdomain is considered separately. In a second step, the solutions of all these subdomains are coupled by imposing boundary conditions. This approach isn't only very fast, it also allows to account for both the slotting effect and the eddy-current reaction field [50, 51]. Moreover, although FB models are often not as straightforward as charge or current models, they do provide a very good insight in the machine's physics.
Note that the division of the problem in subdomains is fundamentally different from the meshing technique that is used in FE and MEC modeling. Indeed, in contrast to the approximated solutions in the FE model's elements or the MEC model's flux tubes, the solution in each subdomain is calculated exactly. Moreover, the number of subdomains in a FB model is much smaller than the amount of elements or flux tubes that is required in FE or MEC models. As a result, FB models are more suited for parameter studies than FE and MEC models.
Evidently, FB models have disadvantages as well. Although they are inherently

fast, their computational time rises when the amount of subdomains and/or the required accuracy is increased. However, as will be discussed in Chapter 5, the impact of that problem can be reduced. Another drawback of FB models is that they sometimes have to assume infinite permeability of soft magnetic materials. This is, however, not a big issue for high-speed SM PMSMs. Due to their high-speed operation and large effective air gap, these machines are typically operated in the linear region of their magnetic materials.
FB models thus combine low computational times, high flexibility, good insight and a capability of accounting for phenomena that are important for high-speed operation. This makes them the ideal tool for this PhD.

1.2.5 Conclusion

In the above, four of the most commonly used modeling techniques have been evaluated for use in the scope of this PhD. As was discussed in Section 1.1, the criteria to which they were evaluated are: capability of accounting for phenomena that relate to high-speed operation, flexibility, computational time and the level to which they provide insight in the studied machines. The technique of Fourier-based modeling was selected as best-suited for the needs of this PhD. It will be discussed extensively in Chapters 2 and 3.

1.3 Aspects of Fourier-Based modeling

There are quite some options when implementing a Fourier-based model, e.g. the magnetic potential that is used or the way in which slotting is accounted for. Therefore, the goal of this section is to justify the choices that were made when implementing the FB model of this PhD.
In the following, five aspects in particular are considered: the choosing of a magnetic potential, the spatial coordinate system and the way in which time dependency, source terms and slotting are accounted for.

1.3.1 Magnetic potential

It was already mentioned that a magnetic potential formulation is used to construct a Fourier-based model. Just like with charge and current models, either the magnetic scalar potential (MSP) or the magnetic vector potential (MVP) can be used. The MSP is often used because of its simplicity [52–60], but it cannot account for current densities. The latter is especially troublesome if, like in this work, eddy-current reaction field has to be accounted for. Moreover, nowadays the majority of FB models uses the magnetic vector potential [43, 61–69], especially in two-dimensional models, where the MVP reduces to a scalar. It is therefore obvious to use the magnetic vector potential in this work.

1.3.2 Spatial coordinate system

In the following, it will be assumed that the magnetic field is two-dimensional. This assumption greatly reduces the model's complexity and, more importantly, its computational time. It does of course introduce an error, e.g. due to the neglecting of the end windings. However, it was earlier shown that, even for machines with a relatively short axial length, this error is small [70].
Literature describes two-dimensional models in Cartesian [71–73], polar [43, 51, 53–56, 60, 63, 65, 68, 74–76] and cylindrical [77–80] coordinates. Evidently, the best-suited coordinate system depends on the studied machine's geometry. As the two-dimensional approximation of the magnetic fields under consideration is circular, the polar coordinate system is the logical choice here. This is illustrated in Figure 1.2, where r is the radial coordinate and ϕ is the angular coordinate.

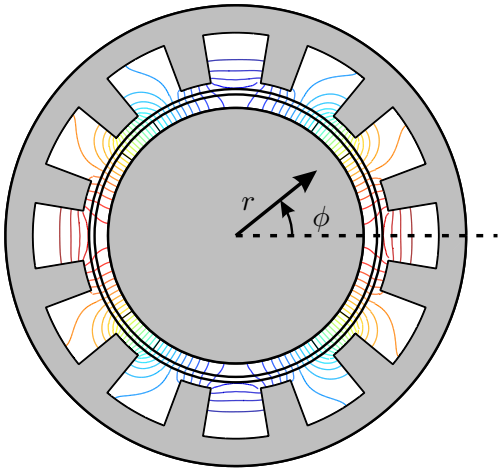

Figure 1.2: Illustration of the polar coordinate system

1.3.3 Time dependency

In Fourier-based models, time dependency can be accounted for in two ways; directly [43, 68, 81, 82] or through multiple static calculations [79, 83–86]. When using multiple static calculations, the time is discretized and the magnetic field is recalculated for every instance of time. This technique has the advantage of simplicity and a very low computational time for every individual static calculation. However, it cannot fully account for the eddy-current reaction field. Moreover, as the field has to be recalculated for every instance of time, the advantage of a low

computational time may be nullified if a lot of time instances have to be considered. These disadvantages can be overcome by directly accounting for the time dependency, i.e. the magnetic potential is not only a function of space, but of time as well. It is therefore clear that time-dependency will be directly accounted for in this work.

1.3.4 Source terms

Traditionally, Fourier-based models can account for two types of source terms; permanent-magnetic materials and externally-imposed current densities. Both can either be imposed directly through the equations for the magnetic potential [43, 64, 68, 87] or using equivalent current sheets [54, 62, 76, 88–90]. The advantage of current sheets is that they are often easier to implement in three-dimensional problems. Moreover, using current sheets is also the most common workaround for the MSP's disability to account for current densities. On the other hand, using current sheets implies a loss of accuracy [75] and is less straightforward than directly imposing the source terms. Therefore, this work will directly account for the source terms.
It should be noted that the vast majority of modern electric machines is powered using a voltage source, especially in high-speed machines. As the existing literature can only cope with the currents resulting from these voltage sources, one of the goals of this PhD is to improve the existing FB model by providing a way to directly account for voltage sources.

1.3.5 Slotting

Accounting for slotting effects is one of the largest challenges within FB modeling. Literature describes three major techniques to model slotted structures.
A first possibility is to use conformal mapping techniques to simplify the machine's geometry to its slotless equivalent [55, 91–95]. After having solved the magnetic field of the slotless machine, the result is mapped back to the original geometry. Although conformal mapping may result in some of the simplest and computationally most efficient models [55], the accuracy of these models is not very high [73, 96]. Increasing the accuracy implies increasing the complexity of the mapping functions [92, 93].
Therefore, nowadays an alternative technique, called the exact subdomain technique is mainly used [50, 64, 67, 86, 97, 98]. This technique considers each slot separately. Although this approach results in larger computational times, it is very accurate and gives a good insight in the effect of the slots. The major downfall is that an infinite permeability of the slots has to be assumed. To overcome that issue, Dubas *et al.* have recently proposed an extension of the exact subdomain technique using superposition [69].
A third technique to account for slotted structures has recently be described by

Sprangers *et al.* in [99]. In this technique, the spatial dependence of the permeability is directly accounted for. Despite the technique's very straightforward approach, it is relatively complex and suffers from inaccuracies due to the Gibb's phenomenon [96].
Because of its accuracy and the large insight it gives, the exact subdomain technique was adopted in this work. Although Dubas' superposition technique and Sprangers' technique with spatially-dependent permeabilities would be an interesting addition, high-speed PMSM typically operate at low induction levels. The limitation of infinite permeabilities is therefore not crucial.

1.3.6 Conclusion

In the above, five aspects of FB models were discussed. Based on that discussion, it was decided that the model in this PhD will be based on a magnetic vector potential formulation of the problem. The model will be formulated in a 2D polar coordinate system and its time dependency will be accounted for directly. The source terms will be implemented directly as well and slotting will be accounted for with the exact subdomain technique.
Note that this section has been limited to a brief discussion of the most important aspects within Fourier-based modeling. Relying on the mathematics presented in Chapters 2 and 3, a more extensive discussion on the different techniques within FB modeling is presented in Chapter 4. By combining that discussion to an overview of the literature, Chapter 4 provides an interesting guide for anyone who wants to build a FB model.

1.4 Scientific goals

It was already mentioned that the goal of this PhD is to study and develop electromagnetic modeling tools for high-speed machines. In the following, that goal is divided in two parts and described in more detail. But first of all, it should be noted that the aim of this thesis is to provide modeling tools for a very broad range of high-speed PMSMs, rather than studying one particular case. Moreover, a lot of the presented results are applicable for permanent-magnet synchronous machines that are operated at normal, or low, speeds as well.

- The first goal of this work is to contribute to a faster, more flexible and more accurate calculation of the magnetic field. This goal is achieved by providing an in-depth study of the physical and mathematical background of Fourier-based modeling. In addition, a study on how to reduce the computational time of FB models to an absolute minimum is performed and the implementation of voltage sources is discussed.
  With respect to the calculation of the magnetic field, the main contributions of this work are: a very general approach that accounts for both slotting and

eddy-current reaction field, an extensive discussion on reducing the computational time of FB models, a direct coupling with the machine's electrical equations in order to account for voltage sources and an overview of the FB model's possibilities and most important literature.

- Secondly, this PhD aims at providing more insight in surface-mounted PMSMs with a shielding cylinder by studying their electromagnetic output quantities, based on the FB model. This goal is achieved by improving the post-processing of FB models and by performing parameter studies of the output quantities.
  Concerning the study of physical output quantities, this PhD has contributed to the existing literature by introducing the concept of torque components and by studying the effect of the SC's design on the performance of high-speed PMSMs.

Note that, in addition to the main goals as described above, a test setup for high-speed PMSMs was developed at Ghent University. The goal of that setup was to provide the research group a practical expertise in high-speed applications. As this setup isn't really in the scope of this work's main goals, it will only be discussed briefly.

1.5 Outline

In accordance with the PhD's goals, this work is structured in three parts.
The first part, which covers Chapters 2-4, provides an extensive discussion on Fourier-based modeling. Chapter 2 focuses on the physical background of Fourier-based modeling, it discusses the magneto-quasi static (MQS) approximation of Maxwell's equations and introduces the magnetic vector potential. Chapter 3 applies the results from Chapter 2 to model PMSMs in general and high-speed PMSMs in particular. This includes sketching the model's context, introducing the subdomain technique and validating the obtained results. In Chapter 4, the knowledge obtained from Chapters 2 and 3 is applied to present an overview of the different possibilities within Fourier-based modeling. By coupling that overview to the existing literature, it may be used as a guideline for anyone who is interested in working with Fourier-based models.
In the second part, i.e. in Chapters 5-8, two improvements of the existing Fourier-based modeling technique are presented. Chapter 5 introduces techniques to reduce the computational time of Fourier-based modeling and briefly discusses some computational issues related to Fourier-based modeling. Chapter 6 presents a technique to account for voltage sources, as opposed to the traditional current-density sources in Fourier-based modeling.
The third part of the PhD focuses on the machine's electromagnetic quantities and obtaining more insight in the high-speed operation of PMSMs. This is done in

Chapters 7-9. In Chapter 7, the calculation of the machine's magnetic flux density, back electromotive force, torque and eddy-current losses is discussed. The chapter also introduces a division of the torque in two components. In Chapter 8, the experimental setup that has been developed in the scope of this PhD is briefly introduced and used to validate some of the previously made calculations. Chapter 9 presents a number of parameter studies that provide some interesting insights in high-speed PMSMs in general and their shielding cylinder in particular.
Finally, Chapter 10 concludes this work.

1.6 Publications

Articles in International SCI Journals

An overview of peer-reviewed journal papers that were published in the scope of this PhD:

- B. Hannon, P. Sergeant and L. Dupré, "2-D Analytical Subdomain Model of a Slotted PMSM With Shielding Cylinder", *Magnetics, IEEE Transactions on*, vol. 50, no. 7, 10 pages, 2014
- B. Hannon, P. Sergeant and L. Dupré, "Voltage Sources in 2D Fourier-Based Analytical Models of Electric Machines", *Mathematical Problems in Engineering*, vol. 2015, Article ID 195410, 8 pages, 2015
- A. Hemeida, B. Hannon, H. Vansompel and P. Sergeant, "Comparison of Three Analytical Methods for the Precise Calculation of Cogging Torque and Torque Ripple in Axial Flux PM Machines", *Mathematical Problems in Engineering*, vol. 2016, Article ID 2171547, 14 pages, 2016
- B. Hannon, P. Sergeant and L. Dupré, "Torque and torque components in high-speed permanent-magnet synchronous machines with a shielding cylinder", *Mathematics and Computers in Simulation*, vol. 130, pp. 70-80, 2016
- B. Hannon, P. Sergeant and L. Dupré, "Time- and Spatial-Harmonic Content in Synchronous Electrical Machines", *Magnetics, IEEE Transactions on*, vol. 53, no. 3, 11 pages, 2017
- B. Hannon, P. Sergeant and L. Dupré, "Study of the Effect of a Shielding Cylinder on the Torque in a Permanent-Magnet Synchronous Machine Considering Two Torque-Producing Mechanisms", *Magnetics, IEEE Transactions on*, in press, 2017
- B. Hannon, P. Sergeant and L. Dupré, "Computational-time reduction of Fourier-Based Analytical Models", *Energy Conversion, IEEE Transactions on*, in press, 2017

Articles in conference proceedings

An overview of the most important conference papers that were published in the scope of this PhD:

- B. Hannon, P. Sergeant and L. Dupré, “2D analytical torque study of slotted high-speed PMSMs considering pole pairs, slots per pole per phase and coil throw”, *International Conference on Electrical Machines (ICEM), 2014*, pp. 2524-2530, 2014
- B. Hannon, P. Sergeant and L. Dupré, “2D analytical torque study of slotless and slotted PMSM topologies at high-speed operation”, *ELECTRIMACS, 2014*, pp. 248-231, 2014
- B. Hannon, P. Sergeant and L. Dupré, “Time- and spatial-harmonic content in electrical machines and its application in Fourier-based models”, *International Conference on Electrical Machines (ICEM), 2016*, pp. 592-598, 2016

Chapter 2

Problem formulation

One of the main goals of this work is predicting the magnetic field in high-speed, permanent-magnet synchronous machines, thereby enabling the calculation of various machine properties, such as torque production, losses, etc. As electromagnetic phenomena are governed by Maxwell's equations and the electromagnetic constitutive relations, the study of electromagnetic problems relies on a mathematical formulation of these physical laws. This chapter aims at providing such a formulation for high-speed machines. The discussion is presented as generally as possible, so that the results are applicable for a wide range of electric actuators.

In the first two sections of this chapter, a very general discussion on electromagnetic problems in stationary and moving materials is presented. In Section 2.3, the magneto quasi-static (MQS) approximation is introduced. Section 2.4 introduces the use of the magnetic vector potential, which results in the final mathematical formulation of the studied problem. The chapter is concluded in Section 2.5.

2.1 Stationary problems

Consider the situation illustrated in Figure 2.1; an electromagnetic problem in an arbitrary domain D is studied using reference system (x_1, x_2, x_3). The problem is stationary, which implies that D does not move with regard to (x_1, x_2, x_3).

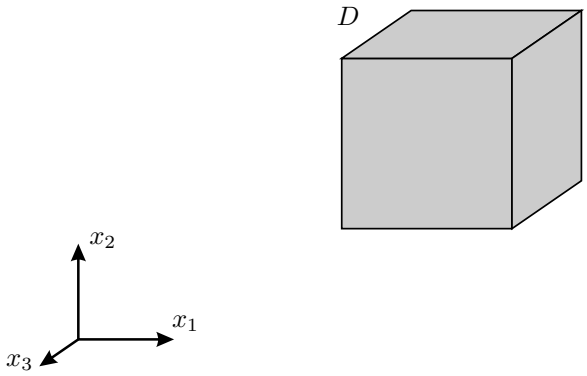

Figure 2.1: A stationary problem; D does not move with respect to (x_1, x_2, x_3)

In the following, a mathematical formulation for the generalized electromagnetic problem of Figure 2.1 is derived. This is done by evaluating Maxwell's equations, the boundary conditions and the constitutive relations.

Maxwell's equations

Maxwell's equations are the starting point for this discussion. In their differential form, these cornerstones of electromagnetism are written as:

Faraday's law	$\nabla \times \mathbf{E} = -\dfrac{\partial \mathbf{B}}{\partial t}$	(2.1a)
Ampère's law	$\nabla \times \mathbf{H} = \mathbf{J} + \dfrac{\partial \mathbf{D}}{\partial t}$	(2.1b)
Gauss' law for electric fields	$\nabla \cdot \mathbf{D} = \rho_e$	(2.1c)
Gauss' law for magnetism	$\nabla \cdot \mathbf{B} = 0$	(2.1d)

Where the vectors **E**, **H**, **D**, **B** and **J** refer to the electric field strength, the magnetic field strength, the electric flux density, the magnetic flux density and the current density respectively. The electric charge density is referred to by ρ_e and the time by t. All of the electromagnetic quantities are spatially referred to the (x_1, x_2, x_3) system.
Note that the combination of Ampère's and Gauss' law implies conservation of the

electric charge:

$$\nabla \cdot \mathbf{J} + \frac{\partial \rho_e}{\partial t} = 0 \tag{2.2}$$

Boundary conditions

In order to ensure physically correct behavior on the boundaries of the studied problem, a set of boundary conditions for **B**, **D**, **H** and **E** has to be imposed. As shown in the following, these conditions are directly derived from Maxwell's equations.
Consider an infinitesimal small pillbox P at the boundary between domains ν and $\nu + 1$, as illustrated in Figure 2.2.

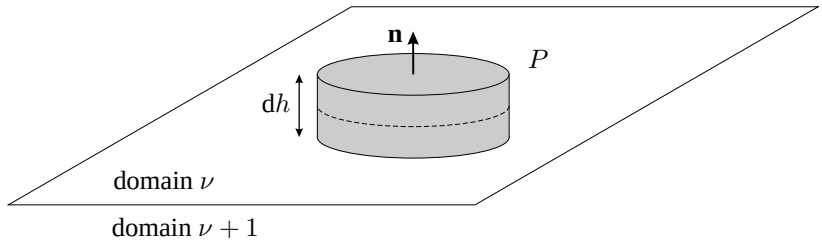

Figure 2.2: A pillbox at the boundary between domains ν and $\nu + 1$

As **B** is a solenoidal vector field (2.1d), the integration of its divergence over the volume of the pillbox is zero. Accounting for the divergence theorem, this can mathematically be written as:

$$\iiint_P \nabla \cdot \mathbf{B} \, \mathrm{d}V = \oiint_{\partial P} \mathbf{B} \cdot \mathbf{n} \, \mathrm{d}s = 0 \tag{2.3}$$

where ∂P is the pillbox' boundary. The surface integral can be split in a part related to the top, a part related to the bottom and a part related to the side of the pillbox. As **B** is finite, letting $\mathrm{d}h \to 0$ implies that the side does not contribute to the integral, i.e. there is no magnetic flux through the side of the pillbox. The above can then be rewritten as:

$$\int_{\text{top}} \mathbf{B}^{(\nu)} \cdot \mathbf{n} \, \mathrm{d}s - \int_{\text{bottom}} \mathbf{B}^{(\nu+1)} \cdot \mathbf{n} \, \mathrm{d}s = 0 \tag{2.4}$$

where $\mathbf{B}^{(\nu)}$ is the magnetic flux density in domain ν and $\mathbf{B}^{(\nu+1)}$ is the magnetic flux density in domain $\nu + 1$.
As the pillbox is assumed infinitely small, (2.4) implies that in every point of the boundary, the following condition for **B** has to be satisfied:

$$\mathbf{n} \cdot \left(\mathbf{B}^{(\nu)} - \mathbf{B}^{(\nu+1)} \right) = 0 \tag{2.5}$$

The above is a condition for **B** at the boundary between domains ν and $\nu+1$.
In a completely similar way the boundary condition for **D** can be found as:

$$\mathbf{n} \cdot \left(\mathbf{D}^{(\nu)} - \mathbf{D}^{(\nu+1)} \right) = \sigma_e \tag{2.6}$$

where σ_e is the electric surface charge density on the considered boundary.
Next, consider an infinitesimal rectangle L at the boundary between domains ν and $\nu+1$, as illustrated in Figure 2.3.

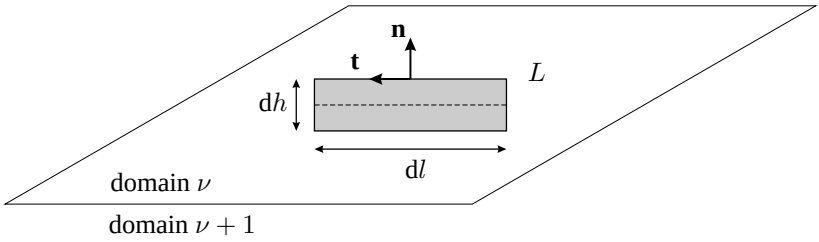

Figure 2.3: A rectangle at the boundary between domains ν and $\nu+1$

Accounting for Ampère's law (2.1b), integration of the curl of **H** over the surface of L can be written as:

$$\iint_L \nabla \times \mathbf{H} \cdot \mathrm{d}\mathbf{s} = \iint_L \left(\mathbf{J} + \frac{\partial \mathbf{D}}{\partial t} \right) \cdot \mathrm{d}\mathbf{s} \tag{2.7}$$

This can be rewritten with the help of Stoke's theorem. Moreover, it is again assumed that $\mathrm{d}h \to 0$, implying that the vertical sides of the rectangle do not contribute to the resulting line integral. This gives:

$$\int_{\text{top}} \mathbf{H}^{(\nu)} \cdot \mathbf{t}\, \mathrm{d}l - \int_{\text{bottom}} \mathbf{H}^{(\nu+1)} \cdot \mathbf{t}\, \mathrm{d}l = \iint_L \left(\mathbf{J} + \frac{\partial \mathbf{D}}{\partial t} \right) \cdot \mathrm{d}\mathbf{s} \tag{2.8}$$

where $\mathbf{H}^{(\nu)}$ is the magnetic field strength in domain ν and $\mathbf{H}^{(\nu+1)}$ is the magnetic field strength in domain $\nu+1$.
The rectangle is infinitesimally small and **D** is finite on the boundary. This implies that the electric flux through L reaches zero as the surface of the rectangle reaches zero. In contrast to the electric flux, the current density can be infinite on the boundary. This may happen in the ideal case of infinite conductivity. Therefore, the flux of the surface current density on the considered boundary does not have to equal zero. The boundary condition for the magnetic field strength can then be written as:

$$\mathbf{n} \times \left(\mathbf{H}^{(\nu)} - \mathbf{H}^{(\nu+1)} \right) = \mathbf{J}_s \tag{2.9}$$

with $\mathbf{J}_s$ the surface current density of the considered boundary.
Chapter 1 showed that, despite the fact that it implies a lower accuracy, some authors do consider surface current densities in order to simplify their calculations.
Using the same technique as for $\mathbf{H}$, the boundary condition for the electric field strength can be found as:

$$\mathbf{n} \times \left(\mathbf{E}^{(\nu)} - \mathbf{E}^{(\nu+1)} \right) = 0 \tag{2.10}$$

The boundary conditions for static problems are thus listed as in (2.11).

$$\mathbf{n} \cdot \left(\mathbf{B}^{(\nu)} - \mathbf{B}^{(\nu+1)} \right) = 0 \tag{2.11a}$$

$$\mathbf{n} \cdot \left(\mathbf{D}^{(\nu)} - \mathbf{D}^{(\nu+1)} \right) = \sigma_e \tag{2.11b}$$

$$\mathbf{n} \times \left(\mathbf{H}^{(\nu)} - \mathbf{H}^{(\nu+1)} \right) = \mathbf{J}_s \tag{2.11c}$$

$$\mathbf{n} \times \left(\mathbf{E}^{(\nu)} - \mathbf{E}^{(\nu+1)} \right) = 0 \tag{2.11d}$$

Constitutive relations

Maxwell's equations are supplemented with the constitutive relations, which link the electric and magnetic field strengths to their respective flux densities. In an absolute vacuum, these relations are written as:

$$\mathbf{D} = \epsilon_0 \mathbf{E} \tag{2.12a}$$

$$\mathbf{B} = \mu_0 \mathbf{H} \tag{2.12b}$$

where ϵ_0 and μ_0 are the electric permittivity and the magnetic permeability of vacuum. As (2.12) is only valid in an absolute vacuum, it is insufficient to model electric machines, where matter is present.
When studying electromagnetic problems in matter, the material's electric and magnetic dipole moments have to be accounted for. These dipole moments have a component that is permanent and a component that is induced by an external field. Accounting for the dipole moments is done by introducing the polarization and the magnetization vectors, i.e. $\mathbf{P}$ and $\mathbf{M}$. The constitutive relations are then rewritten as:

$$\begin{aligned} \mathbf{D} &= \epsilon_0 \mathbf{E} + \mathbf{P} \\ &= \epsilon_0 \mathbf{E} + \mathbf{P}_E + \mathbf{P}_0 \end{aligned} \tag{2.13a}$$

$$\begin{aligned} \mathbf{B} &= \mu_0 \left(\mathbf{H} + \mathbf{M} \right) \\ &= \mu_0 \left(\mathbf{H} + \mathbf{M}_H + \mathbf{M}_0 \right) \end{aligned} \tag{2.13b}$$

where $\mathbf{P}_E$ is the component of $\mathbf{P}$ that is induced by an external electric field and $\mathbf{P}_0$ is the permanent polarization of the material. Similarly, $\mathbf{M}_H$ is the component of $\mathbf{M}$ that is induced by an external magnetic field and $\mathbf{M}_0$ is the permanent magnetization.
If the studied material is assumed linear and isotropic, which is a common assumption in analytical models, the relations between $\mathbf{P}_E$ and $\mathbf{E}$ and between $\mathbf{M}_H$ and $\mathbf{H}$ are determined by a constant electric and magnetic susceptibility, i.e. χ_e and χ_m.

$$\mathbf{P}_E = \epsilon_0 \chi_e \mathbf{E} \tag{2.14a}$$
$$\mathbf{M}_H = \chi_m \mathbf{H} \tag{2.14b}$$

The constitutive relations of (2.13) can then be written in terms of the material's electric permittivity (ϵ) and its magnetic permeability (μ):

$$\begin{aligned} \mathbf{D} &= \epsilon_0 (1 + \chi_e) \mathbf{E} + \mathbf{P}_0 \\ &= \epsilon_0 \epsilon_r \mathbf{E} + \mathbf{P}_0 \\ &= \epsilon \mathbf{E} + \mathbf{P}_0 \end{aligned} \tag{2.15a}$$

$$\begin{aligned} \mathbf{B} &= \mu_0 (1 + \chi_m) \mathbf{H} + \mu_0 \mathbf{M}_0 \\ &= \mu_0 \mu_r \mathbf{H} + \mu_0 \mathbf{M}_0 \\ &= \mu \mathbf{H} + \mu_0 \mathbf{M}_0 \end{aligned} \tag{2.15b}$$

where ϵ_r and μ_r are the material's relative permittivity and relative permeability respectively.
As opposed to vacuum, materials may conduct an electric current when exposed to an electric field. This implies a third constitutive relation, that expresses the relation between the electric field strength and the current density:

$$\mathbf{J} = \sigma \mathbf{E} \tag{2.16}$$

where σ is the conductivity of the material.
Note that permanent magnetic materials are often characterized by their residual magnetic flux density $(\mathbf{B}_0 = \mu_0 \mathbf{M}_0)$ instead of their residual magnetization vector. The constitutive relations in static problems can thus be written as:

$$\mathbf{J} = \sigma \mathbf{E} \tag{2.17a}$$
$$\mathbf{D} = \epsilon \mathbf{E} + \mathbf{P}_0 \tag{2.17b}$$
$$\mathbf{B} = \mu \mathbf{H} + \mathbf{B}_0 \tag{2.17c}$$

Conclusion

The combination of Maxwell's equations (2.1), the boundary conditions (2.11) and the constitutive relations (2.17) now forms a complete mathematical formulation for the problem of Figure 2.1.

2.2 Problems with motion

Typically, authors of analytical models for electric actuators disregard movement. However, considering movement is mandatory if, for example, eddy-currents have to be taken into account. As the effect of eddy-currents may be significant in high-speed actuators, the aim of this section is to provide a theoretical background that allows accounting for moving materials.
Consider a domain D that is moving at a speed **v** with respect to the reference frame (x_1, x_2, x_3). To cope with such problems, a second reference frame, fixed to the moving domain, is considered. This reference system, and all of the quantities expressed within it, are indicated with primes.
The situation is illustrated in Figure 2.4.

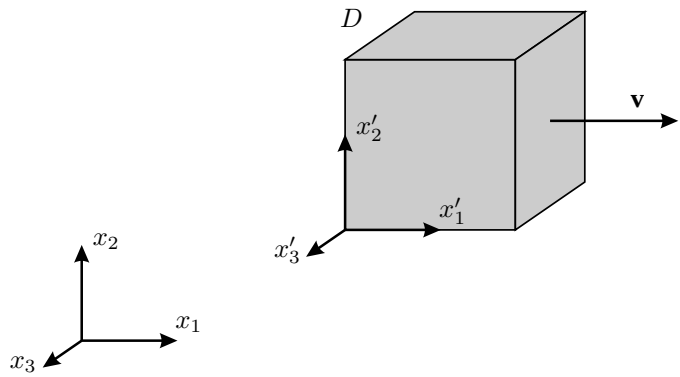

Figure 2.4: A moving problem; D moves with respect to (x_1, x_2, x_3)

Lorentz' transformations can now be used to translate quantities from the unprimed reference system (x_1, x_2, x_3) to the primed reference system (x_1', x_2', x_3') [100,

101]:

$$\mathbf{E}' = \gamma\left(\mathbf{E} - \frac{\gamma-1}{\gamma}\frac{\mathbf{v}\,(\mathbf{v}\cdot\mathbf{E})}{\mathbf{v}^2} + \mathbf{v}\times\mathbf{B}\right) \tag{2.18a}$$

$$\mathbf{H}' = \gamma\left(\mathbf{H} - \frac{\gamma-1}{\gamma}\frac{\mathbf{v}\,(\mathbf{v}\cdot\mathbf{H})}{\mathbf{v}^2} - \mathbf{v}\times\mathbf{D}\right) \tag{2.18b}$$

$$\mathbf{M}' = \gamma\left(\mathbf{M} - \frac{\gamma-1}{\gamma}\frac{\mathbf{v}\,(\mathbf{v}\cdot\mathbf{M})}{\mathbf{v}^2} + \mathbf{v}\times\mathbf{P}\right) \tag{2.18c}$$

$$\mathbf{D}' = \gamma\left(\mathbf{D} - \frac{\gamma-1}{\gamma}\frac{\mathbf{v}\,(\mathbf{v}\cdot\mathbf{D})}{\mathbf{v}^2} + \frac{\mathbf{v}\times\mathbf{H}}{c^2}\right) \tag{2.18d}$$

$$\mathbf{B}' = \gamma\left(\mathbf{B} - \frac{\gamma-1}{\gamma}\frac{\mathbf{v}\,(\mathbf{v}\cdot\mathbf{B})}{\mathbf{v}^2} - \frac{\mathbf{v}\times\mathbf{E}}{c^2}\right) \tag{2.18e}$$

$$\mathbf{P}' = \gamma\left(\mathbf{P} - \frac{\gamma-1}{\gamma}\frac{\mathbf{v}\,(\mathbf{v}\cdot\mathbf{P})}{\mathbf{v}^2} - \frac{\mathbf{v}\times\mathbf{M}}{c^2}\right) \tag{2.18f}$$

$$\mathbf{J}' = \gamma\left(\frac{\mathbf{J}}{\gamma} + \frac{\gamma-1}{\gamma}\frac{\mathbf{v}\,(\mathbf{v}\cdot\mathbf{J})}{\mathbf{v}^2} - \rho\mathbf{v}\right) \tag{2.18g}$$

$$\rho_e' = \gamma\left(\rho_e - \frac{\mathbf{J}\cdot\mathbf{v}}{c^2}\right) \tag{2.18h}$$

where c is the speed of light and γ is the Fitzgerald-Lorentz contraction factor:

$$\gamma = \frac{1}{\sqrt{1 - \frac{|\mathbf{v}|^2}{c^2}}} \tag{2.19}$$

Maxwell's equations

Maxwell's equations are Lorentz-invariant; they are not affected by Lorentz' transformations. This implies that, as expected, Maxwell's equations (2.1) remain valid, regardless which reference system is used.

Boundary conditions

Relative movement of the boundary does have an effect on the boundary conditions. Evidently, if the electromagnetic quantities are expressed in the primed system, the static boundary conditions (2.11) apply. Translating these boundary conditions to the unprimed system is done using Lorentz' transformations (2.18). The calculus is quite extensive, but Costen [102] found that the resulting conditions

are:

$$\mathbf{n} \cdot \left(\mathbf{B}^{(\nu)} - \mathbf{B}^{(\nu+1)} \right) = 0 \tag{2.20a}$$

$$\mathbf{n} \cdot \left(\mathbf{D}^{(\nu)} - \mathbf{D}^{(\nu+1)} \right) = \sigma_e \tag{2.20b}$$

$$\mathbf{n} \times \left(\mathbf{H}^{(\nu)} - \mathbf{H}^{(\nu+1)} \right) + (\mathbf{n} \cdot \mathbf{v}) \left(\mathbf{D}^{(\nu)} - \mathbf{D}^{(\nu+1)} \right) = \mathbf{J}_s \tag{2.20c}$$

$$\mathbf{n} \times \left(\mathbf{E}^{(\nu)} - \mathbf{E}^{(\nu+1)} \right) - (\mathbf{n} \cdot \mathbf{v}) \left(\mathbf{B}^{(\nu)} - \mathbf{B}^{(\nu+1)} \right) = 0 \tag{2.20d}$$

Note that the boundary conditions are only affected by movement if the velocity has a component that is normal to the boundary's surface.

Constitutive relations

Starting from Minkowski's crucial hypothesis that the constitutive relations for stationary matter are valid in the primed system, i.e. $\mathbf{J}' = \sigma \mathbf{E}'$, $\mathbf{D}' = \epsilon \mathbf{E}'$ and $\mathbf{B}' = \mu \mathbf{H}'$, the constitutive relations for moving matter can be found by considering the Lorentz transformations:

$$\frac{\mathbf{J}}{\gamma} + \frac{\gamma - 1}{\gamma} \frac{\mathbf{v}\,(\mathbf{v} \cdot \mathbf{J})}{\mathbf{v}^2} - \rho \mathbf{v} = \sigma \left(\mathbf{E} - \frac{\gamma - 1}{\gamma} \frac{\mathbf{v}\,(\mathbf{v} \cdot \mathbf{E})}{\mathbf{v}^2} + \mathbf{v} \times \mathbf{B} \right) \tag{2.21a}$$

$$\mathbf{D} - \frac{\gamma - 1}{\gamma} \frac{\mathbf{v}\,(\mathbf{v} \cdot \mathbf{D})}{\mathbf{v}^2} + \frac{\mathbf{v} \times \mathbf{H}}{c^2} = \epsilon \left(\mathbf{E} - \frac{\gamma - 1}{\gamma} \frac{\mathbf{v}\,(\mathbf{v} \cdot \mathbf{E})}{\mathbf{v}^2} + \mathbf{v} \times \mathbf{B} \right) \tag{2.21b}$$

$$\mathbf{B} - \frac{\gamma - 1}{\gamma} \frac{\mathbf{v}\,(\mathbf{v} \cdot \mathbf{B})}{\mathbf{v}^2} - \frac{\mathbf{v} \times \mathbf{E}}{c^2} = \mu \left(\mathbf{H} - \frac{\gamma - 1}{\gamma} \frac{\mathbf{v}\,(\mathbf{v} \cdot \mathbf{H})}{\mathbf{v}^2} - \mathbf{v} \times \mathbf{D} \right) \tag{2.21c}$$

Conclusion

Similar as for stationary problems, moving problems are fully described by the above Maxwell equations, boundary conditions and constitutive relations.

2.3 Magneto quasi-static problems

Maxwell's equations, the boundary conditions and the constitutive relations are very generally formulated in the previous sections. However, in the scope of electric actuators, the so-called magneto quasi-static (MQS) approximation, which is also known as the magnetic limit of Galilean electromagnetism, can be used [100, 101]. This approximation consists of two aspects. The *quasi-static* aspect relates to the propagation time of variations in the magnetic field. The *magneto* in magneto quasi-static implies that the magnetic field is dominant with respect to the electric field.

A problem can be considered quasi-static if time-dependent variations are instantly propagated throughout the entire geometry. Mathematically, this condition is written as:

$$f \ll \frac{c}{2\pi l_\lambda} \tag{2.22}$$

where f is the frequency of the time-dependent variations and l_λ is the characteristic dimension of the studied problem. In a rotating, radial-flux machine for example, f is the frequency of the current and l_λ is the machine's diameter.
Evidently, (2.22) implies that the relative speed of the studied materials is much smaller than the speed of light ($\|\mathbf{v}\| \ll c$). This implies that $\gamma \approx 1$. In electric actuators, the quasi-static condition is practically always valid.
If in quasi-static problems the energy of the magnetic field is much larger than the energy of the electric field, the problem can further be simplified to a MQS problem. A commonly used intuitive method to determine whether the magnetic field is dominant is to regard the time-invariant limit of the problem, i.e. the frequency of all of the problem's time-dependent variables is brought to zero. A problem is considered MQS if there is no electric field in the time-invariant limit. This is clearly the case in electric actuators where the source terms in the time-invariant limit are DC current densities and permanent-magnetic materials.
It can easily be reasoned that, if the electric field disappears in the time-invariant limit, the effect of electric charges is negligible. Indeed, the MQS approximation implies neglecting the effect of electric charges.
As indicated by Zangwill [100] and Rousseaux [101], the Lorentz transformations of electromagnetic quantities (2.18) are greatly reduced in MQS problems:

$$\mathbf{E}' = \mathbf{E} + \mathbf{v} \times \mathbf{B} \tag{2.23a}$$
$$\mathbf{H}' = \mathbf{H} \tag{2.23b}$$
$$\mathbf{M}' = \mathbf{M} \tag{2.23c}$$
$$\mathbf{D}' = \mathbf{D} + \frac{\mathbf{v} \times \mathbf{H}}{c^2} \tag{2.23d}$$
$$\mathbf{B}' = \mathbf{B} \tag{2.23e}$$
$$\mathbf{P}' = \mathbf{P} - \frac{\mathbf{v} \times \mathbf{M}}{c^2} \tag{2.23f}$$
$$\mathbf{J}' = \mathbf{J} \tag{2.23g}$$
$$\rho_e' = \rho_e - \frac{\mathbf{J} \cdot \mathbf{v}}{c^2} \tag{2.23h}$$

In the following, Maxwell's equations, the boundary conditions and the constitutive relations in MQS problems are considered.

Maxwell's equations

The Maxwell equations that have to be solved in a MQS problem are written as:

$$\text{Faraday's law} \qquad \nabla \times \mathbf{E} = -\frac{\partial \mathbf{B}}{\partial t} \tag{2.24a}$$

$$\text{Ampère's law} \qquad \nabla \times \mathbf{H} = \mathbf{J} \tag{2.24b}$$

$$\text{Gauss' law for magnetism} \qquad \nabla \cdot \mathbf{B} = 0 \tag{2.24c}$$

It can easily be seen that the influence of electric charges is disregarded. This greatly simplifies the following calculus.

Boundary conditions

As the focus is on the magnetic field, it is sufficient to only regard the boundary conditions for **B** and **H**. In a MQS problem, these conditions are written as:

$$\mathbf{n} \cdot \left(\mathbf{B}^{(\nu)} - \mathbf{B}^{(\nu+1)} \right) = 0 \tag{2.25a}$$

$$\mathbf{n} \times \left(\mathbf{H}^{(\nu)} - \mathbf{H}^{(\nu+1)} \right) = \mathbf{J}_s \tag{2.25b}$$

From (2.25), it can be seen that the MQS approximation disregards the effect of movement on boundary conditions.

Constitutive relations

The constitutive relations to be accounted for in MQS problems are found by substituting (2.23) in (2.17):

$$\mathbf{J} = \sigma \left(\mathbf{E} + \mathbf{v} \times \mathbf{B} \right) \tag{2.26a}$$

$$\mathbf{B} = \mu \mathbf{H} + \mathbf{B}_0 \tag{2.26b}$$

Conclusion

The mathematical formulation of MQS problems is fully described by (2.24)-(2.26). It is clear that the MQS approximation suffices when the goal is to model electric actuators. For that reason, in the rest of this work, only MQS problems are considered. This implies that (2.24), (2.25) and (2.26) form the basis for the model that will be constructed in the following sections.

2.4 Potential formulation

The above mathematical formulation of MQS problems consists of three differential equations (2.24), two boundary conditions (2.25) and two constitutive relations (2.26). Mathematically, this problem is difficult to solve. Therefore, a potential formulation is introduced to rewrite the problem.
The magnetic vector potential **A**, which is a vector quantity, is defined through its curl:

$$\nabla \times \mathbf{A} = \mathbf{B} \tag{2.27}$$

For a complete description of MQS problems, the MVP has to be combined with the electric scalar potential (ESP) [51, 103]. The ESP is indicated as V and defined through its gradient:

$$\nabla V = -\left(\mathbf{E} + \frac{\partial \mathbf{A}}{\partial t}\right) \tag{2.28}$$

Governing equation

In the following, a differential equation for the MVP is derived based on Maxwell's equations (2.24) and the constitutive relations (2.26). This differential equation is called the governing equation. The derivation of the governing equation for the MVP requires some calculus. In a first step, the definition of the MVP (2.27) is substituted in Faraday's law:

$$\nabla \times \mathbf{E} = -\frac{\partial}{\partial t} \nabla \times \mathbf{A} \tag{2.29}$$

Integration of the above gives:

$$\mathbf{E} = -\left(\frac{\partial \mathbf{A}}{\partial t} + \nabla V\right) \tag{2.30}$$

where the integration constant is the gradient of the electric scalar potential. Indeed, (2.30) matches the definition of V (2.28).
A second step in the derivation is choosing a gauge. This is important because the above potential formulation is not uniquely defined. Indeed, if f is an arbitrary scalar field, an alternative formulation can be defined as:

$$\begin{cases} \mathbf{A}_{alt} &= \mathbf{A} + \nabla f \\ V_{alt} &= V - \dfrac{\partial f}{\partial t} \end{cases} \tag{2.31}$$

The lack of uniqueness can now be illustrated by considering the magnetic flux density:

$$\begin{aligned} \mathbf{B} &= \nabla \times \mathbf{A} \\ &= \nabla \times (\mathbf{A} + \nabla f) \\ &= \nabla \times \mathbf{A}_{alt} \end{aligned} \tag{2.32}$$

and the electric field strength:

$$\begin{aligned}\mathbf{E} &= -\left(\frac{\partial}{\partial t}\mathbf{A} + \nabla V\right) \\ &= -\left(\frac{\partial}{\partial t}\mathbf{A} + \frac{\partial \nabla f}{\partial t} + \nabla V - \nabla\frac{\partial f}{\partial t}\right) \\ &= -\left(\frac{\partial}{\partial t}\mathbf{A}_{alt} + \nabla V_{alt}\right)\end{aligned} \tag{2.33}$$

This redundant degree of freedom is tackled by introducing a gauge. When using the MQS approximation, the Coulomb gauge ($\nabla \cdot \mathbf{A} = 0$) is most commonly used. Note that, in the MQS approximation, Coulomb's gauge is Lorentz invariant.
For the third and final step of the derivation, Ampère's law (2.24b) is combined with the definition of the MVP (2.27), the constitutive relations (2.26) and the equation for the electric field strength (2.30):

$$\nabla \times \nabla \times \mathbf{A} = -\mu\sigma\left(\frac{\partial \mathbf{A}}{\partial t} + \nabla V - \mathbf{v} \times (\nabla \times \mathbf{A})\right) + \nabla \times \mathbf{B}_0 \tag{2.34}$$

Using the identity for the curl of the curl and Coulomb's gauge, the governing equation for the MVP can finally be written as:

$$\nabla^2\mathbf{A} - \mu\sigma\frac{\partial \mathbf{A}}{\partial t} + \mu\sigma\left(\mathbf{v} \times (\nabla \times \mathbf{A})\right) = \mu\sigma\nabla V - \nabla \times \mathbf{B}_0 \tag{2.35}$$

Equation (2.35) can be interpreted physically by making a distinction between current densities due to eddy currents and current densities that are externally imposed ($\mathbf{J}_{ext}$).
According to Faraday's law, eddy currents are induced if a conductive material experiences a varying magnetic field. From a given point of view, this can either be because of a time-dependent magnetic field in a stationary material or because of relative movement of the material with respect to a time-invariant magnetic field. These phenomena are accounted for by the time-derivative and the speed-dependent term of (2.35) respectively.
Externally imposed current densities are accounted for by the $\mu\sigma\nabla V$ term in (2.35). Where V is the ESP in the considered problem. In the stator windings of an electrical machine for example, V is the terminal voltage. However, directly accounting for V would imply that every conductor has to be modeled separately, for that $\mathbf{J}_{ext}$ is imposed directly. Assuming a generator reference, this is done by substituting $\mathbf{J}_{ext}$ for $\sigma\nabla V$ in the governing equation for the MVP. The result is an alternative governing equation:

$$\nabla^2\mathbf{A} - \mu\sigma\frac{\partial \mathbf{A}}{\partial t} + \mu\sigma\left(\mathbf{v} \times (\nabla \times \mathbf{A})\right) = \mu\mathbf{J}_{ext} - \nabla \times \mathbf{B}_0 \tag{2.36}$$

Equation (2.36) can now be interpreted by regarding its individual terms. The first term is the Laplacian of the MVP. This term is always present. As mentioned, the time-derivative and the speed-dependent terms account for eddy-currents. They will only be considered in problems where the effect of eddy-currents is non-negligible, i.e. in conductive materials. The source terms are located on the right-hand side of (2.36), they respectively account for externally imposed current densities and residual magnetic flux densities in the studied problem.
Note that most modern electric drives are powered with the help of a voltage-source inverter. This fact advocates the use (2.35) as a governing equation. However, the implementation of V as a source term is complex. Therefore, in Chapter 3, (2.36) will be used to calculate the magnetic field. In order to account for voltage sources, a coupling between the field calculations and the equation for the terminal voltage of an electric machine is proposed in Chapter 6.

Boundary conditions

The definition of the MVP (2.27) and the constitutive relation for the magnetic flux density (2.26b) give the following equation for the magnetic field:

$$\mathbf{H} = \frac{\nabla \times \mathbf{A} - \mathbf{B}_0}{\mu} \tag{2.37}$$

Accounting for the above, the boundary conditions (2.25) can be written in terms of the MVP as:

$$\mathbf{n} \cdot \left(\nabla \times \left(\mathbf{A}^{(\nu)} - \mathbf{A}^{(\nu+1)} \right) \right) = 0 \tag{2.38a}$$

$$\mathbf{n} \times \left(\nabla \times \left(\frac{\mathbf{A}^{(\nu)}}{\mu^{(\nu)}} - \frac{\mathbf{A}^{(\nu+1)}}{\mu^{(\nu+1)}} \right) - \left(\frac{\mathbf{B}_0^{(\nu)}}{\mu^{(\nu)}} - \frac{\mathbf{B}_0^{(\nu+1)}}{\mu^{(\nu+1)}} \right) \right) = \mathbf{J}_s \tag{2.38b}$$

Note that (2.38a) can be simplified by integrating. Condition (2.38a) then imposes continuity of $\mathbf{A}$. This could indeed be expected, if $\mathbf{A}$ would be discontinuous in a given point, the magnetic flux density in that point would be infinite. This violates Gauss' law for magnetism (2.24c). The boundary conditions can now be written as:

$$\mathbf{A}^{(\nu)} - \mathbf{A}^{(\nu+1)} = 0 \tag{2.39a}$$

$$\mathbf{n} \times \left(\nabla \times \left(\frac{\mathbf{A}^{(\nu)}}{\mu^{(\nu)}} - \frac{\mathbf{A}^{(\nu+1)}}{\mu^{(\nu+1)}} \right) - \left(\frac{\mathbf{B}_0^{(\nu)}}{\mu^{(\nu)}} - \frac{\mathbf{B}_0^{(\nu+1)}}{\mu^{(\nu+1)}} \right) \right) = \mathbf{J}_s \tag{2.39b}$$

The magnetic field in an electric actuator can now be found by solving the governing equation (2.36) while accounting for the boundary conditions (2.39).

2.5 Conclusion

In this chapter, the physical and mathematical basis for an analytical model of an electric actuator was presented. Maxwell's equations, the boundary conditions and the constitutive relations were introduced, both for stationary and moving matter. The magneto quasi-static approximation was introduced to simplify the calculation of magnetic fields in electric actuators. The resulting set of physical laws was translated in a mathematical problem formulation that consists of one partial differential equation and two boundary conditions. This problem formulation can be used as the starting point of an analytical model for virtually every electric actuator, as shown in Chapter 3.

Chapter 3

Fourier-based modeling

The previous chapter described a mathematical formulation of electromagnetic problems. The goal of this chapter is to translate that formulation to a model that predicts the magnetic field of electric machines. To do so, the Fourier-based modeling technique, which essentially combines the subdomain method with the technique of separation of variables, is used.
In the following, an extensive discussion on the various aspects of Fourier-based modeling will be presented. The novelty of the discussion is that it provides a widely applicable technique to account for eddy-currents in the machine, which implies that time-dependency is considered. Although some authors have already published time-dependent Fourier-based models, literature lacks a more general approach of the subject. In this work, eddy-currents due to both time-variations in the magnetic fields and movement are considered. Although the results of this chapter are applicable to most radial-flux rotating machines operated in steady-state, the focus is on SM PMSMs.
Section 3.1 introduces the example machine that will be used to clarify some of the more abstract parts of this chapter. In Section 3.2, the model's spatial reference, its time-dependency and some general assumptions are discussed. Section 3.3 describes the actual model. First, the subdomain technique is introduced. Then, a general expression for the MVP and the source terms is derived. Next, the actual solution of the MVP is discussed and finally the determination of the solution's integration constants is discussed. The results, obtained in Section 3.3, are validated in Section 3.4. Finally, Section 3.5 concludes this chapter.

The content of this chapter has been published in the following journal paper:

- B. Hannon, P. Sergeant and L. Dupré, "2-D Analytical Subdomain Model of a Slotted PMSM With Shielding Cylinder", *Magnetics, IEEE Transactions on*, vol. 50, no. 7, 10 pages, 2014

3.1 Example-machine

The discussion in this chapter is rather mathematical. For the sake of clarity, all of the discussed aspects will be illustrated for the case of a high-speed permanent-magnet synchronous machine with two pole pairs, i.e. $p = 2$. A cross-section of this example-machine is shown in Figure 3.1.

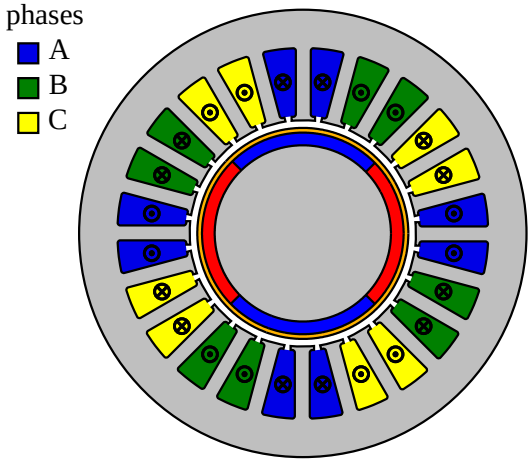

Figure 3.1: Cross-section of the example-machine

As mentioned in Chapter 1, the difference between the machine depicted in Figure 3.1 and a classical PMSM is that the high-speed PMSM is equipped with a conductive sleeve around its magnets, indicated as a yellow ring in the figure. Such a sleeve can be used to retain the magnets during high-speed operation. It is then referred to as a retaining sleeve. However, it can also be used to reduce the overall rotor losses at high-speed operation. If this is the case, the sleeve is referred to as a shielding cylinder. The eddy-currents that are induced in the SC counteract the asynchronous components of the magnetic field, thereby shielding the magnets and the rotor iron from these asynchronous components.

3.2 Model context

The goal of this section is to set the context in which the mathematical formulation of Chapter 2 can be translated into a working model. To do so, a spatial reference system has to be chosen. Moreover, as this work aims at directly accounting for the time-dependency, that aspect has to be discussed as well. Finally, some general assumptions have to be made in order to reduce the calculus.

3.2.1 Spatial coordinate system

As discussed in Chapter 1, a cylindrical coordinate system with the z-axis along the machine's axis will be used in this work. Figure 3.2 shows that coordinate system in the example-machine.

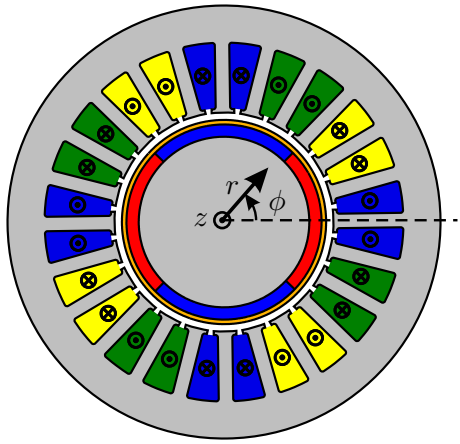

Figure 3.2: Coordinate system in a radial-flux rotational machine

Two-dimensional approximation

Evidently, the geometry of electric machines is three-dimensional. However, often the problem can be assumed invariant along one direction. In radial-flux rotational machines, the problem is usually assumed invariant along the z-direction, i.e. along the machine's axis. This invariant direction is referred to as the longitudinal direction. The invariance along the z-direction implies that, spatially, the magnetic vector potential only depends on r and ϕ. As the field is assumed to be two-dimensional and only depends on the r- and ϕ coordinates, $\mathbf{B} = \nabla \times \mathbf{A}$ implies that the MVP has only one non-zero component; the z-component. This means that:

$$\mathbf{A} = A(r, \phi)\mathbf{e}_z \tag{3.1}$$

In the rest of this work, the 2D approximation is applied. As a result, 3D effects such as end-effects will not be accounted for.

Periodicity

The Fourier-based modeling technique, which will later be used to calculate the MVP, relies on periodicities in the magnetic field. Evidently, the magnetic field in radial-flux rotational machines is periodic in the ϕ-direction with a periodicity of

2π radians. The direction along which this spatial periodicity, T_s, exists is generally referred to as the periodic direction.
The remaining direction, which is the r-direction in the cylindrical coordinate system, is called the normal direction.

Multiple reference systems

Fourier-based models often use multiple spatial reference systems in order to account for movement and/or to reduce the calculus. In this work, movement is directly accounted for, but the model's complexity is minimized by considering multiple reference systems with a circumferential shift. The relation between two systems, e.g. (r, ϕ, z) and (r', ϕ', z'), is then given as:

$$r = r' \tag{3.2a}$$
$$\phi = \phi' - \phi_0 \tag{3.2b}$$
$$z = z' \tag{3.2c}$$

where ϕ_0 is the circumferential shift between both systems.

3.2.2 Time-dependency

As mentioned in Chapter 1, some authors does not directly account for the field's time-dependency. Instead they use multiple static calculations to mimic the effect of time-varying aspects such as movement and sources. This technique implies that, for every instance of time, the time-independent problem is recalculated with updated values for the time-dependent variables. It has the advantage of simplicity and a very low computational burden for every single time step. However, the resulting magnetostatic models can not accurately account for the eddy-current reaction field. Moreover, as the problem has to be recalculated for every instance of time, the advantage of a lower computational burden vanishes if the desired time step is small.
In this work, the more general approach of directly accounting for the time-dependency of the magnetic field is adopted. It was already mentioned that the Fourier-based method relies on periodicities in the magnetic field. This is not only true for the the spatial aspect, it is also true for the time-dependency. The time-period that is used in this work is the mechanical period T_t. In a classical rotational machine that is operating in steady-state for example, T_t equals the time required for the rotor to perform one revolution. However, it is possible that within the machine multiple time-periodicities exist. This is for example the case in machines with multiple rotors that rotate at different speeds. T_t is then the least common multiple of the machine's different periodicities.

3.2.3 Assumptions

In order to enable an analytical solution of the problem with a limited mathematical complexity, a number of assumptions have to be made. Some of these assumptions were already mentioned in the previous sections. This section briefly discusses all the assumptions that are used to construct the model in this chapter.
The first and most fundamental approximation in this work is the assumption that the situation is magneto quasi-static. The consequences and validity of this assumption have been discussed in Section 2.3.
Secondly, the problem is regarded in two dimensions. This means that the problem is assumed invariant in one direction. This approximation implies that 3D effects such as skewing and end effects can not be regarded. This assumption is not strictly necessary to allow for an analytical solution of the problem, but it greatly reduces the required calculus.
The third assumption is that the boundaries of the studied geomtery are either radial, i.e. ϕ is constant, or circumferential, i.e. r is constant. In contrast to the previous assumption, this assumption is required to analytically solve the problem. Boundaries that aren't radial or circumferential have to be simplified.
Fourthly, the machine is assumed to operate in steady-state. This assumption is required because the Fourier-based modeling technique that will be used to solve the problem in Section 3.3 is based on periodicities in the magnetic field. Steady-state operation implies a time-periodicity.
The fifth assumption is that all movement in the studied problem is along the tangential direction, i.e. $\mathbf{v} = v\mathbf{e}_\phi$. Physically, this assumption implies that there is only rotational movement in the machine and that all the moving parts are rotating around the same axis. This axis has to coincide with the longitudinal direction.
Finally, all of the materials in the machine are assumed linear and isotropic. Moreover, all soft-magnetic materials are assumed to have an infinite magnetic permeability.
The above assumptions are listed as:

- Magneto quasi-static situation
- Two-dimensional problem
- All boundaries are either radial or circumferential
- Steady-state operation
- All movement is along the tangential direction
- All materials are linear and isotropic
- Soft-magnetic materials have infinite permeability

3.3 Fourier-based modeling

With the problem fully formulated and the context sketched, a mathematical description of the machine's magnetic field can be obtained. To do so, the differential equation for the magnetic vector potential (2.36) has to be solved while accounting for the boundary conditions (2.39). There are several ways to find a solution for the governing equation. Mostly however, either Green's functions or the Fourier-Based (FB) modeling technique is used. As indicated in Chapter 1, the latter, which essentially combines the subdomain technique and the technique of separation of variables, is used in this work.
The following section aims at describing FB modeling. More specifically, the use of subdomains, separation of variables, the actual solution and the implementation of the boundary conditions are discussed.

3.3.1 Subdomain technique

The governing equation is too complex to be solved analytically in the entire problem domain. To overcome that issue, the studied geometry is divided in a number regions, called subdomains. In each of these subdomains, the problem is greatly simplified and can be solved. The obtained solutions are then linked by imposing the boundary conditions that were introduced in Section 2.4. As a result, the subdomain technique allows to use relatively simple techniques to study complex problems. The technique's major drawback is that every subdomain introduces a set of integration constants. Often these constants have to be calculated numerically, which implies that introducing extra subdomains results in a larger computational time.
In order to obtain an as simple as possible problem, it is important to correctly choose the subdomains. First of all, the governing equation has to be simplified as much as possible. Secondly, it should be relatively easy to impose the boundary conditions.

Governing equation

Section 2.4 introduced the following governing equation:

$$\nabla^2 \mathbf{A} - \mu\sigma \frac{\partial \mathbf{A}}{\partial t} + \mu\sigma \left(\mathbf{v} \times (\nabla \times \mathbf{A})\right) = \mu \mathbf{J}_{ext} - \nabla \times \mathbf{B}_0 \tag{3.3}$$

This equation is greatly simplified if μ and σ are constants. Therefore, a first point of attention is to make sure that the subdomains are chosen so that the magnetic permeability and the electrical conductivity are constant in each subdomain.
As discussed earlier, there are three kinds of terms in (3.3). Firstly, the Laplacian term is a general term that is present in every subdomain. Secondly, the time-derivative and speed-dependent terms account for eddy-currents. They are only

present in electrically conductive subdomains, where the effect of eddy-current is non-negligible. Thirdly, the terms on the right-hand side of (3.3) are source terms. $\mathbf{J}_{ext}$ accounts for externally imposed current densities and $\mathbf{B}_0$ accounts for permanent magnets. For the sake of simplicity, this work does not consider subdomains with multiple source terms or subdomains where both a source term and eddy-currents are present. This implies that only the following governing equations are to be considered:

$$\nabla^2 \mathbf{A} = 0 \tag{3.4a}$$

$$\nabla^2 \mathbf{A} = \mu \mathbf{J}_{ext} \tag{3.4b}$$

$$\nabla^2 \mathbf{A} = -\nabla \times \mathbf{B}_0 \tag{3.4c}$$

$$\nabla^2 \mathbf{A} = \mu\sigma \frac{\partial \mathbf{A}}{\partial t} - \mu\sigma \left(\mathbf{v} \times (\nabla \times \mathbf{A})\right) \tag{3.4d}$$

The simplest governing equation (3.4a) applies in subdomains with no source terms and no eddy-currents. Equations (3.4b) and (3.4c) apply in subdomains with a source term, i.e. an externally imposed current density or residual magnetic flux density. Finally, (3.4d) applies in subdomains where the effect of eddy currents is non-negligible.

Boundary conditions

Boundary conditions are imposed to ensure physically correct behavior of the MVP on the boundary between two subdomains, i.e. to link the solutions of neighboring subdomains. In order to easily impose the boundary conditions, it is assumed that each subdomain has four boundaries, two of which are constant in the r-direction and two of which are constant in the ϕ-direction. Boundaries with a constant r are called circumferential boundaries. Boundaries that have a constant ϕ are called radial boundaries. Only considering circumferential and radial boundaries usually implies that the studied geometry has to be simplified. In the example-machine, this means that the sides of the slots are assumed radial, the rounding of the edges is neglected. This is illustrated in Figure 3.3.
As discussed in the following, the circumferential boundary conditions will determine the integration constants that are introduced when solving the governing equations. The radial boundary conditions will determine the eigenvalues of the solutions.
First, circumferential boundaries are regarded. In a two-dimensional approximation, imposing continuity of the MVP at the circumferential boundary between subdomains ν and $\nu + 1$, where $r = r_\nu$, implies (2.39a):

$$A^{(\nu)}(r_\nu, \phi, t) - A^{(\nu+1)}(r_\nu, \phi, t) = 0 \tag{3.5}$$

The behavior of the tangential component of the magnetic field strength (2.39b) has to be imposed as well. In the two-dimensional approximation, (2.39b) can be

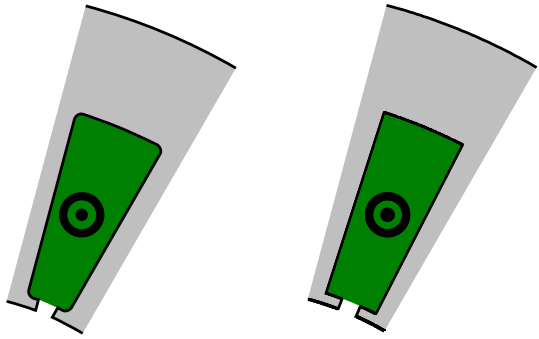

(a) Realsitic (b) Simplified

Figure 3.3: Simplification of the example-machine's geometry

rewritten as:

$$\left.\frac{\partial A^{(\nu)}(r,\phi,t)}{\mu^{(\nu)}\partial r}\right|_{r=r_\nu} - \left.\frac{\partial A^{(\nu+1)}(r,\phi,t)}{\mu^{(\nu+1)}\partial r}\right|_{r=r_\nu} = \frac{B^{(\nu)}_{0,\phi}(r_\nu,\phi,t)}{\mu^{(\nu)}} - \frac{B^{(\nu+1)}_{0,\phi}(r_\nu,\phi,t)}{\mu^{(\nu+1)}} \tag{3.6}$$

The surface current density of the boundary $(\mathbf{J}_s)$ is not considered in the above. The reason is that this work directly considers the spatial distribution of externally imposed current densities. $\mathbf{J}_s$ will then always be zero.

Note that, at the boundary between a subdomain with finite permeability and a region with soft-magnetic material idealized by $\mu = \infty$, (3.6) can be imposed without knowledge of the MVP in the soft-magnetic material. This implies that the problem can be decoupled, i.e. the MVP does not have to be calculated in the soft-magnetic material. This, in turn, implies that continuity of the MVP (3.5) does not have to be imposed at these boundaries.

The boundary conditions of all the circumferential boundaries form a set of equations that determines the integration constants. These constants are introduced when solving the governing equations.

Secondly, radial boundaries are considered. In the context of such boundaries, two types of subdomains are distinguished; subdomains that circumferentially span 2π radians and subdomains that span a smaller range of β_ν radians. Both types of subdomains are shown in Figure 3.4.

If a subdomain spans 2π radians, its radial boundaries coincide. Moreover, they can be located at any angular position. This implies that the boundary conditions are automatically fulfilled if a spatial periodicity of 2π radians is imposed. The subdomain is therefore called a periodic subdomain. Its spatial periodicity $(T_s^{(\nu)})$ will be used in Section 3.3.2 to determine the eigenvalues of the obtained solution.

If, however, the subdomain spans β_ν radians, with $\beta_\nu < 2\pi$, there is no obvious periodicity. The subdomain is then referred to as a non-periodic subdomain. If

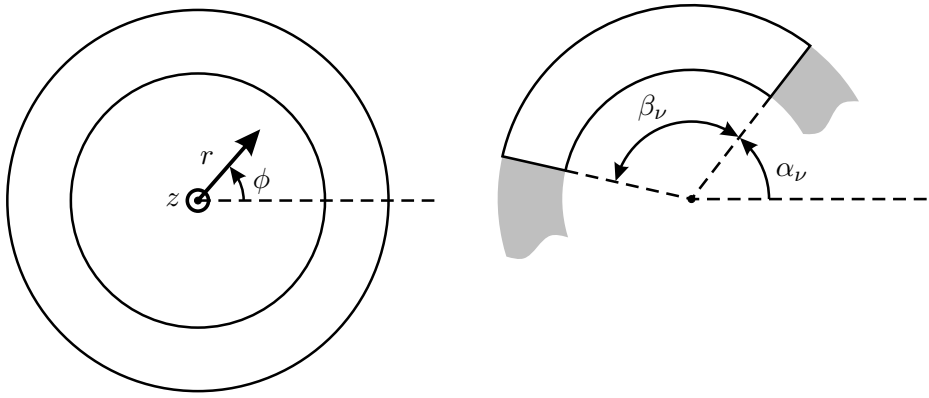

(a) Periodic subdomain

(b) Non-periodic subdomain with soft-magnetic boundaries

Figure 3.4: Types of subdomains

such a subdomain is flanked by idealized soft-magnetic material ($\mu = \infty$) and has no permanent magnetization in the r-direction, continuity of the magnetic field's tangential component gives (2.39b):

$$\left.\frac{\partial A^{(\nu)}(r,\phi,t)}{\partial \phi}\right|_{\phi=\alpha_\nu} = \left.\frac{\partial A^{(\nu)}(r,\phi,t)}{\partial \phi}\right|_{\phi=\alpha_\nu+\beta_\nu} = 0 \tag{3.7}$$

where α_ν is the angular position of the considered subdomain, as illustrated in Figure 3.4.

Equation (3.7) shows that it suffices to impose that the angular derivative of the MVP is zero at the radial boundaries of the considered subdomain to impose continuity of the magnetic field strength's tangential component. It will be shown in Section 3.3.2 that this can be accomplished by imposing a periodicity of twice the subdomain's angular span, i.e. $T_s^{(\nu)} = 2\beta_\nu$ radians. Similar as for periodic subdomains, this periodicity will be used to determine the eigenvalues of the solution. Due to a lack of periodicity, the MVP in the stator teeth cannot be calculated using the classical exact subdomain technique. Therefore, imposing continuity of the MVP at the radial boundary of a non-periodic subdomain is not possible. However, as imposing (3.7) doesn't require knowledge of the MVP in the soft-magnetic material, the problem can be decoupled. Note that this implies that it is not possible to calculate the MVP in the stator iron of the example-machine.

It was shown in the above that imposing the circumferential boundary conditions results in a set of equations. In the following section, this set of equations will be used to determine the integration constants of the solution for the governing equation. Similar, the spatial periodicities, found by imposing the radial boundary conditions, will determine the eigenvalues of the solution.

Subdomains in the example-machine

The simplified geometry of the example-machine can now be divided in subdomains, as shown in Figure 3.5. The problem is decoupled at the rotor and stator iron. This means that the first subdomain $(\nu = 1)$ is the region that contains the magnets. The permeability of the magnets and that of the space between two magnets is assumed equal. The shielding cylinder $(\nu = 2)$ and the air gap $(\nu = 3)$ are the second and third subdomains respectively. Finally, each slot-opening and each slot is a separate subdomain. The slot-openings and their corresponding slots are given an index i. Therefore the corresponding subdomain numbers are $4i$ and $5i$ respectively.

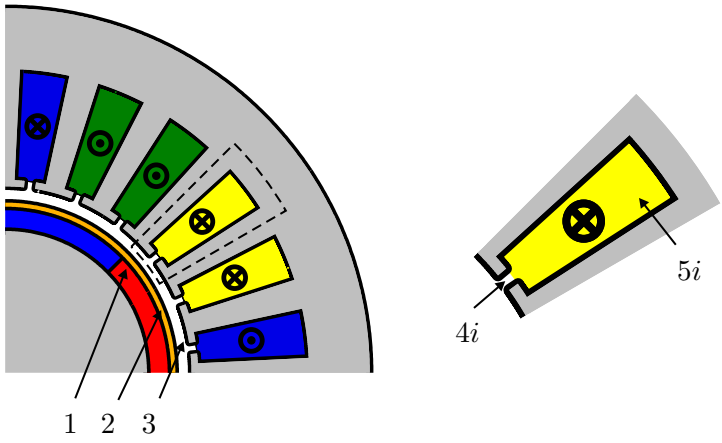

Figure 3.5: Subdomains in the example-machine

3.3.2 Form of the solution

The solutions for the above governing equations will be obtained using the technique of separation of variables. The technique as such is not discussed as it is available in numerous mathematical textbooks, e.g. Kryszig's book on advanced engineering mathematics [104]. Instead, the form of the solution will be presented. This will allow to rewrite the governing equations (3.4) as a set of well-known partial differential equations.
First a basic form of the solution is presented. In a second step, that solution is adapted to account for different reference systems. Finally, a general form of the solution is presented and the concept of harmonic combinations is introduced.

Form of the solution

Using separation of variables implies that the solution will be written in the form of a series. Moreover, as already mentioned in the above, the problem has a periodicity in both space and time. The solution in subdomain ν can thus be written in the form of a Fourier series over space and time:

$$A^{(\nu)}(r,\phi,t) = \sum_{\lambda_n^{(\nu)}} \sum_{\lambda_k^{(\nu)}} A^{(\nu)}_{\lambda_n^{(\nu)},\lambda_k^{(\nu)}}(r) e^{j\left(\lambda_k^{(\nu)}\phi - \lambda_n^{(\nu)} t\right)} \tag{3.8}$$

where $A^{(\nu)}_{\lambda_n^{(\nu)},\lambda_k^{(\nu)}}(r)$ is the, r-dependent, Fourier coefficient of the series. This coefficient contains the integration constants. $\lambda_n^{(\nu)}$ is the eigenvalue related to the time-aspect of the solution and $\lambda_k^{(\nu)}$ is the eigenvalue related to the space-aspect of the solution. As already mentioned, the eigenvalues are determined by the subdomain's periodicity. The time-periodicity is equal for every subdomain; it is the time the rotor needs to perform one revolution (T_t). The spatial periodicity of a subdomain is $T_s^{(\nu)}$ mechanical radians. As discussed in the above, $T_s^{(\nu)}$ is either 2π, for periodic subdomains, or $2\beta_\nu$, for non-periodic subdomains with soft-magnetic boundaries. The eigenvalues are thus:

$$\lambda_n^{(\nu)} = \frac{2n\pi}{T_t} = n\omega \tag{3.9a}$$

$$\lambda_k^{(\nu)} = \frac{2k\pi}{T_s^{(\nu)}} \tag{3.9b}$$

where ω is the mechanical speed of the machine, i.e. $\omega = \frac{2\pi}{T_t}$. n and k are integers, referred to as the time- and spatial-harmonic order respectively.
The solution is now rewritten as:

$$A^{(\nu)}(r,\phi,t) = \sum_{n=-\infty}^{\infty} \sum_{k=-\infty}^{\infty} A^{(\nu)}_{n,k}(r) e^{j(k\phi - n\omega t)} \tag{3.10}$$

in periodic subdomains and as:

$$A^{(\nu)}(r,\phi,t) = \sum_{n=-\infty}^{\infty} \sum_{k=-\infty}^{\infty} A^{(\nu)}_{n,k}(r) e^{j\left(\frac{k\pi}{\beta_\nu}\phi - n\omega t\right)} \tag{3.11}$$

in non-periodic subdomains with soft-magnetic boundaries.

Multiple reference systems

As mentioned in Section 3.2.1, considering multiple reference systems can result in a simplified calculus.

Periodic subdomains all have the same spatial system, it is chosen as indicated in Figure 3.2. In constrast, each non-periodic subdomain with soft-magnetic boundaries is assigned its own spatial reference system. The circumferential shift of that system is chosen so that the angular position of the subdomain (α_ν) corresponds to an angular coordinate equaling zero, i.e. $\phi_0^{(\nu)} = \alpha_\nu$. The equation for the magnetic vector potential in non-periodic subdomains with soft-magnetic boundaries is now rewritten as:

$$A^{(\nu)}(r,\phi,t) = \sum_{n=-\infty}^{\infty} \sum_{k=-\infty}^{\infty} A_{n,k}^{(\nu)}(r) e^{j\left(\frac{k\pi}{\beta_\nu}(\phi-\alpha_\nu)-n\omega t\right)} \tag{3.12}$$

From (3.12), it can now easily be seen that (3.7) is satisfied by imposing:

$$A_{n,k}^{(\nu)}(r) = A_{n,-k}^{(\nu)}(r) \tag{3.13}$$

This in turn shows that the chosen periodicity of $2\beta_\nu$ radians, combined with imposing (3.13) suffices to ensure a correct behavior of the MVP at the soft-magnetic boundaries of a non-periodic subdomain. Moreover, choosing the reference system so that the angular coordinate is zero at one of the soft-magnetic boundaries indeed simplifies the calculus.
Note that imposing a spatial periodicity of β_ν radians might seem a valid option as well. However, this imposes that the MVP is equal at both radial boundaries. This is of course not necessarily true.

General form of the solution

The above shows that the most general form of the solution, valid for both periodic and non-periodic subdomains, is:

$$A^{(\nu)}(r,\phi,t) = \sum_{n=-\infty}^{\infty} \sum_{k=-\infty}^{\infty} A_{n,k}^{(\nu)}(r) e^{j\left(\frac{2k\pi}{T_s^{(\nu)}}\left(\phi-\phi_0^{(\nu)}\right)-n\omega t\right)} \tag{3.14}$$

The fact that the final solution is written in the form of a double Fourier series implies that the time- and spatial-harmonic orders can not be regarded separately. Instead harmonic combinations (n,k) are considered. It's interesting to note that the rotational speed of a harmonic combination can easily be calculated by assuming $\frac{2k\pi}{T_s^{(\nu)}}\phi - n\omega t$ constant. The rotational speed of (n,k) is then found as:

$$\omega_{n,k} = \frac{\mathrm{d}\phi}{\mathrm{d}t} = \frac{n}{k}\omega \tag{3.15}$$

in periodic subdomains and

$$\omega_{n,k} = \frac{\mathrm{d}\phi}{\mathrm{d}t} = \frac{n}{k}\frac{\beta_\nu}{2\pi}\omega \tag{3.16}$$

in non-periodic subdomains with soft-magnetic boundaries.

3.3.3 Source term representation

Electric machines have two major source terms; currents and permanent-magnetic materials. It is of paramount importance to correctly express the time- and spatial dependency of these source terms when modeling electric machines. It was shown earlier that the equation for the MVP takes the form of a double Fourier series. The source terms will be represented in the same form.
There are of course an infinite number of possible source terms. The example-machine is a permanent-magnet synchronous machine. Therefore, the considered source terms are an array of permanent magnets that rotates synchronously and a number of slots that conduct one or more currents.

Permanent magnets

Consider an array of $2p$ permanent magnets with an angular range of 2π mechanical radians, as the one of the example-machine. The remanent magnetic flux density ($\mathbf{B}_0$) of such an array has a r- and a ϕ-component, both of which depend on r and ϕ.
In this section, it is assumed that the magnets are radially magnetized. This implies:

$$\mathbf{B}_0 = B_{0,r}\mathbf{e}_r \tag{3.17}$$

Spatially, the magnets' remanent flux density only depends on ϕ, as illustrated in Figure 3.6 for an array of four magnets with an opening angle of $0.8\frac{\pi}{2}$ radians. The magnets rotate synchronously, i.e. with an angular speed of ω radians per second. From (3.15), it can be seen that this means that the only non-zero harmonic combinations are the ones with equal time- and spatial-harmonic orders. $B_{0,r}$ is then mathematically described as:

$$B_{0,r}(\phi,t) = \sum_{n=-\infty}^{\infty}\sum_{k=-\infty}^{\infty} B_{0,r,n,k}e^{j(k\phi-n\omega t)} \tag{3.18}$$

with

$$B_{0,r,n,k} = \begin{cases} \dfrac{p}{\pi}\dfrac{1-(-1)^{\frac{k}{p}}}{k}B_m \sin\left(\dfrac{k\phi_m}{2}\right) & \text{if } k = n = cp \\ 0 & \text{else} \end{cases} \tag{3.19}$$

with B_m the peak value of the magnets' remanent magnetic flux density and c an integer.
Other magnetization patterns are discussed in [105].

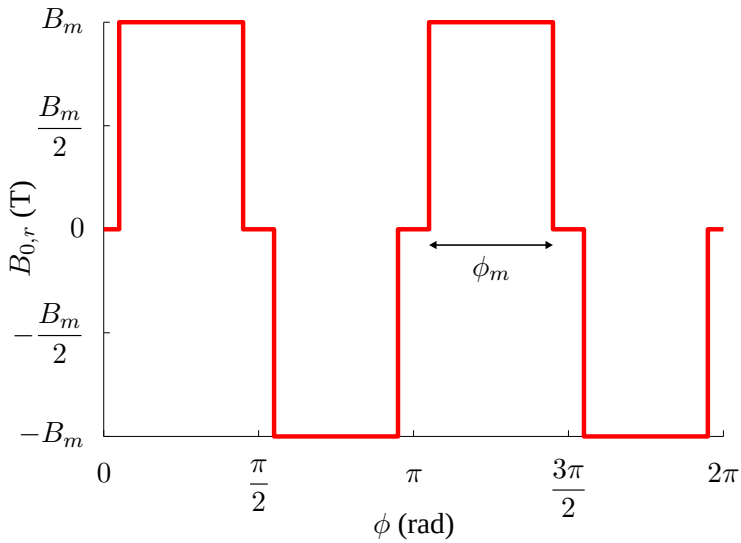

Figure 3.6: Remanent magnetic flux density of an array of four magnets with an opening angle of $\frac{4\pi}{10}$ radians when the gap between two magnets is aligned with $\phi = 0$

Current densities

The second important source that has to be accounted for is the externally imposed current density in the machine (3.4b). From the 2D-approximation, the current density can only have a z-component:

$$\mathbf{J}_{ext}^{(\nu)} = J^{(\nu)}\mathbf{e}_z \tag{3.20}$$

When the machine is powered with a m-phase electrical system, currents will flow in its slots. The currents as such only have a time-dependency, the Fourier representation of the current related to the j^{th} phase of the electrical system is:

$$i^{(j)}(t) = \sum_{n=-\infty}^{\infty} I_n^{(j)} e^{-jn\omega t} \tag{3.21}$$

Note that the current's angular speed isn't necessarily equal to the machine's angular speed (ω). Nevertheless, the machine's periodicity is used so that the representation of $i^{(j)}(t)$ corresponds to that of the MVP. This is justifiable as the current's pulsation will always be a multiple of ω.
It is assumed that the current density is spatially constant in every slot. This means that the current density in a slot is calculated as:

$$J^{(\nu)}(t) = \sum_{j=1}^{m} \frac{N^{(\nu,j)} i^{(j)}(t)}{S^{(\nu)}} \tag{3.22}$$

where $S^{(\nu)}$ is the surface of slot ν and $N^{(\nu,j)}$ is the number of conductors related to phase j in slot ν.
To correspond with the representation of the magnetic vector potential, the current density in slot ν is written as:

$$J^{(\nu)}(t) = \sum_{n=-\infty}^{\infty} \sum_{k=-\infty}^{\infty} J_{n,k} e^{j\left(\frac{2k\pi}{T_s^{(\nu)}}(\phi-\phi_0(\nu))-n\omega t\right)} \tag{3.23}$$

with

$$J_{n,k} = \begin{cases} \sum_{j=1}^{m} \frac{N^{(\nu,j)} I_n^{(j)}}{S^{(\nu)}} & \text{if } k = 0 \\ 0 & \text{else} \end{cases} \tag{3.24}$$

Note that in some models the spatial dependency of the current density within a subdomain is accounted for. This is especially important for slotless machines. Holm's PhD [70] gives a clear description of how the Fourier coefficients of the current density can then be determined.

3.3.4 Solution

In the above, the form of the solution for the MVP has been derived. As the equation is a summation over every harmonic combination, the governing equation can be considered for every time- and spatial-harmonic combination separately. This is a great advantage because it implies that the restriction to either consider eddy-currents or one source term in every subdomain only affects the individual harmonic combinations. Moreover, as shown in the following, considering the governing equation separately for every harmonic order allows to simplify the time-derivative and speed-dependent terms of the governing equation.
From the final form of the solution (3.14), it can be seen that the MVP's time-derivative can very easily be calculated for every time- and spatial-harmonic combination:

$$\frac{\partial \mathbf{A}_{n,k}^{(\nu)}}{\partial t} = -jn\omega \mathbf{A}_{n,k}^{(\nu)} \tag{3.25}$$

The time-derivative of $\mathbf{A}_{n,k}^{(\nu)}$ can thus be written as the product of a constant and $\mathbf{A}_{n,k}^{(\nu)}$ itself.
Another important term is the speed-dependent term of the governing equations. It was assumed in Section 3.2.3 that the speed of subdomain ν only has a ϕ-dependent term, i.e. $\mathbf{v}^{(\nu)} = r\omega^{(\nu)}\mathbf{e}_\phi$. Considering that the rotor of the MVP is calculated as:

$$\nabla \times \mathbf{A}_{n,k}^{(\nu)} = \frac{1}{r}\frac{\partial \mathbf{A}_{n,k}^{(\nu)}}{\partial \phi} - \frac{\partial \mathbf{A}_{n,k}^{(\nu)}}{\partial r} \tag{3.26}$$

, the speed-dependent term can then be calculated for every harmonic combination as:

$$\mathbf{v}^{(\nu)} \times \left(\nabla \times \mathbf{A}_{n,k}^{(\nu)} \right) = -j \frac{2k\pi}{T_s^{(\nu)}} \omega^{(\nu)} \mathbf{A}_{n,k}^{(\nu)} \tag{3.27}$$

where $\omega^{(\nu)}$ is the mechanical rotational speed of subdomain ν.
Implying that, similar to the time-derivative term, the speed-dependent term can be rewritten as the product of a constant and $\mathbf{A}_{n,k}^{(\nu)}$ itself.
For an arbitrary harmonic combination, (n, k), the governing equations (3.4) of subdomain ν can now be written in their scalar form (3.1), as:

$$\frac{\partial^2 A_{n,k}^{(\nu)}}{\partial r^2} + \frac{1}{r} \frac{\partial A_{n,k}^{(\nu)}}{\partial r} + \frac{1}{r^2} \frac{\partial^2 A_{n,k}^{(\nu)}}{\partial \phi^2} = 0 \tag{3.28a}$$

$$\frac{\partial^2 A_{n,k}^{(\nu)}}{\partial r^2} + \frac{1}{r} \frac{\partial A_{n,k}^{(\nu)}}{\partial r} + \frac{1}{r^2} \frac{\partial^2 A_{n,k}^{(\nu)}}{\partial \phi^2} = \mu^{(\nu)} J_{n,k}^{(\nu)} \tag{3.28b}$$

$$\frac{\partial^2 A_{n,k}^{(\nu)}}{\partial r^2} + \frac{1}{r} \frac{\partial A_{n,k}^{(\nu)}}{\partial r} + \frac{1}{r^2} \frac{\partial^2 A_{n,k}^{(\nu)}}{\partial \phi^2} = -\frac{B_{0,\phi,n,k}^{(\nu)}}{r} - \frac{\partial B_{0,\phi,n,k}^{(\nu)}}{\partial r} + \frac{1}{r} \frac{\partial B_{0,r,n,k}^{(\nu)}}{\partial \phi} \tag{3.28c}$$

$$\frac{\partial^2 A_{n,k}^{(\nu)}}{\partial r^2} + \frac{1}{r} \frac{\partial A_{n,k}^{(\nu)}}{\partial r} + \frac{1}{r^2} \frac{\partial^2 A_{n,k}^{(\nu)}}{\partial \phi^2} = j \mu^{(\nu)} \sigma^{(\nu)} \left(\frac{2\pi}{T_s^{(\nu)}} k \omega^{(\nu)} - n\omega \right) A_{n,k}^{(\nu)} \tag{3.28d}$$

Note that (3.28) again underlines the need to represent the source terms as Fourier series.
The governing equations in (3.28) can now be solved with the separation of variables technique, the resulting solutions are discussed in the following.

Laplace

The first of the above equations is the well-known Laplace equation. It governs the magnetic field in source-free subdomains where the effect of eddy-currents is negligible or non-existent, e.g. the air gap. The solution of (3.28a) is written as:

$$A^{(\nu)}(r, \phi, t) = \sum_{n=-\infty}^{\infty} \sum_{k=-\infty}^{\infty} A_{n,k}^{(\nu)}(r) e^{j \left(\frac{2k\pi}{T_s^{(\nu)}} \left(\phi - \phi_0^{(\nu)} \right) - n\omega t \right)} \tag{3.29}$$

with

$$A_{n,k}^{(\nu)}(r) = \begin{cases} C_{n,k}^{(\nu)} + D_{n,k}^{(\nu)} \ln r & \text{if } k = 0 \\ C_{n,k}^{(\nu)} r^{\left| \frac{2k\pi}{T_s^{(\nu)}} \right|} + D_{n,k}^{(\nu)} r^{-\left| \frac{2k\pi}{T_s^{(\nu)}} \right|} & \text{else} \end{cases} \tag{3.30}$$

where $C_{n,k}^{(\nu)}$ and $D_{n,k}^{(\nu)}$ are the integration constants.

Poisson

In subdomains that contain source terms, (3.28b) or (3.28c) applies. These equations are the non-homogenous variant of (3.28a), also known as the Poisson equation. Their solution is written as:

$$A^{(\nu)}(r,\phi,t) = \sum_{n=-\infty}^{\infty} \sum_{k=-\infty}^{\infty} A_{n,k}^{(\nu)}(r) e^{j\left(\frac{2k\pi}{T_s^{(\nu)}}\left(\phi-\phi_0^{(\nu)}\right)-n\omega t\right)} \tag{3.31}$$

with

$$A_{n,k}^{(\nu)}(r) = \begin{cases} C_{n,k}^{(\nu)} + D_{n,k}^{(\nu)} \ln r + P_{n,k}^{(\nu)}(r) & \text{if } k = 0 \\ C_{n,k}^{(\nu)} r^{\left|\frac{2k\pi}{T_s^{(\nu)}}\right|} + D_{n,k}^{(\nu)} r^{-\left|\frac{2k\pi}{T_s^{(\nu)}}\right|} + P_{n,k}^{(\nu)}(r) & \text{else} \end{cases} \tag{3.32}$$

$P_{n,k}^{(\nu)}(r)$ is the particular solution of the Poisson equation:

$$P_{n,k}^{(\nu)}(r) = \begin{cases} \dfrac{jkB_{0,r,n,k}^{(\nu)} - B_{0,\phi,n,k}^{(\nu)}}{2} r \ln r & \text{if } |k| = 1 \\ \dfrac{jkB_{0,r,n,k}^{(\nu)} - B_{0,\phi,n,k}^{(\nu)}}{1-k^2} r & \text{else} \end{cases} \tag{3.33}$$

for subdomains with permanent magnets and

$$P_{n,k}^{(\nu)}(r) = \begin{cases} \dfrac{1}{4}\mu^{(\nu)} J_{n,k} \ln(r) r^2 & \text{if } |k| = 2 \\ \dfrac{1}{4-k^2}\mu^{(\nu)} J_{n,k} r^2 & \text{else} \end{cases} \tag{3.34}$$

for subdomains with external current densities.
In a periodic subdomain that contains p radially magnetized magnet pairs with a span of ϕ_m radians and a remanent magnetic flux density of B_m T, the above is rewritten as:

$$P_{n,k}^{(\nu)}(r) = \begin{cases} -j\dfrac{p}{\pi}\dfrac{1-(-1)^{\frac{k}{p}}}{2} B_m \sin\left(\dfrac{k\phi_m}{2}\right) r \ln r & \text{if } k = n = cp = \pm 1 \\ -j\dfrac{p}{\pi}\dfrac{1-(-1)^{\frac{k}{p}}}{1-k^2} B_m \sin\left(\dfrac{k\phi_m}{2}\right) r & \text{if } k = n = cp \neq \pm 1 \\ 0 & \text{else} \end{cases} \tag{3.35}$$

where c is an integer.
In a non-periodic subdomain with soft-magnetic boundaries that conducts a spatially constant current in the z-direction, the particular solution is written as:

$$P_{n,k}^{(\nu)}(r) = \begin{cases} \frac{1}{4}\mu^{(\nu)} J_{n,k} & \text{if } k = 0 \\ 0 & \text{else} \end{cases} \tag{3.36}$$

Helmholtz

The fourth governing equation (3.28d) can take two forms. If $n\omega = \frac{2\pi}{T_s^{(\nu)}} k\omega^{(\nu)}$, the equation reduces to the Laplace equation. If, however, $n\omega \neq \frac{2\pi}{T_s^{(\nu)}} k\omega^{(\nu)}$, the governing equation is a Helmholtz equation. The physical meaning of these two forms is that if $n\omega = \frac{2\pi}{T_s^{(\nu)}} k\omega^{(\nu)}$, the effect of time-variations in the magnetic field is nullified by the effect of the subdomain's velocity. Harmonic combinations that satisfy this condition will not induce any eddy-current, which mathematically translates to a Laplace equation instead of a Helmholtz equation.
Consider, for example, the shielding cylinder in the example-machine. This conductive sleeve is a periodic subdomain ($T_s^{(\nu)} = 2\pi$) that rotates synchronously ($\omega^{(\nu)} = \omega$). This implies that harmonic combinations with $n = k$ do not introduce eddy-current in the shielding cylinder. Indeed, from (3.15), it can be seen that such combinations rotate synchronously with the shielding cylinder, i.e. they are invariant from the shielding cylinder's point of view.
The solution of (3.28d) can now be written as:

$$A^{(\nu)}(r,\phi,t) = \sum_{n=-\infty}^{\infty} \sum_{k=-\infty}^{\infty} A_{n,k}^{(\nu)}(r) e^{j\left(\frac{2k\pi}{T_s^{(\nu)}}\left(\phi - \phi_0^{(\nu)}\right) - n\omega t\right)} \tag{3.37}$$

with

$$A_{n,k}^{(\nu)}(r) = \begin{cases} C_{n,k}^{(\nu)} + D_{n,k}^{(\nu)} \ln r & \text{if } k = n = 0 \\ C_{n,k}^{(\nu)} r^{\left|\frac{2k\pi}{T_s^{(\nu)}}\right|} + D_{n,k}^{(\nu)} r^{-\left|\frac{2k\pi}{T_s^{(\nu)}}\right|} & \text{if } k = n \neq 0 \\ C_{n,k}^{(\nu)} \mathrm{I}_{\frac{2k\pi}{T_s^{(\nu)}}}(\tau_{n,k} r) + D_{n,k}^{(\nu)} \mathrm{K}_{\frac{2k\pi}{T_s^{(\nu)}}}(\tau_{n,k} r) & \text{else} \end{cases} \tag{3.38}$$

where I_x and K_x are modified Bessel functions of the first and second kind and the x^{th} order, $\tau_{n,k}$ is defined through its square:

$$\tau_{n,k}^2 = j\mu^{(\nu)}\sigma^{(\nu)} \left(\frac{2\pi}{T_s^{(\nu)}} k\omega^{(\nu)} - n\omega \right) \tag{3.39}$$

3.3.5 Integration constants

In the above, equations for the MVP in all of the considered subdomains where obtained; (3.29), (3.31) and (3.37). However, these solutions are not uniquely defined as long as their integration constants $\left(C_{n,k}^{(\nu)} \text{ and } D_{n,k}^{(\nu)}\right)$ haven't been determined. As discussed earlier, the final step in building a Fourier-based model is to determine the integration constants by imposing the circumferential boundary conditions (2.39). In [50], five types of circumferential boundaries were considered. Three of these boundary types are important in this work, i.e. boundaries with a Neumann condition, boundaries with continuous conditions and boundaries with both Neumann and continuous conditions.

Neumann boundaries

At the boundary between subdomain ν and a region with soft-magnetic material ($\mu = \infty$), the problem can be decoupled. This implies that the MVP is not calculated in the soft-magnetic material. Such a boundary is illustrated in Figure 3.7. As the MVP in the soft-magnetic material isn't computed, only continuity of the magnetic field's tangential component (3.6) is imposed. This condition reduces to a Neumann condition as the permeability of the soft-magnetic material is assumed infinite:

$$\left.\frac{\partial A^{(\nu)}(r,\phi,t)}{\partial r}\right|_{r=r_\nu} = B_{0,\phi}^{(\nu)}(r_\nu,\phi,t) \tag{3.40}$$

Evidently, $A^{(\nu)}(r,\phi,t)$ and $B_{0,\phi}^{(\nu)}(r,\phi,t)$ have the same time and spatial periodicities. This implies that the above condition can be rewritten for every harmonic combination separately:

$$\left.\frac{\mathrm{d}A_{n,k}^{(\nu)}(r)}{\mathrm{d}r}\right|_{r=r_\nu} = B_{0,\phi,n,k}^{(\nu)}(r_\nu) \tag{3.41}$$

Note that if $B_{0,\phi}^{(\nu)}(r_\nu,\phi,t) = 0$, the r-derivative of $A^{(\nu)}$ equals zero at $r = r_\nu$. This implies that the flux lines are perpendicular to the boundary.

Continuous boundaries

At the boundary between two subdomains that have equal spatial periodicities, both the MVP (3.5) and the tangential component of the magnetic field (3.6) have to be continuous. An illustration of such a boundary is given in Figure 3.8. As the subdomains have equal time and spatial periodicities, the boundary conditions have to be valid for every harmonic combination separately. Equations (3.5) and

(3.6) are then rewritten as:

$$A_{n,k}^{(\nu)}(r_\nu) = A_{n,k}^{(\nu+1)}(r_\nu) \tag{3.42a}$$

$$\left.\frac{\mathrm{d}A_{n,k}^{(\nu)}(r)}{\mathrm{d}r}\right|_{r=r_\nu} = \left.\frac{\mathrm{d}A_{n,k}^{(\nu+1)}(r)}{\mathrm{d}r}\right|_{r=r_\nu} \tag{3.42b}$$

Mixed boundaries

Consider the boundaries of Figure 3.9. One side of the boundary consists of subdomain ν. This subdomain can either be a periodic subdomain (Figure 3.9(a)) or a non-periodic subdomain with soft-magnetic boundaries (Figure 3.9(b)). The other side of the boundary consists of soft-magnetic material and one or more non-periodic subdomains (ξi). Clearly, the spatial periodicities of the different subdomains are not equal.
Continuity of the MVP between subdomains ν and ξi is imposed as:

$$\begin{aligned}\sum_{n=-\infty}^{\infty}\sum_{k=-\infty}^{\infty} A_{n,k}^{(\xi i)}(r_\nu) e^{j\left(\frac{2k\pi}{T_s^{(\xi i)}}\left(\phi-\phi_0^{(\xi i)}\right)-n\omega t\right)} &= A^{(\xi i)}(r_\nu,\phi,t)\\ &= A^{(\nu)}(r_\nu,\phi,t)\end{aligned} \tag{3.43}$$

Naturally, the above is only valid on the boundary between subdomains ν and ξi. Using the definition of a Fourier coefficient, the above condition can be rewritten as:

$$\begin{aligned}A_{n,k}^{(\xi i)}(r_\nu) &= \frac{\omega}{2\pi}\frac{2}{T_s^{(\xi i)}}\int_0^{\frac{2\pi}{\omega}}\int_{\phi_0^{(\xi i)}}^{\phi_0^{(\xi i)}+\frac{T_s^{(\xi i)}}{2}} A^{(\nu)}(r_\nu,\phi,t) e^{-j\left(\frac{2k\pi}{T_s^{(\xi i)}}\left(\phi-\phi_0^{(\xi i)}\right)-n\omega t\right)}\mathrm{d}\phi\mathrm{d}t\\ &= \sum_{q=-\infty}^{\infty} A_{n,q}^{(\nu)}(r_\nu)\Gamma_{q,k}(\xi i,\nu)\end{aligned} \tag{3.44}$$

where

$$\Gamma_{q,k}(\xi i,\nu) = \begin{cases} e^{-j\frac{2q\pi}{T_s^{(\nu)}}\left(\phi_0^{(\nu)}-\phi_0^{(\xi i)}\right)} & \text{if } \dfrac{q}{T_s^{(\nu)}} = \dfrac{k}{T_s^{(\xi i)}} \\ j\dfrac{T_s^{(\nu)}}{\pi}\dfrac{1-(-1)^k e^{j\frac{q\pi}{T_s^{(\nu)}}T_s^{(\xi i)}}}{qT_s^{(\xi i)}-kT_s^{(\nu)}} e^{-j\frac{2q\pi}{T_s^{(\nu)}}\left(\phi_0^{(\nu)}-\phi_0^{(\xi i)}\right)} & \text{else}\end{cases} \tag{3.45}$$

Continuity of the magnetic field's tangential component is imposed in a similar way:

$$\sum_{n=-\infty}^{\infty}\sum_{k=-\infty}^{\infty}\frac{1}{\mu^{(\nu)}}\left(\left.\frac{\mathrm{d}A_{n,k}^{(\nu)}}{\mathrm{d}r}\right|_{r=r_\nu}-B_{0,\phi,n,k}^{(\nu)}(r_\nu)\right)e^{j\left(\frac{2k\pi}{T_s^{(\nu)}}\left(\phi-\phi_0^{(\nu)}\right)-n\omega t\right)}=f(\phi,t) \tag{3.46}$$

with

$$f(\phi,t)=\begin{cases}\dfrac{1}{\mu^{(\xi i)}}\left(\left.\dfrac{\partial A^{(\xi i)}(r,\phi,t)}{\partial r}\right|_{r=r_\nu}-B_{0,\phi}^{(\xi i)}(r_\nu,\phi,t)\right) & \text{if } \phi\in[\phi_0^{(\xi i)},\phi_0^{(\xi i)}+\dfrac{T_s^{(\xi i)}}{2}]\\ 0 & \text{else}\end{cases} \tag{3.47}$$

Using the definition of a Fourier coefficient in the same way as for continuity of the MVP, the boundary condition can be rewritten as:

$$\begin{aligned}&\frac{1}{\mu^{(\nu)}}\left(\left.\frac{\mathrm{d}A_{n,k}^{(\nu)}}{\mathrm{d}r}\right|_{r=r_\nu}-B_{0,\phi,n,k}^{(\nu)}(r_\nu)\right)=\\&\qquad\sum_{i=1}^{N_s}\sum_{q=-\infty}^{\infty}\frac{1}{\mu^{(\xi i)}}\left(\left.\frac{\mathrm{d}A_{n,k}^{(\xi i)}}{\mathrm{d}r}\right|_{r=r_\nu}-B_{0,\phi,n,k}^{(\xi i)}(r_\nu)\right)\Upsilon_{q,k}(\xi i,\nu)\end{aligned} \tag{3.48}$$

where $\Upsilon_{q,k}(\xi i,\nu)$ is defined as:

$$\Upsilon_{q,k}(\xi i,\nu)=\begin{cases}\dfrac{\varsigma}{2}\dfrac{T_s^{(\xi i)}}{T_s^{(\nu)}}e^{-j\frac{2k\pi}{T_s^{(\nu)}}\left(\phi_0^{(\xi i)}-\phi_0^{(\nu)}\right)} & \text{if } \dfrac{q}{T_s^{(\xi i)}}=\dfrac{k}{T_s^{(\nu)}}\\ j\dfrac{\varsigma}{2}\dfrac{T_s^{(\xi i)}}{\pi}\dfrac{1-(-1)^q e^{-j\frac{k\pi}{T_s^{(\nu)}}T_s^{(\xi i)}}}{qT_s^{(\nu)}-kT_s^{(\xi i)}}e^{-j\frac{2k\pi}{T_s^{(\nu)}}\left(\phi_0^{(\xi i)}-\phi_0^{(\nu)}\right)} & \text{else}\end{cases} \tag{3.49}$$

with $\varsigma=1$ if ν is a periodic subdomain and $\varsigma=2$ if ν is a non-periodic subdomain with soft-magnetic boundaries.

Special boundaries

There are two types of special boundaries in which the above is not valid. A first special boundary is the center-point of the machine ($r=0$). In this point, it has to be imposed that the MVP is finite. Secondly, the outer boundary of the studied

problem has to be considered. This boundary can either be situated at infinity or at a constant radius, e.g. the outer radius of the machine. It is then assumed that the MVP is constant at that boundary, i.e. there is no magnetic flux passing through the outer boundary. As the MVP is only defined except for a constant, the constant value for the MVP at the outer boundary is free to choose. Usually it is chosen to be zero.
The special boundaries do not always occur. If the problem is decoupled at a soft-magnetic boundary, the MVP doesn't have to be calculated at the inner and/or outer boundary. Note that if the outer boundary isn't considered, the MVP will still only be defined except for a constant. This constant is again free to choose.

System of boundary conditions

When applied to a specific problem, the above boundary conditions form a system of equations for the unknown integration constants $\left(C_{n,k}^{(\nu)} \text{ and } D_{n,k}^{(\nu)}\right)$. For every time-harmonic order n, this system can be written in its matrix form as:

$$[C_n^1] \cdot [X_n] = -[C_n^2] \cdot [J_n] + [C_n^3] \cdot [B_n] \tag{3.50}$$

where $[X_n]$ contains all of the integration constants linked to n, i.e. the integration constants of each subdomain and each spatial harmonic order. This implies that if N_{bc} is the amount of boundary conditions, $[X_n]$ has a size of $N_{bc} \times 1$. Analogously, $[B_n]$ and $[J_n]$ are $N_{bc} \times 1$ row vectors that contain all of the spatial harmonic coefficients of the remanent magnetic induction and the current density in each of the subdomains. $[C_n^1]$, $[C_n^2]$ and $[C_n^3]$ are $N_{bc} \times N_{bc}$ coefficient matrices.

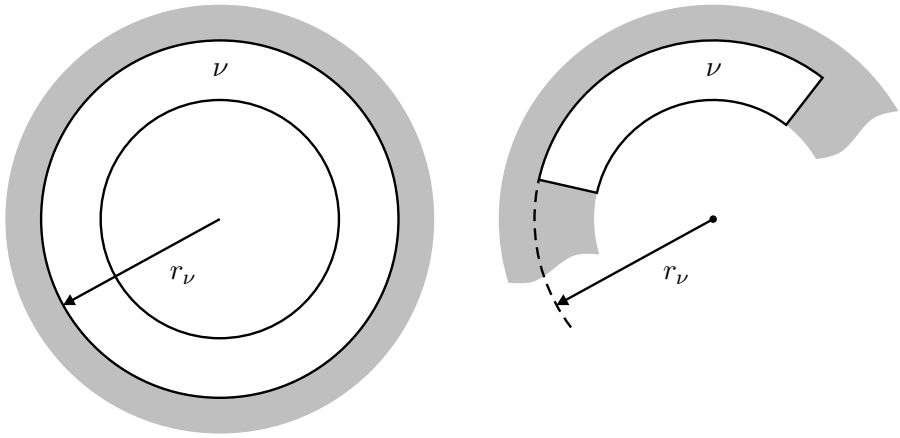

(a) Periodic subdomain (b) Non-periodic subdomain

Figure 3.7: Neumann boundaries at $r = r_\nu$, gray area is soft-magnetic material

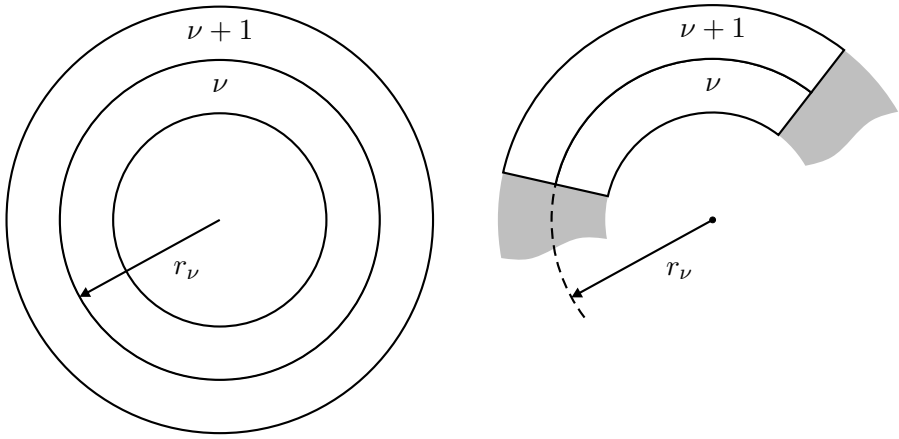

(a) Periodic subdomain (b) Non-periodic subdomain

Figure 3.8: Continuous boundaries at $r = r_\nu$, gray area is soft-magnetic material

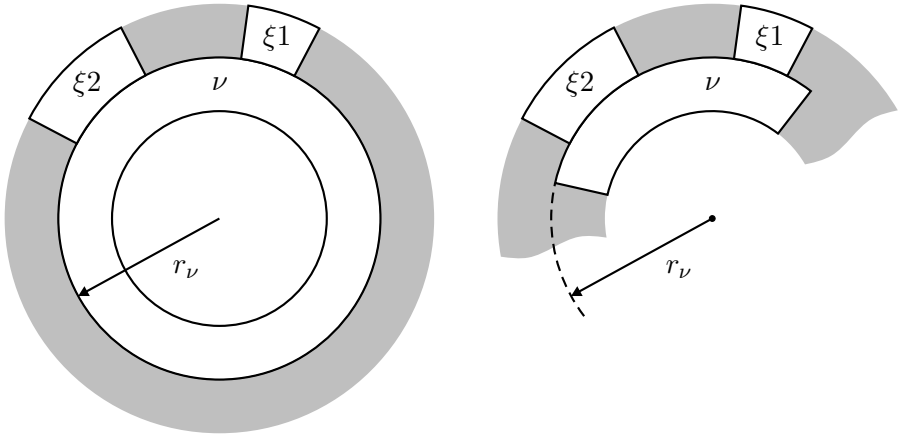

(a) Periodic subdomain (b) Non-periodic subdomain

Figure 3.9: Mixed boundaries at $r = r_\nu$, gray area is soft-magnetic material

3.4 Validation

In order to validate the above sketched framework, a FB model for radial-flux PMSMs was constructed. The model was made very general in the sense that it is fully parametrized and that it can account for machines with various topologies, i.e. machines with an inner or an outer rotor, with or without a shielding cylinder and with semi-closed, open or no stator slots. The model was also made so that it can account for any stator-winding topology that can be determined with the star-of-slots method (SoS).
First, the studied machine topologies will briefly be introduced. Next, for each of these geometries the resulting magnetic field is visualized and the obtained flux densities are compared to results from a FE model.

3.4.1 Studied topologies

Twelve different machine topologies have been studied, six of which have an inner rotor and six of which have an outer rotor.
All of the inner rotor machines have the same geometrical parameters, the same winding configuration and an equal amount of pole pairs. The only parameters that vary are the presence of a shielding cylinder and the slot type, i.e. semi-closed, open or no slots. Cross sections of the studied inner rotor machines are shown in Figure 3.11.
Similar as for the inner-rotor machines, the only variable parameters of the six outer-rotor machines are the slot type and whether or not there is a SC. Cross sections of the outer-rotor machines are shown in Figure 3.18.
The actual parameters of the studied machines are listed in Table 3.1, where RY indicates the rotor yoke, PM the permanent magnets, SC the shielding cylinder, AG the air gap, SO the slot openings, SL the slots and SY the stator yoke. Note that, depending on whether no-load or armature-reaction conditions are regarded, B_m is 1.2 or 0 T and J is 0 or 5 $\frac{\text{A}}{\text{mm}^2}$. The applied stator current is sinusoidal. In machines without a SC r_3 and σ_{SC} are neglected. Similarly, in slotless machines and machines with open slots, r_5 and δ are neglected.

3.4.2 Validation

The Fourier-based model, constructed with the framework presented in this chapter, was used to calculate the MVP in all of the non-ferromagnetic parts of the machine at both no-load and armature-reaction conditions. Next, the resulting MVP was used to calculate the magnetic flux density in the center of the air gap using the definition of the MVP (2.27):

$$\mathbf{B} = \frac{1}{r}\frac{\partial A}{\partial \phi}\mathbf{e}_r - \frac{\partial A}{\partial r}\mathbf{e}_\phi \tag{3.51}$$

Table 3.1: Parameters of the validated machines

Parameter	Symbol	Inner rotor	Outer rotor
Number of slots	N_s	12	15
Number of pole pairs	p	2	7
Number of phases	m	3	5
Remanent flux density of a magnet	B_m	1.2 or 0 T	1.2 or 0 T
Angular span of a magnet	ϕ_m	72.00°	20.57°
Current density in the slots (RMS)	J	0 or 5 $\frac{\text{A}}{\text{mm}^2}$	0 or 5 $\frac{\text{A}}{\text{mm}^2}$
Frequency of the applied current	f	1000 Hz	1000 Hz
Radius of the RY - external boundary	r_0	0.00 mm	79.20 mm
Radius of the RY - PM boundary	r_1	47.25 mm	72.20 mm
Radius of the PM - SC boundary	r_2	52.25 mm	67.70 mm
Radius of the SC - AG boundary	r_3	54.25 mm	66.70 mm
Radius of the AG - SO boundary	r_4	57.25 mm	63.70 mm
Radius of the SO - SL boundary	r_5	62.00 mm	60.70 mm
Radius of the SL - SY boundary	r_6	75.20 mm	44.20 mm
Radius of the SY external boundary	r_7	85.20 mm	0.00 mm
Opening angle of the slot openings	δ	6.93°	5.54°
Opening angle of the slots	ϵ	18.78°	15.02°
Conductivity of the SC	σ_{SC}	$5.96.10^7$ $\frac{\text{S}}{\text{m}}$	$5.96.10^7$ $\frac{\text{S}}{\text{m}}$

In the theoretical discussion of Section 3.3, an infinite summation of the time- and spatial-harmonic orders was used. Evidently, when implementing a FB model, these infinite summations have to be truncated. In all of the following calculations, the time-harmonic orders range between -130 and 130. In the periodic subdomains, the same range was used for the spatial-harmonic orders, while in the non-periodic subdomains the spatial-harmonic orders where chosen to range between -15 and 15. The iron parts of the machine were assumed infinitely permeable and all of the other parts were assumed to have a permeability equal to that of an absolute vacuum (μ_0).

For each of the studied geometries, the field images at no-load and armature-reaction, and the corresponding radial and tangential components of the magnetic flux density in the center of the air gap $(r = r_{ac})$, are shown in Figures 3.12-3.17 and 3.19-3.24. Note that the field images and the magnetic flux densities are those at $t = 0$, i.e. the magnet array is aligned with the $\phi = 0$ axis and the current in phase A is maximal.

To validate the results obtained from the FB model, the magnetic flux densities are compared to results from a transient FE model. This FE model was made in a commercial software package and its mesh and time-step were fixed to ensure an accurate result.

The resulting comparison shows that the theoretical framework, sketched in the

previous sections, is indeed capable of accurately predicting the magnetic field in an electric machine. This is also confirmed by Table 3.2, which shows the percentage deviation between the analytically obtained magnetic flux density in the center of the air gap and the results obtained from the FE model. This deviation is calculated as:

$$d = \frac{\int_0^{2\pi} |B_{FEM}(r_{ac}, \phi, 0) - B_{ANA}(r_{ac}, \phi, 0)| \mathrm{d}\phi}{\int_0^{2\pi} |B_{FEM}(r_{ac}, \phi, 0)| \mathrm{d}\phi} \cdot 100\% \tag{3.52}$$

Table 3.2 also shows the computational times required to build and solve the system of boundary conditions, i.e. the time required to compute the integration constants. By way of comparison, the computational time of the FE models is shown as well. It is clear that the FB model is much faster than the FE model.

Observing Table 3.2 and Figures 3.12-3.17 and 3.19-3.24, some interesting conclusions can be drawn.

First of all, it is clear that the error on B_ϕ is generally larger than the error on B_r. The reason is that B_ϕ tends to be more capricious than B_r, as shown in Figures 3.12-3.17 and 3.19-3.24. On the one hand, this implies a larger importance of high harmonic content, which may imply errors in the analytically obtained results. On the other hand, a more capricious course is also more difficult to be accurately predicted by the FE model.

A second point of interest is that the results for the slotless machines are more accurate than those for the slotted machines. The mathematical reason for this is that the infinite summations of the mixed boundary conditions (3.44 and 3.48), which only occur in slotted machines, are truncated. This implies that the slotting effect is not exactly accounted for, which evidently introduces an extra error. Note that the effect of slotting on the deviation is larger for B_ϕ than for B_r. This was indeed expected, as slotting has a larger effect on B_ϕ.

Further to this, it can be noted that the error due to slotting is almost completely introduced at the edge between the slots and the teeth, or at the edge between the slot openings and the tooth tips for machines with semi-closed slots. This is illustrated in Figure 3.10. Note that the edges are located at the extrema of Figures 3.10(b) and 3.10(c).

Figure 3.10 also illustrates why the percentage deviation of B_ϕ at no load is so large in the inner-rotor machines with semi-closed slots. Indeed, the very large difference in periodicity between the air-gap subdomain and the slot openings results in very abrupt changes of the azimuthal component of the flux density.

Thirdly, Table 3.2 shows a clear difference in computational time between the topologies with a SC and those without. The reason for higher computational times when a SC is present is that it introduces complex numbers in the system of boundary conditions, as can be seen from (3.37).

Finally, the effect of the studied machine's complexity on the computational time

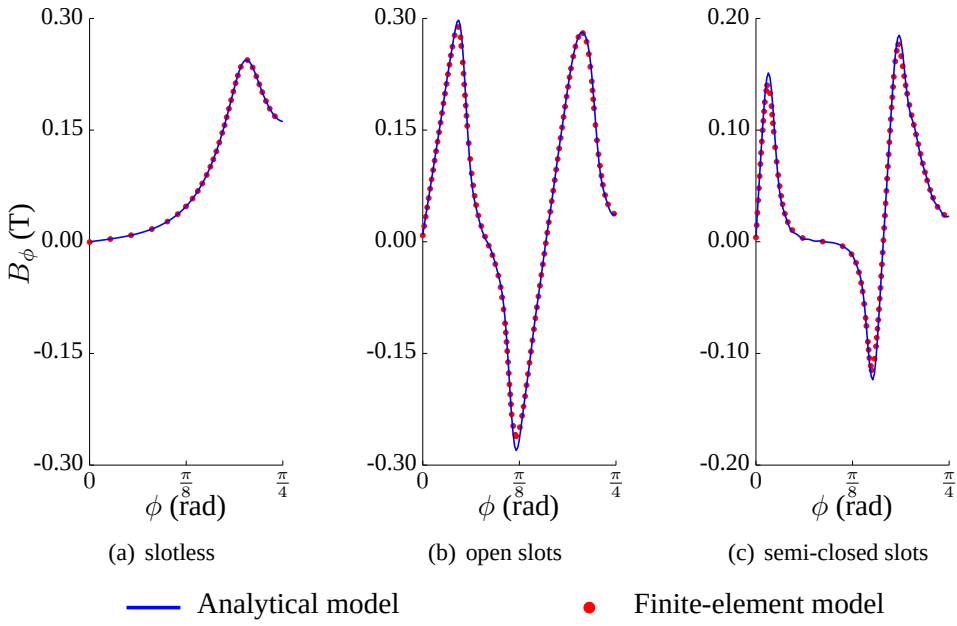

(a) slotless (b) open slots (c) semi-closed slots

Figure 3.10: $B_\phi(r_{ac}, \phi, 0)$ at no load in the inner rotor machines with a SC

can be considered. It was expected that the computational time would drastically increase with the complexity of the studied machine. The reason is twofold.
First of all, there is a difference between problems where every subdomain has the same spatial periodicity, i.e. the slotless machines, and problems with various spatial periodicities, i.e. the slotted machines. The main reason is that, as opposed to problems with various spatial periodicities, problems with only one spatial periodicity allow to solve the system of boundary conditions separately for every spatial harmonic order, see (3.41), (3.42), (3.44) and (3.48). This results in more, but much smaller, systems. This in turn is expected to result in a significantly lower computational time. As can be seen from Table 3.2, this expectation is not met. The reason is that the model for slotless machines requires more *for loops*. As the model was implemented in Matlab, which doesn't efficiently handle *for loops*, the effect of smaller systems is greatly nullified.
Secondly, the number of integration constants is directly related to the amount of subdomains. By introducing slots or slot openings, the amount of integration constants increases, which results in a drastic increase of the time required to solve the system of boundary conditions. This can clearly be seen when observing the difference in computational time between the machines with open slots and the machines with semi-closed slots.
Note that, despite the fact that the presented computational times are considerably

lower than those of the FE models, they are relatively high for analytical models. Moreover, they may be unacceptably high for optimization purposes. For that reason, the next chapter will focus on how to reduce the computational time of Fourier-based models.

Table 3.2: Percentage root-mean-squared deviation and computational time of the obtained results. NL indicates the no-load situation and AR indicates armature-reaction conditions.

Machine type	Slot type	SC	Deviation (%)				Computational time (s)			
							FB model		FE model	
			NL		AR		NL	AR	NL	AR
			B_r	B_ϕ	B_r	B_ϕ				
Inner rotor	slotless	no	0.003	0.008	0.009	0.003	105.41	106.11	1629	1809
		yes	0.028	0.025	0.069	0.014	333.71	332.95	1462	1600
	open	no	0.033	0.907	0.003	0.059	159.80	159.42	4408	4547
		yes	0.124	0.736	0.235	1.024	297.24	297.37	3960	4210
	semi-closed	no	0.045	1.945	0.217	0.091	333.09	328.04	4260	4096
		yes	0.042	2.749	0.035	0.565	515.71	517.31	4035	3651
Outer rotor	slotless	no	0.016	0.036	0.011	0.048	105.43	106.07	3148	2729
		yes	0.047	0.042	0.031	0.103	333.09	332.84	2949	2577
	open	no	0.017	0.115	0.041	0.035	173.25	173.70	2452	2478
		yes	0.050	0.082	0.048	0.046	318.84	318.00	3213	2870
	semi-closed	no	0.022	0.043	0.136	0.018	426.82	426.29	2472	2466
		yes	0.025	0.086	0.111	0.039	635.59	636.02	2345	2743

3.5 Conclusion

In the above sections, the physical basis of Chapter 2 was translated to a mathematical framework for Fourier-based models. This resulted in a broadly applicable set of equations for the MVP. As these equations contain unknown integration constants, various boundary conditions were discussed as well. The obtained system of unknowns, i.e. the integration constants, and equations, i.e. the boundary conditions, gives a unique solution for the magnetic field of the studied problem.
Although the theoretical discussion, conducted in Section 3.3, applies to a very broad range of electric actuators (induction machines, DC machines, etc.), the focus is on permanent-magnet synchronous machines. This is not different in the rest of this work where, unless mentioned otherwise, only SM PMSMs will be considered. A number of such machines was used to, successfully, validate the mathematical framework in Section 3.4. The results of that validation led to some interesting findings on the accuracy and computational time of Fourier-based models.
It was also noted in Section 3.4 that the FB model's computational times may be considered unacceptably high when a lot of machines have to be evaluated. Therefore, the following chapter will focus on how the computational time can be reduced.

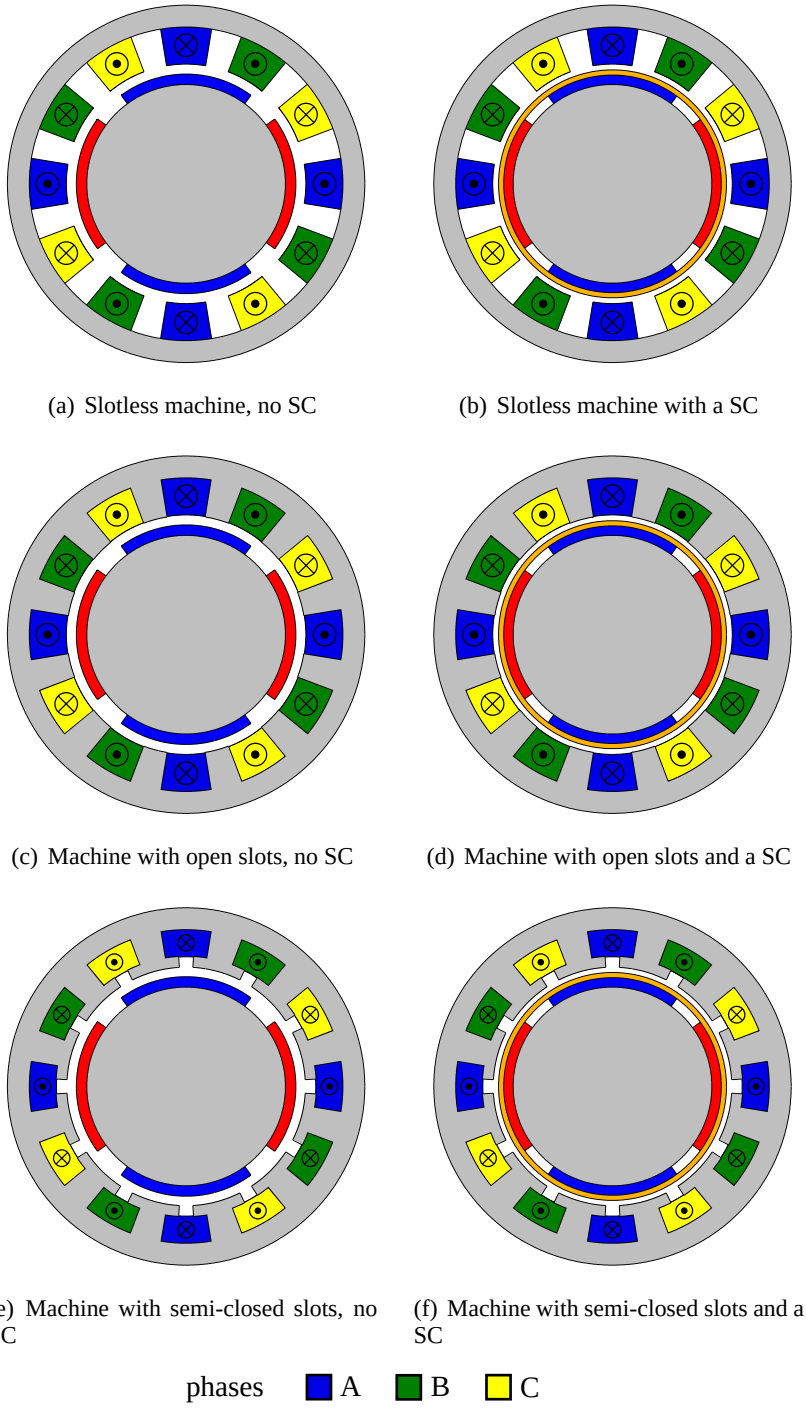

(a) Slotless machine, no SC

(b) Slotless machine with a SC

(c) Machine with open slots, no SC

(d) Machine with open slots and a SC

(e) Machine with semi-closed slots, no SC

(f) Machine with semi-closed slots and a SC

Figure 3.11: Examples of the studied inner-rotor machine topologies

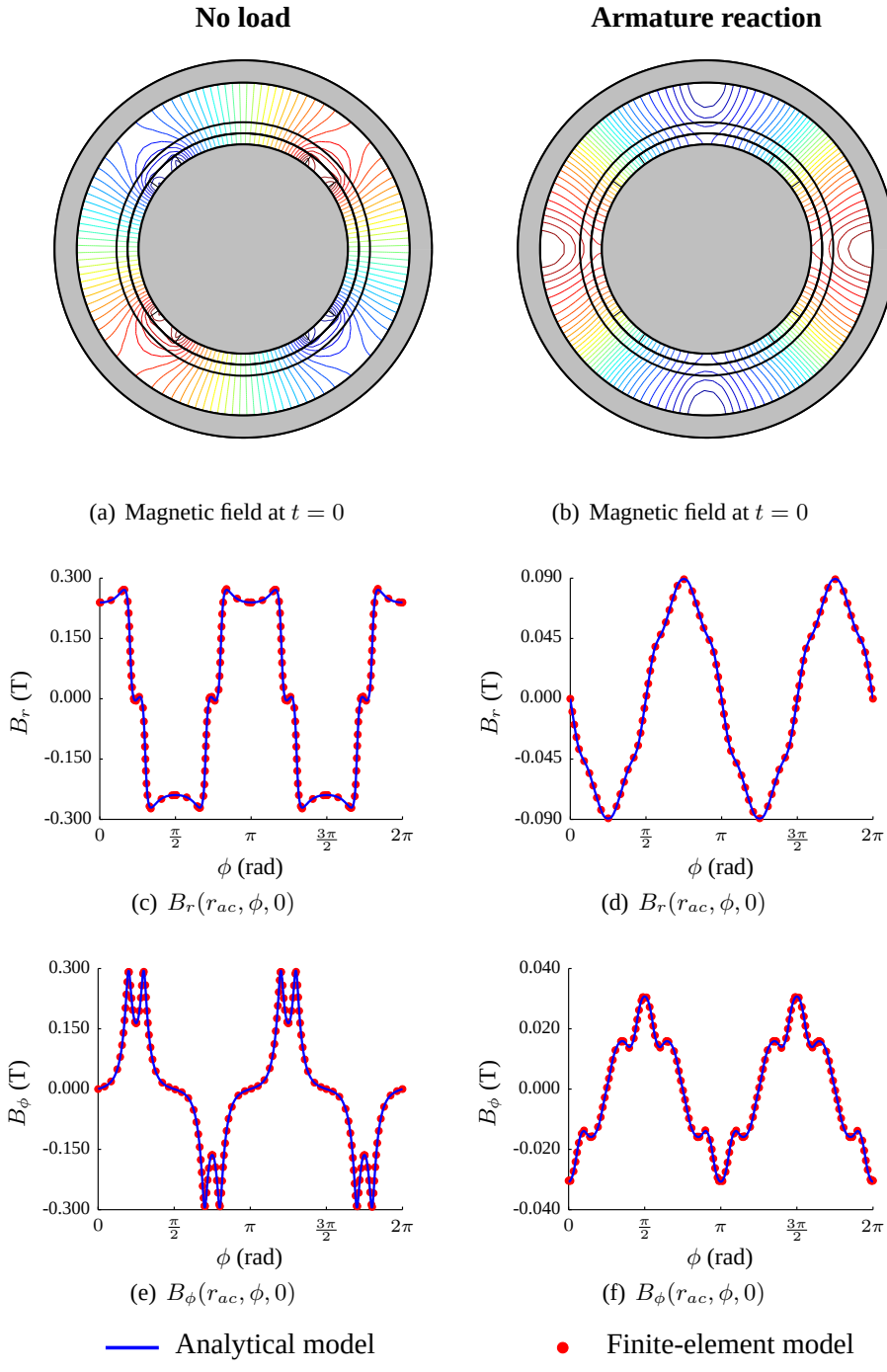

Figure 3.12: Validation of the slotless inner-rotor machine with no SC

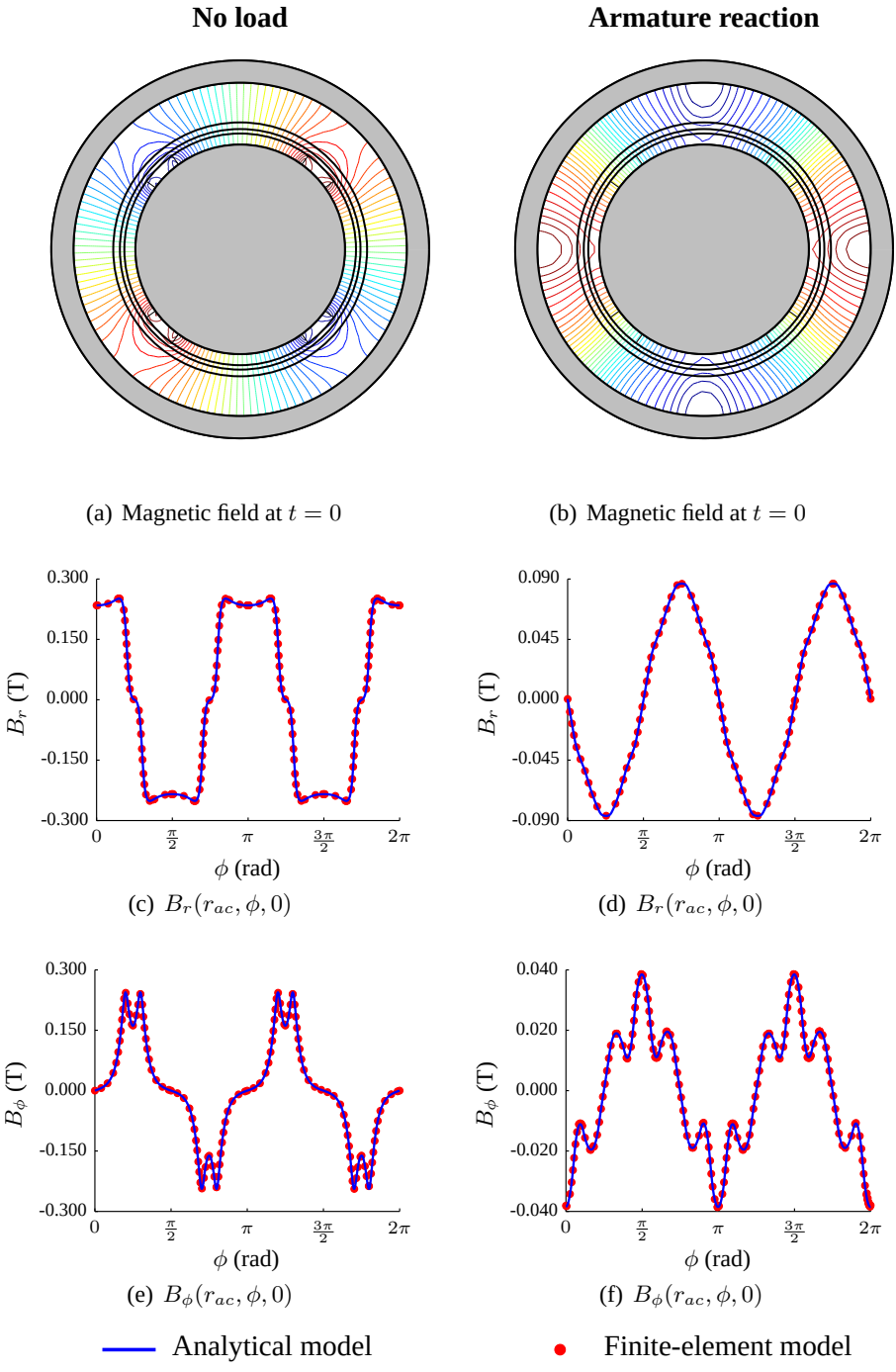

(a) Magnetic field at $t = 0$

(b) Magnetic field at $t = 0$

(c) $B_r(r_{ac}, \phi, 0)$

(d) $B_r(r_{ac}, \phi, 0)$

(e) $B_\phi(r_{ac}, \phi, 0)$

(f) $B_\phi(r_{ac}, \phi, 0)$

Figure 3.13: Validation of the slotless inner-rotor machine with a SC

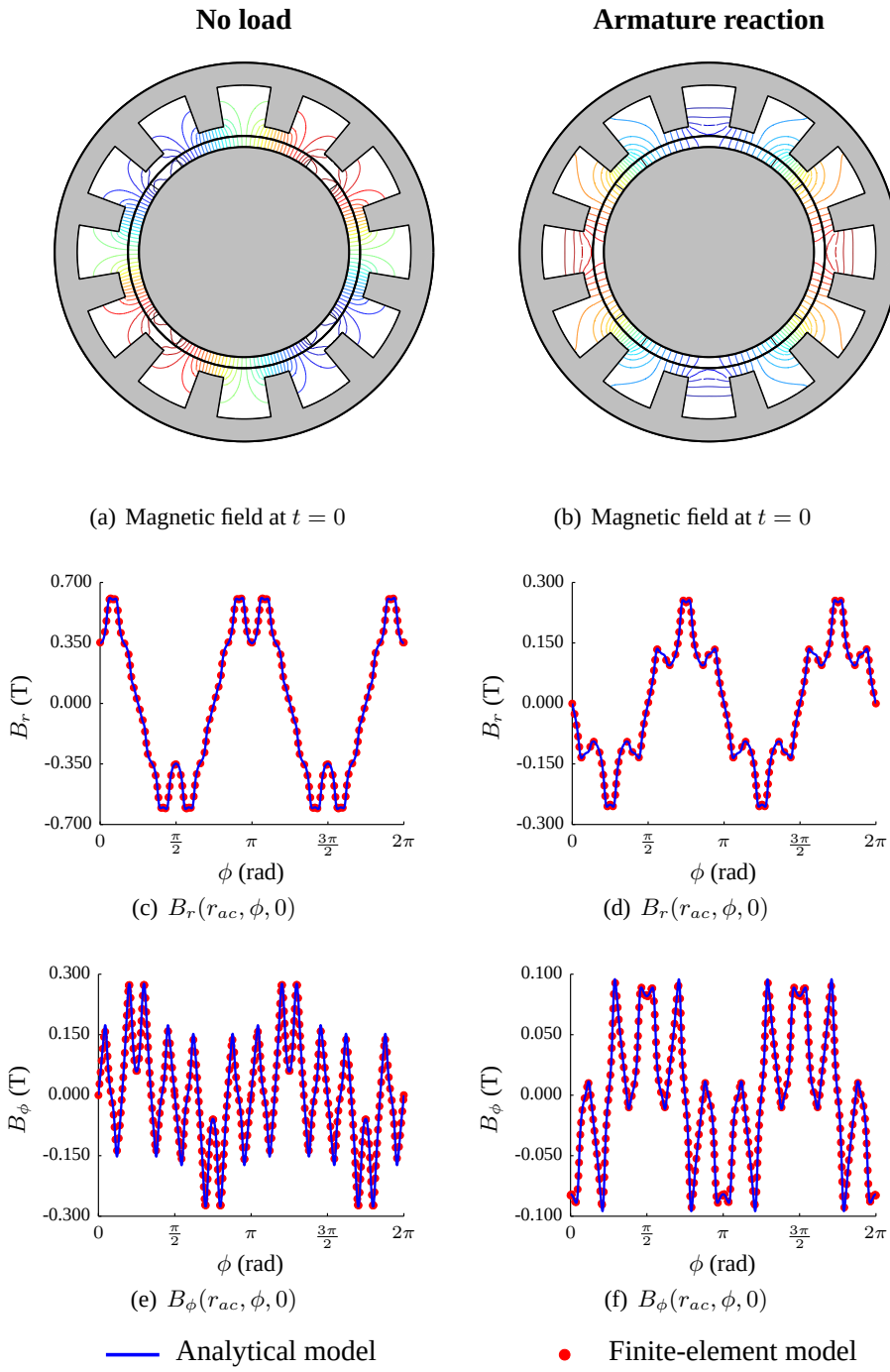

(a) Magnetic field at $t = 0$

(b) Magnetic field at $t = 0$

(c) $B_r(r_{ac}, \phi, 0)$

(d) $B_r(r_{ac}, \phi, 0)$

(e) $B_\phi(r_{ac}, \phi, 0)$

(f) $B_\phi(r_{ac}, \phi, 0)$

Figure 3.14: Validation of the inner-rotor machine with open slots and no SC

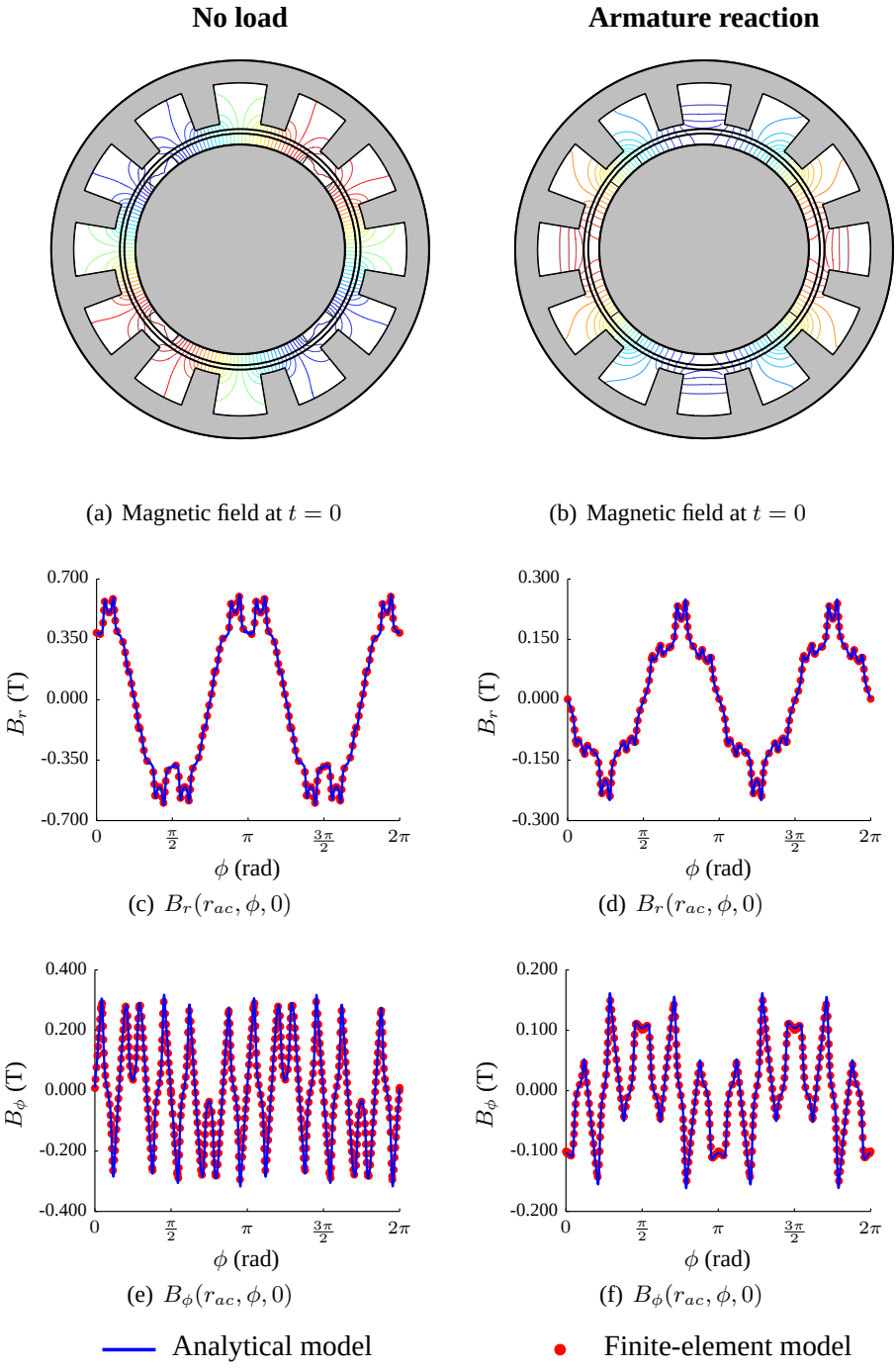

Figure 3.15: Validation of the inner-rotor machine with open slots and a SC

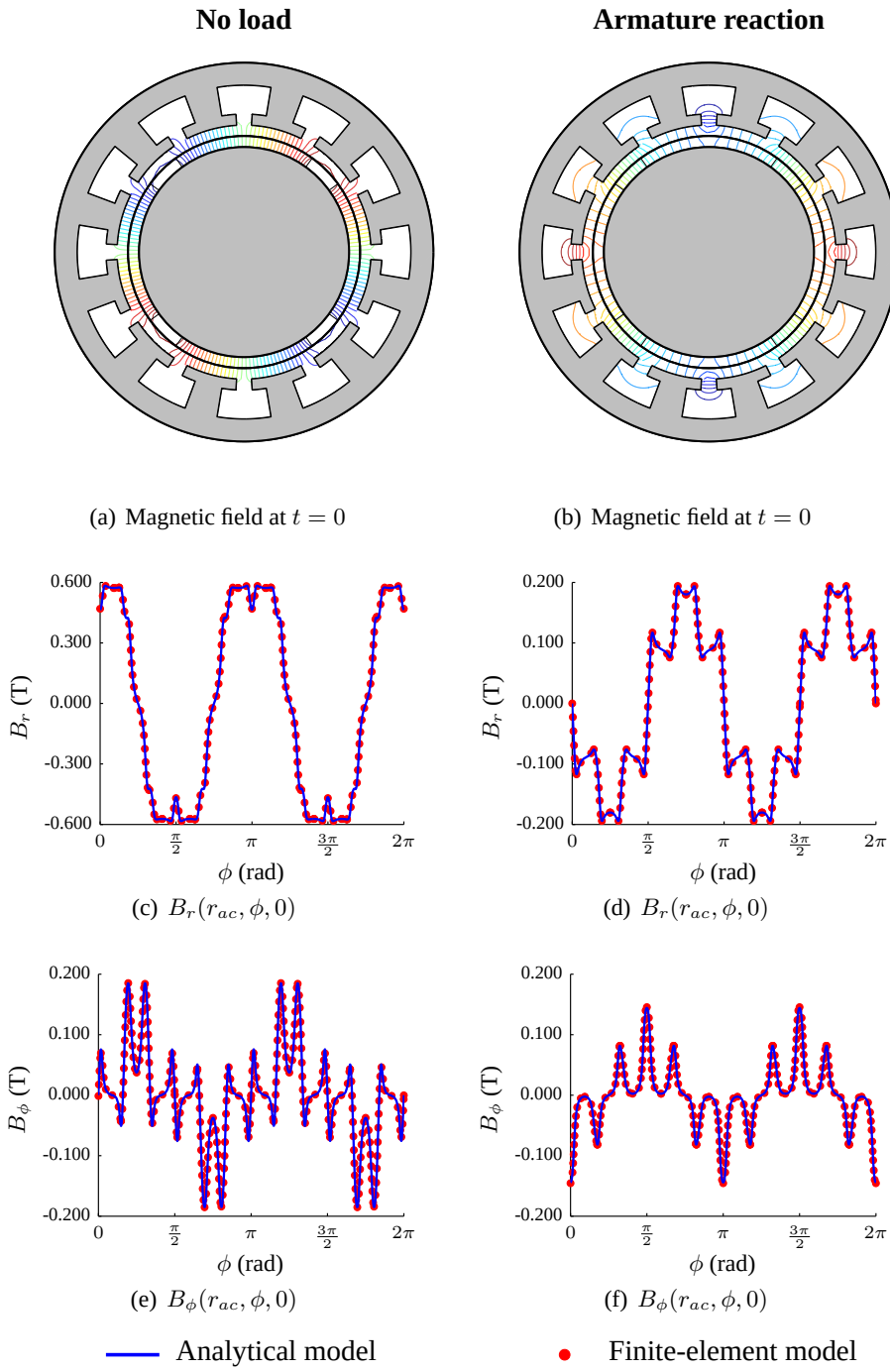

(a) Magnetic field at $t = 0$

(b) Magnetic field at $t = 0$

(c) $B_r(r_{ac}, \phi, 0)$

(d) $B_r(r_{ac}, \phi, 0)$

(e) $B_\phi(r_{ac}, \phi, 0)$

(f) $B_\phi(r_{ac}, \phi, 0)$

Figure 3.16: Validation of the inner-rotor machine with semi-closed slots and no SC

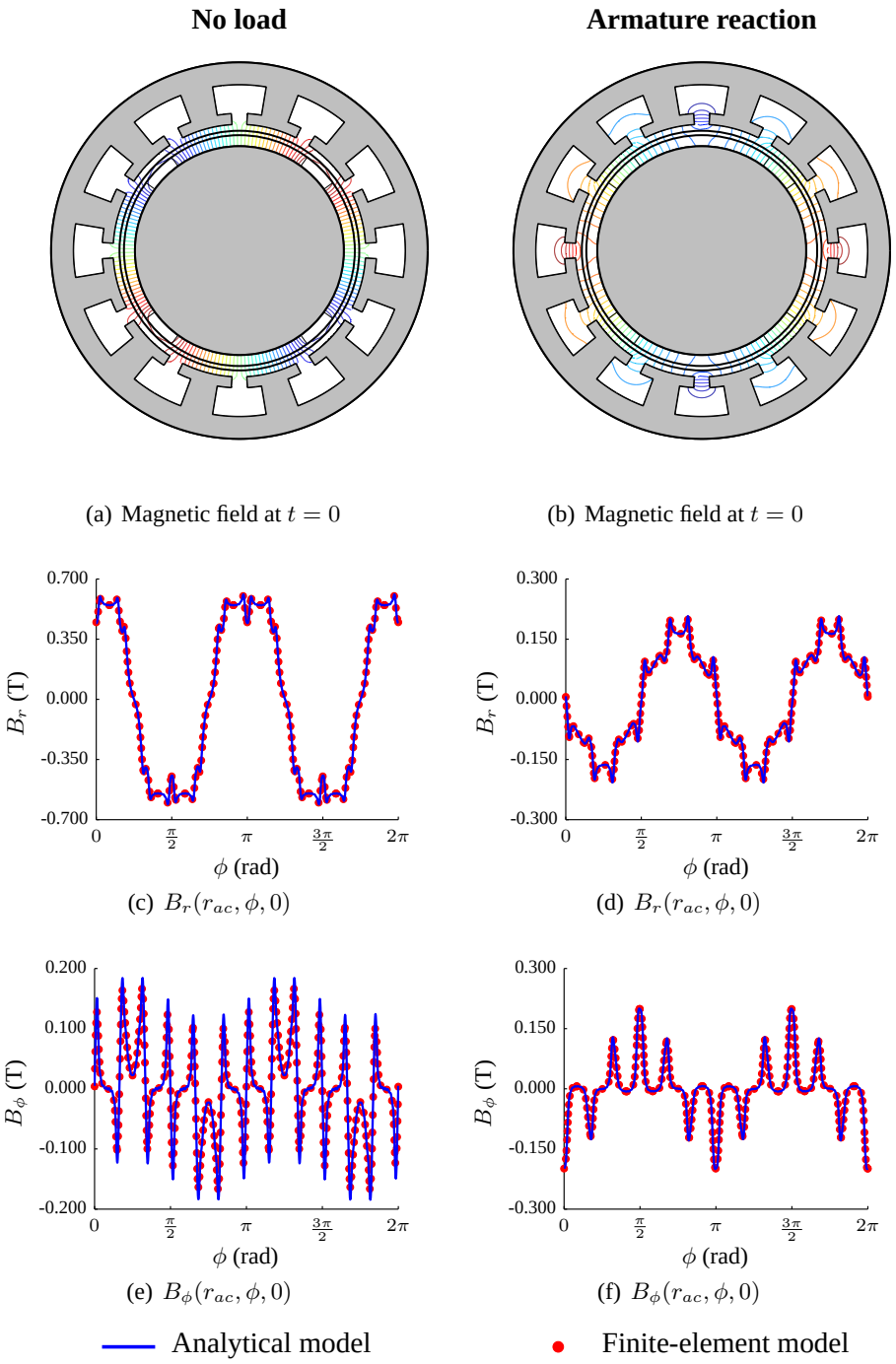

(a) Magnetic field at $t = 0$

(b) Magnetic field at $t = 0$

(c) $B_r(r_{ac}, \phi, 0)$

(d) $B_r(r_{ac}, \phi, 0)$

(e) $B_\phi(r_{ac}, \phi, 0)$

(f) $B_\phi(r_{ac}, \phi, 0)$

Figure 3.17: Validation of the inner-rotor machine with semi-closed slots and a SC

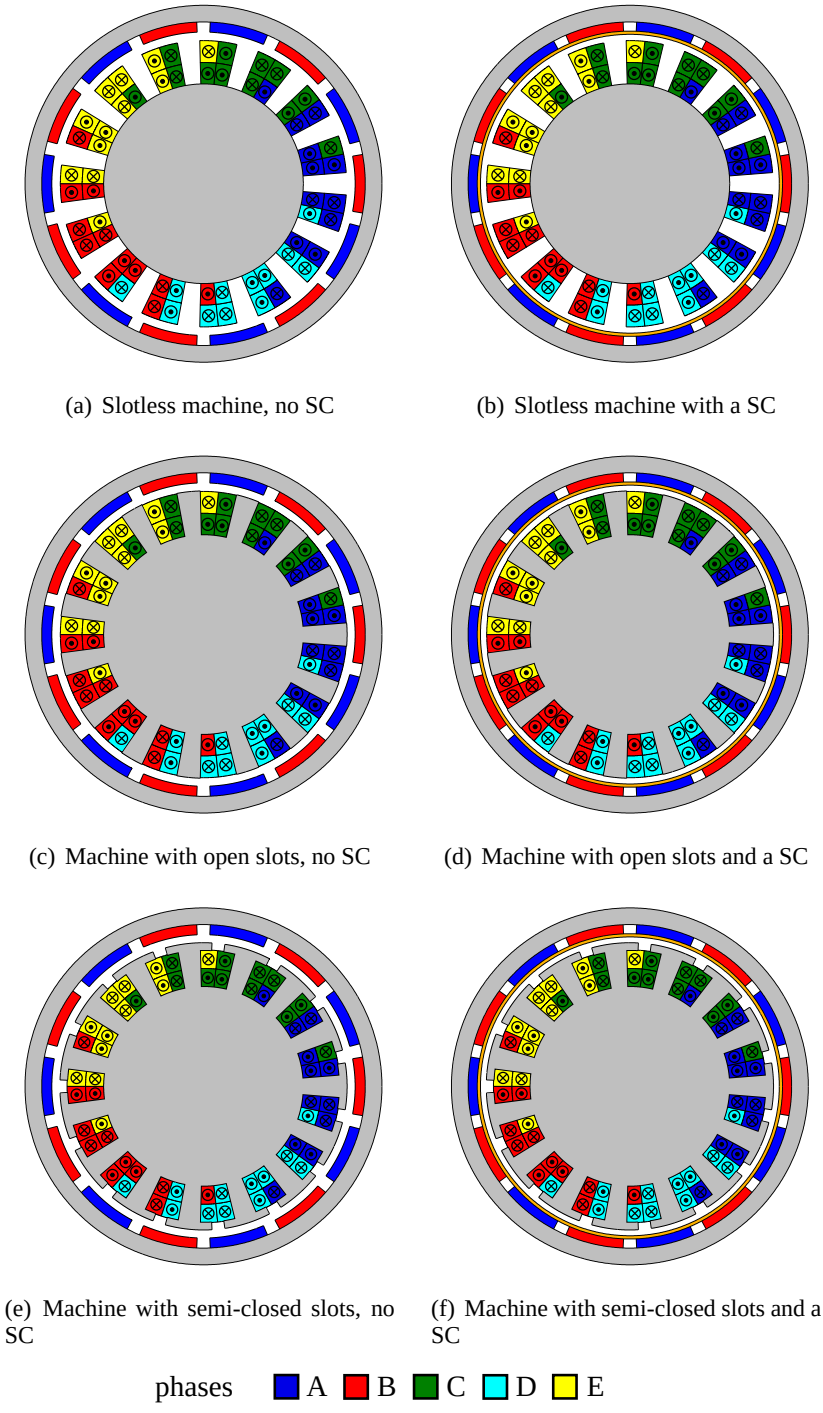

(a) Slotless machine, no SC

(b) Slotless machine with a SC

(c) Machine with open slots, no SC

(d) Machine with open slots and a SC

(e) Machine with semi-closed slots, no SC

(f) Machine with semi-closed slots and a SC

Figure 3.18: Examples of the studied outer-rotor machine topologies

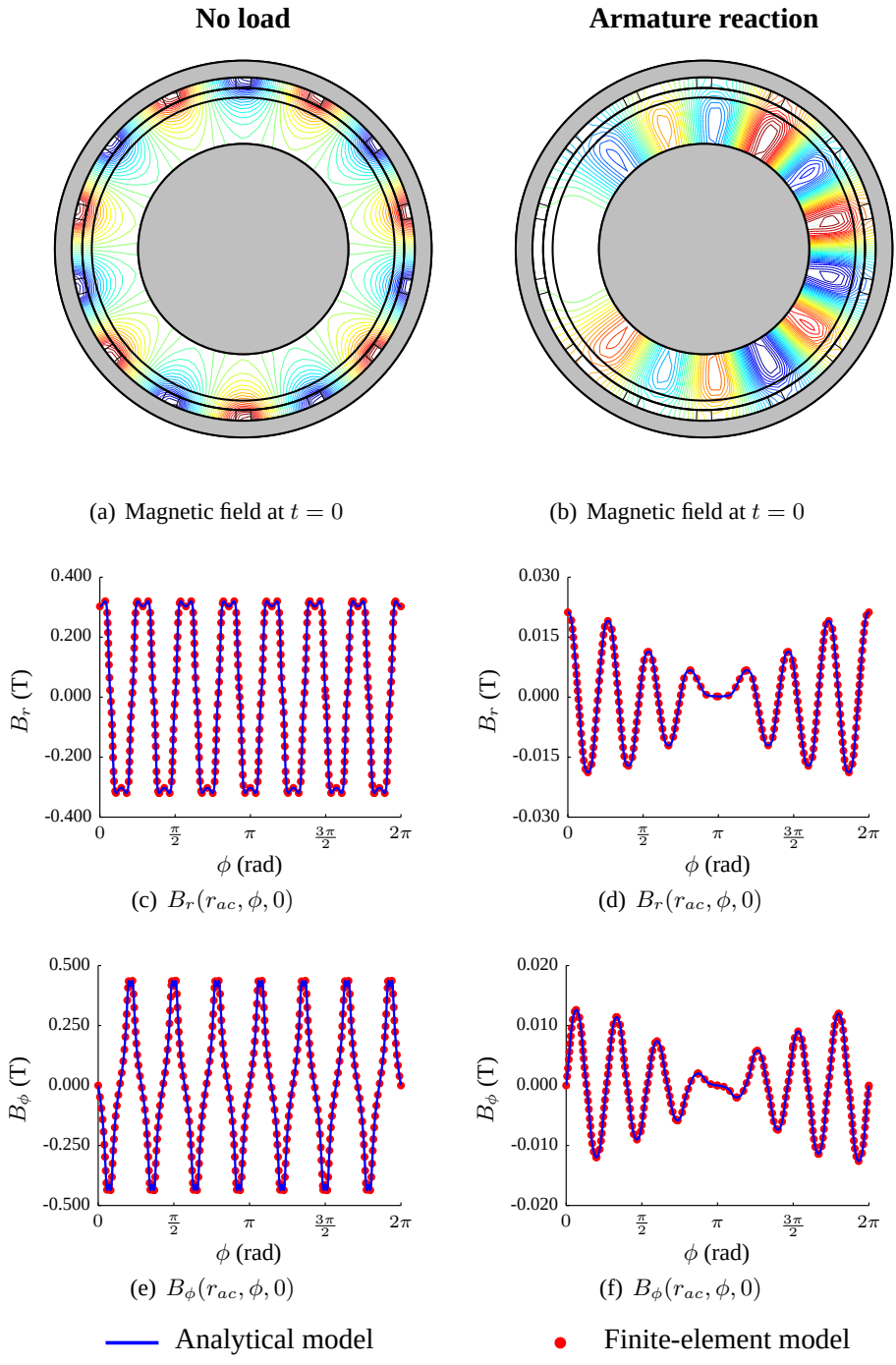

Figure 3.19: Validation of the slotless outer-rotor machine with no SC

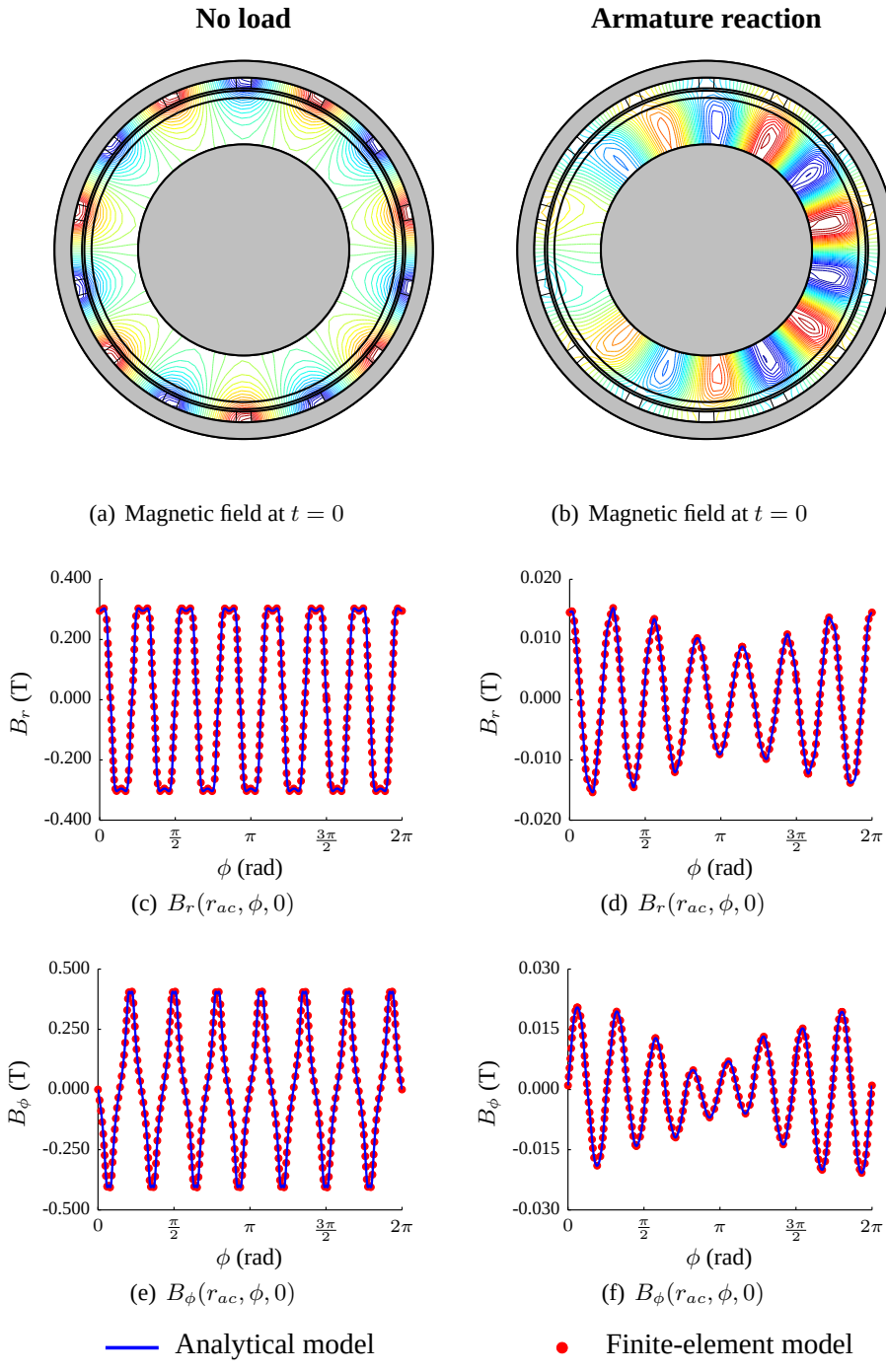

(a) Magnetic field at $t = 0$

(b) Magnetic field at $t = 0$

(c) $B_r(r_{ac}, \phi, 0)$

(d) $B_r(r_{ac}, \phi, 0)$

(e) $B_\phi(r_{ac}, \phi, 0)$

(f) $B_\phi(r_{ac}, \phi, 0)$

Figure 3.20: Validation of the slotless outer-rotor machine with a SC

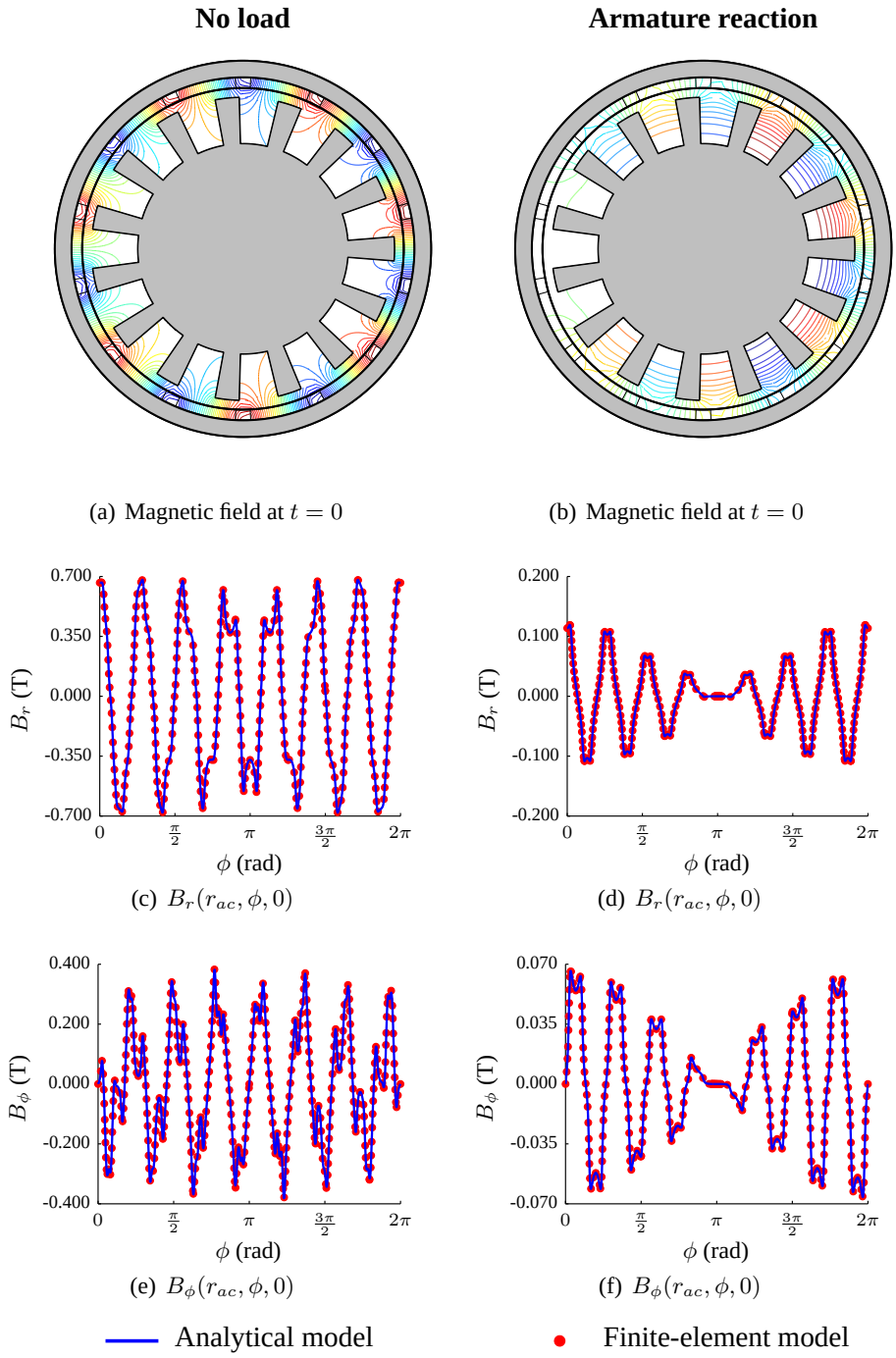

(a) Magnetic field at $t = 0$

(b) Magnetic field at $t = 0$

(c) $B_r(r_{ac}, \phi, 0)$

(d) $B_r(r_{ac}, \phi, 0)$

(e) $B_\phi(r_{ac}, \phi, 0)$

(f) $B_\phi(r_{ac}, \phi, 0)$

Figure 3.21: Validation of the outer-rotor machine with open slots and no SC

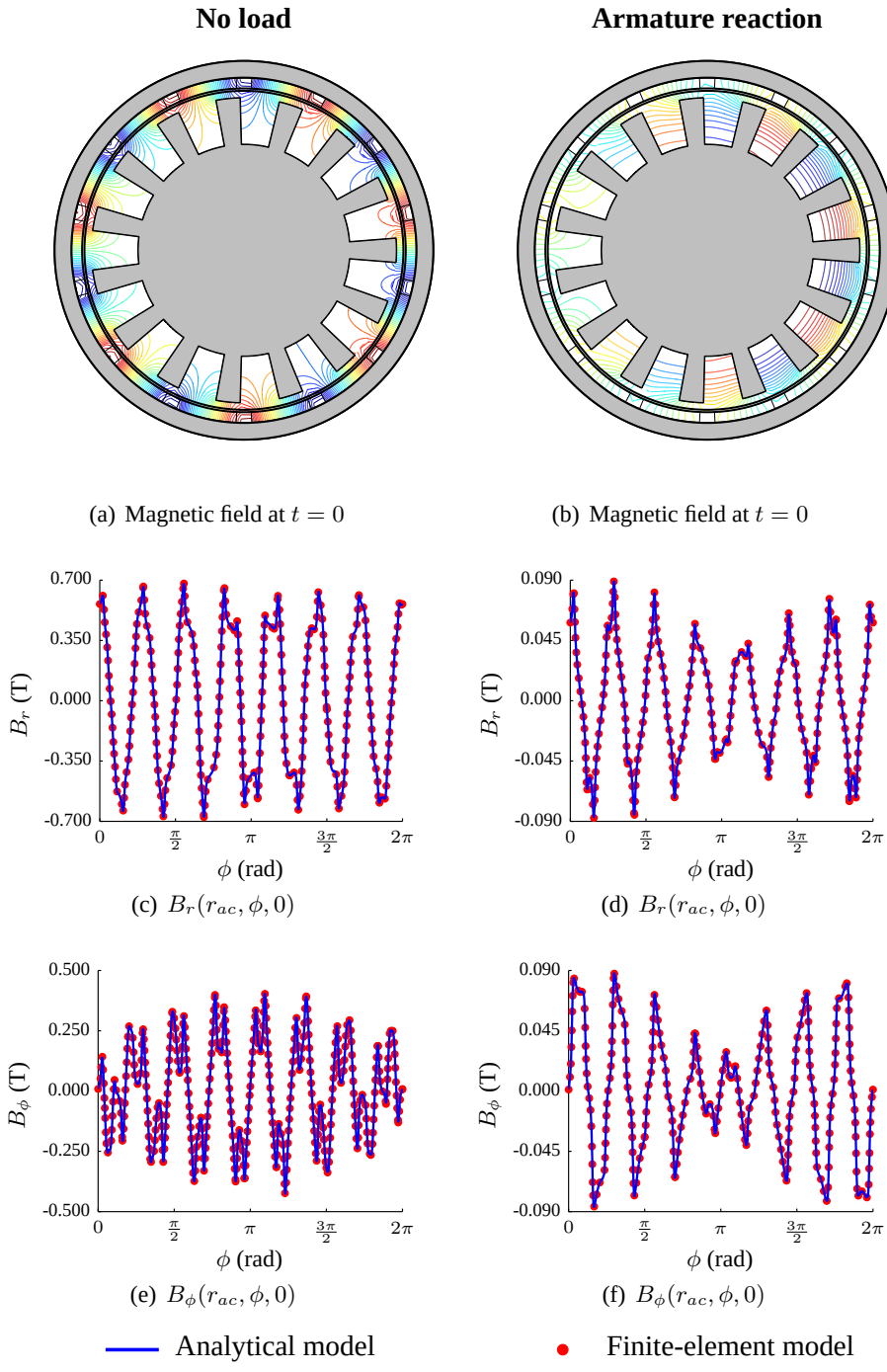

Figure 3.22: Validation of the outer-rotor machine with open slots and a SC

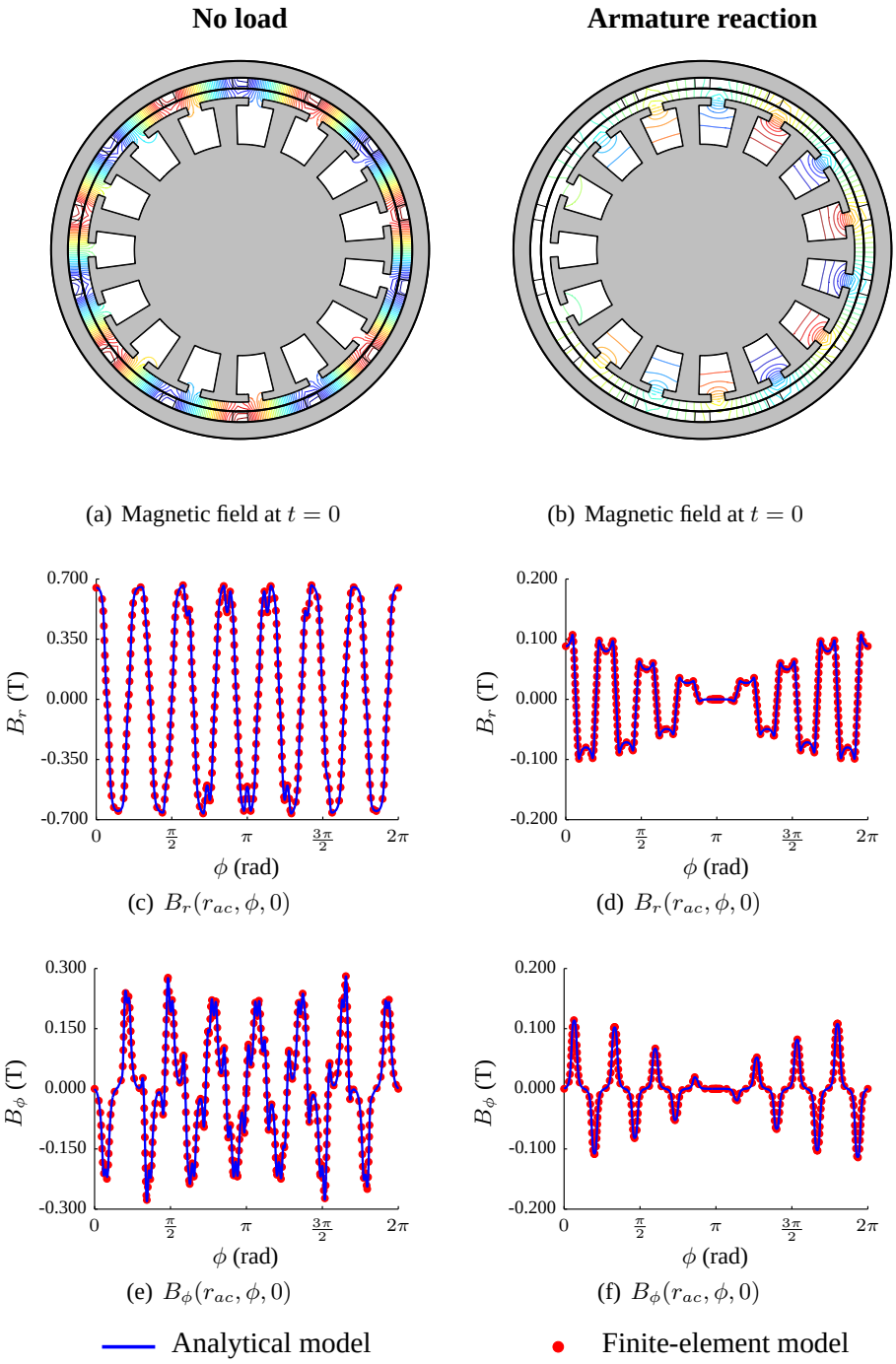

(a) Magnetic field at $t = 0$

(b) Magnetic field at $t = 0$

(c) $B_r(r_{ac}, \phi, 0)$

(d) $B_r(r_{ac}, \phi, 0)$

(e) $B_\phi(r_{ac}, \phi, 0)$

(f) $B_\phi(r_{ac}, \phi, 0)$

Figure 3.23: Validation of the outer-rotor machine with semi-closed slots and no SC

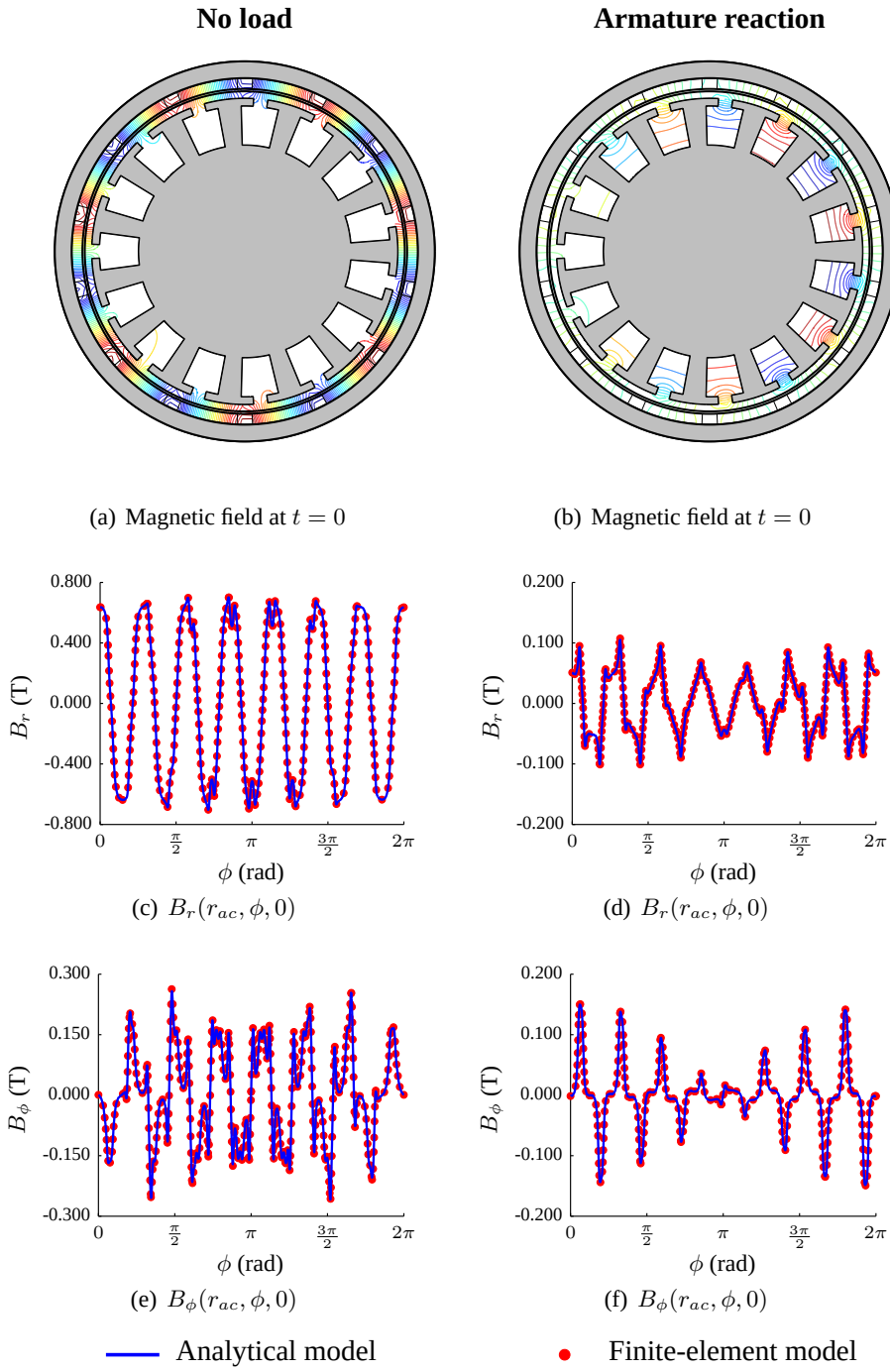

(a) Magnetic field at $t = 0$

(b) Magnetic field at $t = 0$

(c) $B_r(r_{ac}, \phi, 0)$

(d) $B_r(r_{ac}, \phi, 0)$

(e) $B_\phi(r_{ac}, \phi, 0)$

(f) $B_\phi(r_{ac}, \phi, 0)$

Figure 3.24: Validation of the outer-rotor machine with semi-closed slots and a SC

Chapter 4

Aspects of FB modeling; an overview

Section 1.3 presented a concise overview of the aspects within FB modeling that are important in the scope of this work. However, literature presents a far broader range of FB modeling techniques, that may be interesting for other research topics. Now that the physical and mathematical context of FB modeling has been provided, a more extensive evaluation of the very broad range of techniques within Fourier-based modeling can be performed. Evidently, the goal of such an evaluation is not to select the best-suited techniques for this PhD, that was already done in Section 1.3. Instead, this chapter aims at providing an in-depth discussion on all of the most important aspects of FB modeling. By coupling that discussion to the existing literature, this chapter may serve as a starting point for anyone interested in building a Fourier-based model.

Based on the available literature, a number of interesting aspects of FB modeling were identified. Some of those were already briefly discussed in Chapter 1, but will be considered more extensively here.

The first, and probably the most fundamental choice when constructing a FB model is which magnetic potential will be used. It goes without saying that this choice is one of the aspects that needs a more detailed discussion. A second interesting aspect is the choice of a well-suited coordinate system. Thirdly, the way in which the field's time dependency is accounted for is very important as well. The fourth aspect of interest relates to the representation and implementation of the source terms. A fifth interesting aspect is how slotted structures are accounted for. Sixthly, the way FB models can account for eccentricity of the rotor is an interesting aspect. Finally, the obtained magnetic potential has to be translated to meaningful values such as magnetic flux density, torque, losses,...

All of the above seven aspects will be discussed in Sections 4.1-4.7 of this chapter. A conclusion is formulated in Section 4.8.

4.1 Choosing a magnetic potential

Fourier-based models use a magnetic potential to rewrite the magneto-quasi-static formulation of Maxwell's equations in the form of a single partial differential equation (PDE). The two most commonly used magnetic potentials are the magnetic scalar potential and the magnetic vector potential. The goal of this section is to discuss the advantages and disadvantages of both.

4.1.1 Magnetic scalar potential

The magnetic scalar potential, which is indicated as φ, is a scalar quantity. It is defined through its gradient:

$$-\nabla\varphi = \mathbf{H} \tag{4.1}$$

where $\mathbf{H}$ is the magnetic field strength.
From this definition and Maxwell's equations, which were discussed in Section 2.3, a differential equation for the MSP in the linear case can be derived:

$$\nabla^2\varphi = \frac{\nabla\cdot\mathbf{B}_0}{\mu} \tag{4.2}$$

where $\mathbf{B}_0$ is the residual magnetic flux density and μ is the magnetic permeability. In a problem that is formulated using the MSP, the boundary conditions between subdomains ν and $\nu+1$, i.e. (2.25) are written as:

$$\mathbf{n}\cdot\left(\nabla\left(\mu^{(\nu)}\varphi^{(\nu)}-\mu^{(\nu+1)}\varphi^{(\nu+1)}\right)+\left(\mathbf{B}_0^{(\nu)}-\mathbf{B}_0^{(\nu+1)}\right)\right)=0 \tag{4.3a}$$

$$\mathbf{n}\times\nabla\left(\varphi^{(\nu)}-\varphi^{(\nu+1)}\right)=\mathbf{J}_s \tag{4.3b}$$

where $\mathbf{n}$ is the unit vector, normal to the boundary, and $\mathbf{J}_s$ is the boundary's current density.
Due to its scalar nature, the MSP is very easy to use. That is the reason why it has long been a commonly used magnetic potential in Fourier-based models. Nowadays it is still often used in three-dimensional problems [57, 106, 107], where use of the MVP requires extensive vector calculus. The MSP's main drawback, however, is that it can only be defined in current-free regions. This can easily be seen from its governing equation (4.2), which lacks a current-density term. There are two major workarounds to avoid the need for current-free regions.
The first, and most commonly used, workaround is to replace the current density in the studied region with a current sheet on its boundary [54]. This current sheet is then accounted for through the boundary conditions (4.3). However, using current sheets may imply a loss of accuracy [75], especially in slotless machines.
The second workaround is to use a combination of the reduced magnetic scalar potential and the electric vector potential. However, as the analytical derivation of the electric vector potential is often devious, use of this workaround is very rare in

FB models. Nevertheless, interested readers may find an extensive discussion on the subject in the book of Kuczmann [103].

4.1.2 Magnetic vector potential

The MVP, which is a vector quantity, is defined through its curl:

$$\nabla \times \mathbf{A} = \mathbf{B} \tag{4.4}$$

It was shown in Section 2.4 that in the linear case, the MVP's governing equation can be written as:

$$\nabla^2 \mathbf{A} - \mu\sigma \frac{\partial \mathbf{A}}{\partial t} + \mu\sigma \left(\mathbf{v} \times (\nabla \times \mathbf{A})\right) = \mu \mathbf{J}_{ext} - \nabla \times \mathbf{B}_0 \tag{4.5}$$

Its boundary conditions are:

$$\mathbf{A}^{(\nu)} - \mathbf{A}^{(\nu+1)} = 0 \tag{4.6a}$$

$$\mathbf{n} \times \left(\nabla \times \left(\frac{\mathbf{A}^{(\nu)}}{\mu^{(\nu)}} - \frac{\mathbf{A}^{(\nu+1)}}{\mu^{(\nu+1)}} \right) - \left(\frac{\mathbf{B}_0^{(\nu)}}{\mu^{(\nu)}} - \frac{\mathbf{B}_0^{(\nu+1)}}{\mu^{(\nu+1)}} \right) \right) = \mathbf{J}_s \tag{4.6b}$$

It is evident that the MVP's vectorial nature implies a more extensive calculus. This complexity is the main reason not to use the MVP, especially in 3D models. However, in 2D problems, where it reduces to a scalar, the MVP is by far the most popular magnetic potential [43, 63, 108, 109]. The primary reason for that is the MVP's ability to account for subdomains with a current density. Note that some authors do use the MVP to study three-dimensional problems. This can either be done directly [110] or by using the second-order MVP [111].

4.1.3 Conclusion

Due to its flexibility, the MVP is usually the best-suited magnetic potential to study electric machines. However, in current-free problems or problems where the MVP's vector calculus is too complex, the MSP may be preferred. Note that the current-sheet workaround cannot be used to account for eddy-current reaction field. This implies that, if such a reaction field is non-negligible, the MVP should be used.

The mathematical framework and implementation of a two-dimensional FB model that uses the MVP, is discussed in Chapters 2 and 3. A clear discussion on the implementation of a 2D Fourier-based model using the MSP is provided in [53], an equally interesting paper that focuses on the MVP is Gysen's very generally formulated work [109]. For three-dimensional models, Meessen [106], Gerling [110] and Jumayev [111] present a comprehensive implementation of the MSP, the MVP and the second-order MVP respectively.

4.2 Coordinate systems

As already mentioned, this work focuses on models that apply a two-dimensional approximation. This implies that the problem is assumed invariant along one direction. That direction is referred to as the longitudinal (l) direction. The other two directions are the periodic (ρ) direction, along which the problem is periodic, and the normal (η) direction.
Note that, as the problem is invariant along the longitudinal direction, the MVP can be considered to be a scalar:

$$\mathbf{A} = A\mathbf{e}_l \tag{4.7}$$

The (η, ρ, l) coordinate system is a generalized coordinate system. In order to model an actual machine, a specific coordinate system has to be chosen. The earliest publications on Fourier-based modeling tended to use a Cartesian coordinate system. However, for most geometries, this implies simplifying the geometry while only resulting in a slightly less complex model. Nowadays the choice is mostly determined by the geometry of the studied problem. For example, when the goal is to model a radial-flux rotational machine in two dimensions, a polar coordinate system (r, ϕ, z) may be used [43, 51, 53–56, 60, 63, 65, 74–76, 112]. Two dimensional models of tubular linear machines use a cylindrical coordinate system (r, ϕ, z) [77–80]. 2D approximations of axial-flux machines are usually modeled in a Cartesian coordinate system (x, y, z) [71–73]. The use of different coordinate systems for various problems is illustrated in Figure 4.1 for a problem in Cartesian coordinates, e.g. Figure 4.1(a): an axial-flux DC brake, for a problem in polar coordinates, e.g. Figure 4.1(b): a permanent-magnet synchronous machines and for a problem in cylindrical coordinates, e.g. Figure 4.1(c): a tubular linear machine.

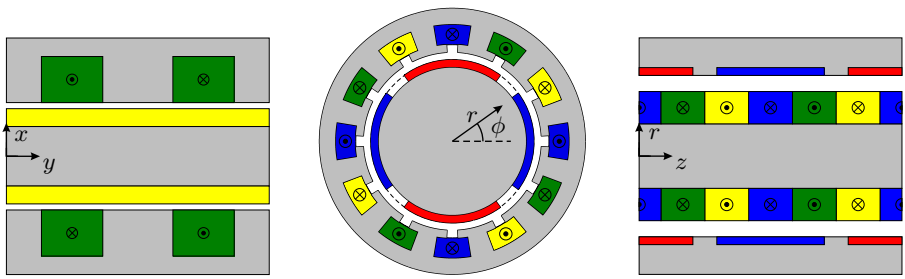

(a) Axial-flux DC brake (b) PMSM (c) Tubular linear machine

Figure 4.1: Simplification of the example-machine's geometry

In the following, the above coordinate systems are linked to the generalized coordinate system and the homogeneous solutions of their η-dependent parts are introduced.

4.2.1 Coordinate systems

Table 4.1 links the generalized coordinates to the Cartesian, polar and cylindrical coordinate systems.

Table 4.1: Coordinate systems

Coordinate system	η-direction	ρ-direction	l-direction
Cartesian	x	y	z
Polar	r	ϕ	z
Cylindrical	r	z	ϕ

Note that the only difference between problems that apply a polar coordinate system and problems that apply a cylindrical coordinate system is the direction along which they are periodic and invariant.

4.2.2 Homogeneous solution of the PDE

As shown in [50, 113], the general form of the magnetic potentials' solutions can be written as:

$$\varphi^{(\nu)}(\eta,\rho,t) = \sum_{n=-\infty}^{\infty}\sum_{k=-\infty}^{\infty} \varphi_{n,k}^{(\nu)}(\eta) e^{j\left(\frac{2k\pi}{T^{(\nu)}}\left(\rho-\rho_0^{(\nu)}\right)-n\omega t\right)} \tag{4.8}$$

for the MSP and

$$A^{(\nu)}(\eta,\rho,t) = \sum_{n=-\infty}^{\infty}\sum_{k=-\infty}^{\infty} A_{n,k}^{(\nu)}(\eta) e^{j\left(\frac{2k\pi}{T^{(\nu)}}\left(\rho-\rho_0^{(\nu)}\right)-n\omega t\right)} \tag{4.9}$$

for the MVP.
In (4.8) and (4.9), n refers to the time-harmonic order, k refers to the spatial-harmonic order, ν refers to a subdomain, $T^{(\nu)}$ is the spatial periodicity of subdomain ν, ω is the rotational speed of the studied device and $\rho_0^{(\nu)}$ is the lower ρ boundary of subdomain ν. All of these symbols and the derivation of the general form were also discussed in Chapter 3.
The η-dependent part of (4.8) and (4.9) depends on the PDE's simplification in subdomain ν. It can be proven that the differential equation for the MSP can either be a Laplace or a Poisson equation [114, 115]. The differential equation for the MVP, on the other hand, can either be a Laplace, a Poisson or a Helmholtz equation, as was discussed in Chapter 3. Knowing this, the homogeneous solutions of (4.8) and (4.9) can be written in full for each of the coordinate systems.
In Cartesian coordinates, the solution for the MSP in subdomain ν is written as:

$$\varphi^{(\nu)}(x,y,t) = \sum_{n=-\infty}^{\infty}\sum_{k=-\infty}^{\infty} \varphi_{n,k}^{(\nu)}(x) e^{j\left(\frac{2k\pi}{T^{(\nu)}}\left(y-y_0^{(\nu)}\right)-n\omega t\right)} \tag{4.10}$$

where

$$\varphi_{n,k}^{(\nu)}(x) = \begin{cases} C_{n,k}^{(\nu)} e^{|\frac{2k\pi}{T^{(\nu)}}|x} + D_{n,k}^{(\nu)} e^{-|\frac{2k\pi}{T^{(\nu)}}|x} & \text{Laplace} \\ C_{n,k}^{(\nu)} e^{|\frac{2k\pi}{T^{(\nu)}}|x} + D_{n,k}^{(\nu)} e^{-|\frac{2k\pi}{T^{(\nu)}}|x} + P_{n,k}^{(\nu)}(x) & \text{Poisson} \end{cases} \tag{4.11}$$

where $C_{n,k}^{(\nu)}$ and $D_{n,k}^{(\nu)}$ are integration constants and $P_{n,k}^{(\nu)}(x)$ is the particular solution of the Poisson equation, the form of which depends on the subdomain's source term.
Similarly, the solution for the MVP is written as:

$$A^{(\nu)}(x,y,t) = \sum_{n=-\infty}^{\infty} \sum_{k=-\infty}^{\infty} A_{n,k}^{(\nu)}(x) e^{j\left(\frac{2k\pi}{T^{(\nu)}}\left(y - y_0^{(\nu)}\right) - n\omega t\right)} \tag{4.12}$$

where

$$A_{n,k}^{(\nu)}(x) = \begin{cases} C_{n,k}^{(\nu)} e^{|\frac{2k\pi}{T^{(\nu)}}|x} + D_{n,k}^{(\nu)} e^{-|\frac{2k\pi}{T^{(\nu)}}|x} & \text{Laplace} \\ C_{n,k}^{(\nu)} e^{|\frac{2k\pi}{T^{(\nu)}}|x} + D_{n,k}^{(\nu)} e^{-|\frac{2k\pi}{T^{(\nu)}}|x} + P_{n,k}^{(\nu)}(x) & \text{Poisson} \\ C_{n,k}^{(\nu)} e^{\sqrt{\left(\frac{2k\pi}{T^{(\nu)}}\right)^2 + \tau_{n,k}^2}\, x} + D_{n,k}^{(\nu)} e^{-\sqrt{\left(\frac{2k\pi}{T^{(\nu)}}\right)^2 + \tau_{n,k}^2}\, x} & \text{Helmholtz} \end{cases} \tag{4.13}$$

In polar coordinates, the solution for the MSP in subdomain ν is written as:

$$\varphi^{(\nu)}(r,\phi,t) = \sum_{n=-\infty}^{\infty} \sum_{k=-\infty}^{\infty} \varphi_{n,k}^{(\nu)}(r) e^{j\left(\frac{2k\pi}{T^{(\nu)}}\left(\phi - \phi_0^{(\nu)}\right) - n\omega t\right)} \tag{4.14}$$

where

$$\varphi_{n,k}^{(\nu)}(r) = \begin{cases} C_{n,k}^{(\nu)} r^{|\frac{2k\pi}{T^{(\nu)}}|} + D_{n,k}^{(\nu)} r^{-|\frac{2k\pi}{T^{(\nu)}}|} & \text{Laplace} \\ C_{n,k}^{(\nu)} r^{|\frac{2k\pi}{T^{(\nu)}}|} + D_{n,k}^{(\nu)} r^{-|\frac{2k\pi}{T^{(\nu)}}|} + P_{n,k}^{(\nu)}(r) & \text{Poisson} \end{cases} \tag{4.15}$$

For the MVP:

$$A^{(\nu)}(r,\phi,t) = \sum_{n=-\infty}^{\infty} \sum_{k=-\infty}^{\infty} A_{n,k}^{(\nu)}(r) e^{j\left(\frac{2k\pi}{T^{(\nu)}}\left(\phi - \phi_0^{(\nu)}\right) - n\omega t\right)} \tag{4.16}$$

where

$$A_{n,k}^{(\nu)}(r) = \begin{cases} C_{n,k}^{(\nu)} r^{|\frac{2k\pi}{T^{(\nu)}}|} + D_{n,k}^{(\nu)} r^{-|\frac{2k\pi}{T^{(\nu)}}|} & \text{Laplace} \\ C_{n,k}^{(\nu)} r^{|\frac{2k\pi}{T^{(\nu)}}|} + D_{n,k}^{(\nu)} r^{-|\frac{2k\pi}{T^{(\nu)}}|} + P_{n,k}^{(\nu)}(r) & \text{Poisson} \\ C_{n,k}^{(\nu)}\, \mathrm{I}_{\frac{2k\pi}{T^{(\nu)}}}(\tau_{n,k} r) + D_{n,k}^{(\nu)}\, \mathrm{K}_{\frac{2k\pi}{T^{(\nu)}}}(\tau_{n,k} r) & \text{Helmholtz} \end{cases} \tag{4.17}$$

where $\mathrm{I}_{\frac{2k\pi}{T^{(\nu)}}}$ is the $\frac{2k\pi}{T^{(\nu)}}$-order modified Bessel function of the first kind and, similarly, $\mathrm{K}_{\frac{2k\pi}{T^{(\nu)}}}$ is the $\frac{2k\pi}{T^{(\nu)}}$-order modified Bessel function of the second kind.
In cylindrical coordinates, at last, the solution for the MSP in subdomain ν is written as:

$$\varphi^{(\nu)}(r,z,t) = \sum_{n=-\infty}^{\infty} \sum_{k=-\infty}^{\infty} \varphi_{n,k}^{(\nu)}(r) e^{j\left(\frac{2k\pi}{T^{(\nu)}}\left(z-z_0^{(\nu)}\right)-n\omega t\right)} \tag{4.18}$$

where

$$\varphi_{n,k}^{(\nu)}(r) = \begin{cases} C_{n,k}^{(\nu)} \mathrm{I}_1\left(\dfrac{2k\pi}{T^{(\nu)}} r\right) + D_{n,k}^{(\nu)} \mathrm{K}_1\left(\dfrac{2k\pi}{T^{(\nu)}} r\right) & \text{Laplace} \\ C_{n,k}^{(\nu)} \mathrm{I}_1\left(\dfrac{2k\pi}{T^{(\nu)}} r\right) + D_{n,k}^{(\nu)} \mathrm{K}_1\left(\dfrac{2k\pi}{T^{(\nu)}} r\right) + P_{n,k}^{(\nu)}(r) & \text{Poisson} \end{cases} \tag{4.19}$$

For the MVP:

$$A^{(\nu)}(r,z,t) = \sum_{n=-\infty}^{\infty} \sum_{k=-\infty}^{\infty} A_{n,k}^{(\nu)}(r) e^{j\left(\frac{2k\pi}{T^{(\nu)}}\left(z-z_0^{(\nu)}\right)-n\omega t\right)} \tag{4.20}$$

where

$$A_{n,k}^{(\nu)}(r) = \begin{cases} C_{n,k}^{(\nu)} \mathrm{I}_1\left(\dfrac{2k\pi}{T^{(\nu)}} r\right) + D_{n,k}^{(\nu)} \mathrm{K}_1\left(\dfrac{2k\pi}{T^{(\nu)}} r\right) & \text{Laplace} \\ C_{n,k}^{(\nu)} \mathrm{I}_1\left(\dfrac{2k\pi}{T^{(\nu)}} r\right) + D_{n,k}^{(\nu)} \mathrm{K}_1\left(\dfrac{2k\pi}{T^{(\nu)}} r\right) + P_{n,k}^{(\nu)}(r) & \text{Poisson} \\ C_{n,k}^{(\nu)} \mathrm{I}_1\left(\sqrt{\left(\dfrac{2k\pi}{T^{(\nu)}}\right)^2 + \tau_{\tau_{n,k}}^2} r\right) & \text{Helmholtz} \\ \quad + D_{n,k}^{(\nu)} \mathrm{K}_1\left(\sqrt{\left(\dfrac{2k\pi}{T^{(\nu)}}\right)^2 + \tau_{\tau_{n,k}}^2} r\right) & \end{cases} \tag{4.21}$$

Note that, both in polar and cylindrical coordinates, solutions with ordinary instead of modified Bessel functions are possible as well. However, modified Bessel functions are preferred because they are smoother than their ordinary counterparts.

4.2.3 Conclusion

In the above, the three coordinate systems that are most commonly used in literature are introduced. Their coordinates are linked to those of the generalized coordinate system. Moreover, the homogeneous parts of their solutions were discussed as well.

4.3 Time dependency

Evidently, the magnetic field is not only dependent on space, but on time as well. In the above, the magneto-quasi-static approximation of Maxwell's equations was used. However, a lot of authors further simplify the problem by using the magneto-static approximation. This implies that they do not consider the physical effects of time-dependency. This choice between the magneto-static and the magneto-quasi-static approximation is a first aspect of time dependency that is discussed in this section.
However, even if the physical effects of time-dependency are neglected, the actual magnetic field is still time-dependent. If not accounted for directly, multiple static calculations can be used to calculate the field at various time-instances. The choice between multiple static calculations and direct time-dependency is the second aspect of time dependency that will be addressed in this section.

4.3.1 Static versus quasi-static problems

The physical consequence of assuming static conditions is that the eddy-current reaction field is neglected. In the potential formulation, this means that the time-derivative and speed-dependent terms of (4.5) are disregarded. Evidently, the magneto-static approximation is simpler than the magneto-quasi static one, it may therefore be preferred if the effect of eddy-currents is small.
Note that, as the MSP assumes current-free regions, it can not account for eddy-current reaction field. Evidently, this means that using the MSP inherently implies assuming magneto-static conditions.

4.3.2 Multiple static calculations versus direct time-dependency

Regardless of whether the magneto-static or the magneto-quasi-static approximation is used, the magnetic field in the studied problem will almost always vary in time. This time-dependency can either be accounted for directly or through multiple static calculations. Direct time-dependency implies that the equations for the magnetic potential are written as a function of time. This approach was used in Section 4.2. Another approach is to divide the problem's period in a number of time instances. The time-independent problem is then solved for each of these instances of time, i.e. with updated values of the rotor position and currents.
Indirect time-dependency has two major advantages. Firstly, it is simpler than directly accounting for the time-dependency. Indeed, neglecting the time-dependency allows disregarding the time-harmonic orders. This, in turn, results in a single Fourier series instead of the double Fourier series of (4.8) and (4.9). The latter also explains the second major advantage of multiple static calculations; due to the absence of time-harmonic orders, every single time step is calculated very fast.
Directly accounting for the field's time dependency, on the other hand, allows for

a more accurate solution. Indeed, allowing for a time-dependent solution implies that the MQS approximation can be used. Moreover, if the solution as such is time-dependent, the problem does not have to be recalculated for every time step. This implies that, although FB models with an indirect time-dependency can very quickly compute results for a single instance of time, the computational burden of FB models with direct time-dependency isn't necessarily larger when a complete period has to be calculated.
Because of the above, most authors of magneto-static models use indirect time-dependency, while authors of magneto-quasi static models tend to directly account for the time dependency. However, if only the fundamental time-harmonic is considered, eddy-current reaction field can be accounted for in models that use an indirect time-dependency. This was, a.o. done by Boughrara et al [66] to model induction machines.

4.3.3 Conclusion

Two aspects of time-dependency were discussed in the above.
First, it was noted that, depending on the importance of the eddy-current reaction field, either the simpler magneto-static approximation or the more complete magneto-quasi-static approximation can be used.
Next, models with multiple static calculations and models with a direct time-dependency were compared. It was concluded that models with an indirect time-dependency are simpler to implement and may be preferred in magneto-static models. Models with a direct time-dependency are to be preferred in magneto-quasi-static models, especially if the effect of higher time-harmonic orders is relevant.
Interesting examples of magneto-static models that apply the technique of multiple static calculations have been published in [50, 64, 92, 116]. Magneto-quasi static models that directly account for time-dependency may be found in [51, 81, 117] and lastely, publications on quasi-static models with an indirect time-dependency can be found in [66].
Because of the non-negligible effect of the eddy-current reaction field in high-speed PMSMs, this work uses the MQS approximation. As a lot of time-dependent values have to be studied and because of the fact that time-harmonic content is important, time-dependency will directly be accounted for.

4.4 Source terms

Obviously, there can only be a magnetic field if the studied problem contains source terms, i.e. materials with a residual magnetic flux density and/or externally imposed current densities. The latter can either be imposed directly or by applying a voltage source. There are thus three types of sources that have to be discussed; residual magnetic flux densities, external current sources and external

voltage sources. In the following, the way in which each of these sources is accounted for is discussed.

4.4.1 Residual magnetization

There are two ways in which materials with residual magnetic flux densities can be implemented; directly or through equivalent currents. In both techniques, a Fourier representation of the residual magnetization has to be available. In its most general form, that representation is:

$$\mathbf{B}_0^{(\nu)} = \sum_{n=-\infty}^{\infty} \sum_{k=-\infty}^{\infty} \left(B_{0,\eta,n,k}^{(\nu)}(\eta)\mathbf{e}_\eta + B_{0,\rho,n,k}^{(\nu)}(\eta)\mathbf{e}_\rho \right) e^{j\left(\frac{2k\pi}{T^{(\nu)}}\left(\rho-\rho_0^{(\nu)}\right)-n\omega t\right)} \tag{4.22}$$

where $B_{0,\eta,n,k}^{(\nu)}(\eta)$ and $B_{0,\rho,n,k}^{(\nu)}(\eta)$ depend on the magnetization pattern.
The PDEs for both the MSP and the MVP can directly account for permanent magnetic materials. To do that, a particular solution for the appropriate Poisson equation has to be determined. Next, that solution has to be substituted in the appropriate potential equation, as presented in Section 4.2. Directly accounting for residual magnetic flux densities is definitely the most straightforward approach. Moreover, mostly it isn't more complex than using current sheets. Therefore, nowadays the vast majority of authors directly accounts for permanent magnetic materials [65, 118–121].
As already mentioned, the alternative is to represent the permanent magnets by equivalent current densities. Two types of current densities have to be considered; the equivalent volume current densities ($\mathbf{J}_m$), which manifest in the entire magnet volume, and the equivalent surface current densities ($\mathbf{j}_m$), which manifest on the magnet's boundaries. They are calculated as:

$$\begin{aligned} \mathbf{J}_m &= \nabla \times \mathbf{M}_0 \\ \mathbf{j}_m &= \mathbf{M}_0 \times \mathbf{n} \end{aligned} \tag{4.23}$$

where $\mathbf{M}_0 = \mu_0 \mathbf{B}_0$ is the residual magnetization vector and $\mathbf{n}$ is the outward facing unit vector, normal to the magnet's boundary.
Evidently, in a 2D approximation, the volume current densities are reduced to surface current densities. They are therefore implemented in the same way as the externally imposed current densities. Similarly, the equivalent surface current densities are reduced to current sheets. These are accounted for through the boundary conditions: (4.3) or (4.6).
Whereas working with equivalent current densities used to be widespread in FB modeling, nowadays it is only used in some specific cases. For example in three-dimensional models, where analytical solutions of the Poisson equation may be complicated [111] or in models that apply Schwarz-Christoffel transformations to account for slotting [95, 122].

4.4.2 Externally imposed current densities

Similar to accounting for residual magnetization, accounting for externally imposed current densities can either be done directly or by considering a current sheet instead. The externally imposed current density is therefore again expressed as a Fourier series:

$$\mathbf{J}_{ext}^{(\nu)} = \sum_{n=-\infty}^{\infty} \sum_{k=-\infty}^{\infty} J_{ext,n,k}^{(\nu)} e^{j\left(\frac{2k\pi}{T^{(\nu)}}\left(\rho-\rho_0^{(\nu)}\right)-n\omega t\right)} \mathbf{e}_l \tag{4.24}$$

As the MSP assumes current-free regions, directly accounting for current densities is only possible for problems that are formulated in the MVP. To do so, the particular solution of the Poisson equation is again substituted in the appropriate solution for the MVP.
In slotted machines, the current density is then often assumed uniform in every subdomain [50, 65, 75]. However, some authors do consider spatial dependency of the current density within a single slot [64, 123]. Evidently, in slotless machines, where the entire slotting region is a single subdomain, the spatial dependency of the current density is accounted for as well [43, 87].
As an alternative to directly accounting for external current densities, a surface current density ($\mathbf{J}_s$) can be imposed through the boundary conditions; (4.3) or (4.6). $\mathbf{J}_s$ then has to be calculated so that the totally imposed current is constant. In two-dimensional problems this implies that its line integral has to equal the surface integral of the original current density.
As shown by Atallah *et al.*, using equivalent current sheets reduces the model's accuracy [75]. This is especially true in slotless machines, where the winding's thickness isn't negligible with respect to the pole pitch. For that reason, equivalent current sheets are usually avoided. In recent literature, the use of equivalent current sheets is limited to models that use the MSP [61], 3D models [111] or models in which slotting is accounted for through Schwarz-Christoffel transformation [59, 121].

4.4.3 Voltage sources

Mostly, publications on Fourier-based models assume idealized current waveforms in the machine's coils. However, as the vast majority of modern machines is powered with a voltage source, this assumption might be a too rough approximation. It is therefore often more interesting to apply a realistic voltage signal. However, as discussed in Chapter 2, directly imposing voltage sources through the PDE is too complex. To avoid that complexity, the magnetic calculations can be coupled with the classical equation for the terminal voltage in an electric machine.
Such a coupling was not available in literature at the start of this PhD. As pulse-width modulation (PWM) effects, originating from a voltage source, may be of great importance in high-speed machines, accounting for voltage sources adds to

the accuracy of FB models. Therefore, the coupling of electric and magnetic calculations will be discussed in the scope of this PhD. The result has been published in [124] and will be discussed in details in Chapter 6. However, coupling the electric and magnetic calculation may add quite some complexity to the model.

4.4.4 Conclusion

In the above, three types of sources were considered; residual magnetization, externally imposed current density and voltage sources. It was discussed that both residual magnetization and external current densities can either be imposed directly through the PDE or, with the help of equivalent currents, through the boundary conditions. As the direct technique is more straightforward and usually doesn't add to the complexity, it should be preferred. Accounting for sources through the boundary conditions can be interesting in some specific cases. It was also discussed that, although it increases the model's complexity, accounting for voltage sources may result in more realistic results.

4.5 Slotting

Accounting for slotted geometries is probably one of the most challenging aspects of Fourier-based modeling. It is therefore not surprising that literature describes a large number of techniques to model slotting effects. These techniques can be divided in three categories; techniques that use conformal mapping, techniques that use exact subdomain modeling and techniques that allow for subdomains with a variable permeability. All of these techniques will be discussed in the following.

4.5.1 Conformal mapping

Models that apply conformal mapping do not directly calculate the field in a slotted geometry. Instead, the solution for a slotless machine is calculated and the slotting effect is accounted for a posteriori, by multiplication with a permeance function. The determination of that permeance function is performed by consecutive conformal transformations, which map the slotted geometry in its slotless equivalent. One of these transformations is the Schwarz-Christoffel transformation. Therefore, models that apply conformal mapping are often referred to as Schwarz-Christoffel models. A detailed discussion on conformal transformations is beyond the scope of this work, but papers that clearly describe the mapping process may be found in [55, 93, 122, 125].

The simplest permeance functions are one dimensional, i.e. they only vary in the ρ-direction. This is of course a very coarse approximation; the effect of slotting on the magnetic field diminishes when moving away from the slots.

In [55], Zhu *et al.* proposed a two-dimensional relative permeance function. By accounting for the permeance function's η-dependency, a more accurate result was

obtained. Because of their simplicity, two-dimensional relative permeance functions have been widely used in the past. However, as was shown in [93], relative permeance function can not accurately predict the tangential component of the magnetic field. The inaccuracy of the field's tangential component may result in a significant error in some post-processing calculations such as the torque [113].
To avoid errors in the field's tangential component, Zarko *et al.* proposed a more complete solution of the conformal transformations by considering their complex nature [93]. Although this technique is more complex, it results in a much more accurate model.
All of the above techniques provide closed-form solutions for the magnetic field. This makes those models very interesting in terms of computational time and ease of use. However, the transformations introduce distortions of the geometry, especially the magnet edges and paths with a constant η are affected. The latter is important because such paths are often used as integration paths, e.g. to compute the torque. Moreover, the above permeance functions are determined assuming a single slot. This implies that influence of neighboring slots is neglected. To avoid errors due to deformation of the geometry and/or neglection of neighboring slots, various authors have recently used numerical techniques to perform the mapping process [85, 122, 126]. An additional benefit of that technique is that it allows for more complex geometries.

4.5.2 Exact subdomain

Whereas models that apply conformal mapping account for slotting a posteriori, exact subdomain models directly account for the slotting effect. This is achieved by considering each slot as a non-periodic subdomain.
The advantage of that approach is that it is much more straightforward than models that are based on conformal mapping. Moreover, it was shown in [73, 96] that the exact subdomain method is more accurate than the technique with complex permeance functions.
The most important downfall of the exact subdomain method is that its computational time is rather high. The reason for that is twofold. Firstly, by introducing every slot as a separate subdomain, the amount of subdomains rises significantly. As this also implies more integration constants, the time required to solve the system of boundary conditions increases. Secondly, whereas models with permeance functions will only contain periodic subdomains, exact subdomain models have both periodic and non-periodic subdomains, as discussed in Chapter 3. This implies that boundary conditions have to be imposed between subdomains with different periodicities. This, in turn, implies that the boundary conditions can not be imposed for every time- and spatial-harmonic combination separately. As a result, the solution can not be written in closed-form and the size of the system that has to be solved may become very large.
Despite these downfalls, the technique's accuracy and its straightforward approach

have made it the most widely used technique to account for slotting. To counter the relatively high computational times, Ackermann *et al.* presented an approximation that does allow for a closed-form solution [127]. In addition, one of the goals of this work is to provide techniques to reduce the computational time of exact subdomain models. That discussion is presented in Chapter 5.
Until recently, non-periodic subdomains could only be considered if they are enclosed by infinitely permeable material at their periodic boundaries. However, in [69] Dubas *et al.* have presented a technique that does allow for regular non-periodic boundaries. They do this by rewriting the MVP as the superposition of a part that is periodic in the ρ-direction ($A^{(\nu p)}(\eta,\rho,t)$) and a part that is periodic in the η-direction ($A^{(\nu\eta)}(\eta,\rho,t)$):

$$A^{(\nu)}(\eta,\rho,t) = A^{(\nu\rho)}(\eta,\rho,t) + A^{(\nu\eta)}(\eta,\rho,t) \tag{4.25}$$

where

$$\begin{aligned} A^{(\nu\rho)}(\eta,\rho,t) &= \sum_{n=-\infty}^{\infty}\sum_{k=-\infty}^{\infty} A_{n,k}^{(\nu\rho)}(\eta) e^{j\left(\frac{2k\pi}{T^{(\nu)}}\left(\rho-\rho_0^{(\nu)}\right)-n\omega t\right)} \\ A^{(\nu\eta)}(\eta,\rho,t) &= \sum_{n=-\infty}^{\infty}\sum_{k=-\infty}^{\infty} A_{n,k}^{(\nu\eta)}(\rho) e^{j\left(\frac{2k\pi}{T^{(\nu)}}\left(\eta-\eta_0^{(\nu)}\right)-n\omega t\right)} \end{aligned} \tag{4.26}$$

The periodic boundary conditions are then imposed on $A^{(\nu\eta)}(\eta,\rho,t)$ while at these boundaries $A^{(\nu\rho)}(\eta,\rho,t)$ is forced to be zero and similarly, the normal boundary conditions are imposed on $A^{(\nu\rho)}(\eta,\rho,t)$ while $A^{(\nu\eta)}(\eta,\rho,t)$ is kept zero.
This superposition technique is a relatively simple way to account for any non-periodic subdomain. Which doesn't only imply that teeth with a finite permeability can be accounted for, it also means that the magnetic field can be calculated in the soft-magnetic parts of a slotted geometry. This was not possible with earlier techniques. However, the amount of integration constants is again increased, which will further increase the computational time.

4.5.3 Variable permeability

Recently, Sprangers *et al.* have proposed a technique that allows for subdomains in which the permeability varies [99]. To achieve this, a Fourier series is used to express the permeability's variation along the ρ-direction and the constitutive relation between the magnetic flux density and the magnetic field strength is written using convolution matrices. The differential equation is then formulated in its matrix form, so that it can be solved with a variable permeability.
Spranger's approach is very interesting since, like Dubas' superpositions technique, it enables calculation of the field in the soft magnetic parts of a slotted structure. Moreover, it is not restricted to subdomains with a variable permeability; the same principles can also be used to account for subdomains with a variable

conductivity [82]. Apart from its complexity, the main downfall of this technique is that it suffers from Gibb's phenomenon, i.e. the Fourier series representing the permeability does not converge at the boundary between a slot and a tooth. This introduces inaccuracies in the computation of the field and results in higher computational times.

4.5.4 Conclusion

In the above, three techniques to account for slotting were introduced; using a permeance function that alters the magnetic field's computation a posteriori [55, 93, 122, 125], considering each slot, and possibly each tooth, as a separate subdomain [50, 86, 105, 117] and allowing for subdomains with a variable permeability [96, 99]. Only Dubas' superposition technique and Spranger's technique with variable permeabilities are capable of accounting for soft-magnetic materials with a finite permeability and computing the field in the soft-magnetic parts of a slotted geometry.
The advantage of using permeance functions is that a relatively good accuracy can be achieved with a closed-form solution, especially when using complex permeance functions. However, as discussed in [128], using complex permeance functions implies that the results can not be integrated analytically. This may be unwanted, for example, if the torque has to be studied.
Because of their straightforward approach and very high accuracy, exact subdomain models are nowadays the most widely used models that account for slotting. Using the superposition technique adds another advantage to this type of models; the possibility to compute the field in the soft-magnetic parts of a slotted structure. Despite their complexity and problems with the Gibb's phenomenon, models that account for subdomains with a variable permeability are definitely an interesting option to calculate the field in slotted structures.
Note that quite some comparative studies of different techniques to account for slotting have been published in literature [73, 96, 129].

4.6 Eccentricity

Although not a lot of Fourier-based models account for eccentricity, it is worth mentioning that there are two techniques capable of doing so. The first technique uses perturbation functions, the second technique accounts for eccentricity via superposition.

4.6.1 Perturbation functions

To account for eccentricity of the rotor, Kim *et al.* used two coordinate systems, one in the center of the stator and the other in the center of the rotor [84, 130]. The

relation between both coordinate systems was expressed using a perturbation function. Although Kim obtained very good results, his technique is rather complex.

4.6.2 Superposition

In [131], Li *et al.* avoided the complexity of perturbation functions by using superposition instead. Their approach is to divide the eccentric machine in a number of sections. For each of these sections the equivalent air gap length is determined. Next, a non-eccentric machine is studied for each of these air gap lengths. The obtained results are then put together so that each section of the original eccentric machine corresponds to the correct section of a non-eccentric machine. Clearly, this technique is much simpler than Kim's perturbation technique. However, it will introduce errors, especially at the boundaries between sections. Moreover, as different computations are required to study a single machine, a higher computational time may be expected. Nevertheless, Li presented very good results for the magnetic flux density and the back EMF.

4.6.3 Conclusion

This section discussed two techniques to study the effect of rotor eccentricity on the machine's magnetic field. The major advantage of Li's superposition technique is its simplicity. However it is expected to have a non-negligible error. Especially if quantities that are sensitive to errors in the magnetic field, such as torque, have to be studied. Despite the perturbation technique's higher complexity, it is more straightforward.

4.7 Physical output quantities

All of the above aspects are very specific to FB modeling, i.e. they apply to the calculation of the MSP or the MVP. However, these potentials are only of interest if they can be translated to the machine's physical output quantities such as the flux density, back EMF, torque and eddy currents. As the computation of these quantities is not specific for FB models, they will only very briefly be discussed here. A more detailed discussion on their calculation is provided in Chapter 7.

4.7.1 Magnetic flux density and magnetic field

The magnetic flux density and the magnetic field can readily be calculated from the constitutive relation (2.26b) and the definition of the magnetic potentials, i.e. (4.1) or (4.4). In most of the publications on FB modeling, results for the magnetic flux density are used to validate the presented model [75, 93, 99].

4.7.2 Back electromotive force

The back electromotive force (EMF) of a coil can be found from the integral form of Faraday's law, which can be written in terms of the coupled flux (ψ) as:

$$e(t) = -\frac{\partial \psi(t)}{\partial t} \tag{4.27}$$

The physical flux is found as the integration of the magnetic flux density over a surface of the coil. Note that the exact position of each coil is usually not available. Therefore, the boundaries of the integration surface are not exactly known. To cope with that, most authors of slotless machines assume the conductors to be located in the center of slots [105, 132]. In machines with stator slots, the magnetic potential is often averaged over the slot in order to calculate the flux [116, 124, 133].

4.7.3 Torque and forces

The most commonly used way to calculate forces is by integrating Maxwell's stress tensor over the surface of the volume on which the force acts:

$$\mathbf{F} = \iint_S \mathbf{\Gamma} \mathrm{d}s \tag{4.28}$$

where $\mathbf{\Gamma}$ is Maxwell's stress tensor, which can be calculated as:

$$\mathbf{\Gamma} = \mu_0 (\mathbf{n} \cdot \mathbf{H})\mathbf{H} - \frac{\mu_0}{2}(\mathbf{H} \cdot \mathbf{H})\mathbf{n} \tag{4.29}$$

where, in turn, **n** is the unit vector, normal to the integration surface.
The torque is then calculated by multiplying with the radius. Note that, alternatively, the torque could be calculated using Lorentz force or Poynting's theorem. It is beyond the scope of this work to elaborate on that, but more information can be found in [70].

4.7.4 Eddy currents and eddy-current losses

From Faraday's law (2.24a) and the constitutive relations (2.26a), the current density in any subdomain can easily be written in terms of the magnetic potential. Note that it is not necessary to have considered the eddy-current reaction field to do an a posteriori calculation of the eddy currents.
The eddy-current loss is calculated as the volume integral of the eddy current divided by the electric conductivity [79, 134, 135]:

$$P_{ec} = \iiint_V \frac{\mathbf{J} \cdot \mathbf{J}}{\sigma} \mathrm{d}v \tag{4.30}$$

Evidently, (4.30) reduces to the multiplication of the stack length and a surface integral in two-dimensional models.

The problem with (4.30) is that, in the polar and cylindrical coordinate system, the equation for **J** may include modified Bessel functions, as can be seen from (4.16), (4.18) and (4.20). As the analytical integration of these functions is not possible, the Poynting theorem is often used to calculate the eddy-current losses [68, 136, 137]. By integrating the Poynting vector $(\mathbf{S})$ along a surface, the power passing through that surface is calculated:

$$\begin{aligned} P_S &= \iint_S \mathbf{S} \cdot \mathrm{d}\mathbf{s} \\ &= \iint_S \mathbf{E} \times \mathbf{H} \cdot \mathrm{d}\mathbf{s} \end{aligned} \tag{4.31}$$

If the integration surface encloses the rotor, integration of **S** gives the total power, i.e. the sum of the mechanical power and the power losses, that goes from the stator to the rotor. By subtracting the mechanical power, which can be calculated from the torque, the eddy-current losses are isolated.
Note that there are other techniques to isolate the eddy-current losses from the mechanical power; in [137] Joule's equation (4.30) is used and in [70] calculation of P_S in rotor coordinates is combined with an interpretation of the slip of individual harmonic components of the magnetic field.
Note as well that two-dimensional models can not account for segmentation of conductive subdomains in the l-direction. To overcome that issue, Nair *et al.* coupled a classical 2D Fourier-based model with the current vector potential in [138].
As the Poynting theorem directly applies the solution of the magnetic field, it can only account for eddy-current losses of subdomains in which the eddy-current reaction field is considered.

4.7.5 Conclusion

The above is a very brief introduction on some of the most important quantities that can be calculated from a Fourier-based model. The way in which the magnetic flux density, the back EMF, the forces, the torque, the eddy currents and the eddy-current losses are calculated was introduced. One important remark with respect to Fourier-based modeling is that the classical way of calculating eddy-current losses, i.e. using Joule's equation, can not always be used. An alternative that uses Poynting's theorem was proposed.

4.8 Conclusion

In this section an overview of the most important aspects within FB modeling was presented. The discussion is based on an identification of seven aspects that are important in FB modeling.
Based on the presented results, choices were made about the implementation of

the FB model in this PhD. It was decided that the magnetic vector potential will be used to reformulate Maxwell's equations in a cylindrical coordinate system. Like the source terms, the time dependency will be accounted for directly. Slotting will be considered using the exact subdomain technique. And finally, eccentricity will be disregarded.

Chapter 5

Computational considerations

The previous chapters described and validated a theoretical framework to simulate electric machines. It was, however, also shown that the resulting model may require an unacceptably long computational time. Therefore, this chapter focuses on how to avoid excessive computational times and, more broadly, on how to avoid computational problems in general. Three aspects will be discussed in the following.
The first aspect relates to numerical problems that are introduced when solving systems with both very large and very small numbers. This problem has been considered by Gysen *et al* in [50] and [109] and will therefore only briefly be discussed in this work, i.e. in Section 5.1. In Section 5.2, a second aspect will be discussed: the effect of the studied machine's topology on the computational time. This discussion was not yet conducted in literature. Thirdly, Section 5.3 discusses how the computational time can be reduced with a preliminary study of the machine's harmonic content. Although the harmonic content of synchronous machines is a well-studied subject, the existing literature does not provide a complete overview of the time- and spatial harmonic content of synchronous machines in general. Therefore, Appendix B extensively discusses the harmonic content in synchronous machines. The findings from that appendix are applied in Section 5.3 to reduce the computational time of Fourier-based models. Finally, Section 5.4 summarizes this chapter.

The content of this chapter has been published in the following journal papers:

- B. Hannon, P. Sergeant and L. Dupré, "Time- and Spatial-Harmonic Content in Synchronous Electrical Machines", *Magnetics, IEEE Transactions on*, vol. 53, no. 3, 11 pages, 2017
- B. Hannon, P. Sergeant and L. Dupré, "Computational-time reduction of Fourier-Based Analytical Models", *Energy Conversion, IEEE Transactions on*, in press, 2017

5.1 Rescaling

The implementation of a Fourier-based model usually requires to numerically solve the system of boundary conditions. However, it can readily be seen from (3.29), (3.31) and (3.37) that high harmonic orders may result in integration constants with both very large and very small coefficients. This, in turn, may result in a quasi-singular system, which introduces numerical errors in the system's solution. To avoid such errors, (3.29) and (3.31) can be rescaled so that the bases of the exponents are close to one. This can, for example, be done by dividing r by the mean radius of the considered subdomain.
In contrast to the power functions of (3.29) and (3.31), rescaling the Bessel functions of (3.37) isn't possible. If, however, these functions introduce numerical errors, it is possible to replace them by either (3.29) or the zero function. Which of both alternatives is best-suited depends on the skin depth. If the thickness of the material is smaller than the skin depth of the considered harmonic combination, the eddy-currents may be neglected and (3.37) can be replaced by (3.29). If the thickness of the material is larger than the skin depth of the considered harmonic combination, the most reasonable approximation is to assume that the field, related to the harmonic combination in question, is completely blocked. Equation (3.37) is then replaced by the zero function.

5.2 Machine geometry

Table 3.2 and Figure 3.10 clearly indicated that, for a given set of cut-off harmonic orders, both the FB model's accuracy and its computational time strongly depend on the machine's geometry.
It was discussed in Section 3.4 that a lower number of subdomains results in a lower computational time. This fact may be a reason to simplify the geometry of machines with semi-closed slots to a similar geometry with open slots. As illustrated in Figure 5.1, this is done by setting the opening angle of the slots to that of the original slot openings.
Evidently, this implies that the current density has to be recalculated to keep the total current constant.
To illustrate the accuracy and the possible gain of the above technique, it was applied to one of the machines that were studied in Chapter 3, i.e. to the inner-rotor machine with semi-closed slots and no shielding cylinder. As can be seen from Table 5.1, the accuracy of the simplified model, with respect to the FE model, is comparable to that of the original model. The presented deviations are those of the magnetic flux density in the center of the air gap. Evidently, the model with simplified slots will not be accurate in the slots.
Table 5.1 also shows that there is a significant difference in required computational time between the original and the simplified model. More specifically, a reduction of the computational time of more than 50% is achieved. The simplified model's

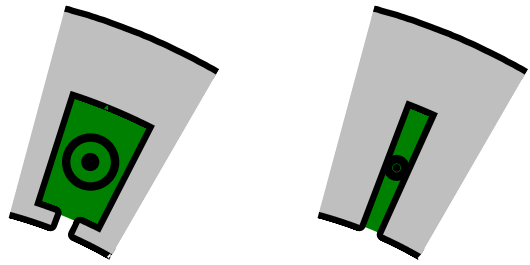

(a) Original slot (b) Simplified slot

Figure 5.1: Simplification of the machine with semi-closed slots

accuracy is quasi identical to that of the original model. Note that for machines with a smaller air gap it is expected that the accuracy of the simplified model will be slightly lower.

Table 5.1: Simplification of the slots in the inner-rotor machine with semi-closed slots and no SC; accuracy and computational time. NL indicates the no-load situation and AR indicates armature-reaction conditions.

Model	Deviation with respect to FE (%)				Computational time (s)	
	NL		AR		NL	AR
	B_r	B_ϕ	B_r	B_ϕ		
original	0.045	1.945	0.217	0.091	333.09	328.04
simplified	0.046	1.939	0.213	0.097	160.00	159.35
FE					4260.00	4096.00

5.3 Harmonic content

In Chapter 3, every time- and spatial harmonic combination (n, k), with n and k smaller than their respective cut-off harmonics, was considered. This resulted in very high computational times. Indeed, the amount of harmonic combinations is directly related to the amount of integration constants, which in turn determines the size of the system that has to be solved. As the computational time is about quadratic to the size of the system, decreasing the amount of harmonic combinations may result in a drastic decrease of the computational time.
A discussion on which time and spatial harmonics are present in electric machines was given in [139] and is repeated in Appendix B. The following briefly summarizes the results of that discussion for no-load, armature-reaction and load condi-

tions.

No load

As discussed in Appendix B, the magnetic field will be identical but spatially rotated over $\frac{2\pi}{N_s}$ radians after $\frac{T_t}{N_s}$ seconds if the machine is operated at no-load. This periodicity applies to the MVP of periodic subdomains, i.e. $T_s^{(\nu)} = 2\pi$, for every time- and spatial-harmonic combination (n, k) separately:

$$A_{n,k}(r)e^{j(k\phi - n\omega t)} = A_{n,k}(r)e^{j\left(k\left(\phi + \frac{2\pi}{N_s}\right) - n\omega\left(t + \frac{T_t}{N_s}\right)\right)} \tag{5.1}$$

From (5.1), a relationship between n and k was obtained.

$$k - n = cN_s \tag{5.2}$$

where c is an integer.
This means that, for no-load conditions, the time-harmonic orders are determined by the harmonic spectrum of the magnets while the machine's geometry, i.e. the slots, determine the present spatial harmonic orders. The harmonic combinations thus have to satisfy (5.3).

$$\begin{cases} n \in h_m \\ k - n = cN_s \end{cases} \tag{5.3}$$

with h_m the set of time-harmonic orders for which the residual magnetic flux density is nonzero.

Armature reaction

Appendix B shows that for the armature-reaction field, a similar approach can be made. The time-harmonic orders in the magnetic field are now determined by the harmonic spectrum of the applied current, i.e. $n \in h_c$. The spatial-harmonic orders are solely determined by the winding distribution; the effect of the geometry is already incorporated in the winding distribution.
If m is the number of phases and τ is the machine's period, i.e. the greatest common divisor of the number of pole pairs (p) and the number of slots (N_s), the time periodicity of the armature-reaction field is mathematically expressed as:

$$A_{n,k}(r)e^{j(k\phi - n\omega t)} = A_{n,k}(r)e^{j\left(k\left(\phi + \frac{2\pi}{\upsilon m\tau}\right) - n\omega\left(t + \frac{T_t}{\upsilon m\tau}\right)\right)} \tag{5.4}$$

with $\upsilon = 1$ if $\frac{N_s}{\tau}$ is odd and $\upsilon = 2$ if $\frac{N_s}{\tau}$ is even.
From (5.4) the following relation between the time- and spatial-harmonic orders is obtained:

$$k - n = c\upsilon m\tau \tag{5.5}$$

This means that, under armature-reaction conditions, the harmonic combinations in the magnetic field have to satisfy (5.6).

$$\begin{cases} n \in h_c \\ k - n = cvm\tau \end{cases} \tag{5.6}$$

Load

Finally, since saturation is neglected, the load field is the superposition of the no-load and armature-reaction fields. The time-harmonic orders are now introduced by both the rotor magnets and the stator currents. This means that, under load conditions, the harmonic combinations in the magnetic field have to satisfy (5.7).

$$\begin{cases} n \in (h_m \cup h_c) \\ k - n = cvm\tau \end{cases} \tag{5.7}$$

As a conclusion it can be stated that the harmonic combinations, present in the magnetic field of synchronous machines under load conditions, can be predicted using (5.7). Furthermore, from the stator's point of view, the magnetic field is identical but rotated over $\frac{2\pi}{m\tau}$ or $\frac{\pi}{m\tau}$ mechanical radians after $\frac{T_t}{m\tau}$ or $\frac{T_t}{2m\tau}$ seconds. Depending on whether $\frac{N_s}{\tau}$ is odd or even.
By means of illustration, Figure 5.2 shows the difference between machines with an odd and an even amount of slots per period. More information can be found in Appendix B.

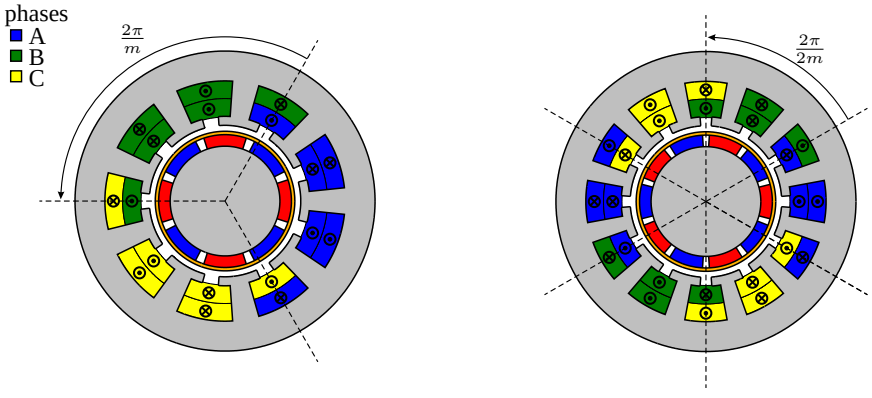

(a) Machine with $\frac{N_s}{\tau}$ odd (b) Machine with $\frac{N_s}{\tau}$ even

Figure 5.2: Difference between machines with $\frac{N_s}{\tau}$ odd and even

5.3.1 Harmonic combinations

When simulating a machine with the use of a Fourier-based model, the number of considered time- and spatial-harmonic orders is always limited. The cut-off harmonic orders, i.e. the highest time- and spatial-harmonics that are taken into account, have to be carefully chosen. On the one hand, a sufficient amount of harmonic orders is required to obtain accurate results. On the other hand, the amount of considered harmonic orders should be as low as possible in order to avoid excessive computational times. However, by applying the above results, the amount of harmonic combinations can be reduced without affecting the accuracy. Indeed, the field components related to harmonic combinations that do not satisfy the requirements imposed in (5.3), (5.6) or (5.7) will be zero. These combinations can thus be disregarded.
Note that the imposed relations between the time and spatial harmonic combinations were found assuming a basic spatial period of 2π mechanical radians. They are therefore only valid in periodic subdomains.

5.3.2 Interdependence of the slots

Although (5.3), (5.6) and (5.7) do not apply to the magnetic vector potential in non-periodic subdomains, the time periodicities found in the above are still valid for the machine's total magnetic field.
Consider two subsequent, non-periodic subdomains; ξi and $\xi i + 1$. These subdomains, which can either be slots or slot openings, have starting angles of α_i and α_{i+1} radians and an opening angle of β radians. Equation (5.1) implies that, under no-load conditions, the magnetic field in subdomain $\xi i + 1$ lags the magnetic field in subdomain ξi by $\frac{T_t}{N_s}$ seconds. A relation can then be found between the magnetic vector potentials of both subdomains:

$$A_{n,k}^{(\xi i)}(r)e^{j\left(\frac{k\pi}{\beta}(\phi-\alpha_i)-n\omega t\right)} = A_{n,k}^{(\xi i+1)}(r)e^{j\left(\frac{k\pi}{\beta}(\phi+\frac{2\pi}{N_s}-\alpha_{i+1})-n\omega\left(t+\frac{T_t}{N_s}\right)\right)} \tag{5.8}$$

and since $\alpha_{i+1} = \alpha_i + \frac{2\pi}{N_s}$:

$$A_{n,k}^{(\xi i)}(r) = A_{n,k}^{(\xi i+1)}(r)e^{-jn\frac{2\pi}{N_s}} \tag{5.9}$$

For the armature-reaction and load fields, a similar periodicity was found. Analogously as in the above, the following relations can be found:

$$A_{n,k}^{(\xi i)}(r) = A_{n,k}^{(\xi i+\frac{N_s}{\upsilon m\tau})}(r)e^{-jn\frac{2\pi}{\upsilon m\tau}} \tag{5.10}$$

Equations (5.9)-(5.10) show a relation between the Fourier coefficients of different slot openings and slots. This implies that fewer coefficients have to be calculated using the boundary condition equations, which results in a lower computational time. This lower computational time is again achieved without loss of accuracy.

5.3.3 Real functions

Although the general expression for the magnetic vector potential (3.14) contains complex components, the magnetic vector potential is a real function. This implies that the Fourier coefficients linked to harmonic combinations (n, k) and $(-n, -k)$ have to be complex conjugate. Mathematically this implies:

$$A_{n,k}^{(\nu)}(r) = \left(A_{-n,-k}^{(\nu)}(r)\right)^* \tag{5.11}$$

The above relation, which is valid for every subdomain, implies that only half of the integration constants have to be calculated, which results in a large reduction of the computational time.

5.3.4 Evaluation

To evaluate the effect of a preliminary study on the computational time, the above was used to optimize the model of Chapter 3. Next, the calculations of Section 3.4 were repeated. The comparison between the original and the optimized model is summarized in Tables 5.2 and 5.3. It can clearly be seen that there's an enormous gain in computational efficiency while obtaining the same accuracy for the flux density in the center of the air gap. Moreover, when comparing Tables 5.1, 5.2 and 5.3, it can be seen that the computational time of the optimized FB model is now significantly lower than that of the FE model.
Note that the no-load situation is indicated as NL, while the armature-reaction situation is indicated as AR.

Table 5.2: Percentage root-mean-squared deviations and computational times of the inner-rotor machines. NL indicates the no-load situation and AR indicates armature-reaction conditions.

Machine type	Slot type	SC	Model	Deviation (%)				Computational time (s)	
				NL		AR		NL	AR
				B_r	B_ϕ	B_r	B_ϕ		
Inner rotor	slotless	no	original	0.003	0.008	0.009	0.003	105.41	106.11
			optimized	0.003	0.008	0.009	0.003	0.11	0.07
			FE					1629.00	1809.00
		yes	original	0.028	0.025	0.069	0.014	333.71	332.95
			optimized	0.028	0.025	0.069	0.014	0.30	0.21
			FE					1462.00	1600.00
	open	no	original	0.033	0.907	0.003	0.059	159.80	159.42
			optimized	0.033	0.907	0.003	0.059	0.75	0.03
			FE					4408.00	4547.00
		yes	original	0.124	0.736	0.235	1.024	297.24	297.37
			optimized	0.124	0.736	0.235	1.024	1.57	0.06
			FE					3960.00	4210.00
	semi-closed	no	original	0.045	1.945	0.217	0.091	333.09	328.04
			optimized	0.045	1.945	0.217	0.091	2.44	0.08
			FE					4260.00	4096.00
		yes	original	0.042	2.749	0.035	0.565	515.71	517.31
			optimized	0.042	2.749	0.035	0.565	3.27	0.11
			FE					4035.00	3651.00

Table 5.3: Percentage root-mean-squared deviations and computational times of the outer-rotor machines. NL indicates the no-load situation and AR indicates armature-reaction conditions.

Machine type	Slot type	SC	Model	Deviation (%)				Computational time (s)	
				NL		AR		NL	AR
				B_r	B_ϕ	B_r	B_ϕ		
Outer rotor	slotless	no	original	0.016	0.036	0.011	0.048	105.43	106.07
			optimized	0.016	0.036	0.011	0.048	0.05	0.16
			FE					3148.00	2729.00
		yes	original	0.047	0.042	0.031	0.103	333.09	332.84
			optimized	0.047	0.042	0.031	0.103	0.09	0.48
			FE					2949.00	2577.00
	open	no	original	0.017	0.115	0.041	0.035	173.25	173.70
			optimized	0.017	0.115	0.041	0.035	0.26	0.07
			FE					2452.00	2478.00
		yes	original	0.050	0.082	0.048	0.046	318.84	318.00
			optimized	0.050	0.082	0.048	0.046	0.47	0.12
			FE					3213.00	2870.00
	semi-closed	no	original	0.022	0.043	0.136	0.018	426.82	426.29
			optimized	0.022	0.043	0.136	0.018	1.12	0.20
			FE					2472.00	2466.00
		yes	original	0.025	0.086	0.111	0.039	635.59	636.02
			optimized	0.025	0.086	0.111	0.039	1.34	0.25
			FE					2345.00	2743.00

5.4 Conclusion

In this chapter, two issues of Fourier-based models were discussed; numerical errors due to quasi-singular systems of boundary conditions and excessive computational times.
The first issue was tackled in Section 5.1 by rescaling the equations for the MVP.
The second issue was discussed in Sections 5.2 and 5.3. Sections 5.2 considered the effect of the machine's geometry on the computational time. It also proposed a simplification of the slots to avoid an unnecessary high computational burden, a reduction of more than 50% in computational time was achieved. In Section 5.3, the focus was on how a preliminary knowledge of the studied machine's harmonic content can reduce the computational time. It was shown that the computational time can be reduced by up to more than 100 times while maintaining the model's accuracy.
The problem of unacceptably high computational burden, encountered in the previous chapter, was solved in this chapter. As explained in Chapter 1, the reduction of the model's computational time was one of the major goals of this thesis. Evidently, in the following chapters, only the optimized model will be used.

Chapter 6

Voltage sources

The framework presented in Chapter 3 requires a current density as input. However, nowadays most electric drives are powered with the help of a voltage source. To overcome that mismatch, this chapter extends the magnetic calculations of Chapter 3 with the equation for the terminal voltage of an electric machine. This technique has already proven its worth in finite-element models [140], but was not yet translated to Fourier-based analytical models.
The discussion of this chapter consists of two major parts.
Firstly, a very general discussion on the technique of coupling magnetic calculations with the equation for the terminal voltage of electric machines is presented. This discussion is spread over Sections 6.1-6.3. Section 6.1 reformulates the magnetic calculations of Chapter 3. In Section 6.2 the equation for the terminal voltage is rewritten so that it can be used in FB models. These two aspects are combined in Section 6.3, resulting in a model that directly accounts for the terminal voltage of electric machines. In the second part of this chapter, the presented work is validated with the help of a finite-element model. This is done in Section 6.4. Section 6.5 concludes the work.

The content of this chapter has been published in the following journal paper:

- B. Hannon, P. Sergeant and L. Dupré, “Voltage Sources in 2D Fourier-Based Analytical Models of Electric Machines”, *Mathematical Problems in Engineering*, vol. 2015, Article ID 195410, 8 pages, 2015

6.1 Magnetic equations

Chapter 3 resulted in a set of unknown integration constants, which have to be determined by the problem's boundary conditions. As discussed in Section 3.3.5, these boundary conditions can be imposed separately for every time harmonic order (n). This implies that, for time-harmonic order n, the resulting system is written in its matrix form as:

$$[C_n^1] \cdot [X_n] = -[C_n^2] \cdot [J_n] + [C_n^3] \cdot [B_n] \tag{6.1}$$

where $[X_n]$ is a row vector that contains all of the integration constants linked to n, i.e. the integration constants of each subdomain and each spatial harmonic order. This implies that if N_{bc} is the amount of boundary conditions, $[X_n]$ has a size of $N_{bc} \times 1$. Analogously, $[B_n]$ and $[J_n]$ are $N_{bc} \times 1$ row vectors that contain all of the spatial harmonic coefficients of the remanent magnetic induction and the current density in each of the subdomains. $[C_n^1]$, $[C_n^2]$ and $[C_n^3]$ are $N_{bc} \times N_{bc}$ coefficient matrices.
As the goal is to impose N_c terminal voltages instead of N_ν current densities, where N_c is the amount of coils and N_ν is the amount of subdomains, $[J_n]$ is rewritten in function of the coils' currents.
The $(n,k)^{\text{th}}$ harmonic combination of the current density in subdomain ν can be written as:

$$J_{n,k}^{(\nu)} = \sum_{c=1}^{N_c} W_k^{(c,\nu)} I_n^{(c)} \tag{6.2}$$

In (6.2) $W_k^{(c,\nu)}$ is the k^{th} spatial-harmonic order of coil c's winding density in subdomain ν, i.e. $W_k^{(c,\nu)}$ expresses the amount of conductors per m^2. Note that the winding density is positive where the coil's reference current is along the z-axis and negative otherwise.
The above implies that if $[W]$ is the $N_c \times N_{bc}$ matrix, so that each cell contains a $W_k^{(c,\nu)}$, (6.1) can be rewritten as:

$$\begin{aligned} [C_n^1] \cdot [X_n] &= -[C_n^2] \cdot [W]^\intercal \cdot [I_n] + [C_n^3] \cdot [B_n] \\ &= -[C_n^4] \cdot [I_n] + [C_n^3] \cdot [B_n] \end{aligned} \tag{6.3}$$

As both the coils' currents and the field's integration constants are unknown, the system described by (6.3) is underdetermined and an extra N_c equations are required. In the following section, these equations will be derived from the equation for the terminal voltage of an electric machine.

6.2 Electric equations

The goal of this section is to provide equations for the current in each of the coils. This is done in two steps. First the equations for the terminal voltage of the machine

are presented. Next, the flux linkage of the machine's coils is discussed in order to rewrite these equations in function of the remanent magnetism ($[B_n]$), the terminal voltages ($[V_n]$) and the magnetic field's integration constants ($[X_n]$).

6.2.1 Current in the coils

The following discussion starts from the classical equation for the terminal voltage of an arbitrary coil c in an electric machine:

$$v^{(c)}(t) = Ri^{(c)}(t) + \frac{\mathrm{d}\psi_{tot}^{(c)}(t)}{\mathrm{d}t} \tag{6.4}$$

The flux coupled with coil c $\left(\psi_{tot}^{(c)}(t)\right)$ can now be divided in a component related to the active part of the coil $\left(\psi^{(c)}(t)\right)$ and a component related to the end windings $\left(\psi_{ew}^{(c)}(t)\right)$. The above then results in:

$$\begin{aligned} v^{(c)}(t) &= Ri^{(c)}(t) + \frac{\mathrm{d}\psi_{ew}^{(c)}(t)}{\mathrm{d}t} + \frac{\mathrm{d}\psi^{(c)}(t)}{\mathrm{d}t} \\ &= Ri^{(c)}(t) + L_{ew}\frac{\mathrm{d}i^{(c)}(t)}{\mathrm{d}t} + \frac{\mathrm{d}\psi^{(c)}(t)}{\mathrm{d}t} \end{aligned} \tag{6.5}$$

Note that, for simplicity reasons, it is assumed that every coil has the same ohmic resistance R and the same inductance of the end-windings L_{ew}. These values can be obtained with classical formulas, such as the ones found in [141].
The functions in (6.5) can be written in terms of their Fourier series:

$$\sum_{n=-\infty}^{\infty} V_n^{(c)} e^{-jn\omega t} = \sum_{n=-\infty}^{\infty} RI_n^{(c)} e^{-jn\omega t} + L_{ew}\frac{\mathrm{d}I_n^{(c)} e^{-jn\omega t}}{\mathrm{d}t} + \frac{\mathrm{d}\Psi_n^{(c)} e^{-jn\omega t}}{\mathrm{d}t} \tag{6.6}$$

The above can be rewritten for every time harmonic order n separately:

$$V_n^{(c)} = RI_n^{(c)} - jn\omega L_{ew} I_n^{(c)} - jn\omega \Psi_n^{(c)} \tag{6.7}$$

Implying that the current's n^{th} harmonic order can be calculated as:

$$I_n^{(c)} = \frac{V_n^{(c)} + jn\omega\Psi_n^{(c)}}{R - jn\omega L_{ew}} \tag{6.8}$$

It can easily be reasoned that substitution of (6.8) in the governing equation will allow to account for the terminal voltage as a source. However, $\Psi_n^{(c)}$ has to be calculated from the magnetic field, i.e. from the solution of the governing equation. This prevents a direct coupling between the calculation of the magnetic field and the equation for the terminal voltage. To overcome that problem, $\Psi_n^{(c)}$ is rewritten in terms of the magnetic vector potential in the following section.

6.2.2 Flux linkage

The goal of this section is to express the flux related to the active part of an arbitrary coil c as a function of the magnetic vector potential. In a first step the flux coupled with a single turn of the coil is derived, in a second step the flux coupled with the entire coil is regarded.

Flux coupled with a single turn

The physical flux through a single turn κ of coil c is calculated by integrating the flux density over a surface spanned by that turn:

$$\psi^{(\kappa)}(t) = \iint\limits_{S_\kappa} \mathbf{B} \cdot \mathrm{d}\mathbf{a} = \oint\limits_{C_\kappa} \mathbf{A} \cdot \mathrm{d}\mathbf{s} \tag{6.9}$$

Where the definition of the MVP and Stokes' theorem were used. S_κ is the surface of the turn, C_κ is the boundary of that surface.
Since the magnetic vector potential is assumed to only have a z-component, the integration of **A** along the turn's contour will only be non-zero along the z-direction. Noting that the MVP is independent of z, this implies that the integration along the contour of the turn can be rewritten as:

$$\psi^{(\kappa)}(t) = l_s \left(A^{(i^+_{N_s})}(r_{\kappa^+}, \phi_{\kappa^+}, t) - A^{(i^-_{N_s})}(r_{\kappa^-}, \phi_{\kappa^-}, t) \right) \tag{6.10}$$

where l_s is the stack length of the studied machine. $i^+_{N_s}$ is the slot in which the direction of the integration is along the positive z-axis; **A** and d**s** then have the same direction and sense. $i^-_{N_s}$ represents the slot in which the coil returns, the integration direction is opposed to the z-axis and thus to **A**.
Equation (6.10) can now be rewritten as:

$$\psi^{(\kappa)}(t) = \sum_{i_{N_s}=1}^{N_s} l_s w_\kappa^{(c,i_{N_s})} A^{(i_{N_s})}(r_\kappa^{(i_{N_s})}, \phi_\kappa^{(i_{N_s})}, t) \tag{6.11}$$

where $w^{(\kappa,i_{N_s})}$ is 1 in the slot that contains the going conductor of κ, -1 in the slot that contains the returning conductor and 0 in the other slots.
Usually, the exact position of the turn can not be determined, i.e. $\left(r_\kappa^{(i_{N_s})}, \phi_\kappa^{(i_{N_s})}\right)$ is unknown. For that reason, the average MVP in the considered slot is used. Doing so results in one MVP value for every subdomain. This value will be referred to as $\alpha^{(i_{N_s})}(t)$ in the following. The flux coupled with a single turn κ of coil c can then be written as:

$$\psi^{(\kappa)}(t) = \sum_{i_{N_s}=1}^{N_s} l_s w_\kappa^{(c,i_{N_s})} \alpha^{(i_{N_s})}(t) \tag{6.12}$$

Flux coupled with a coil

The flux coupled with coil c is calculated by summing the fluxes coupled with each of its turns. From (6.12), it can be written that:

$$\psi^{(c)}(t) = \sum_{i_{N_s}=1}^{N_s} l_s N^{(c,i_{N_s})} \alpha^{(i_{N_s})}(t) \tag{6.13}$$

where

$$N^{(c,i_{N_s})} = \sum_{\kappa} w_{\kappa}^{(c,i_{N_s})} \tag{6.14}$$

which implies that $N^{(c,i_{N_s})}$ equals the amount of conductors that coil c has in slot i_{N_s}. If i_{N_s} contains going conductors of c, $N^{(c,i_{N_s})}$ is positive. If not, $N^{(c,i_{N_s})}$ is negative.
The n^{th} time-harmonic coefficient of $\psi(t)^{(c)}$ can now be written as:

$$\Psi_n^{(c)} = \sum_{i_{N_s}=1}^{N_s} l_s N^{(c,i_{N_s})} \alpha_n^{(i_{N_s})} \tag{6.15}$$

where $\alpha_n^{(i_{N_s})}$ is the n^{th} time-harmonic coefficient of $\alpha^{(i_{N_s})}(t)$.
Since $\alpha^{(i_{N_s})}(t)$ is a direct function of the MVP in slot i_{N_s}, which in turn is determined by the integration constants and the source terms, (6.15) can be written in its matrix form as:

$$\Psi_n^{(c)} = l_s[N^{(c)}] \cdot \left([C_n^5] \cdot [X_n] + [C_n^6] \cdot [I_n] + [C_n^7] \cdot [B_n]\right) \tag{6.16}$$

where $[N^{(c)}]$ is a $1 \times N_s$ matrix describing the winding configuration of coil c, i.e. $[N^{(c)}]_{1,i_{N_s}} = N^{(c,i_{N_s})}$. $[C_n^5]$, $[C_n^6]$ and $[C_n^7]$ are coefficient matrices. They are determined by averaging the equations for the MVP.
It can easily be seen that the above effectively expresses the flux linkage of coil c in terms of the machine's geometry ($[C_n^5] \cdots [C_n^7]$), the integration constants ($[X_n]$) and the classical source terms ($[I_n]$ and $[B_n]$).

6.3 A new system of equations

In (6.3) the system of a traditional Fourier-based analytical model was reformulated in terms of the currents flowing through the coils of the machine. However, as these currents are unknown, that system was underdetermined. Therefore, in Section 6.2 an equation for the current density was proposed (6.8), combining this equation with the equation for the flux coupled with a coil (6.16) gives:

$$I_n^{(c)} = \frac{V_n^{(c)} + jn\omega l_s[N^{(c)}] \cdot \left([C_n^5] \cdot [X_n] + [C_n^6] \cdot [I_n] + [C_n^7] \cdot [B_n]\right)}{R - jn\omega L_{ew}} \tag{6.17}$$

The above equation for the current is valid in each of the N_c coils. A matrix notation for the resulting set of equations can be found:

$$[I_n] = \frac{[V_n] + jn\omega l_s[N] \cdot \left([C_n^5] \cdot [X_n] + [C_n^6] \cdot [I_n] + [C_n^7] \cdot [B_n]\right)}{R - jn\omega L_{ew}} \tag{6.18}$$

where $[V_n]$ is a $N_c \times 1$ matrix containing all of the coils' terminal voltages and $[N]$ is a $N_c \times N_s$ matrix whose c^{th} row equals $[N^{(c)}]$. Rearranging gives:

$$[C_n^8] \cdot [X_n] + [C_n^9] \cdot [I_n] = [C_n^{10}] \cdot [B_n] + [C_n^{11}] \cdot [V_n] \tag{6.19}$$

where $[C_n^8]$, $[C_n^9]$, $[C_n^{10}]$ and $[C_n^{11}]$ are matrices with respective sizes of $N_c \times N_{bc}$, $N_c \times N_c$, $N_c \times N_{bc}$ and $N_c \times N_c$. They are calculated as:

$$[C_n^8] = -\frac{jn\omega l_s[N] \cdot [C_n^5]}{R - jn\omega L_{ew}} \tag{6.20a}$$

$$[C_n^9] = I_{N_c} - \frac{jn\omega l_s[N] \cdot [C_n^6]}{R - jn\omega L_{ew}} \tag{6.20b}$$

$$[C_n^{10}] = \frac{jn\omega l_s[N] \cdot [C_n^7]}{R - jn\omega L_{ew}} \tag{6.20c}$$

$$[C_n^{11}] = \frac{I_{N_c}}{R - jn\omega L_{ew}} \tag{6.20d}$$

where I_{N_c} is the identity matrix of size N_c.
The above implies that the combination of (6.3) and (6.19) is a system of equations that uniquely defines both the integration constants in each of the subdomains and the currents in each of the coils. This system is written in matrix form as:

$$\begin{bmatrix} [C_n^1] & [C_n^4] \\ [C_n^8] & [C_n^9] \end{bmatrix} \cdot \begin{bmatrix} [X_n] \\ [I_n] \end{bmatrix} = \begin{bmatrix} [C_n^3] \cdot [B_n] \\ [C_n^{10}] \cdot [B_n] + [C_n^{11}] \cdot [V_n] \end{bmatrix} \tag{6.21}$$

Solving this system for every time harmonic order will uniquely define the MVP and the currents. It can readily be seen that (6.21) enables to directly impose a voltage signal to the coils instead of the classical approach of imposing a current density to the subdomains.

6.4 Validation

The goal of this section is to validate the above theory. To do so, the inner-rotor machine with open slots and a shielding cylinder, as introduced in Chapter 3, is used. The machine is connected in a delta configuration and coils belonging to the same phase are connected in series. In order to obtain an easily reproducible validation, sinusoidal voltages with an amplitude of 255 volt and a phase shift of

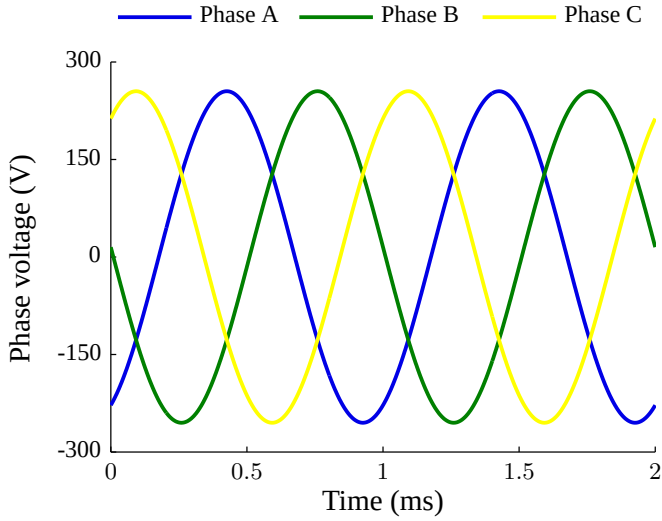

Figure 6.1: Applied phase voltages

206.6°, i.e. $u_A(t) = -255\cos(p\omega t + 0.4643)$, are applied to the phases. The applied voltages are shown in Figure 6.1.
Evidently, the no-load field equals that of the validation in Chapter 3. The obtained armature-reaction and load fields and the corresponding magnetic flux densities in the center of the air gap are shown in Figure 6.2. The results were compared to FEM calculations and a very good correspondence is noted. Respective errors of 0.025% and 0.354% are obtained for the radial and tangential components of the flux density under armature-reaction conditions. Under load conditions, errors of 0.032% and 0.167% are obtained.
Apart from the magnetic field and its flux density, the current and the different components of the phase voltages can also be calculated. For phase A, the current, calculated from the FB model, is compared to the current obtained from the FE model in Figures 6.3. Figure 6.4 shows different components of the voltage; the terminal voltage (V), the resistive voltage drop (RI), the inductive voltage drop (jXI) and the back EMF.

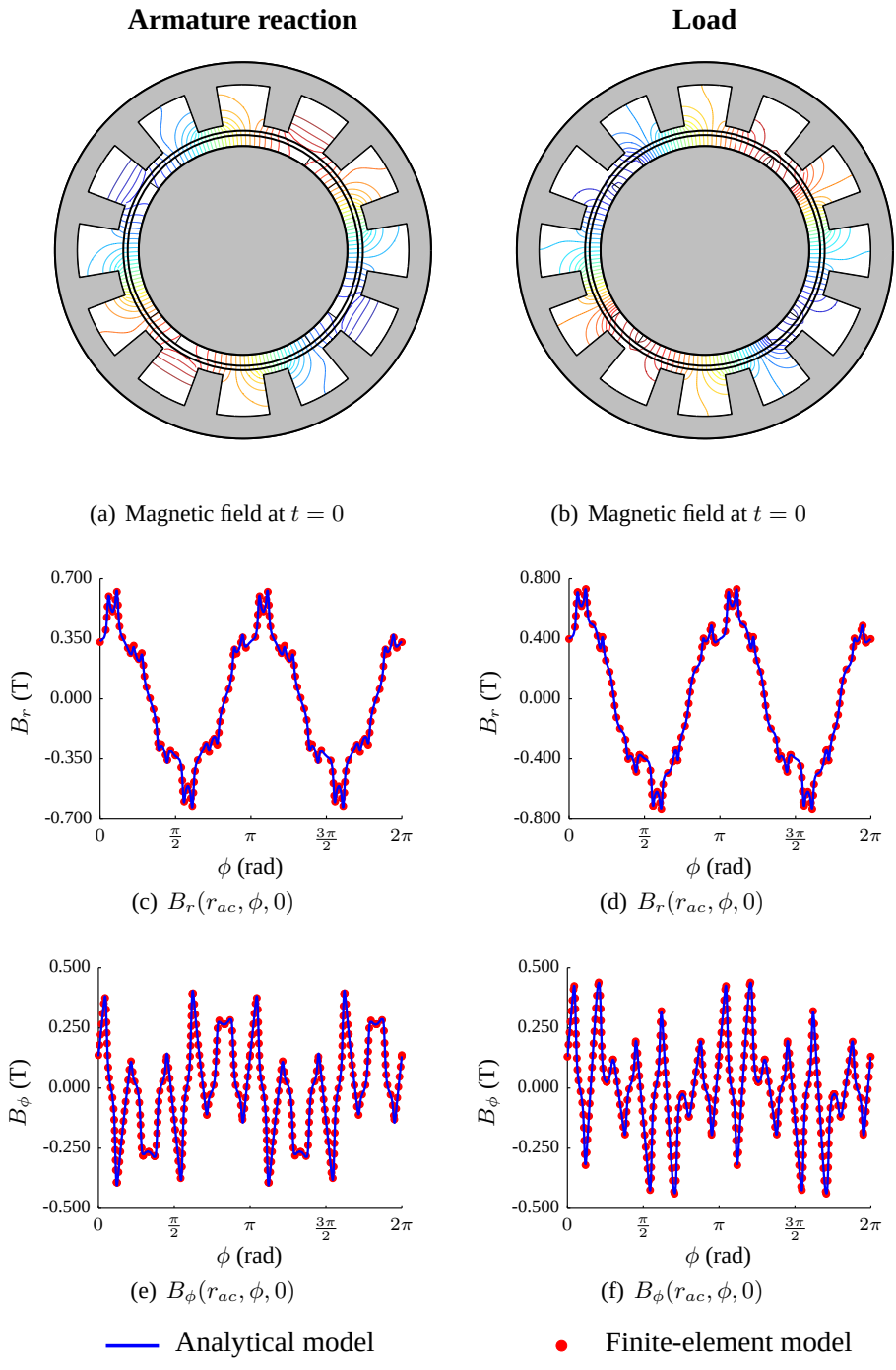

(a) Magnetic field at $t = 0$

(b) Magnetic field at $t = 0$

(c) $B_r(r_{ac}, \phi, 0)$

(d) $B_r(r_{ac}, \phi, 0)$

(e) $B_\phi(r_{ac}, \phi, 0)$

(f) $B_\phi(r_{ac}, \phi, 0)$

Figure 6.2: Validation of the voltage-fed inner-rotor machine with open slots and a SC

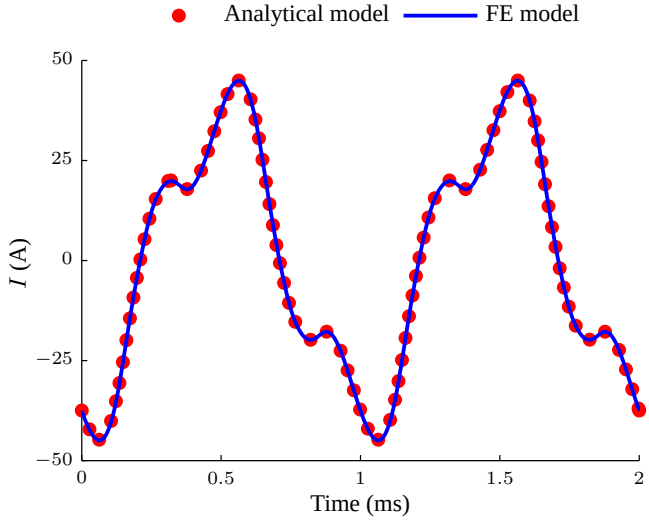

Figure 6.3: Validation of the line current of phase A

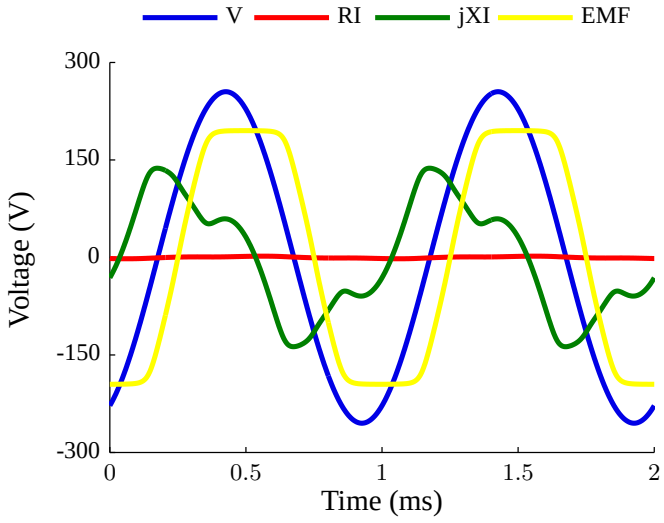

Figure 6.4: Phase voltages of phase A

6.5 Conclusion

In this section a coupling between the magnetic calculation of Chapter 3 and the equation for the terminal voltage of an electric machine were combined. The result is a model that can directly account for voltage sources. The technique was validated by comparison with a FE model. For the sake of an easily reproducible validation, sinusoidal voltage were applied. More realistic PWM voltage can be applied in exactly the same way. This will be done in the parameter studies of Chapter 9.

Although the implementation of the above presented coupling might add to the model's complexity, it allows to easily account for realistic voltage sources instead of idealized current sources. This improves the accuracy and usability of the FB model. As mentioned in Chapter 1, that is one of the goals of this thesis.

Chapter 7

Calculation of electromagnetic quantities

In the previous chapters, the focus was on the calculation of the magnetic field. However, when designing an electric machine, the interest is in its electromagnetic properties, rather than in its magnetic field. Therefore, this chapter focuses on how results from the magnetic field calculation can be used to compute physical quantities that are interesting from a design perspective. Apart from some general machine parameters such as the flux density and the back EMF, two electromagnetic properties are of special interest for high-speed PMSMs; the torque and the eddy-current losses in the rotor.
In the scope of this PhD, the prototype of a high-speed generator for a combined heat and power (CHP) unit was developed in collaboration with a Belgian SME. In the first part of this chapter, i.e. in Section 7.1, that prototype machine is introduced. The second part of this chapter, presented in Sections 7.2-7.5, discusses the actual calculation of the machine's electromagnetic properties. In that discussion, the prototype design is used as a reference. Finally, Section 7.6 concludes this chapter.

The content of this chapter has been published in the following journal paper:

- B. Hannon, P. Sergeant and L. Dupré, "Torque and torque components in high-speed permanent-magnet synchronous machines with a shielding cylinder", *Mathematics and Computers in Simulation*, vol. 130, pp. 70-80, 2016

7.1 Prototype machine

As already mentioned, in the scope of this PhD, Ghent University partnered with a Belgian company to design a high-speed SM PMSM for a micro CHP unit. This collaboration has resulted in a test setup with two prototype machines that were mounted back-to-back. The actual test setup will be discussed in Chapter 8. However, as mentioned, the prototype designed for the micro CHP application will be used as a reference in this chapter.
In the context of rising energy prices, decentralized power generation has become increasingly popular in recent years. One possibility is to combine the generation of heat and electric power, thereby reducing overall energy losses. Such CHP units can be implemented both on a very large, industrial scale or in smaller units. The application in this case is a residential, low-power CHP unit that is powered by a high-speed micro turbine. In order to minimize the system's maintenance while maximizing its efficiency, it was decided to implement a high-speed SM PMSM generator in a direct-drive configuration. This generator was designed at Ghent University under the supervision of prof. dr. ir. Sergeant. The machine's topology, as shown in Figure 7.1, is the same as that from the example machine used in Chapter 3. Its parameters are listed in Table 7.1.

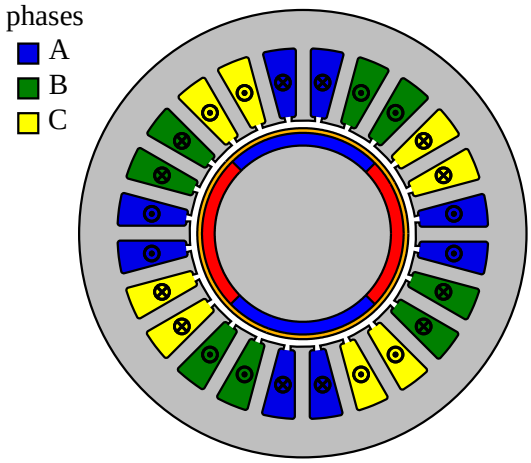

Figure 7.1: Cross-section of the prototype machine

One of the interesting features of the machine is the retaining sleeve, made from AISI 303 stainless steel. The permanent magnets are N42SH-type NdFeB magnets.
As explained in Chapter 3, the slots and the slot openings have to be simplified for the FB model. This is done while keeping their surfaces constant, resulting in an opening angle of $3.46°$ for the slot openings (δ) and $9.42°$ for the slots (ϵ).
Note that the retaining sleeve was not designed to function as a shielding cylinder.

Table 7.1: Parameters of the validated machines

Parameter	Symbol	Value
Number of slots	N_s	24
Number of pole pairs	p	2
Number of phases	m	3
Residual flux density of the magnets	B_m	1.28 T
Angular span of a magnet	ϕ_m	90.00°
Nominal line voltage	V_{nom}	150 V
Nominal current	I_{nom}	6 A
Number of windings per slot	N	10
Nominal frequency	f_{nom}	1000 Hz
Nominal speed	$n_{r,nom}$	30,000 rpm
Radius of the RY - PM boundary	r_1	17.50 mm
Radius of the PM - SC boundary	r_2	20.50 mm
Radius of the SC - AG boundary	r_3	21.00 mm
Radius of the AG - SO boundary	r_4	23.00 mm
Radius of the SO - SL boundary	r_5	23.80 mm
Radius of the SL - SY boundary	r_6	37.50 mm
Radius of the SY external boundary	r_7	45.00 mm
Stack length	l_s	28.00 mm
Tooth width	w_t	3.00 mm
Tooth-tip width	w_τ	4.72 mm
Permeability of the magnets	μ_{PM}	$1.05\mu_0$ $\frac{\mathrm{H}}{\mathrm{m}}$
Conductivity of the magnets	σ_{PM}	$6.94.10^5$ $\frac{\mathrm{S}}{\mathrm{m}}$
Permeability of the sleeve	μ_{SC}	$1.008\mu_0$ $\frac{\mathrm{H}}{\mathrm{m}}$
Conductivity of the sleeve	σ_{SC}	$1.38.10^6$ $\frac{\mathrm{S}}{\mathrm{m}}$

It may therefore be expected that its presence will increase the rotor losses. Moreover, as its conductivity and permeability are rather low, the retaining sleeve does not shield the magnets. This can easily be validated by considering the penetration depth of harmonic combination (n, k) in the sleeve. That penetration depth can, at least for the fundamental time-harmonic order, be calculated as:

$$\delta_{n,k} = \sqrt{\frac{2}{|n-k|\omega\sigma_{SC}\mu_{SC}}} \tag{7.1}$$

It will be shown in Section 7.2 that the dominant harmonic combinations of the prototype are $(2, -22)$ and $(2, 26)$. Their penetration depth in the sleeve is about 19 mm. As the sleeve is only 0.5 mm, this implies that the magnets are virtually unshielded. This could compromise the validity of the assumption that the eddy-current reaction field of the magnets is negligible. However, the conductivity of the

magnets is still only half that of the sleeve. Therefore, the assumption of negligible eddy-current reaction field of the magnets is still justifiable.

7.2 Magnetic flux density

As already discussed in Section 3.4, the magnetic flux density can be obtained directly from the definition of the magnetic vector potential (2.27). In a 2D cylindrical coordinate system, this implies:

$$\mathbf{B} = \frac{1}{r}\frac{\partial A}{\partial \phi}\mathbf{e}_r - \frac{\partial A}{\partial r}\mathbf{e}_\phi \tag{7.2}$$

The magnetic flux density was extensively discussed and validated in Section 3.4. This will not be repeated here. However, Section 3.4 visualized the magnetic flux density at a given instance of time, such a visualization does not provide a lot of information. Therefore, in the following, two other visualizations of the magnetic flux density will be introduced; the harmonic map and the total asynchronous distortion.

7.2.1 Harmonic map

The harmonic map is a visualization of the flux density's amplitude for every harmonic combination. Figure 7.2 illustrates the concept for the radial and tangential components of the prototype's flux density in the center of the air gap at no-load conditions. Evidently, a similar visualization could be made for the flux density's norm or even its phase angle, depending on the needs.
Note that the synchronous harmonic combinations are displayed on a green background. The oversynchronous harmonic combinations, i.e. the combinations that rotate faster than the rotor, are displayed on a yellow background. The background of the undersynchronous harmonic combinations is left blank.
Figure 7.2 only shows the positive time-harmonic orders. This is because, as discussed in Chapter 5, there is a symmetry between harmonic combinations (n, k) and $(-n, -k)$. Note as well that Figure 7.2 is a good illustration of the discussion on harmonic content in synchronous machines, see Chapter 5 and Appendix B.
The harmonic map may not be directly interesting when designing electric machines. But, it can be a very interesting tool to interpret results from other calculations.

7.2.2 Total asynchronous distortion

Although the harmonic map is an interesting visualization tool, it is not very effective at quantifying the harmonic content. A commonly-used parameter that does

represent the amount of non-fundamental harmonics is the total harmonic distortion (THD). However, the THD is used for signals with either spatial- or time-harmonic orders, e.g. to quantify the harmonic distortion of a voltage signal. In this work, it is important to consider both time- and spatial-harmonic orders and to differ between synchronous harmonic components, i.e. components with $n = k$, and asynchronous harmonic components, i.e. components with $n \neq k$. To do so, the total asynchronous distortion (TAD) is introduced as:

$$\mathrm{TAD} = \sqrt{\frac{\sum\limits_{n \neq k} |\mathbf{B}_{n,k}|^2}{\sum\limits_{n=k} |\mathbf{B}_{n,k}|^2}} \tag{7.3}$$

Using the above, the TAD can be calculated for the r- and ϕ-components of the prototype's no-load flux density in the center of the air gap. TAD_r is found to be 3.01% and TAD_ϕ is 22.66%. This indeed matches Figure 7.2, which shows a relatively larger presence of asynchronous harmonic combinations for the ϕ-component of the flux density.

7.2.3 Conclusion

In the above, the flux density was discussed. As **B** was already extensively validated in previous chapters, the discussion in this section is limited to the introduction of the harmonic map and the total asynchronous distortion. Both are not directly applicable for the design of an electric machine, but will prove to be interesting tools to interpret the results of the following sections.
As expected from a diametrically wound machine with multiple slots per pole and per phase, the asynchronous content of the prototype machine is rather small. This was clearly illustrated by the harmonic maps in Figure 7.2. Moreover, as the radial component of the magnetic field is dominant and TAD_r is low the overall TAD will be low as well.

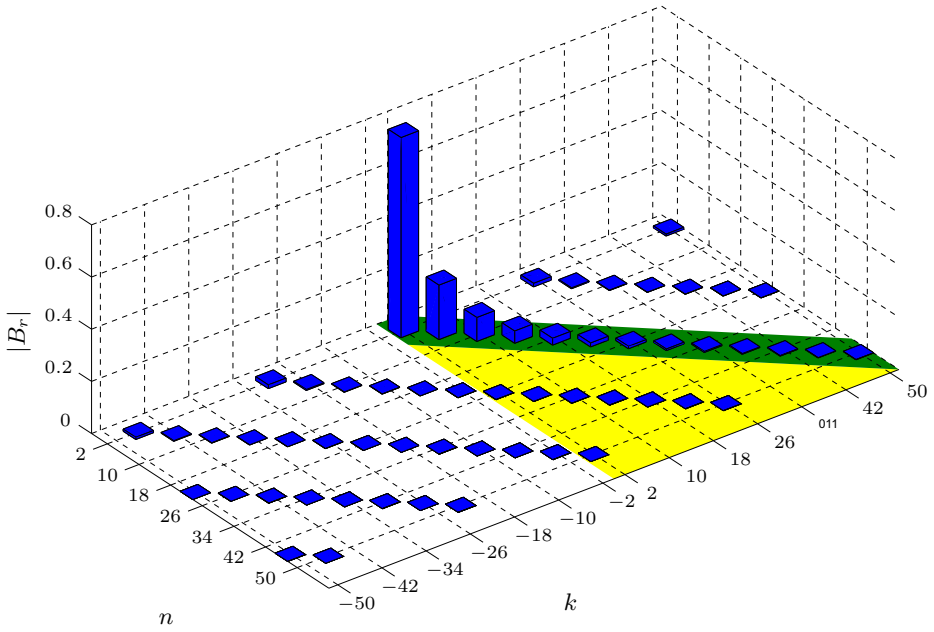

(a) Radial component

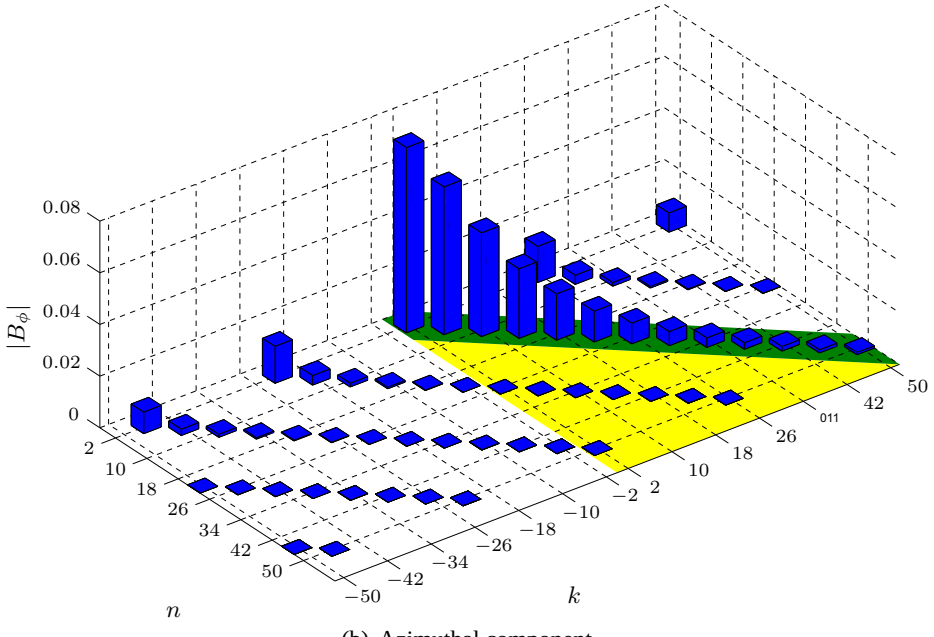

(b) Azimuthal component

Figure 7.2: Harmonic maps of the no-load magnetic flux density in the center of the prototype's air gap

7.3 Back EMF

Evidently, the back EMF is an important design parameter for electric machines. Not only its peak value, which cannot exceed the limitations of the power electronics, is important. Its harmonic content has to be considered as well. In this section, the computation of the back EMF is briefly discussed.
The back EMF was actually already calculated in the previous chapter. Indeed, in Section 6.2.2, the flux linked with each of the machine's coils was calculated. Its time-derivative was then used to compute the counter-electromotive force needed in the equation for the terminal voltage (6.5). The obtained formula for the back EMF in coil c is:

$$e^{(c)}(t) = \sum_{i_{N_s}=1}^{N_s} \sum_{n=-\infty}^{\infty} jn\omega l_s N^{(c,i_{N_s})} \alpha_n^{(i_{N_s})} e^{-jn\omega t} \tag{7.4}$$

where $N^{(c,i_{N_s})}$ is the amount of conductors that coil c has in slot i_{N_s}. $N^{(c,i_{N_s})}$ is oriented. This means that it is positive if i_{N_s} contains going conductors of c and negative if c's conductors are returning in i_{N_s}. As explained in Chapter 6, $\alpha_n^{(i_{N_s})}$ is the spatially averaged MVP in slot i_{N_s}. In this work, the averaging is performed via integration:

$$\alpha_n^{(i_{N_s})} = \frac{1}{S^{(i_{N_s})}} \iint_S A(r, \phi, t)\, \mathrm{d}s \tag{7.5}$$

Note that, whereas in Chapter 6 the entire counter-electromotive force was used, here the no-load voltage is studied, i.e. the flux in the coils is solely due to the magnets.
The results from the prototype's back EMF calculation are compared to results from a FE model in Figure 7.3(a). It can be seen that the results are in very good agreement. The RMS deviation is 0.054%. The harmonic content of the back EMF is shown in Figure 7.3(b).
As the back EMF has no spatial dependency, its THD can be calculated as:

$$\mathrm{THD} = \sqrt{\frac{\sum\limits_{|n|\neq p} |E_n|^2}{\sum\limits_{|n|=p} |E_n|^2}} \tag{7.6}$$

For the prototype machine, a value of 19.64% is obtained. Note that the harmonic distortion is mainly due to the third harmonic, as can be seen from Figure 7.3(b). The effect of this harmonic will of course be nullified if the machine's coils are connected in a star configuration.

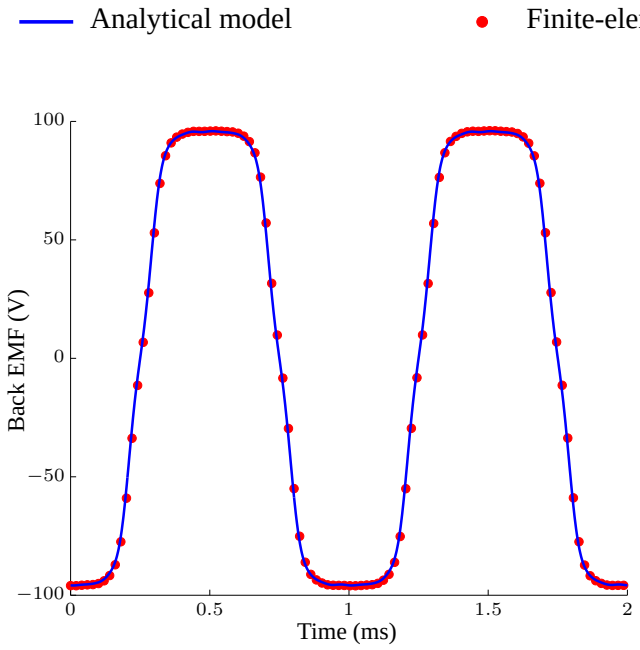

(a) Time domain

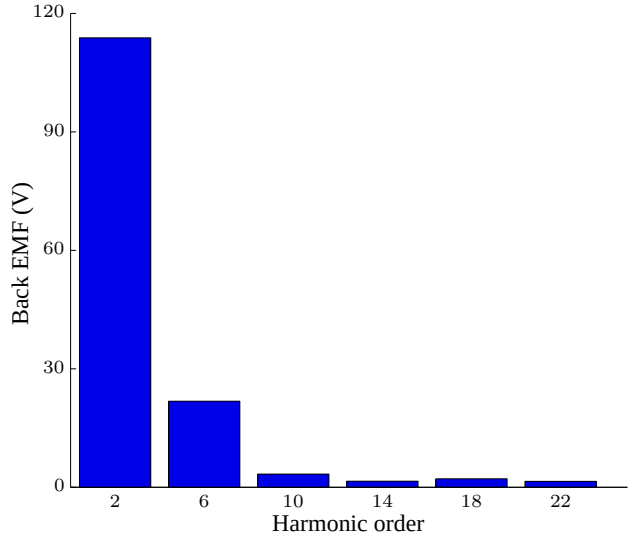

(b) Frequency domain

Figure 7.3: Back EMF of the prototype machine

7.4 Torque

The machine's torque is probably one of its most important electromagnetical parameters. This is especially true for high-speed applications, where the torque ripple often has to be minimized. In this section, the calculation of the torque is discussed and the concept of torque components is introduced. These torque components are an especially interesting tool to study high-speed PMSMs.

7.4.1 Torque calculation

The torque acting on a certain volume can be computed by integrating the cross product of the radius and Maxwell's stress tensor $(\mathbf{\Gamma})$ over the surface of that volume:

$$\mathbf{T} = \oint_S \mathbf{r} \times \mathbf{\Gamma} \mathrm{d}s \tag{7.7}$$

where the stress tensor is defined as:

$$\mathbf{\Gamma} = \mu(\mathbf{n} \cdot \mathbf{H})\mathbf{H} - \frac{\mu}{2}(\mathbf{H} \cdot \mathbf{H})\mathbf{n} \tag{7.8}$$

In the above, $\mathbf{n}$ is the outer unit vector, normal to the integration surface S.
The torque acting on the entire rotor (T) can then be calculated by choosing the integration surface as a cylinder with radius r_3 and an axis that is coaxial to the machine's axis, see Figure 7.4(a).

$$\begin{aligned} T(t) &= \frac{l_s r_3^2}{\mu_4} \int_0^{2\pi} B_r^{(4)}(r_3, \phi, t) B_\phi^{(4)}(r_3, \phi, t) \, \mathrm{d}\phi \\ &= \sum_{n=-\infty}^{\infty} \sum_{s=-\infty}^{\infty} T_{n,s} e^{-j(n+s)\omega t} \end{aligned} \tag{7.9}$$

where the superscript (4) refers to the air gap subdomain, n is the time-harmonic order related to $B_r^{(4)}$ and s is the time-harmonic order related to $B_\phi^{(4)}$. $T_{n,s}$ is calculated as:

$$T_{n,s} = 2\pi \frac{l_s r_3^2}{\mu_4} \sum_{k=-\infty}^{\infty} B_{r,n,k}^{(4)}(r_3) B_{\phi,s,-k}^{(4)}(r_3) \tag{7.10}$$

The radial and tangential components of the flux density are calculated from the definition of the MVP.
After having obtained the torque, its net value (T_{net}) can be calculated as the average torque over one period. The torque ripple can be calculated as well. In this work, it will be expressed as a percentage of the net torque:

$$T_{\Delta\%} = \frac{|\max(T(t)) - \min(T(t))|}{\mathrm{mean}(T(t))} \tag{7.11}$$

Note that it can be seen from (7.9) and (7.10) that net torque is the result of interaction between opposite harmonic combination, i.e. (n, k) and $(-n, -k)$. Indeed, those combinations have the same rotational speed. In general, torque can only be produced due to the interaction of harmonic combinations with opposite spatial harmonic orders, i.e. k and $-k$.

7.4.2 Torque components

In a machine that is equipped with a shielding cylinder, the total torque is composed of two torque-producing mechanisms.
A first component of the torque is due to the classical interaction between the magnets and the stator currents. It is referred to as the torque produced in the magnets $(T^{(2)})$, the superscript (2) referring to the PM subdomain. This component of the torque is dominated by synchronous harmonic combinations.
A second component of the torque is the result of interaction between the magnetic field and the eddy-currents in the shielding cylinder. It is referred to as the torque produced in the SC $(T^{(3)})$, the superscript (3) referring to the subdomain of the SC. This component of the torque is dominated by asynchronous harmonic combinations. Indeed, synchronous combinations do not induce eddy-currents in the SC. Note that $T^{(3)}$ can intuitively be explained by considering the SC as the squirrel cage of an induction machine. The slip with respect to the synchronous combinations is then zero, therefore only asynchronous harmonic combinations can produce torque.
$T^{(2)}$ and $T^{(3)}$ are fictitious torque components, they do not occur separately. Nevertheless, considering these components can be very useful to get a better understanding of the machine's physics.
The torque produced in the magnets can be calculated in a similar way as the total torque. However, now a cylinder with radius r_2 is chosen as the integration surface. This is illustrated in Figure 7.4(b). $T^{(2)}$ can then be calculated as:

$$T^{(2)}(t) = \sum_{n=-\infty}^{\infty} \sum_{s=-\infty}^{\infty} T_{n,s}^{(2)} e^{-j(n+s)\omega_m t} \tag{7.12}$$

where $T_{n,s}^{(2)}$ is calculated as:

$$T_{n,s}^{(2)} = 2\pi \frac{l_s r_2^2}{\mu_{PM}} \sum_{k=-\infty}^{\infty} B_{r,n,k}^{(2)}(r_2) B_{\phi,s,-k}^{(2)}(r_2) \tag{7.13}$$

Since $T^{(2)}$ and $T^{(3)}$ are the only torque components that make up T, the torque produced in the shielding cylinder can be calculated as in (7.14).

$$T^{(3)} = T - T^{(2)} \tag{7.14}$$

Similar to $T_{\Delta\%}$, $T^{(2)}_{\Delta\%}$ and $T^{(3)}_{\Delta\%}$ are also calculated as percentages of the average total torque (T_{net}):

$$T^{(2)}_{\Delta\%} = \frac{|\max(T^{(2)}(t)) - \min(T^{(2)}(t))|}{\text{mean}(T(t))} \tag{7.15a}$$

$$T^{(3)}_{\Delta\%} = \frac{|\max(T^{(3)}(t)) - \min(T^{(3)}(t))|}{\text{mean}(T(t))} \tag{7.15b}$$

Figure 7.5(a) shows the torque and its components in the prototype machine for a third of an electrical period. For the total torque, the RMS deviation between the FB and the FE model is 0.24%. Note that there is a small offset between the FB and FE results for $T^{(2)}$ and $T^{(3)}$. The reason is that the FE model is not very effective at calculating quantities on the boundaries between two materials, which is required to calculate $T^{(2)}$.

The net torque is 0.4631 Nm, $T^{(2)}_{net}$ is 0.4632 Nm and $T^{(3)}_{net}$ is -0.0001 Nm. The total torque ripple is 12.20%, $T^{(2)}_{\Delta\%}$ is 13.63% and $T^{(3)}_{\Delta\%}$ is 1.17%. In Figure 7.5(b), the harmonic content of the torque and its components is shown.

Note that, from Figure 7.2, it could have been expected that $T^{(3)}_{net}$ would be negative. Indeed, the undersynchronous harmonic combinations dominate the oversynchronous ones. Like in an induction machine, those combinations produce a braking force. In this situation, $T^{(3)}$ is almost negligible with respect to $T^{(2)}$. However, its role may be much more important when the SC's conductivity is increased and/or the machine's asynchronous content is higher.

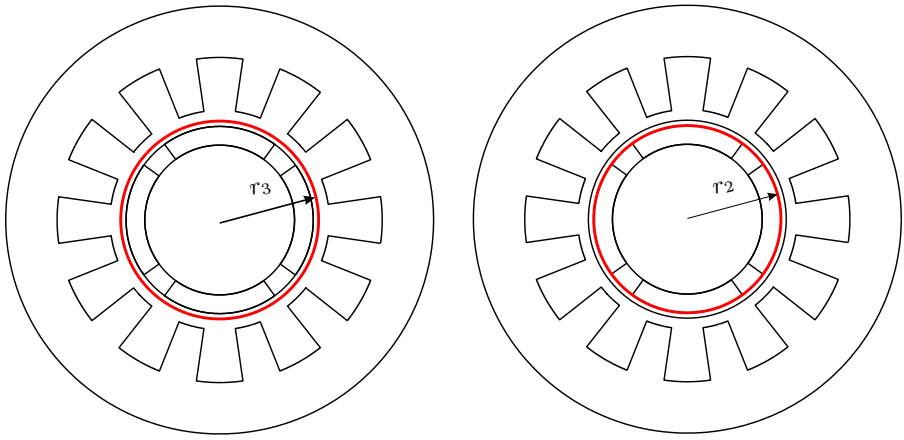

(a) Integration surface for T (b) Integration surface for $T^{(2)}$

Figure 7.4: Integration surface for torque calculation

7.4.3 Conclusion

In this section, the calculation of the torque using Maxwell's stress tensor was discussed. Moreover, the torque was divided in a component related to the shielding cylinder and a component related to the magnets. Although these components are not physically divisible, their computation can provide a lot of insight in the machine's operation.

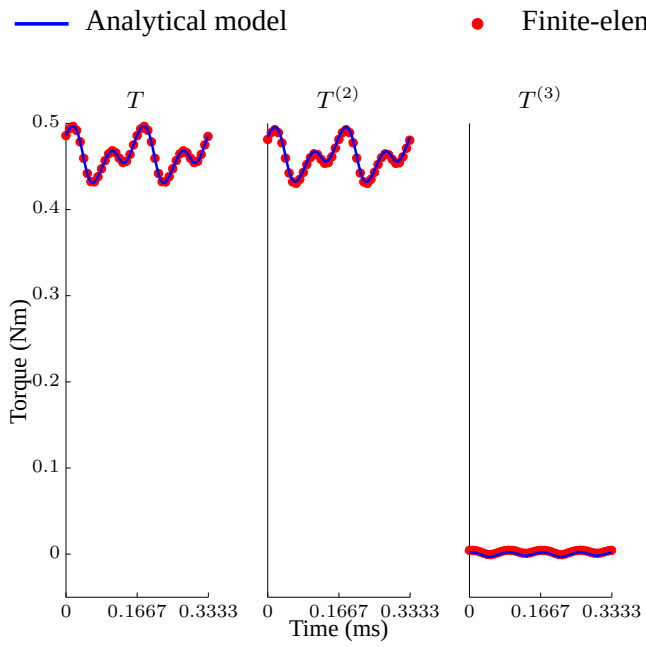

(a) Time domain

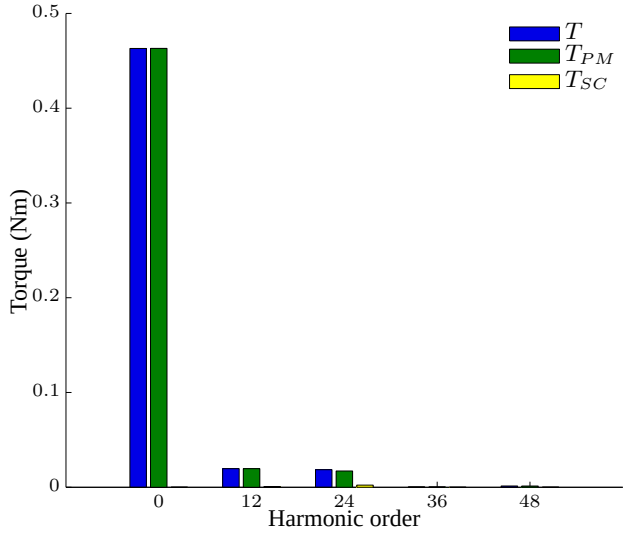

(b) Frequency domain

Figure 7.5: Torque and torque components of the prototype machine

7.5 Eddy currents and eddy-current losses

It was already pointed out earlier that eddy-currents and the losses they cause in the rotor are of great importance in high-speed PMSMs. In this work, both the eddy-currents in the shielding cylinder and the magnets are considered. Their calculation will be discussed in the following.

7.5.1 Eddy current calculation

The calculation of the eddy currents in the SC is relatively straightforward. From the constitutive relation for the current density (2.26a) and by assuming that there is no externally imposed voltage in the SC, the following equation can be obtained:

$$J^{(3)}(r,\phi,t) = \sum_{n=-\infty}^{\infty} \sum_{k=-\infty}^{\infty} j\sigma^{(3)}(n-k)\omega A_{n,k}^{(3)}(r) e^{j(k\phi - n\omega t)} \tag{7.16}$$

Figure 7.6(a) shows a contour plot of the resulting current density in the prototype machine at $t = 0$, i.e. the magnets are aligned with phase A and the current through that phase is at its maximum.
Although the conductivity of the permanent magnets (σ_{PM}) was assumed 0 during the computation of the field, a similar approach can be used to calculate the eddy-currents in the magnets. However, in a two-dimensional model, there is no guarantee that the net current in each of the magnets is zero. This implies that current may be flowing from one magnet to the other, which is of course not realistic. To cope with that problem, a spatially constant current density $\left(C^{i_m}(t)\right)$ is added [64, 76, 88, 142]:

$$J^{(2,i_m)}(r,\phi,t) = \sum_{n=-\infty}^{\infty} \left(\sum_{k=-\infty}^{\infty} j\sigma^{(2)}(n-k)\omega A_{n,k}^{(2)}(r) e^{j(k\phi - n\omega t)} \right) - C_n^{(i_m)}(t) \tag{7.17}$$

where i_m refers to the number of the considered magnet and $C_n(t)$ is calculated as:

$$\begin{aligned} C_n^{i_m}(t) &= \iint_{S^{(im)}} j\sigma^{(2)}(n-k)\omega A_{n,k}^{(2)}(r) e^{j(k\phi - n\omega t)} \,\mathrm{d}s \\ &= \int_{-\phi_0^{(i_m)}+\omega t}^{-\phi_0^{(i_m)}+\phi_m+\omega t} \int_{r_2}^{r_3} j\sigma^{(2)}(n-k)\omega r A_{n,k}^{(2)}(r) e^{j(k\phi - n\omega t)} \,\mathrm{d}r \,\mathrm{d}\phi \end{aligned} \tag{7.18}$$

where $\phi_0^{(i_m)}$ is the initial position of magnet i_m.
Figure 7.6(b) shows a contour plot of the current density in the second magnet of the prototype machine at $t = 0$.
Figure 7.7 shows the temporal evolution of the current density in different points of the SC, i.e. $(r_3, 0)$, $(\frac{r_2+r_3}{2}, 0)$ and $(r_2, 0)$ and the magnets, i.e. $(\frac{r_1+r_2}{2}, 0)$. Where

the ϕ-axis is as in Figure 3.2. It can be seen that a good agreement with the FE model is achieved.

7.5.2 Eddy-current loss calculation

Classically, the eddy-current losses are calculated from Joule's formula:

$$P_{ec}(t) = \iiint_V \frac{\mathbf{J} \cdot \mathbf{J}}{\sigma} \, \mathrm{d}v \tag{7.19}$$

This equation is used to calculate the eddy-current losses in the magnets. For a 2D model, it can be rewritten as (7.20).

$$P_{ec}^{(2)}(t) = l_s \iint_{S^{(i_m)}} \frac{J^{(2)}(r,\phi,t) J^{(2)}(r,\phi,t)}{\sigma^{(2)}} \, \mathrm{d}s \tag{7.20}$$

Joule's formula is, however, not effective at computing the losses in the shielding cylinder. This is because the r-dependent part of $J^{(3)}(r,\phi,t)$ contains Bessel functions. These functions can not be integrated analytically. To cope with this problem, the Poynting vector $(\mathbf{S})$ can be used [68, 143, 144]:

$$\mathbf{S} = \mathbf{E} \times \mathbf{H} \tag{7.21}$$

The integration of $\mathbf{S}$ over a closed surface determines the energy flowing through that surface. This implies that the total power transmitted to the rotor can be calculated by integrating the Poynting vector over the surface of a cylinder that includes the rotor, e.g. the cylinder shown in Figure 7.4(a). However, as discussed by Markovic and Perriard in [137], it is possible to directly compute the power dissipated in the SC. Essentially, their technique implies considering Poynting's vector in rotor coordinates, i.e. substituting $\theta + \omega t - \theta_0$ for ϕ, with θ the rotor angular coordinate and θ_0 the initial position of the rotor.

$$\begin{aligned} P_{ec}^{(3)}(t) &= \frac{r_3 l_s}{\mu} \int_0^{2\pi} E_z^{(4)} \cdot B_\theta^{(4)} \, \mathrm{d}\theta \\ &= \sum_{n=-\infty}^{\infty} \sum_{s=-\infty}^{\infty} P_{n,s}^{(3)} e^{-j(n+s)\omega t} \end{aligned} \tag{7.22}$$

where n is the time-harmonic order related to $E_z^{(4)}$ and s is the time-harmonic order related to $B_\theta^{(4)}$. $P_{n,s}$ is calculated as:

$$P_{n,s} = 2\pi \frac{l_s r_3}{\mu} \sum_{k=-\infty}^{\infty} -j(n-k)\omega A_{n,k}^{(4)}(r_3) B_{s,-k}^{(4)}(r_3) \tag{7.23}$$

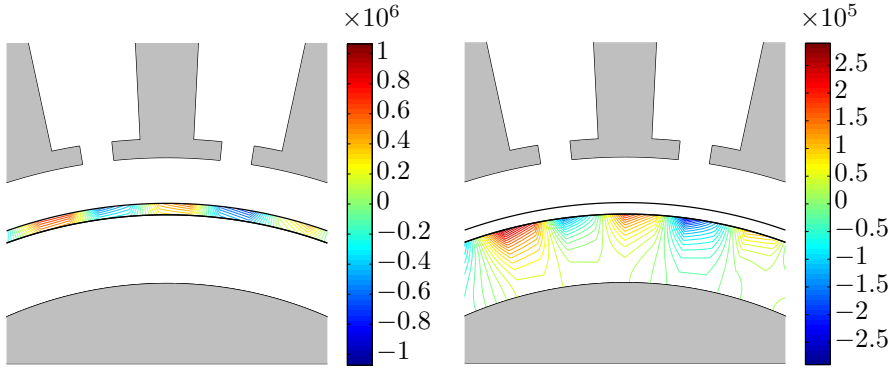

(a) Eddy currents in the SC at $t = 0$ (b) Eddy currents in the PM at $t = 0$

Figure 7.6: Eddy currents $\left(\frac{A}{m^2}\right)$ at $t = 0$

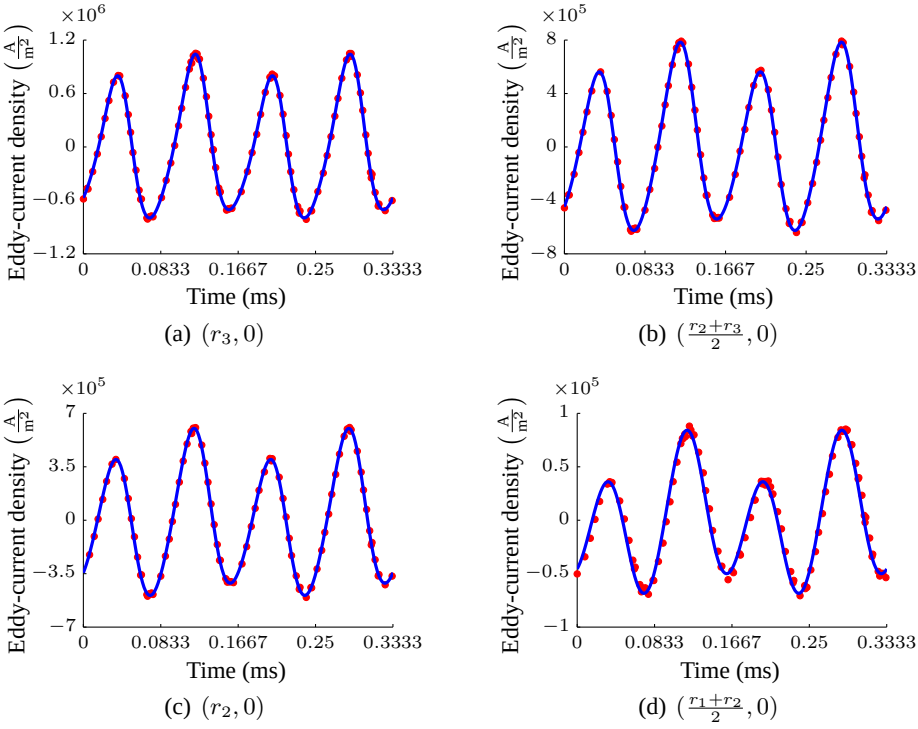

(a) $(r_3, 0)$ (b) $(\frac{r_2+r_3}{2}, 0)$

(c) $(r_2, 0)$ (d) $(\frac{r_1+r_2}{2}, 0)$

Figure 7.7: Eddy currents in various points of the SC and the PM

Note that the eddy-current losses in the magnets are not included in P if the latter is calculated from (7.22). The reason is that the Poynting vector is calculated directly from the magnetic and electric fields. As the eddy-currents in the magnets are not directly included in the calculation of those fields, their losses can not be accounted for by the integration of **S**.
Finally, the interest is in the average value of the eddy-current losses, the instantaneous eddy-current losses are not considered here.
By means of validation, the eddy-current losses of the prototype were computed and validated with the FE model. In the shielding cylinder, the eddy-current loss was calculated as 0.269 W with the FB model and 0.270 W with the FE model. In the permanent magnets the eddy-current losses were calculated as 0.091 W and 0.087 W respectively. These losses are very low because the asynchronous content of the prototype is very low. Especially because at this point a sinusoidal current is assumed. It will become clear from the following sections that the eddy-current losses may become much larger when the machine's magnetic field has a larger asynchronous content, e.g. when more realistic current waveforms are imposed.

7.5.3 Conclusion

In this section the calculation and validation of both the eddy currents and their losses was discussed. It should be noted that while the eddy-current losses in the magnets were computed from Joule's formula, this is not analytically possible for the eddy-current losses in the SC. The latter are therefore computed using Poynting's theorem. Good agreements with a time-stepped FE model were obtained for all of the calculations.

7.6 Conclusion

In this chapter, the calculation of various electromagnetic properties of electric machines was discussed. Each of those calculations was successfully validated with a finite element model. The machine, used for those validations, is the prototype machine for a micro CHP unit, developed in collaboration with a Belgian company. The harmonic content of the studied machine is very low. Although this doesn't compromise the validations of this chapter, it does result in a very low torque in the SC and very low eddy-current losses. However, in machines with a higher harmonic content, the effect of the SC is much more important.

Chapter 8

Test setup

In addition to the theoretical work that has been presented in the previous chapters, a test setup for PMSMs operating at high speeds was built in the scope of this PhD. The primary goal of that setup was to complement the obtained theoretical knowledge with some practical experience.
The main focus of the work at the test setup has been to build an in-house, fully customizable drive for the SM PMSMs that were introduced in Chapter 7. As this drive, which has been extensively covered in [145–149], is not really in the scope of this dissertation, it will only briefly be discussed. Instead, the focus of this chapter will be on a description of the setup and the measurements.
The following chapter starts with an introduction of the setup's hardware and the control strategies that were implemented. This is done in Section 8.1. In Section 8.2, measurements of the no-load voltage and line currents are presented and compared to results from the FB model. Section 8.3 concludes this chapter.

8.1 Introduction

In this section, the test setup, which is shown in Figure 8.1, is discussed. In addition, a brief discussion on the implemented control strategies is provided as well.

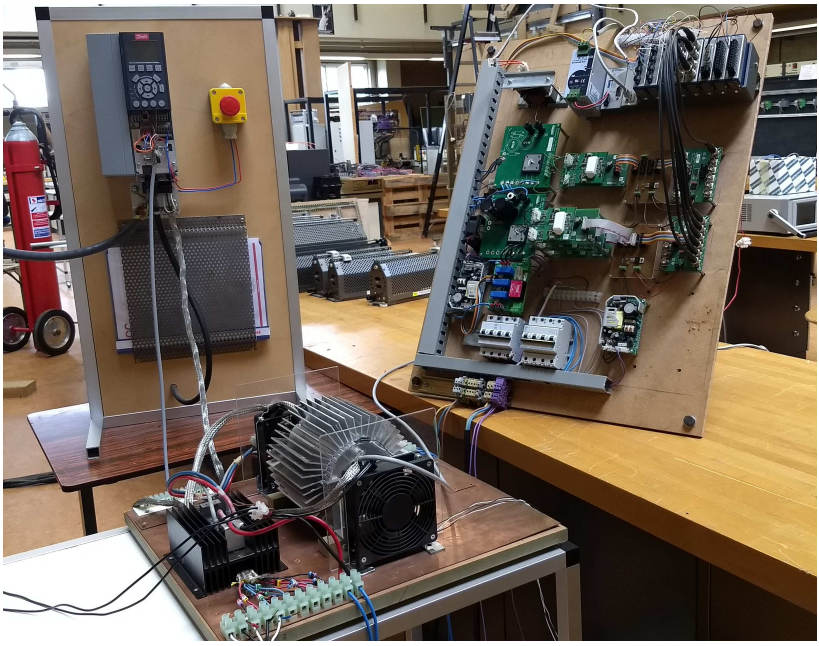

Figure 8.1: Overview of the setup

The setup comprises two parts; the electric machines and the power electronics. Both will be discussed in the following.

8.1.1 Electric machines

It was already mentioned that the electric machines that are used in this setup were constructed in the scope of designing a generator for a micro CHP unit. The resulting machine has been discussed in Section 7.1. For the setup, two of those machines were mounted in a custom-designed back-to-back configuration, as shown in Figure 8.2. The goal of that configuration is to use one machine as a motor while the other operates as a generator. This allows to perform loss measurements without having to measure the torque, which is particularly difficult at high speed. Apart from the two electric machines, Figure 8.2 also shows an exterior shaft and an additional rotor that is placed outside the housing. The goal of the shaft is to enable mounting an encoder. Both that encoder and the additional rotor are foreseen to provide the necessary position feedback for the control. The encoder is used

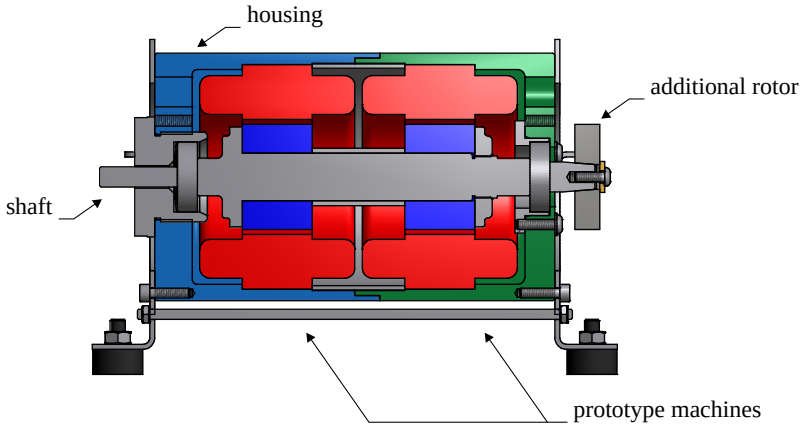

Figure 8.2: Cross section of the machines

for field-oriented control (FOC) of the machine. The additional rotor is combined with a set of Hall sensors to provide position feedback for a brushless DC (BLDC) control.
Although both machines have an identical geometry, they have slightly different winding schemes. One of both machines has a traditional winding; its coils are connected in series and its phases are connected in a star configuration, as shown in Figure 8.3(a). As the star point of this machine is internal, it is referred to as the internal star-point machine. The winding scheme of the second machine is analogous, but the ends of all coils are accessible. This winding scheme, shown in Figure 8.3(b), allows for more flexibility. However, in the scope of this work, the coils were always connected in series and the phases were connected in a star configuration. The second machine is referred to as the external star-point machine.
Note that in Figure 8.3, the depicted connections are those of phase A and the Y in Figure 8.3(a) refers to the internal star point of the machine.
While testing it was found that there has been an error during the production of the external star-point machine. As will be discussed in Section 8.2, its back EMF was found to be only half the expected value. This could be due to a problem with the permanent magnets, but it is more likely that there is a problem with the windings of the machine.

8.1.2 Power electronics

The machine operating as a motor can be controlled with two different sets of power electronics; a commercial drive or the custom-made drive that was built in-house.

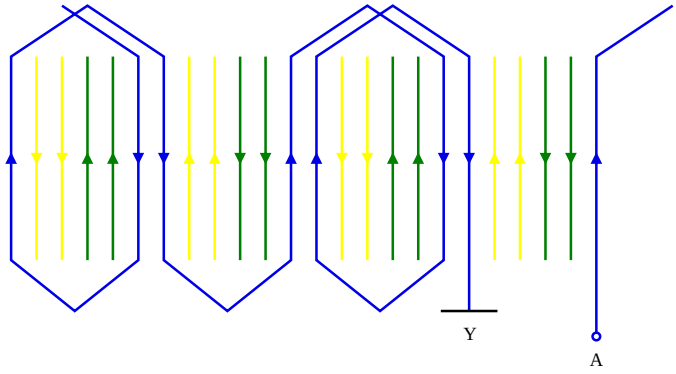

(a) Internal star-point machine

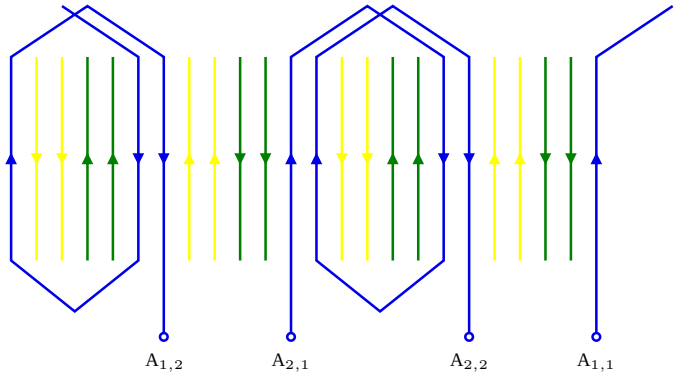

(b) External star-point machine

Figure 8.3: Winding schemes

Commercial drive

In a first stage, a VLT®AutomationDrive FC 300 from Danfoss was used to control the machine. This drive allows for a sensorless control or a FOC with position feedback. Both of these controls have been implemented, but neither was stable at speeds exceeding 22,000 rpm.

Custom drive

As the commercial drive doesn't succeed at accelerating the setup to its nominal speed of 30,000 rpm, and because the flexibility of a commercial drive is limited, a custom-made drive was constructed to power the test setup.
The architecture of the drive comprises four parts; the control part, the transformation part, the power stage and the measurement part.
The control part provides the user-interface, processes the control algorithm and

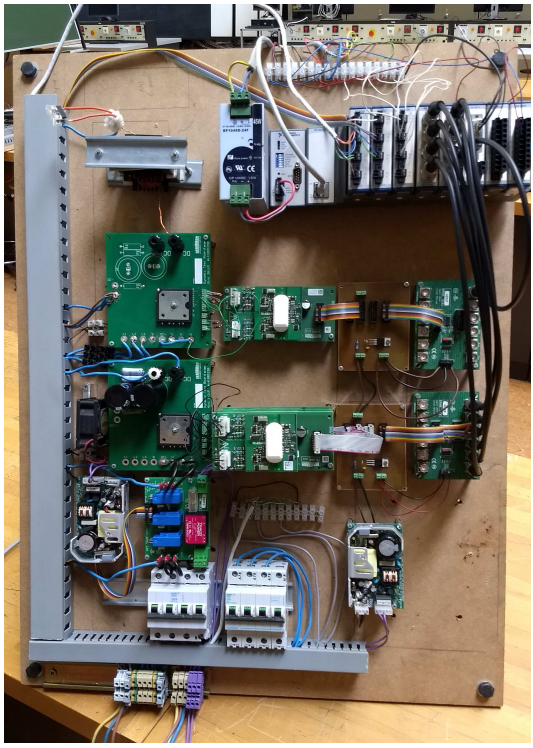

Figure 8.4: Custom-made drive for the test setup

outputs the switching signal. It contains a PC for the user-interface and a compact RIO module from National Instruments to implement the actual control algorithm. Its output is a low voltage transistor-transistor logic (LVTTL) signal.
As the LVTTL signal cannot be applied directly to the IGBT drivers, it is rescaled in the transformation part. The printed-circuit boards that have been used to do so were designed at Ghent University.
The power stage of the driver contains a buck converter and a three-phase inverter. By providing a separate buck converter, it is possible to control the voltage level with both pulse-width modulation (PWM) and pulse-amplitude modulation (PAM).
The measurement part provides the control algorithm with the required information about the motor's operation. It contains three current measurements, i.e. two line-currents and the current through the DC bus, and three voltage measurements, i.e. one per phase.
Figure 8.5 shows an overview of the power electronics.
The custom drive was successfully used to implement two different BLDC controls; one with position feedback and a sensorless one. More information about the drive and the control algorithms can be found in [145–149].

8.1.3 Control strategies

Four different control strategies have been implemented on the setup. Using the commercial drive, two FOCs were used; one with position feedback and a sensorless one [149]. Both use PWM to control the amplitude of the voltage. Similarly, the custom drive was used to implement a BLDC control with and without position feedback [145, 147, 148]. Both of those controls use the drive's buck convertor to control the amplitude of the voltage, i.e. they apply PAM.

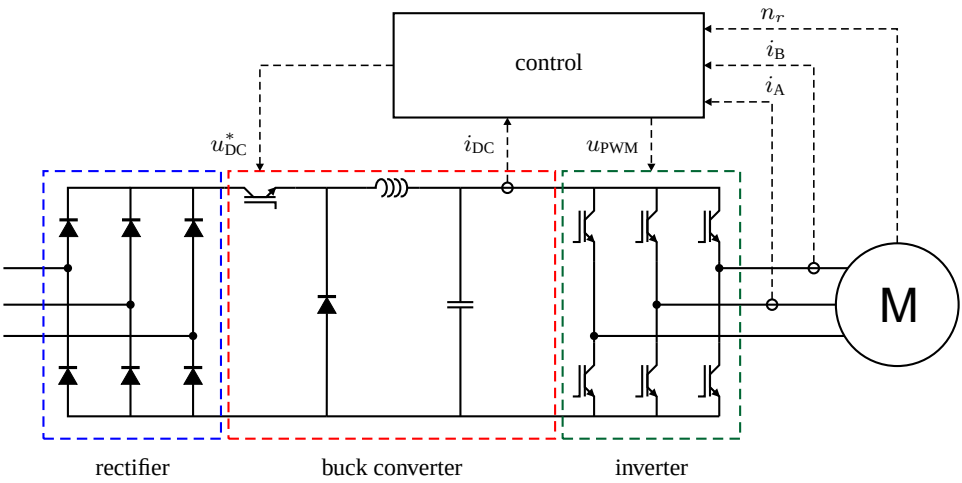

Figure 8.5: Overview of the power electronics of the test setup

8.2 Measurements

In this section, measurements of the no-load voltage and the currents in the machine will be compared to results that were obtained from the Fourier-based model.

8.2.1 No-load voltage

Figure 8.6 shows the no-load voltage at 20,000 rpm. It can readily be seen that the agreement between the FB model and the measurements is very good for the interior star-point machine. However, there is a large deviation with the measurement from the exterior star-point machine. As already mentioned, this implies that there must have been an error during the production of the machine. This can either be a problem with the magnets or a problem with the winding configuration. As the deviation is almost exactly a factor two, it is most likely that the exterior star-point machine was not wound correctly.

Note that the faulty machine compromises the possibility to determine the prototype's efficiency using the back-to-back configuration. Indeed, as the machines cannot be assumed identical, it cannot be assumed that they contribute equally to the measured losses. Therefore, no efficiency measurements will be performed in this work.
Another interesting observation is that the measured signal contains spikes. Those spikes are due to electromagnetic coupling between the power signal and the measured signal. Indeed, the frequency of the spikes matches the switching frequency of the inverter.

8.2.2 Terminal voltage and current

Another validation that can be performed on the test setup is whether the current predicted by the Fourier-based model with a voltage source matches the measured current. However, as the internal star-point machine has to be used, the phase voltages, which are the input of the FB model, cannot be measured directly. Therefore, this validation is performed in four steps. These steps will be discussed in the following.
Evidently, the first step is to measure the current and line voltage. This is done while operating the motor at 10,682 rpm, the generator is not loaded. Results from that measurement are shown in Figure 8.7.
In the second step, the measured current is used as an input for the FB model with a current source to calculate the phase voltages. The obtained voltage of phase A is shown in Figure 8.8. This voltage will be used as an input for the FB model with a voltage source.
The third step is to compare the calculated and measured voltages. This is done in Figure 8.9 for the voltage between phases A and B. It can be seen that the agreement between the measured and the calculated voltage is very good. This implies that the voltage calculated in the previous step can be used as an input for the FB model.
Finally, the FB model with a voltage source can be used to compute the current in the machine. From Figure 8.10, it can be seen that there is, again, a good agreement between the calculations and the measurements. This validates the current calculations of the FB model.

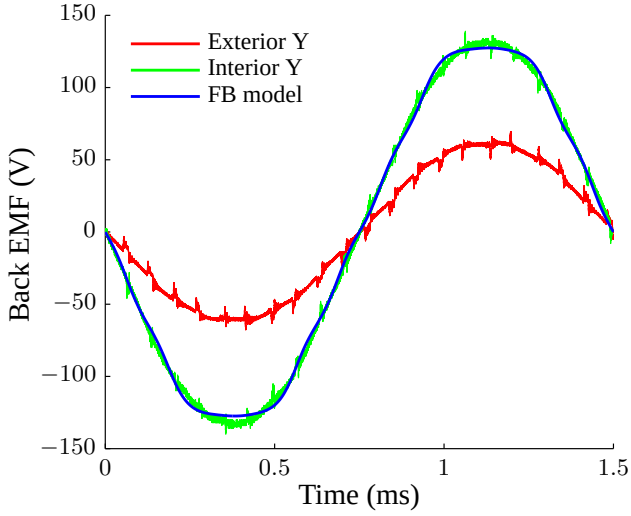

Figure 8.6: No-load voltages in the prototype machine at 20,000 rpm

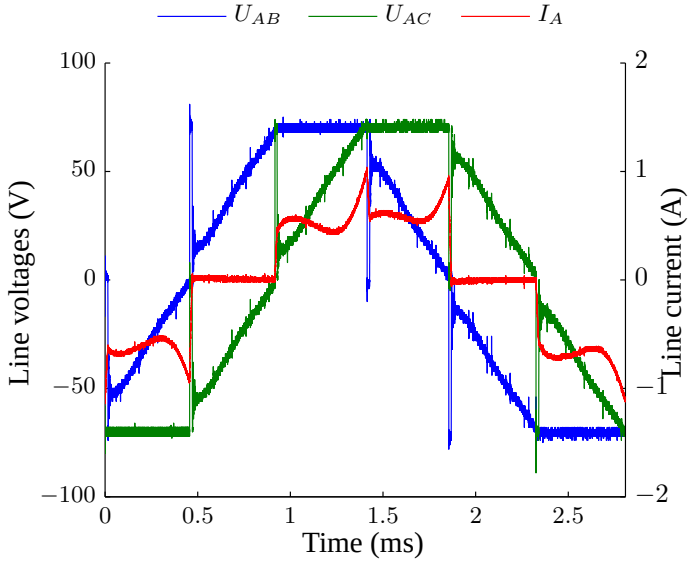

Figure 8.7: Current and line voltages in the internal star-point machine at 10,682 rpm

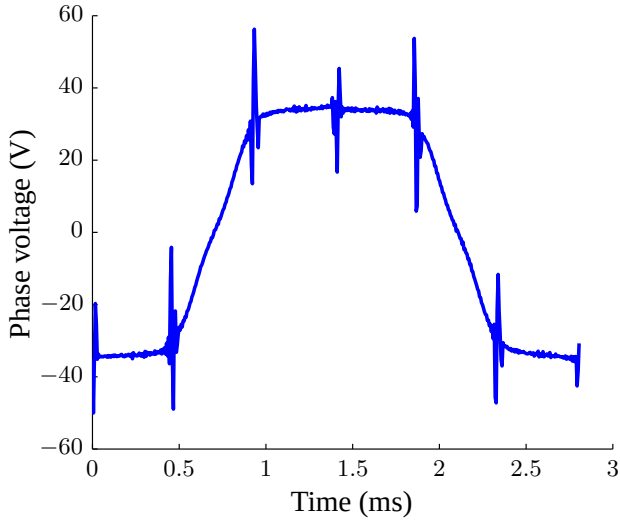

Figure 8.8: Calculated phase voltage of phase A

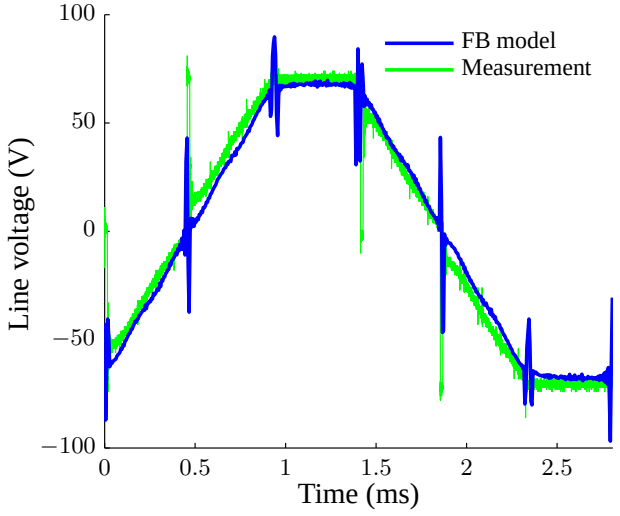

Figure 8.9: Voltage between phases A and B

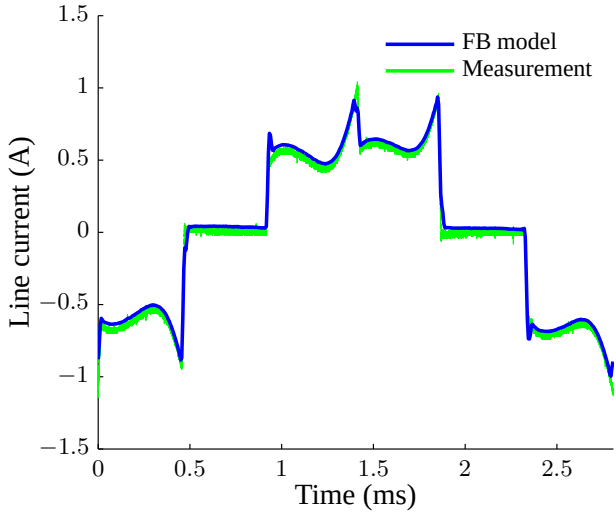

Figure 8.10: Current in phase A

8.3 Conclusion

In this chapter, the test setup that has been developed in the scope of this PhD was briefly introduced. It was also used to validate some of the calculations that were made earlier in this work; the calculation of the back EMF and the calculation of the phase currents. Although it was found that one of the setup's machines is faulty, a good agreement between the measurements and the calculations was obtained for the other machine. This indicates that the assumptions that were made in Section 3.2.3, e.g. neglecting saturation and end-effects, are valid.

Chapter 9

Parameter studies

The primary goal of this chapter is to gain more insight in the effect of the shielding cylinder on the torque and the eddy-current losses in high-speed PMSMs. To achieve that goal, a number of parameter studies will be performed, all of which focus on the two most important design variables of the SC; its thickness and its conductivity. The question is how these parameters affect the net torque, the torque ripple and the eddy-current losses. In order to gradually increase the discussion's complexity, the parameter studies are performed for three different sources; first a sinusoidal current source, then an idealized BLDC current and finally a BLDC voltage source.
Note that the studies performed in this chapter are merely theoretical; the studied machine is chosen to highlight the investigated phenomena, rather than to represent a realistic design. Moreover, the parameter ranges may extend to unrealistic values. As the goal is to identify trends and gain more insight in high-speed PMSMs in general, rather than to design an actual machine, that is not a problem.
In the first part of this chapter, i.e. in Section 9.1, the studied machine is introduced. The second part of this chapter discusses the actual parameter studies. This is done in Sections 9.2-9.4. Finally, Section 9.5 concludes this chapter by listing the most important observations that were made throughout the chapter.

The content of this chapter has been published in the following journal paper:

- B. Hannon, P. Sergeant and L. Dupré, "Study of the Effect of a Shielding Cylinder on the Torque in a Permanent-Magnet Synchronous Machine Considering Two Torque-Producing Mechanisms", *Magnetics, IEEE Transactions on*, in press, 2017

9.1 Studied machine

A cross section of the machine that will be used for the parameter studies is shown in Figure 9.1. The machine was chosen to have open slots and a single slot per pole and per phase. This will significantly increase the asynchronous harmonic content with respect to the prototype of Chapters 7 and 8. Although this makes the machine less realistic, it magnifies the physical phenomena that this chapter wants to investigate.

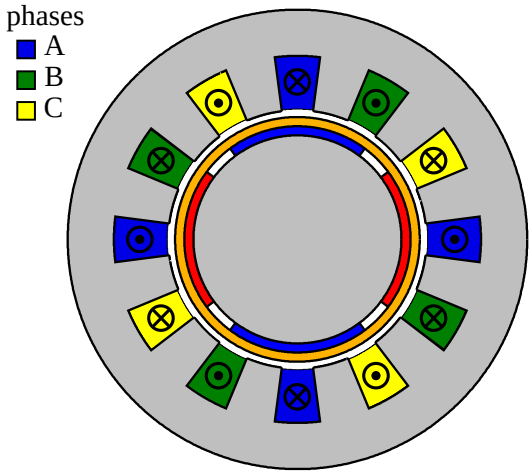

Figure 9.1: Cross-section of the studied machine

The parameters of the studied machine are listed in Table 9.1, where RY indicates the rotor yoke, PM the permanent magnets, SC the shielding cylinder, AG the air gap, SL the slots and SY the stator yoke.
Note that the subdomain numbering remains the same as in Figure 3.5. Quantities that relate to a subdomain are therefore indicated with the superscript of that subdomain. For example, the torque produced in the magnets is referred to as $T^{(2)}$.

Table 9.1: Parameters of the studied machine

Parameter	Symbol	Value
Number of slots	N_s	12
Number of pole pairs	p	2
Number of phases	m	3
Residual flux density of the magnets	B_m	1.20 T
Angular span of a magnet	ϕ_m	72.00°
Nominal current density (RMS)	J_{nom}	5.10^6 $\frac{\mathrm{A}}{\mathrm{m}^2}$
Number of windings per slot	N	10
Nominal frequency	f_{nom}	1000 Hz
Nominal speed	$n_{r,nom}$	30,000 rpm
Radius of the RY - PM boundary	r_1	22.50 mm
Radius of the PM - SC boundary	r_2	25.00 mm
Radius of the SC - AG boundary	r_3	26.50 mm
Radius of the AG - SL boundary	r_4	28.50 mm
Radius of the SL - SY boundary	r_6	40.40 mm
Radius of the SY external boundary	r_7	50.00 mm
Stack length	l_s	31.00 mm
Tooth opening angle	ε	15°
Permeability of the magnets	μ_{PM}	μ_0 $\frac{\mathrm{H}}{\mathrm{m}}$
Conductivity of the magnets	σ_{PM}	$6.94.10^5$ $\frac{\mathrm{S}}{\mathrm{m}}$
Permeability of the sleeve	μ_{SC}	μ_0 $\frac{\mathrm{H}}{\mathrm{m}}$
Conductivity of the sleeve	σ_{SC}	$4.83.10^7$ $\frac{\mathrm{S}}{\mathrm{m}}$

9.2 Sinusoidal current

In a first step, the machine is supplied with a three-phase sinusoidal current, imposed along the machine's direct axis. The current in phase A, which has an amplitude of 76.27 A, is shown in Figure 9.2 during one mechanical period.

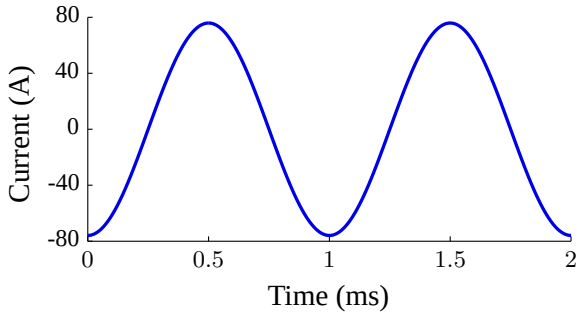

Figure 9.2: Current in phase A

Figure 9.3 shows a harmonic map of the magnetic flux density in the center of the air gap. It is important to note that the undersynchronous harmonic combinations dominate the oversynchronous ones. It can also be seen that the dominant asynchronous harmonic combinations are $(2, -10)$ and $(2, 14)$.

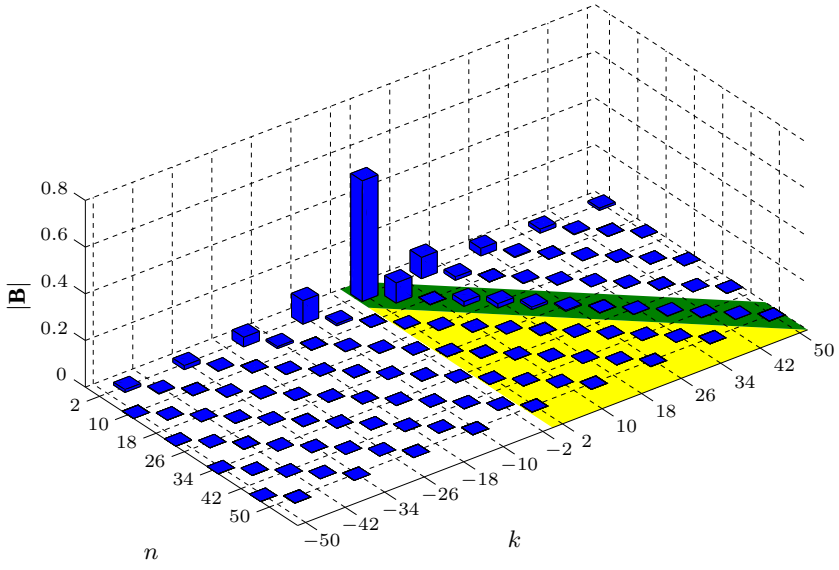

Figure 9.3: Harmonic map of $|\mathbf{B}|$ in the center of the air gap when a sinusoidal current is applied

9.2.1 Torque as a function of the SC's conductivity

This first study considers the torque as a function of the SC's conductivity. The latter is varied between 0 and 10^8 $\frac{\text{S}}{\text{m}}$ while maintaining the SC's thickness at 1.5 mm. The resulting evolution of the net torque is shown in Figure 9.4.

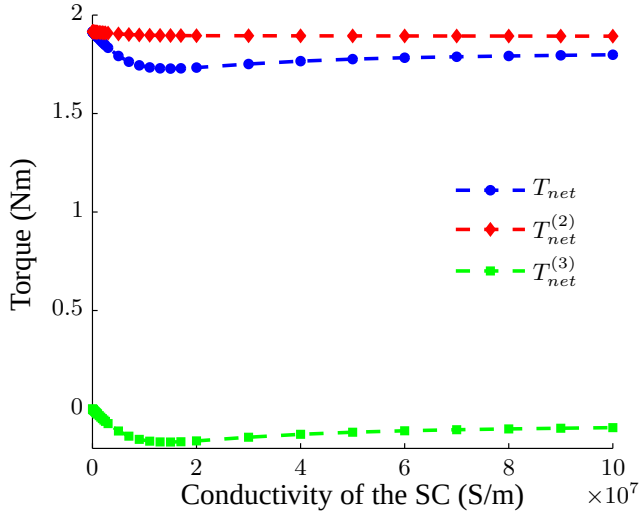

Figure 9.4: Net torque as a function of the σ_{SC}

Net torque in the magnets

At first sight, Figure 9.4 shows a constant $T_{net}^{(2)}$. As the synchronous harmonic combinations, which cause $T_{net}^{(2)}$ aren't expected to depend on σ_{SC}, this seems logical. However, when plotting $T_{net}^{(2)}$ separately, as done in Figure 9.5, it can be observed that $T_{net}^{(2)}$ does change. Indeed, initially $T_{net}^{(2)}$ shows a steep decrease. This decrease reduces around the point were the conductivity of the shielding cylinder is so that the penetration depth of the dominant asynchronous harmonic combinations, i.e. $(2, -10)$ and $(2, 14)$, equals the thickness of the shielding cylinder. This point is indicated as σ_δ.

By studying the harmonic combinations of the torque $\left(T_{n,s}^{(2)}\right)$ and the flux density at the outer radius of the magnets $\left(B_{r,n,k}^{(2)}(r_2) \text{ and } B_{\phi,n,k}^{(2)}(r_2)\right)$, an explanation for the evolution of $T_{net}^{(2)}(\sigma_{SC})$ can be found.

Firstly, it was noted that the evolution of $T_{net}^{(2)}$ is completely dominated by the changes in $T_{2,-2}^{(2)}$. The second most important variations are observed in $T_{6,-6}^{(2)}$, but

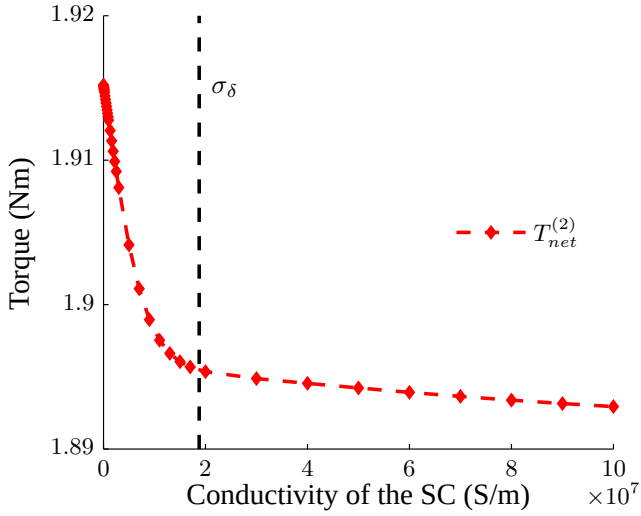

Figure 9.5: Net torque in the magnets as a function of the σ_{SC}, detail of Figure 9.4

they barely have an effect. Note that, evidently, the same changes are observed in the symmetric counterparts of the above-mentioned harmonic combinations, i.e. in $T_{-2,2}^{(2)}$ and $T_{-6,6}^{(2)}$. Moreover, as they are conjugates of the same complex Fourier series, those symmetric combinations ought to be considered together. Therefore, the following notation will be used in the rest of this chapter: $T_{|2,-2|}^{(2)} = T_{2,-2}^{(2)} + T_{-2,2}^{(2)}$. The evolution of $T_{|2,-2|}^{(2)}$ and $T_{|6,-6|}^{(2)}$, relative to the situation where $\sigma_{SC} = 0$, is shown in Figure 9.6(a).

Figure 9.6 clearly confirms that the variation of $T_{net}^{(2)}$ is mainly caused by the evolution of $T_{|2,-2|}^{(2)}$. After an initial decrease, $T_{|6,-6|}^{(2)}$ increases. However, this increase does not counter the decrease of $T_{|2,-2|}^{(2)}$.

Secondly, the changes in the harmonic content of the torque signal can be explained by studying the evolution of the related magnetic flux density harmonics, see (7.12). The synchronous harmonic combinations $\left(\mathbf{B}_{|2,-2|}^{(2)} \text{ and } \mathbf{B}_{|6,-6|}^{(2)}\right)$ determine the course of $T_{|2,-2|}^{(2)}$ and $T_{|6,-6|}^{(2)}$ respectively. Their evolution is depicted in Figures 9.6(b)-9.6(e). Note that it was not expected that these synchronous harmonic combinations would be affected by the conductivity of the shielding cylinder. The reason that they are is that, due to the slotting effect, all spatial-harmonic orders related to a single time-harmonic order are coupled, as was explained in Section 3.3.5. This implies that the effect σ_{SC} has on the asynchronous harmonic

combinations propagates to the synchronous combinations via the slotting effect. As the torque harmonics are the result of multiplying the r- and the ϕ-components of the magnetic flux density, their course is determined by the relative change of B_r and B_ϕ. Therefore, Figures 9.6(b)-9.6(e) do not only show the evolution of B_r and B_ϕ, they also differ between the component of the flux density that changes slower (dashed, grayed-out lined) and the component of the flux density that changes more quickly (colored, full line).

For example, the initial increase of $B^{(2)}_{r,|2,-2|}$ does not translate in an increasing $T^{(2)}_{|2,-2|}$ because $B^{(2)}_{\phi,|2,-2|}$ decreases faster. At higher σ_{SC}, the change of $B^{(2)}_{r,|2,-2|}$ does dominate the change of $B^{(2)}_{\phi,|2,-2|}$, but by then $B^{(2)}_{r,|2,-2|}$ is already decreasing.

Note that, although that isn't directly visible from Figure 9.6, $T^{(2)}_{|2,-2|}$ is positive while $T^{(2)}_{|6,-6|}$ is negative. Indeed, whereas $B^{(2)}_{r,|2,-2|}$ and $B^{(2)}_{\phi,|2,-2|}$ have the same sign, $B^{(2)}_{r,|6,-6|}$ and $B^{(2)}_{\phi,|6,-6|}$ have opposite signs. This also explains why the evolution of $B^{(2)}_{\phi,|6,-6|}$ is inverse to that of $T^{(2)}_{|6,-6|}$.

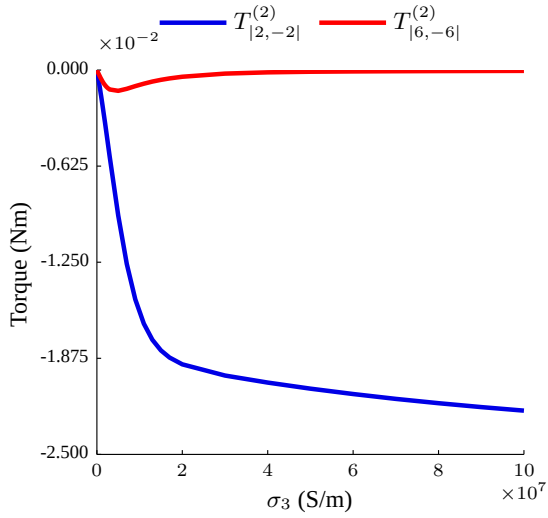

(a) Evolution of $T^{(2)}_{|2,-2|}$ and $T^{(2)}_{|6,-6|}$, relative to $\sigma_{SC} = 0$

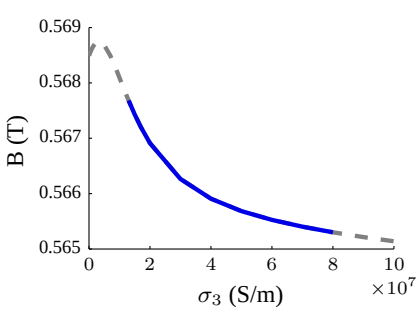

(b) $B^{(2)}_{r,|2,-2|}(r_2)$

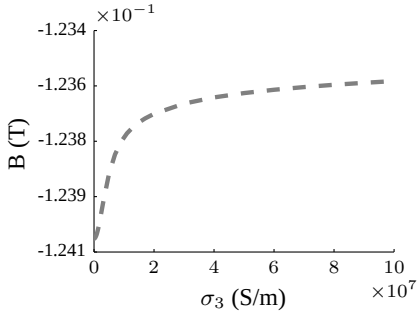

(c) $B^{(2)}_{r,|6,-6|}(r_2)$

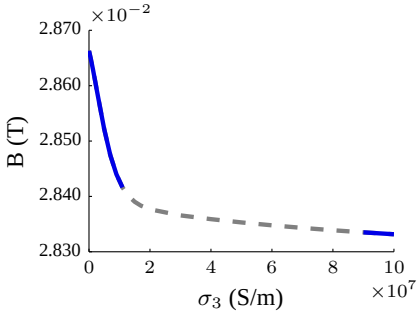

(d) $B^{(2)}_{\phi,|2,-2|}(r_2)$

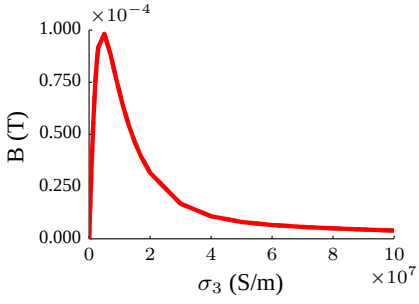

(e) $B^{(2)}_{\phi,|6,-6|}(r_2)$

Figure 9.6: Harmonic study of the net torque in the magnets, the component of **B** that changes more quickly is highlighted

Net torque in the shielding cylinder

The evolution of $T_{net}^{(3)}(\sigma_{SC})$ is plotted in Figure 9.7. Initially, an almost linear increase of its absolute value is noted. However, after reaching a maximum, $\left|T_{net}^{(3)}\right|$ becomes inversely proportional to $\sqrt{\sigma_{SC}}$. This evolution is very similar to the speed-torque characteristic of an induction machine [150] and can, qualitatively, be explained in a similar way. Indeed, as already mentioned, the shielding cylinder may be regarded as the rotor of a solid-rotor induction machine. This means that, for a given component of the magnetic field (n, k), the torque production in the SC depends on the stator resistance (R), the resistance of the SC (R_{SC}), the stator leakage inductance (L_{ls}), the rotor leakage inductance (L_{lr}), the magnetization inductance (L_m), the slip $(s_{n,k})$ and the pulsation $(\omega_{n,k})$ [150]:

$$T_{net,n,k}^{(3)} \sim \frac{R_{SC}}{\left(R + \left(1 + \frac{L_{ls}}{L_m}\right)\frac{R_{SC}}{s_{n,k}}\right)^2 + \omega_{n,k}^2\left(L_{ls} + \left(1 + \frac{L_{ls}}{L_m}\right)L_{lr}\right)^2} \tag{9.1}$$

The resistance of the SC is determined by Pouillet's law (9.2):

$$R_{SC} \sim \frac{l_s}{\sigma_{SC} t_{ec}} \tag{9.2}$$

with l_s the stack length and t_{ec} the radial thickness of the SC's part in which the eddy currents flow.
R_{SC} is therefore inversely proportional to σ_{SC} if t_{ec} can be assumed constant. However, the latter is only true for low σ_{SC}. At high conductivities, the skin effect is no longer negligible, t_{ec} is then not constant, but inversely proportional to $\sqrt{\sigma_{SC}}$. According to Pouillet's law, R_{SC} will then be inversely proportional to $\sqrt{\sigma_{SC}}$. The threshold value, after which R_{SC} may no longer be assumed inversely proportional to σ_{SC}, is the conductivity at which the penetration depth of the dominant asynchronous combinations (t_δ) equals the thickness of the SC.
At low conductivities of the shielding cylinder, R_{SC} will thus be high and will dominate the denominator of (9.1). Indeed:

$$R_{SC}\frac{1 + \frac{L_{ls}}{L_m}}{s_{n,k}} \gg R \tag{9.3a}$$

$$R_{SC}\frac{1 + \frac{L_{ls}}{L_m}}{s_{n,k}} \gg \omega_{n,k}\left(L_{ls} + \left(1 + \frac{L_{ls}}{L_m}\right)L_{lr}\right) \tag{9.3b}$$

Equation (9.1) can then be approximated as:

$$\begin{aligned} T_{net,n,k}^{(3)} &\sim \frac{R_{SC}}{\left(\left(1+\frac{L_{ls}}{L_m}\right)\frac{R_{SC}}{s_{n,k}}\right)^2} \\ &\sim \frac{1}{R_{SC}} \\ &\sim \begin{cases} \sigma_{SC} & \text{if } t_\delta > t_{SC} \\ \sqrt{\sigma_{SC}} & \text{if } t_\delta < t_{SC} \end{cases} \end{aligned} \tag{9.4}$$

Taking into account that, in this study, the point at which $t_\delta = t_{SC}$ is situated after the area in which $\left|T_{net}^{(3)}\right|$ increases, the above confirms the linear behavior at low σ_{SC} in Figure 9.7.
At high σ_{SC}, R_{SC} will be low and thus:

$$R_{SC}\frac{1+\frac{L_{ls}}{L_m}}{s_{n,k}} \ll R \tag{9.5}$$

Which implies that (9.1) can be approximated as:

$$\begin{aligned} T_{net,n,k}^{(3)} &\sim \frac{R_{SC}}{R^2+\omega_{n,k}^2\left(L_{ls}+\left(1+\frac{L_{ls}}{L_m}\right)L_{lr}\right)^2} \\ &\sim R_{SC} \\ &\sim \begin{cases} \dfrac{1}{\sigma_{SC}} & \text{if } t_\delta > t_{SC} \\ \dfrac{1}{\sqrt{\sigma_{SC}}} & \text{if } t_\delta < t_{SC} \end{cases} \end{aligned} \tag{9.6}$$

This shows that, at high σ_{SC}, $|T_{net}^{(3)}|$ will decrease proportionally to $\frac{1}{\sigma_{SC}}$ until $t_\delta = t_{SC}$ after which $\left|T_{net}^{(3)}\right|$ becomes proportional to $\frac{1}{\sqrt{\sigma_{SC}}}$. This is also confirmed by Figure 9.7, where it should be noted that the conductivity for which $t_\delta = t_{SC}$ is located in the transition area between an increasing and a decreasing $T_{net}^{(3)}$. This implies that, in this parameter study, only the decrease proportional to $\frac{1}{\sqrt{\sigma_{SC}}}$ is visible. A final remark is that the maximum of $\left|T_{net}^{(3)}\right|$ depends on the ratio between the resistances and the inductances and thus on the entire machine geometry.

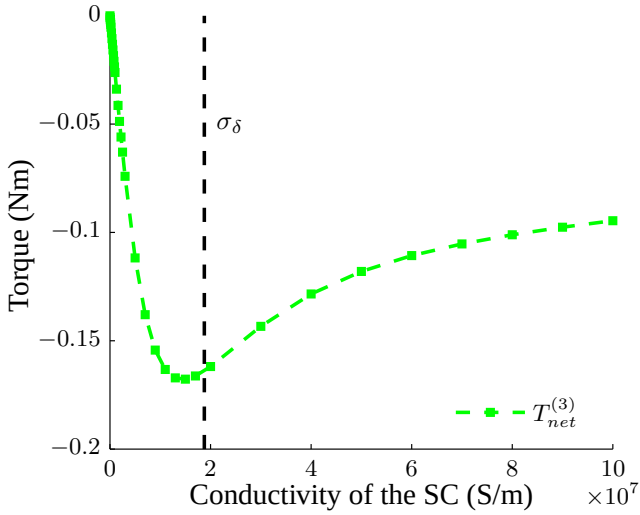

Figure 9.7: Net torque in the SC as a function of σ_{SC}, detail of Figure 9.4

Torque ripple

In Figure 9.8, the percentage torque ripple, as defined in (7.11) and (7.15b), is shown as a function of σ_{SC}.

It can be seen that there is a shift of the ripple from $T^{(2)}$ to $T^{(3)}$ when σ_{SC} is increased. This is explained by a stronger shielding effect. Note that the small increase at very low σ_{SC} is due to a stronger decrease of T_{net} than of $T^{(2)}$'s ripple. The total torque ripple is almost constant. The small variation of $\Delta T_{\%}$ is due to the variation of $T_{net}(\sigma_{SC})$. This is confirmed by Figure 9.9, which shows an evolution that is inverse to the evolution of $T_{net}(\sigma_{SC})$.

$\Delta T_{\%}^{(2)}(\sigma_{SC})$ shows an evolution that is similar to the evolution of $T_{net}^{(2)}(\sigma_{SC})$, but its maximum is shifted towards a lower value of σ_{SC}. The latter is due to the initial increase of $T_{net}(\sigma_{SC})$.

Overall, the evolution of $\Delta T_{\%}^{(3)}(\sigma_{SC})$ is as expected. The increase of σ_{SC} implies a better shielding effect which, in turn, translates in an increasing torque ripple. The increase stagnates when t_δ becomes smaller than t_{SC}, because at that moment the SC already blocks most of the asynchronous content.

Finally, it should be noted that the sum of $\Delta T_{\%}^{(2)}$ and $\Delta T_{\%}^{(3)}$ does not equal $\Delta T_{\%}$. This implies a time (Δt) shift between $T^{(2)}$ and $T^{(3)}$, as illustrated in Figure 9.10. The reason for Δt is the different nature of $T^{(2)}$ and $T^{(3)}$. $T^{(2)}$ will reach a maximum depending on the alignment of the magnets and the stator teeth, while $T^{(3)}$ reaches a maximum depending on the rate at which the magnetic field changes.

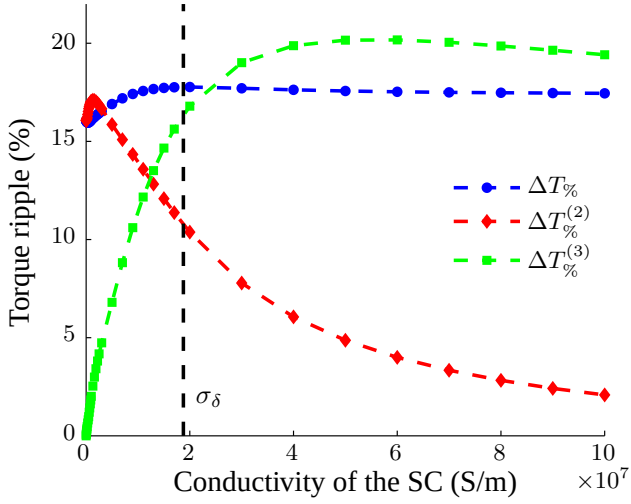

Figure 9.8: Torque ripple and its components as a function of σ_{SC}

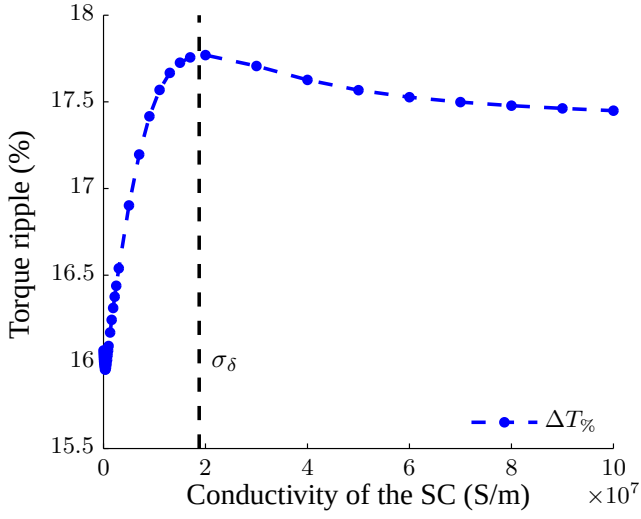

Figure 9.9: Total torque ripple as a function of σ_{SC}, detail of Figure 9.8

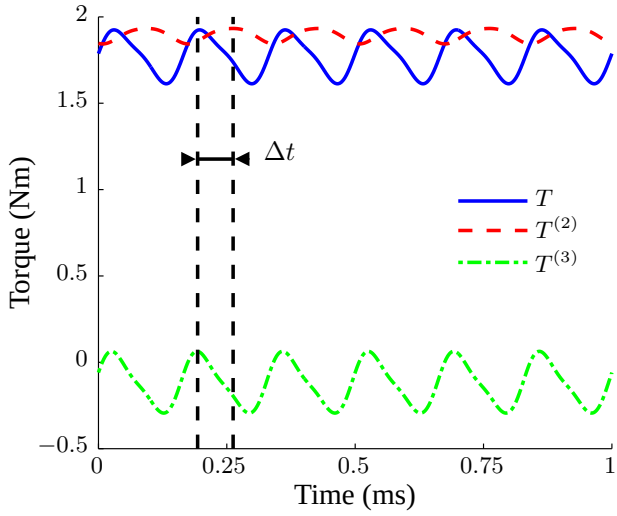

Figure 9.10: Torque and torque components as a function of time, $\sigma_{SC} = 4.83.10^7 \frac{\text{S}}{\text{m}}$

Conclusion

This first parameter study highlighted a number of interesting observations. Firstly, studying the net torque as a function of σ_{SC} showed that the torque in the SC indeed has the same characteristics as the torque in an induction machine. It was also shown that, unlike expected, $T^{(2)}$ does exhibit a dependency of σ_{SC}. Although this dependency might be considered negligible, it did lead to another interesting observation; via the slotting effect, the presence of a SC affects the magnetic field's synchronous components. In addition, study of the torque ripple learned that, although there is a shift of torque ripple from the magnets to the SC, the total torque ripple is almost constant. Moreover, Figure 9.10 showed that there is a time-shift between the torque in the magnets and the torque in the shielding cylinder. Finally, all of the above shows that there is a clear benefit to divide the torque in its components.

9.2.2 Torque as a function of the SC's thickness

In this study, the effect of the shielding cylinder's thickness ($t_{SC} = r_3 - r_2$) on the torque is analyzed. This is done by varying r_3 while r_2 is kept constant. To ensure a comparison that is as fair as possible, all of the other distances are kept constant. This implies that r_1 is constant while the variation of r_4, r_5 and r_6 is equal to the variation of r_2. None of the other parameters, listed in Table 9.1, are changed.

Net torque

The expectation is that the net torque will decrease when the thickness of the shielding cylinder is increased. Indeed, the net torque level is proportional to the average magnetic flux density, which, in turn, is inversely proportional to the thickness of the effective air gap ($t_{AG,eff}$). Obviously, $t_{AG,eff}$, which is determined by all the non-magnetic material between the stator and rotor iron, is affected when changing t_{SC}. The above would imply that the evolution of T_{net} as a function of t_{SC} can be predicted when the torque at a reference thickness is known:

$$T_{net}(t_{SC}) = T_{net}(t_{SC,ref}) \frac{t_{AG,eff,ref}(t_{SC,ref})}{t_{AG,eff}(t_{SC})} \tag{9.7}$$

Note that $t_{AG,eff}$ is not simply proportional to t_{SC}. The slotting effect has to be taken into account. This can be done using Carter's factor (k_c):

$$k_c = \frac{1}{1 - \tau_c \frac{N_s \delta}{2\pi}} \tag{9.8}$$

with:

$$\tau_c = \frac{2}{\pi} \left(\arctan \frac{w_s}{2t_{AG}} - \frac{2t_{AG}}{w_s} \ln \sqrt{1 + \left(\frac{w_s}{2t_{AG}} \right)^2} \right) \tag{9.9}$$

where t_{AG} is the combined thickness of the magnets, the SC and the air gap ($t_{AG} = r_4 - r_1$) and w_s is the width of the slots at the border with the air gap ($w_s = \delta r_4$). The thickness of the effective air gap can now be calculated as:

$$t_{AG,eff} = k_c t_{AG} \tag{9.10}$$

The expectation is thus that the evolution of $T_{net}(t_{SC})$ may be predicted using (9.7), where $t_{AG,eff}$ is calculated as in (9.10). In Figure 9.11 Carter's torque prediction, where the torque at $t_{SC} = 0$ was chosen as a reference, is depicted with a black line. The analytically calculated torque is indicated with blue dots.
It can be seen that there is a large deviation between Carter's torque prediction and the actual torque. The reason is that the prediction is not taking into account the torque production in the shielding cylinder. This can easily be validated by analyzing the torque components, as shown in Figure 9.12. An important observation is that (9.7) is now successfully used to predict $T_{net}^{(2)}$ while $T_{net}^{(3)}$ accounts for the difference between T_{net} and $T_{net}^{(2)}$.
Two effects determine the evolution of $T_{net}^{(3)}(t_{SC})$. First, an increasing t_{SC} results in a decrease of the SC's resistance, which in turn leads to higher eddy currents and thus a larger importance of $T_{net}^{(3)}$. Evidently, this effect will stagnate when $t_{SC} > \delta_{dom}$. On the other hand, $T_{net}^{(3)}$ also suffers from a larger effective air gap, which implies a decreasing importance of $T_{net}^{(3)}$ when increasing t_{SC}.

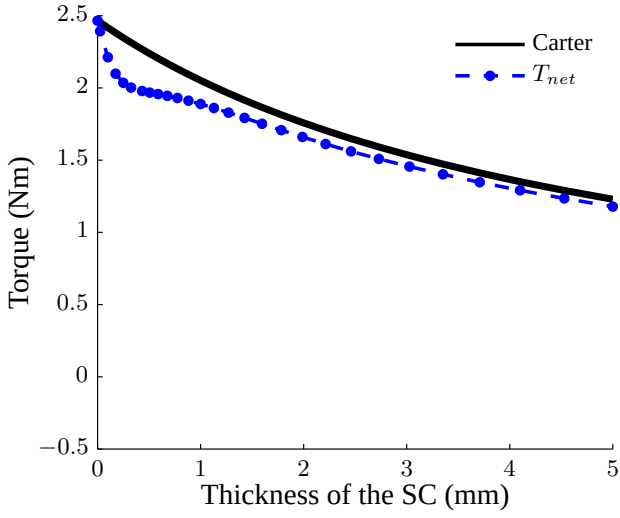

Figure 9.11: Comparison of the actual torque and its prediction by Carter

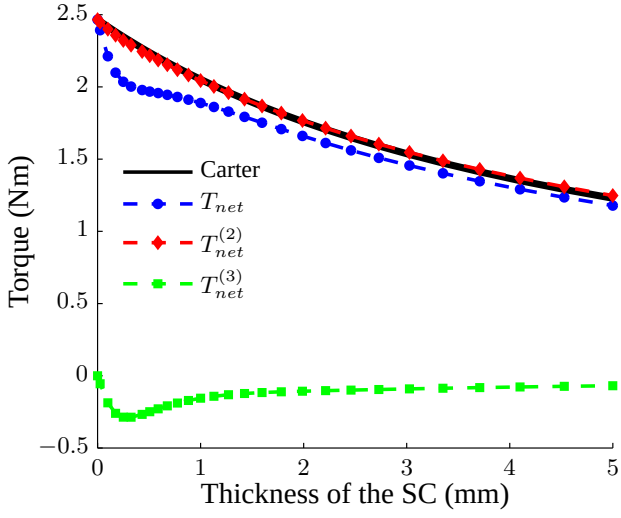

Figure 9.12: Evolution of torque and its components as a function of t_{SC}

Torque ripple

In Figure 9.13, the ratio of the torque ripple with respect to T_{net} is shown for the overall torque and its components. Initially, there is a minor increase of $\Delta T^{(2)}_{\%}$. This is because T_{net} decreases faster than $T^{(2)}$'s ripple. After this small increase, the effect of the SC is clearly illustrated; the amount of ripple in $T^{(2)}$ strongly decreases because of a higher shielding effect and a larger effective air gap.
The evolution of $\Delta T^{(3)}_{\%}(t_{SC})$ is similar to the evolution of $T^{(3)}_{net}(t_{SC})$. However, the thickness related to its maximum may be different, depending on the evolution of $T_{net}(t_{SC})$.

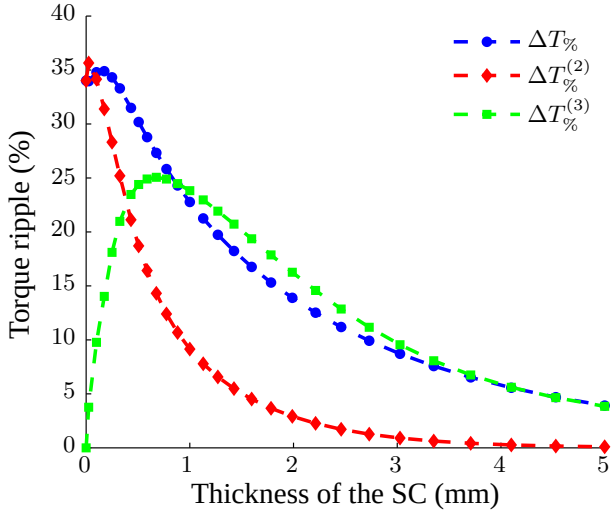

Figure 9.13: Evolution of the torque ripple as a function of t_{SC}

Conclusion

Studying the torque at various thicknesses of the shielding cylinder has again illustrated that considering the torque components helps to get a better understanding of the machine's physics. For the net torque level for example, it was shown that $T^{(2)}$ evolves in accordance with Carter's factor, as expected from a classical synchronous machine. This is not true for $T^{(3)}$, which explains why the evolution of T does not meet the initial expectations.

9.2.3 Eddy-current losses as a function of the SC's conductivity

For this study, the conductivity of the shielding cylinder is again varied between 0 and $10^8 \frac{\mathrm{S}}{\mathrm{m}}$. However, instead of studying the torque, the eddy-current losses in the machine are analyzed. The result is shown in Figure 9.14.

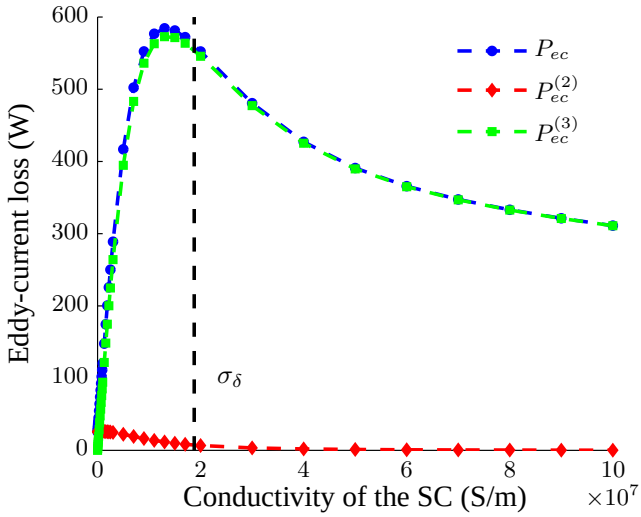

Figure 9.14: Evolution of the eddy-current losses in function of σ_{SC}

The eddy-current losses in the shielding cylinder, which are proportional to J_{SC}^2 and inversely proportional to σ_{SC}, demonstrate a strong initial increase as the eddy currents in the shielding cylinder increase. However, once the penetration depth of the dominant asynchronous harmonics becomes smaller than the thickness of the shielding cylinder, i.e. $\sigma_{SC} > \sigma_\delta$, the increase of the eddy currents stagnates. The continued increase of σ_{SC} will then result in a decrease of the eddy-current losses. As the conductivity of the shielding cylinder already exceeds σ_δ, that decrease is inversely proportional to the square root of σ_{SC}.
Figure 9.14 also illustrates that the shielding cylinder effectively shields the magnets; $P_{ec}^{(2)}$ strongly decreases if σ_{SC} is increased. However, this decrease is completely countered by a much stronger increase of $P_{ec}^{(3)}$. This means that, at least under sinusoidal stator currents, the losses in the magnets are so low that their reduction doesn't compensate for the additional losses in the shielding cylinder.

9.2.4 Eddy-current losses as a function of the SC's thickness

The last parameter study with a sinusoidal current considers the eddy-current losses as a function t_{SC}. The results are presented in Figure 9.15.

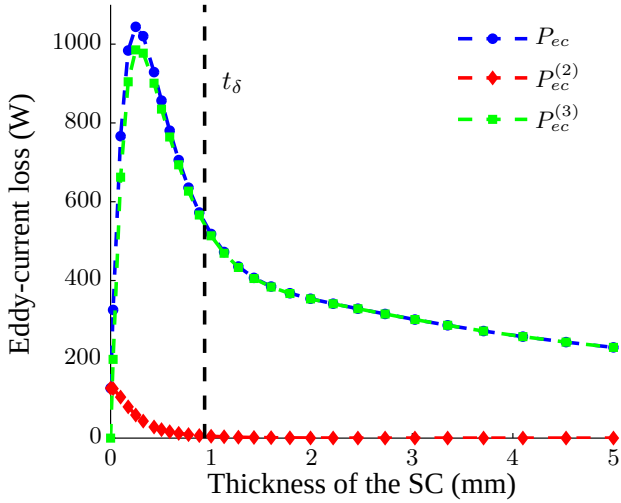

Figure 9.15: Evolution of the eddy-current losses in function of t_{SC}

Similar to varying σ_{SC}, the losses in the shielding cylinder show an initial increase due to higher eddy-currents. However, they start decreasing before the thickness of the shielding cylinder equals the penetration depth of the dominant asynchronous combinations, i.e. $t_{SC} = t_\delta$. The reason is that, in addition to the reduced resistance of the shielding cylinder, increasing the effective air gap reduces the eddy-current losses. Indeed, as the air gap grows, the effect of asynchronous harmonic combinations that are related to the slotting effect decreases.

9.2.5 Conclusion

In this section, the torque and the eddy currents were evaluated while imposing a sinusoidal current. This led to a number of interesting observations. First of all, dividing the torque in its components has proven very useful to gain insight in PMSMs with a SC. It has, for example, confirmed that the torque production in the SC is similar to that in an induction machine. It also enabled observing a relation between σ_{SC} and the net torque in the magnets. This was unexpected, as it implies that the synchronous harmonic combinations depend on the shielding cylinder's conductivity. Another interesting observation is that, when the importance of harmonic combinations with a high time-harmonic order is small, adding a SC may increase the machine's eddy-current losses instead of decreasing them.

9.3 Ideal BLDC current

In this section, the sinusoidal current is replaced by a trapezoidal current, i.e. the idealized current of a brushless DC control. To reduce excessive voltage peaks, slopes of 10° electric are foreseen. In order to obtain the same RMS value as in Section 9.2, the peak value of the applied current is set to 66.56 A. Figure 9.16 shows the current in phase A during one mechanical period.

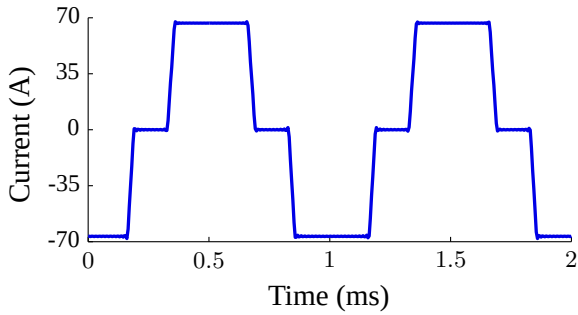

Figure 9.16: Current in phase A

Figure 9.17 shows a harmonic map of the magnetic flux density in the center of the air gap. Just like for the sinusoidal current, the dominant asynchronous harmonic combinations are $(2, -10)$ and $(2, 14)$. However, the harmonic content of higher time-harmonic orders is considerably larger. Especially combinations $(10, -2)$ and $(14, 2)$, which are indicated in red, are important.

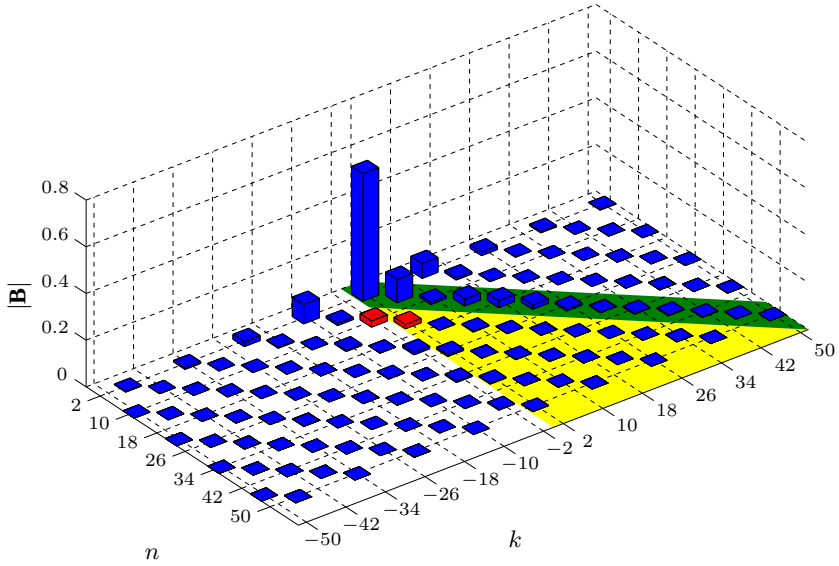

Figure 9.17: Harmonic map of $|\mathbf{B}|$ in the center of the air gap when an idealized BLDC current is applied

9.3.1 Torque as a function of the SC's conductivity

Except for the trapezoidal stator current, this parameter study is identical to the one in Section 9.2.1.

Net torque

The net torques, as plotted in Figure 9.18, show a very similar course as when the machine is excited with a sinusoidal current. However, Figure 9.19 shows $T^{(2)}_{net}$ separately, demonstrating an initial increase before decreasing. The course of $T^{(2)}_{net}$ can be explained in a similar way as when a sinusoidal current is applied. However, now $T^{(2)}_{|2,-2|}$ and $T^{(2)}_{|14,-14|}$ are the two most important torque harmonics. Moreover, at very low conductivities ($\sigma_{SC} < 6.10^5$), the variation of $T^{(2)}_{|14,-14|}$ dominates that of $T^{(2)}_{|2,-2|}$. As $T^{(2)}_{|14,-14|}$ increases at these low conductivities, so does $T^{(2)}_{net}$. This is illustrated in Figure 9.20.
Note that, as the current does not contain any 6^{th} harmonics, $T^{(2)}_{|6,-6|}$ remains unchanged with respect to Section 9.2.

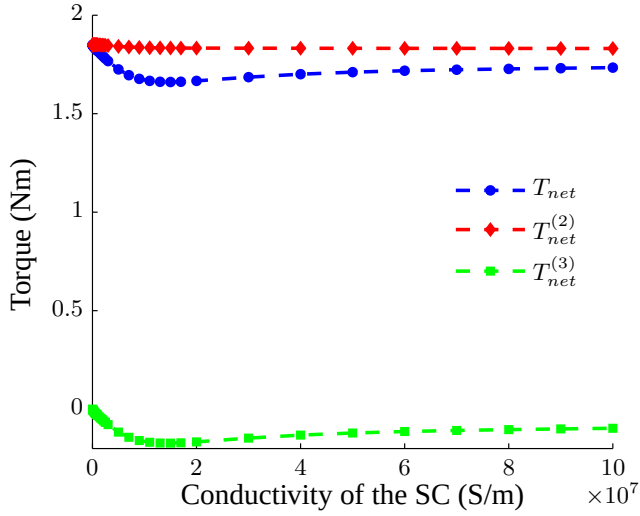

Figure 9.18: Torque as a function of σ_{SC}

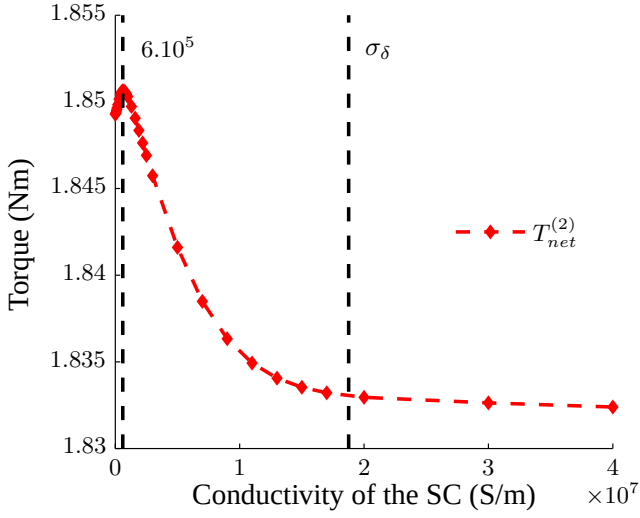

Figure 9.19: Torque in the magnets as a function of σ_{SC}, detail of Figure 9.18

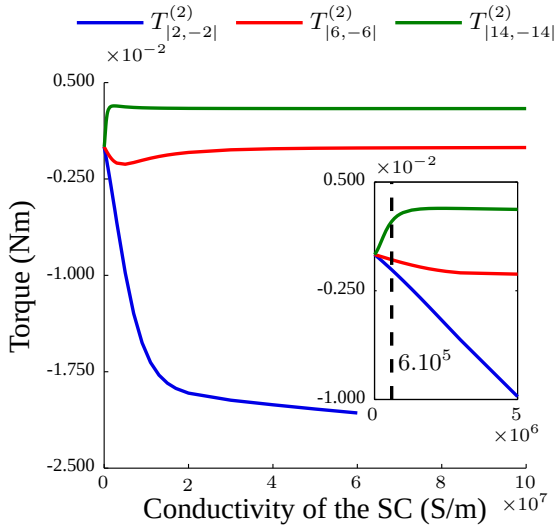

(a) Evolution of $T^{(2)}_{|2,-2|}$ and $T^{(2)}_{|6,-6|}$, relative to $\sigma_{SC} = 0$

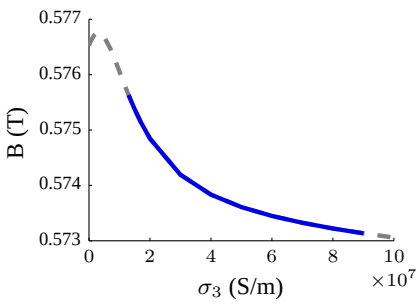

(b) $B_{r,|2,-2|}$

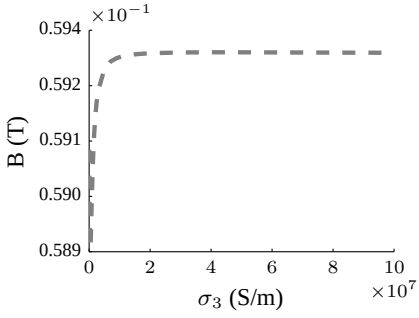

(c) $B_{r,|14,-14|}$

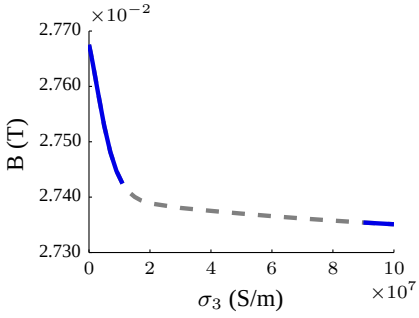

(d) $B_{\phi,|2,-2|}$

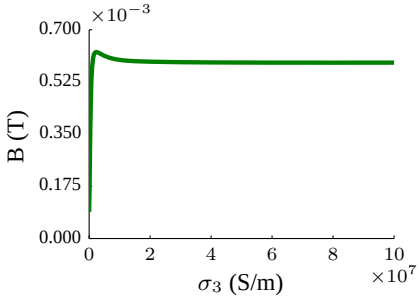

(e) $B_{\phi,|14,-14|}$

Figure 9.20: Harmonic study of the net torque in the magnets, the component of **B** that changes more quickly is highlighted

Torque ripple

As can be seen in Figure 9.21, the evolution of the torque ripple does show significant differences with that of the sinusoidal current in Figure 9.8. This is of course due to a more important presence of asynchronous harmonic combinations in the field. The evolution of $\Delta T_{\%}^{(2)}$, for example, shows an initial decrease until $\sigma_{SC} = 6.10^5 \frac{\text{S}}{\text{m}}$. After this local minimum, the torque ripple briefly increases before it steadily decreases again. A detail of this behavior is shown in Figure 9.22.

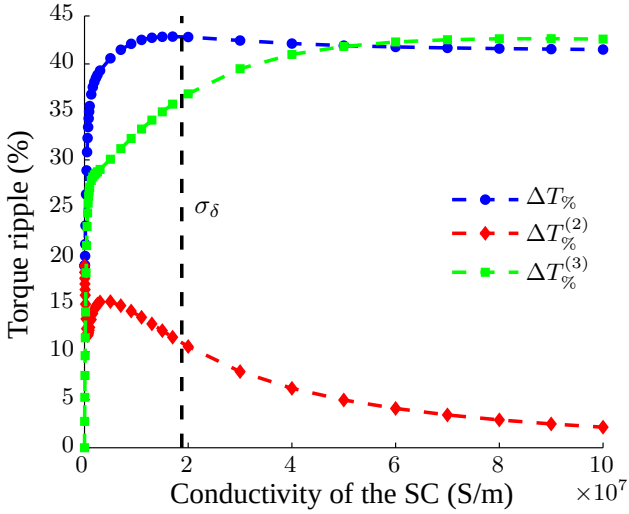

Figure 9.21: Torque ripple as a function of σ_{SC}

The reason for $\Delta T_{\%}^{(2)}$'s initial decrease is that some of the asynchronous combinations with higher time-harmonic order, e.g. $(10, -2)$ and $(14, 2)$, are already greatly shielded when $\sigma_{SC} = 6.10^5 \frac{\text{S}}{\text{m}}$. This is earlier than expected; according to (7.1), the conductivity at which the penetration depth of $(10, -2)$ and $(14, 2)$ equals t_{SC} is $1.88.10^7 \frac{\text{S}}{\text{m}}$, as illustrated by the $\sigma_{SC} = \sigma_\delta$ line in Figure 9.22. However, Figure 9.28 in Section 9.3.3 indeed confirms this much lower penetration depth. Note that the quick shielding of combinations $(10, -2)$ and $(14, 2)$ also explains the very steep initial increase of $\Delta T_{\%}^{(3)}$.
The brief increase that follows is mainly due to the evolution of $\mathbf{B}_{|6,-6|}$. Although this component of the flux density gets shielded more effectively at higher σ_{SC}, initially its decrease is entirely due to the decrease of its radial component. At low σ_{SC}, its angular component increases. Moreover, proportionally, this increase is larger than the decrease of the radial component. The result is an increasing $\Delta T_{\%}^{(2)}$.

Once the SC's conductivity exceeds the point at which the penetration depth of $(6, -6)$ equals t_{SC}, the angular component starts decreasing as well. Note that, as already mentioned, the behavior of this asynchronous combination propagates to the synchronous combination with the same time-harmonic order, i.e. $(6, 6)$. The above described evolution can therefore, indirectly, be observed in Figure 9.6.

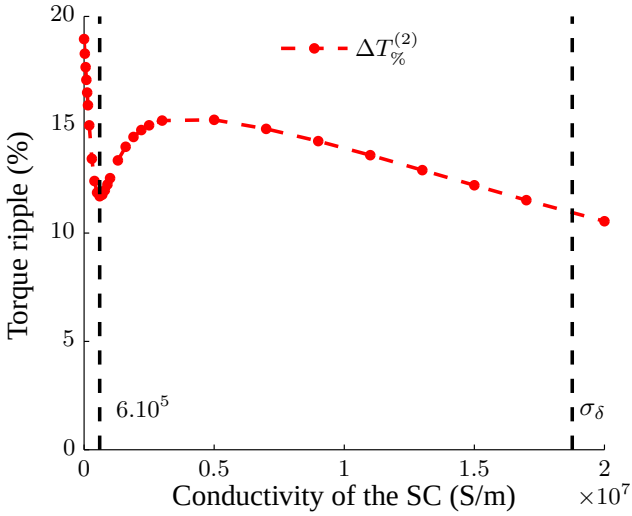

Figure 9.22: Torque ripple in the magnets as a function of σ_{SC}, detail of Figure 9.21

Conclusion

First of all, the above parameter study proved that accounting for higher time-harmonic orders is important. Although their effect on the net torque is limited, the torque ripple is definitely affected. Another important note is that harmonic combinations with a higher time-harmonic order have a much smaller penetration depth than originally expected.

9.3.2 Torque as a function of the SC's thickness

As in Section 9.2.2, in this study the conductivity is kept constant at $4.83.10^7$ $\frac{\text{S}}{\text{m}}$ while varying t_{SC} between 0 and 5 mm.

Net torque

As shown in Figure 9.23, the evolution of the net torque is entirely similar to that in Section 9.2.2. $T_{net}^{(2)}$ is again accurately predicted using Carter's factor, while $T_{net}^{(3)}$ accounts for the deviation between Carter's prediction and T_{net}.

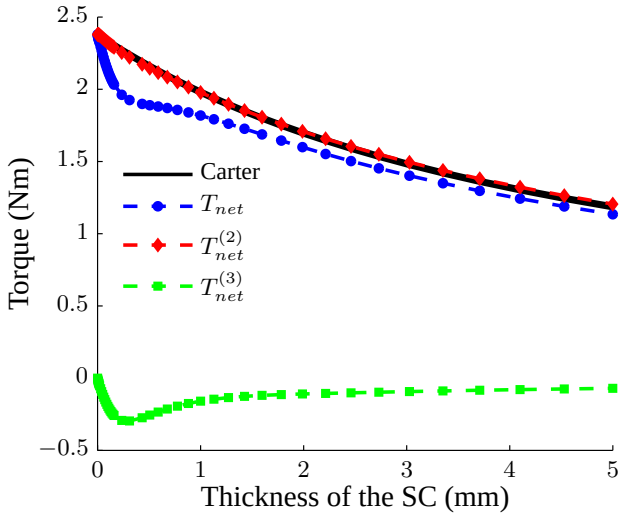

Figure 9.23: Torque as a function of t_{SC}

Torque ripple

The torque ripples as a function of t_{SC} are shown in Figure 9.24. These ripples are subject to the same mechanisms as in the Section 9.3.1. The shielding of harmonic combinations $(10, -2)$ and $(14, 2)$ at $t_{SC} = 0.01$ mm explains the initial decrease of $\Delta T_{\%}^{(2)}$ and the very steep increase of $\Delta T_{\%}^{(3)}$. $\Delta T_{\%}^{(2)}$ then increases again until $(6, -6)$ is effectively shielded.

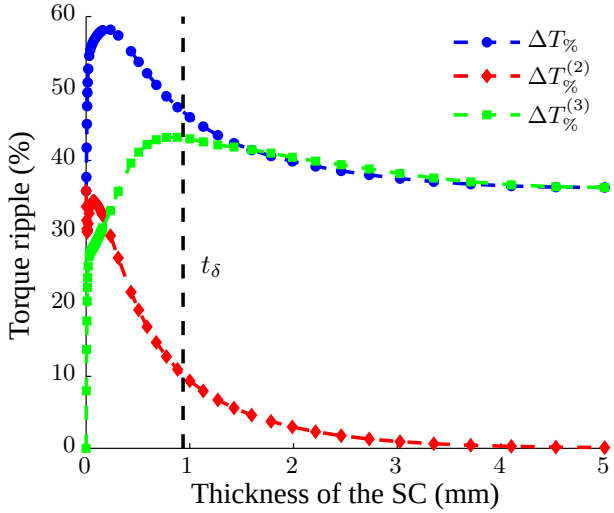

Figure 9.24: Torque ripple as a function of t_{SC}

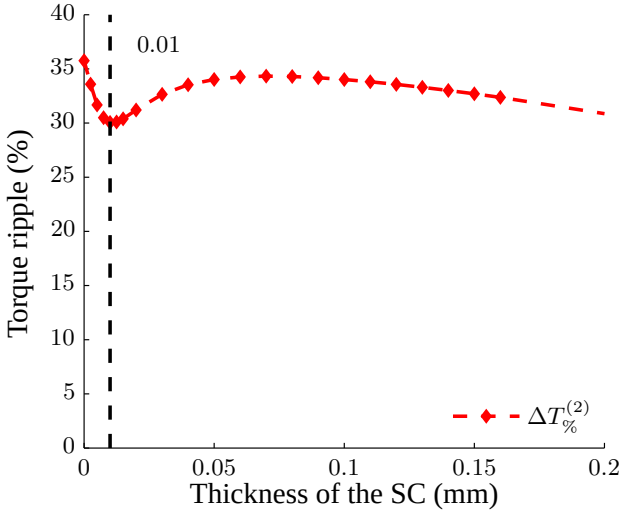

Figure 9.25: Torque ripple in the magnets as a function of t_{SC}, detail of Figure 9.24

9.3.3 Eddy-current losses as a function of the SC's conductivity

The eddy-current losses are plotted as a function of σ_{SC} in Figure 9.26. It can readily be seen that the losses in the magnets are much larger than when a sinusoidal current is applied, as in Figure 9.14. This indicates that the effect of harmonic combinations with higher time-harmonic orders is large. However, those losses quickly reduce if the conductivity of the SC is increased. Indeed, as already discussed in Section 9.3.1, the penetration depth of those harmonic combinations is very small.

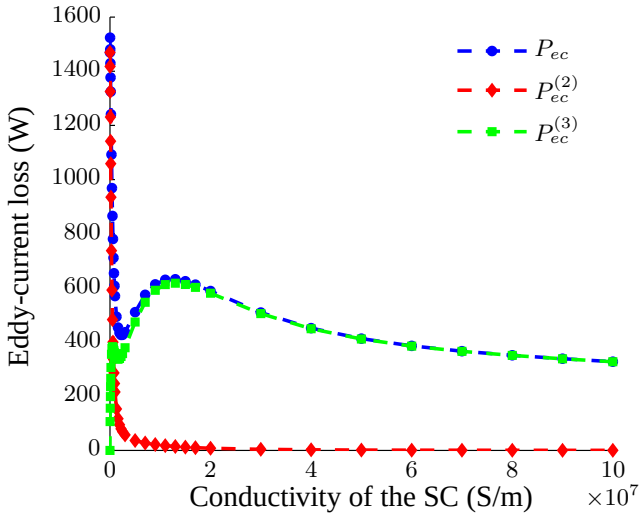

Figure 9.26: Eddy-current losses as a function of σ_{SC}

Figure 9.27 shows a zoom of $P_{ec}^{(3)}(\sigma_{SC})$. One can see that $P_{ec}^{(3)}(\sigma_{SC})$ has a much more capricious course than when a sinusoidal current is applied, reaching two local maxima before finally decreasing steadily. To explain this behavior, the harmonic content of $P_{ec}^{(3)}$ has been evaluated. As shown in Figure 9.28(a), it was found that the combined effect of $P_{|2,-2|}^{(3)}$, $P_{|10,-10|}^{(3)}$, $P_{|14,-14|}^{(3)}$, $P_{|22,-22|}^{(3)}$ and $P_{|26,-26|}^{(3)}$ determines the course of $P_{ec}^{(3)}(\sigma_{SC})$. As long as $\sigma_{SC} < 5.10^5$ $\frac{\text{S}}{\text{m}}$, the increase of $P_{|2,-2|}^{(3)}$, $P_{|10,-10|}^{(3)}$ and $P_{|14,-14|}^{(3)}$ dominates, even as $P_{|22,-22|}^{(3)}$ and $P_{|26,-26|}^{(3)}$ start descending. It is only after $P_{|10,-10|}^{(3)}$ and $P_{|14,-14|}^{(3)}$ have reached a maximum that the continued increase of $P_{|2,-2|}^{(3)}$ is, temporary, overruled. As σ_{SC} exceeds $1.6.10^6$ $\frac{\text{S}}{\text{m}}$, the increase of $P_{|2,-2|}^{(3)}$ will again dominate the evolution of $P_{ec}^{(3)}$. Resulting in an increase of $P_{ec}^{(3)}$. $P_{ec}^{(3)}$ only starts to decrease again after

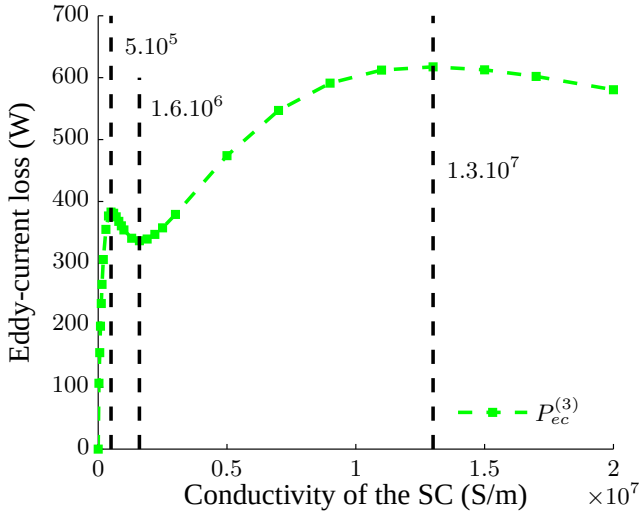

Figure 9.27: Eddy-current losses in the shielding cylinder as a function of σ_{SC}, detail of Figure 9.26

$1.3.10^7$ $\frac{\text{S}}{\text{m}}$, i.e. when $P_{|2,-2|}^{(3)}$ decreases again.

An explanation for the evolution of the eddy-current harmonics is to be found in the evolution of their corresponding electric field, $E(r_3)$, and angular flux density, $B_\phi(r_3)$, components, see (7.22). For each eddy-current loss harmonic, the dominant harmonic combination of $E(r_3)$ and $B_\phi(r_3)$ is sketched in Figures 9.28(b)-9.29(k). These figures also indicate which of both $(E(r_3)$ or $B_\phi(r_3))$ dominates the evolution of the corresponding torque harmonic.

Finally, Figures 9.28(b)-9.29(k) also show the conductivity at which the penetration depth of the considered harmonic combination equals the thickness of the shielding cylinder according to (7.1) and the conductivity at which the corresponding power harmonic reaches its maximum. These conductivities are indicated as σ_δ and σ_n respectively, where n is the time-harmonic order of the considered harmonic combination. The above illustrates what was found earlier in Section 9.3.1; the penetration depth of asynchronous combinations with higher time-harmonic orders cannot be predicted using (7.1).

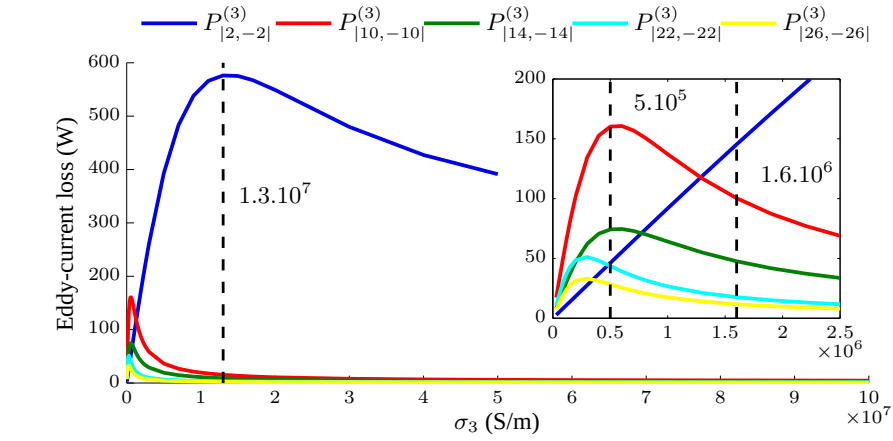

(a) Evolution of eddy-current loss harmonics as a function of σ_{SC}

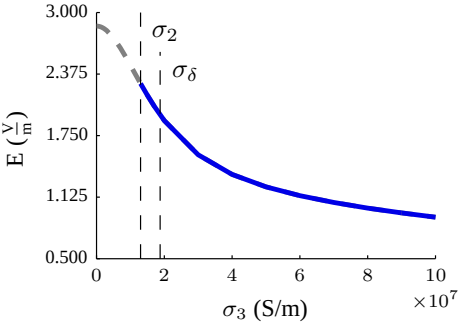

(b) $E_{|2,14|}$

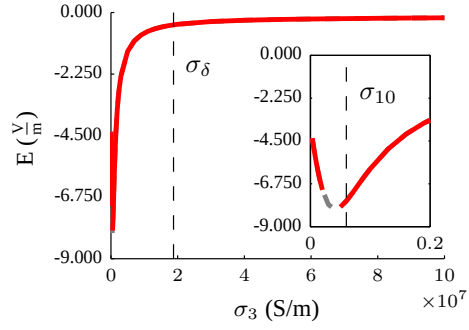

(c) $E_{|-10,2|}$

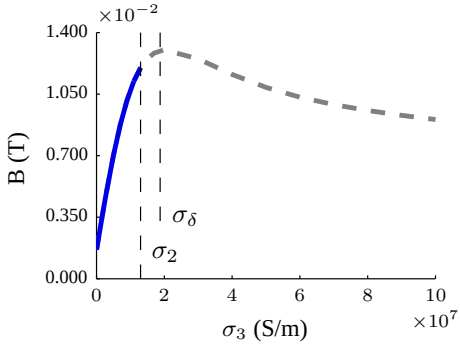

(d) $B_{\phi,|2,14|}$

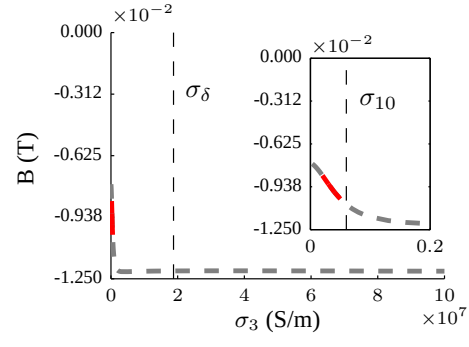

(e) $B_{\phi,|-10,2|}$

Figure 9.28: Harmonic study of $T^{(2)}_{net}(\sigma_{SC})$

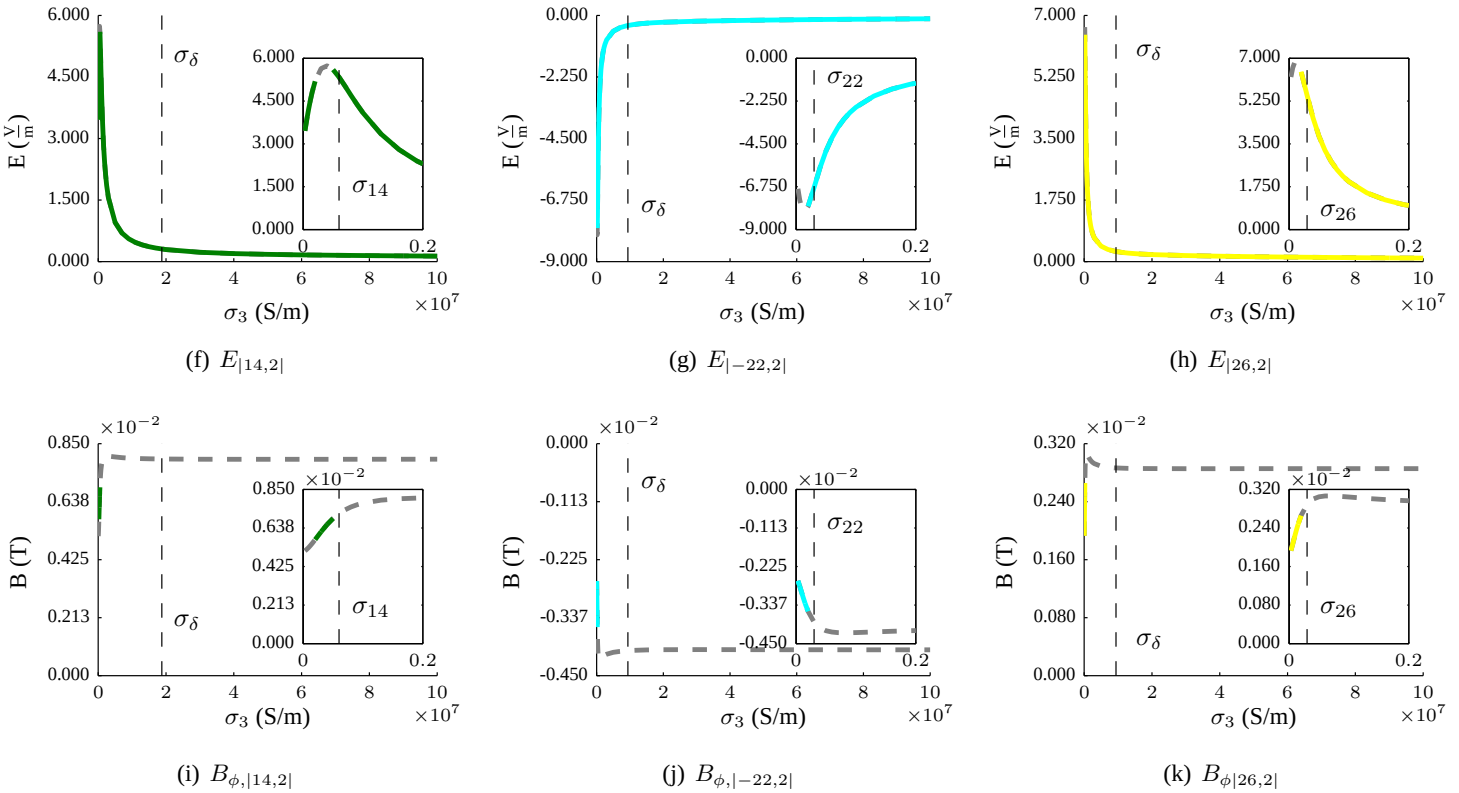

(f) $E_{|14,2|}$ (g) $E_{|-22,2|}$ (h) $E_{|26,2|}$

(i) $B_{\phi,|14,2|}$ (j) $B_{\phi,|-22,2|}$ (k) $B_{\phi|26,2|}$

Figure 9.28: Harmonic study of $T^{(2)}_{net}(\sigma_{SC})$

9.3.4 Eddy-current losses as a function of the SC's thickness

The last parameter study with the idealized BLDC current analyzes the eddy-current loss as a function of t_{SC}. The results, shown in Figure 9.29, are similar to the results from the previous section. The same harmonic combinations determine the evolution of $P_{ec}^{(3)}$, which is shown in more detail in Figure 9.30. However, in addition to the shielding effect, now the variation of the effective air gap plays an important role as well.

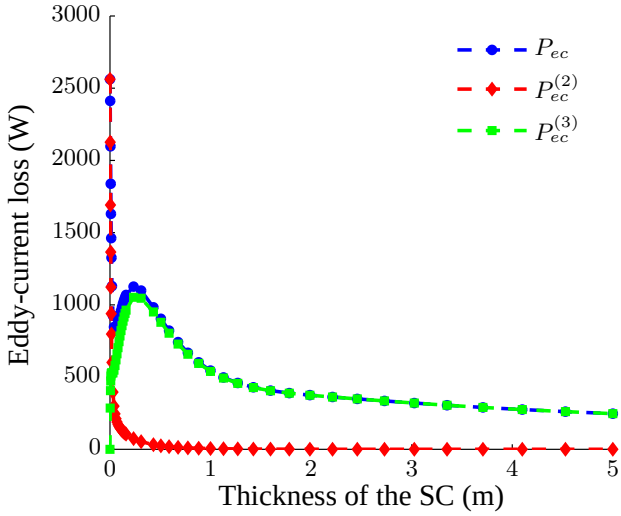

Figure 9.29: Eddy-current losses as a function of t_{SC}

9.3.5 Conclusion

As a conclusion of the parameter studies in which an idealized BLDC current is imposed, it can be stated that accounting for higher harmonics in the currents is very important. Indeed, both the torque ripple and the eddy-current losses exhibit significant differences with respect to the parameter studies of Section 9.2. In addition, it was found that the penetration depth of harmonic combinations with higher time-harmonic orders cannot be predicted accurately using (7.1). This section also presented an interesting discussion on the evolution of the eddy-current losses in the SC as a function of σ_{SC}. Especially Figure 9.28 provides a lot of insight in how $P_{ec}^{(3)}$ evolves.

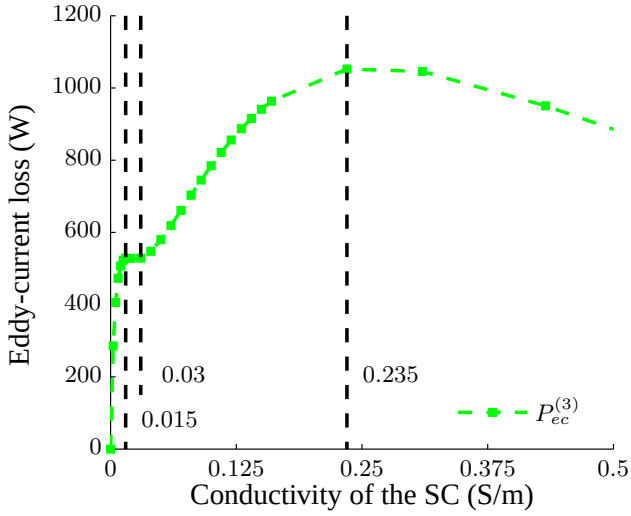

Figure 9.30: Eddy-current losses in the shielding cylinder as a function of t_{SC}, detail of Figure 9.29

9.4 BLDC voltage

In the final set of parameter studies, a pulse-amplitude modulated BLDC voltage, i.e. voltage blocks of 120° electrical, are imposed. The peak value (52.65 V) and time shift of these blocks are chosen so that the resulting current density aligns with the back EMF and has a RMS value of 5.10^6 $\frac{\mathrm{A}}{\mathrm{m}^2}$ when the machine's parameters are as in Figure 9.1 and Table 9.1. The phase voltage is shown in Figure 9.31(a). As indicated, the first switch occurs at 39.71°. The current, resulting from the imposed voltage is shown in Figure 9.31(b). It can readily be seen that the harmonic content of this current is much less dominant than that of the trapezoidal current in Section 9.3.
Figure 9.32 shows a harmonic map of the magnetic flux density in the center of the air gap.

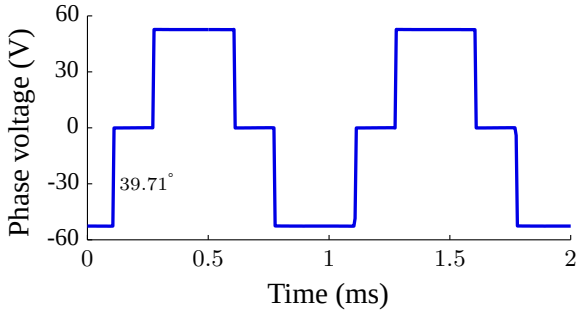

(a) Phase voltage in phase A

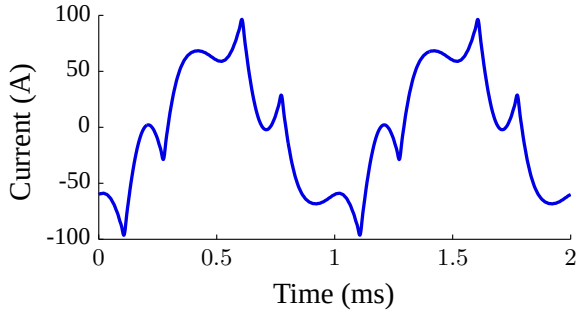

(b) Current in phase A

Figure 9.31: Current and voltage of phase A

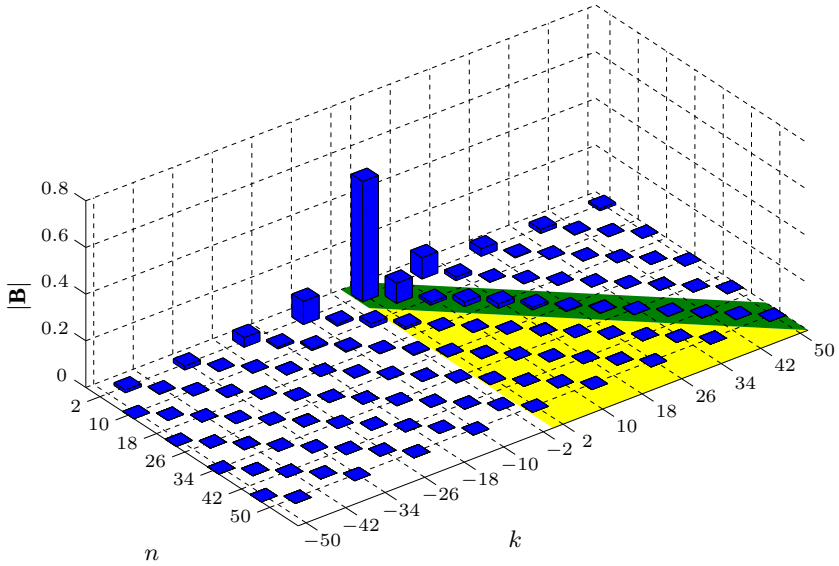

Figure 9.32: Harmonic map of $|\mathbf{B}|$ in the center of the air gap when a BLDC voltage is applied

9.4.1 Torque as a function of the SC's conductivity

This parameter study is a repetition of the studies that were performed in Sections 9.2.1 and 9.3.1, but now the voltage of Figure 9.31(a) is imposed.

Net torque

One can see from 9.33 that the net torque in the magnets behaves differently than in Sections 9.2.1 and 9.3.1. As shown in more detail in Figure 9.34, $T_{net}^{(2)}$ now changes more drastically and increases instead of decreasing.
The reason is that, in addition to the indirect effect of the SC on the synchronous harmonic combinations, the SC's conductivity also affects the current through the windings. Indeed, it has an effect on the machine's inductance. As the voltage is now fixed, varying σ_{SC} implies changing the current. Evidently, this affects the torque in the magnets as well. The evolution of the RMS value of the current density in phase A is shown in Figure 9.35. Note that the effect of the dominant harmonic combination's penetration depth can clearly be seen.

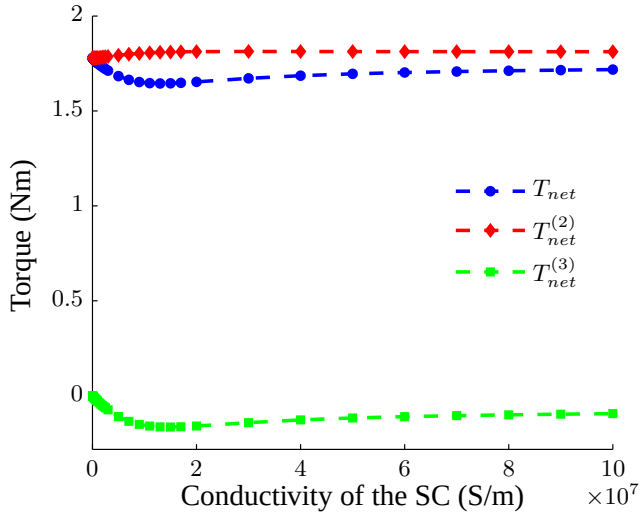

Figure 9.33: Torque as a function of σ_{SC}

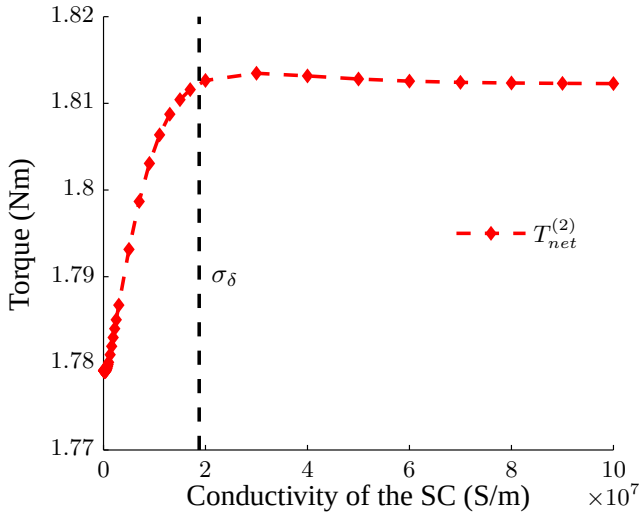

Figure 9.34: Torque in the magnets as a function of σ_{SC}, detail of Figure 9.33

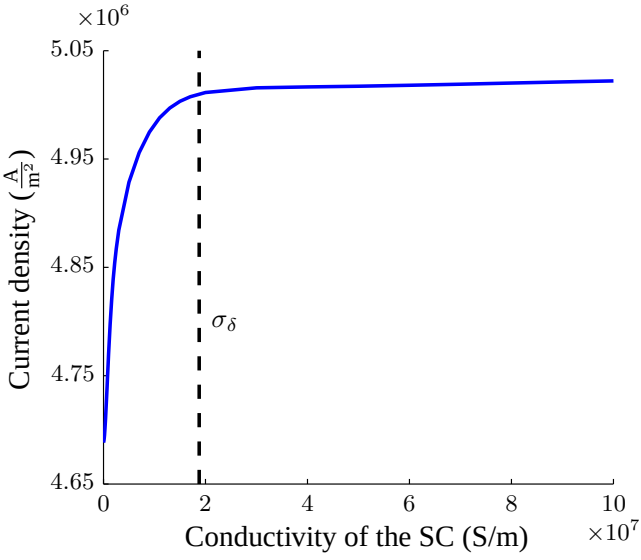

Figure 9.35: RMS value of the current density in phase A as a function of σ_{SC}

Torque ripple

Figure 9.36 shows the evolution of the torque ripples as a function of the SC's conductivity. It is clear that the evolution is very similar to that of the parameter study in which the idealized BLDC current is imposed. However, as illustrated in Figure 9.37, $\Delta T_{\%}^{(2)}$ reaches its minimum at a different conductivity, i.e. $16 \cdot 10^5$ $\frac{\text{S}}{\text{m}}$ instead of $6 \cdot 10^5$ $\frac{\text{S}}{\text{m}}$. This is, amongst others, due to the changing of the current waveform at different conductivities, which in turn affects the relative importance of different harmonic combinations.

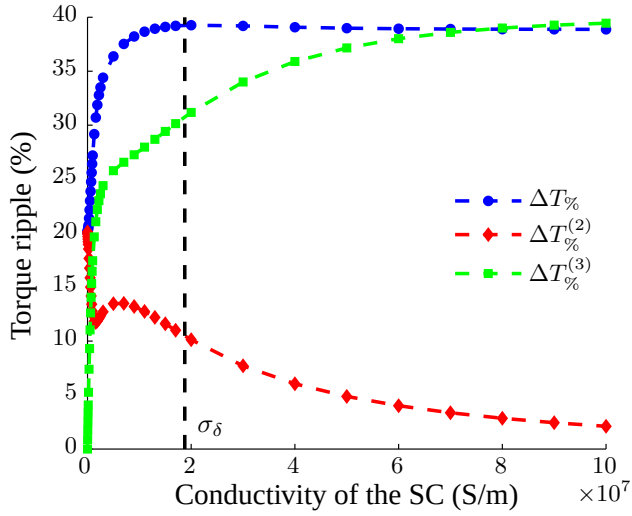

Figure 9.36: Torque ripple as a function of σ_{SC}

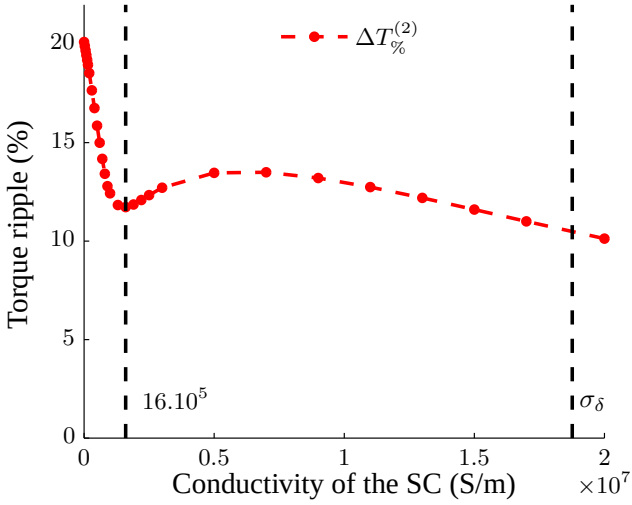

Figure 9.37: Torque ripple in the magnets as a function of σ_{SC}, detail of Figure 9.36

9.4.2 Eddy-current losses as a function of the SC's conductivity

Figure 9.38 shows the evolution of the eddy current losses as a function of σ_{SC}. It can be seen that the lower harmonic content of the current, when compared to the idealized BLDC current, results in much lower losses in the magnets. The evolution of the different loss components is similar, but less pronounced, to the evolutions found in Section 9.3.3.

9.4.3 Conclusion

This last set of parameter studies has again demonstrated a number of interesting aspects of high-speed PMSMs.

First of all, it was found that the conductivity of the shielding cylinder affects the inductance of the machine, and therefore its current as well. That is also the reason why in this section no parameter study of t_{SC} has been performed; varying t_{SC} has an even larger effect on the machine's inductance. The results obtained from such a study would therefore be mainly determined by the variations in the current instead of by the actual thickness of the shielding cylinder.

Secondly, the importance of the current's time-harmonic content has been illustrated by the much lower losses in the magnets when compared to the study with the idealized BLDC current.

Finally, this section showed that it is indeed interesting to be able to impose the

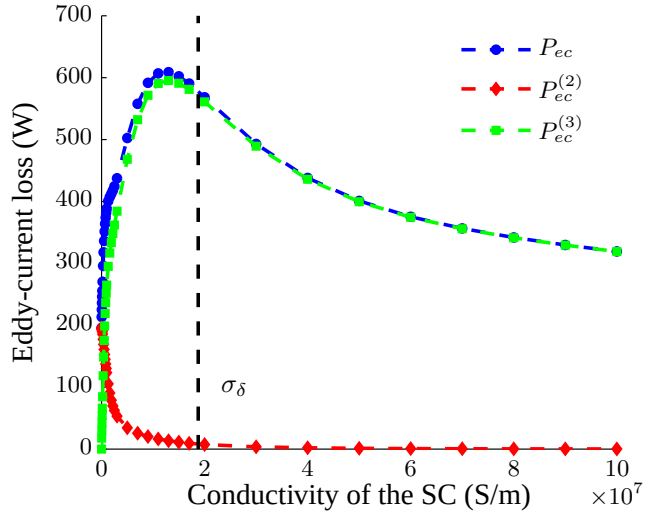

Figure 9.38: Eddy-current losses as a function of σ_{SC}

voltage instead of a fixed current waveform. Indeed, the parameter variations have an effect on the current.

9.5 Conclusion

In the above chapter, the effect of the shielding cylinder's conductivity and thickness on the torque and the eddy-current losses has been studied for various source terms. During these studies, a great number of interesting observations was made. The following lists the most important findings of this chapter in three categories.
A first set of important observations relates to the division of the torque in a component related to the magnets and a component related to the shielding cylinder. It was found such a division is indeed interesting. This is probably best illustrated by Figures 9.12 and 9.23, where it provides an explanation for the fact that the total torque cannot be predicted using Carter's factor.
The division of the torque has also allowed to observe that the torque in the shielding cylinder has the same characteristics as the torque in an induction machine, as shown in a.o. Figure 9.7. This validates the hypothesis that the torque produced in the SC is due to interaction with asynchronous harmonic combinations in the magnetic field.
Another finding related to the torque in the magnets and the torque in the SC is that their ripples are shifted in time with respect to each other, as illustrated in Figure 9.10. This could indeed have been expected as the phenomena that cause these

ripples, i.e. alignment with the rotor and variation of the magnetic field, do not necessarily synchronize in time.
Finally, it was observed that, unlike expected, the torque in the magnets depends on the SC's conductivity, as shown in Figure 9.5. By studying the harmonic content of the machine, as in Figure 9.6, it was found that variations in the asynchronous content of the machine propagate to the synchronous harmonic combinations through the slotting effect.
The second set of noteworthy observations relates to the presence of higher time-harmonic orders. As can clearly be seen from the differences between for example Figures 9.14, 9.26 and 9.38, accounting for higher time-harmonic orders in the current or voltage signal may be very important. Especially when studying the torque ripple or the eddy-current losses.
Another interesting finding is that the penetration depth of harmonic combinations with higher time-harmonic orders is much smaller than expected. This has been illustrated in Figure 9.28. Predicting the actual penetration depth proofs to be a complicated problem and is not really in the scope of this work. It was therefore not considered here.
The last set of interesting observation relates to the Fourier-based model itself. First of all it should be noted that the FB model has really proven its value in analyzing electric machines. One good illustration of that is the harmonic study of Figure 9.28.
The differences between the results in Sections 9.2-9.4 clearly illustrate that imposing the correct source term to the FB model is paramount. It is for example not satisfactory to assume an idealized current waveform, as illustrated by the dependency of the current on the SC's conductivity, shown in Figure 9.35.
Although it remains difficult to extrapolate the above findings quantitatively to other machines, the results do provide a better understanding of high-speed SM PMSMs.

Chapter 10

Concluding remarks

The following chapter concludes this dissertation by listing its most important aspects. This is done based on the goals that were set in the introduction.
This chapter also provides insights in what the possibilities for future research are.

10.1 Conclusion

In Section 1.4, two major goals were set for this PhD. The first goal was to contribute to a faster, more flexible and more accurate calculation of the magnetic field in electric machines. The second goal was to provide more insight in surface-mounted permanent-magnet synchronous machines with a shielding cylinder.

As motivated in Chapter 1, Fourier-based analytical models were chosen to tackle both of the above-mentioned goals. As this work has been the first at Ghent University to elaborate on the technique of Fourier-based analytical modeling, it was opted to start the dissertation with a thorough discussion on its basics. This was done by sketching the physical background of Fourier-based modeling in Chapter 2 and by discussing its implementation in Chapter 3. Both of these chapters are formulated in a very general way. They can therefore be used as the basis for studies on a much broader set of electric machines than the SM PMSMs considered in this work.

In addition to Chapters 2 and 3, an extensive overview of the possibilities of FB models is provided in Chapter 4. More specifically, the choosing of a magnetic potential and a spatial coordinate system, the way in which time dependency, source terms, the slotting effect and eccentricity are accounted for and the computation of electromagnetic quantities is discussed. This discussion is coupled to the existing literature on Fourier-based modeling. As a result, Chapter 4 can be used as an overview for anyone who wants to use, or study, FB modeling.

Based on the previous, the first actual goal was met in Chapters 5 and 6; contributing to the technique of Fourier-based modeling.

Chapter 5 focused on reducing the computational time of FB models. This was achieved by simplifying the machine's geometry and by using preliminary knowledge on the harmonic content of electric machines. The latter is especially interesting as it can reduce the computational time by more than 99% without affecting the accuracy of the model.

Chapter 6, focused on increasing the flexibility and accuracy of FB models by coupling the magnetic calculations of the FB model to the classical equation for the terminal voltage of an electric machine. The resulting model can account for voltage sources, as opposed to the current-density sources in traditional FB models. This is, for example, interesting in optimization procedures of voltage-fed systems or if the effect of PWM voltages on the machine's performance has to be evaluated.

The second goal, i.e. providing more insight in the physics of high-speed PMSMs, has been tackled in Chapters 7-9.

Chapter 7 introduced the calculation of electromagnetic properties, based on the results from the FB model. Its major contribution is that it proposes a division of the torque in two components; one related to the magnets and an other to the shielding cylinder. This division has proven to be very useful to gain more insight in SM PMSMs with a SC.

In Chapter 8, an experimental setup for high-speed PMSMs was introduced. Al-

though the majority of the work on that setup is not in the scope of this dissertation, it was used to validate some of the calculation that have been performed in previous Chapters.
Finally, Chapter 9 evaluates the effect of the SC's design on the torque and the eddy-current losses in SM PMSMs with the help of various parameter studies. This has resulted in a number of interesting insights in the high-speed operation of PMSMs. Apart from confirming the usefulness of dividing the torque in its components, it was found that, unlike expected, the SC does affect the machine's synchronous harmonic content. Another interesting finding is that whether or not a SC reduces the eddy-current losses greatly depends on the harmonic content of the applied current.

10.2 Recommendations for future research

Although this work provides quite some research on Fourier-based modeling and high-speed machines, there are a number of aspects that have not been considered and would be interesting for future research.

A first interesting idea concerns the application of the FB models that were presented in this PhD. These models have a lot of potential in optimization procedures. Especially because the models with a voltage source can, relatively easy, be coupled to models of power electronic systems. This would allow to consider the entire electric drive and its control algorithm. Something that is especially interesting because of the increasing popularity of integrated drives.

A second idea relates to the slotting effect and the eddy-current reaction field of the magnets. As mentioned in Chapter 4, Dubas [69] and Spranger [99] have recently developed techniques to account for the slotting effect without the need to assume an infinite permeability of the stator yoke. As these techniques also allow to calculate the magnetic potential in the stator yoke, their implementation would allow to calculate additional electromagnetic quantities such as the stator's iron losses. The same techniques could be applied to consider the eddy-current reaction field of the magnets. This would further improve the accuracy of the model.
Moreover, during this PhD an effort to formulate an alternative for Dubas' superposition technique and Spranger's technique of variable permeabilities has been made. Although that effort did not yet result in a working model, the investigated technique is promising. Especially because it is expected to be more computationally efficient than the superposition technique and less sensitive to Gibb's phenomenon than the technique of variable permeabilities. The development of this technique is thus definitely an interesting idea for future research.

Thirdly, there is still a lot of research that can be conducted on the shielding cylinder. One example is a more detailed study on the penetration depth of harmonic combinations with higher time-harmonic orders. Other possibilities are an evaluation of its effect on other electromagnetic quantities, such as the iron losses in the stator yoke.

Finally, it would be interesting to extend the study of this PhD to other machine types. It would, for example, be interesting to evaluate the effect of the shielding cylinder in machines with fractional-slot concentrated windings. Although these machines often rotate at lower speeds, their harmonic content is typically much larger. Another possibility is studying solid-rotor induction machines.

Appendix A

Star of slots

The so-called star-of-slots (SoS) is a technique that is used to assign the phases of the applied current system to the slots of an electrical machine. It is described by a large number of authors [141, 151, 152] and can be used for both integral and fractional slot windings. N. Bianchi *et al.* have extended the technique to determine the winding layout of single layer [151] and multilayer [152] topologies. An extensive description of the SoS technique is beyond the scope of this appendix. However, an understanding of the SoS's basics is required for the discussion in Appendix B. Therefore, this appendix briefly introduces the technique in Section A.1. In Section A.2 the concept of slot groups is introduced, the results of that discussion will be used in Appendix B.

A.1 Star of slots

The star of slots technique consists of four steps, each of which will briefly be explained in the following.
In a first step, the machine's periodicity (τ) is calculated as the greatest common divisor of the number of slots and the number of pole pairs:

$$\tau = \gcd(N_s, p) \tag{A.1}$$

Secondly, a system of $\frac{N_s}{\tau}$ phasors, called spokes, with a mutual shift of $p\frac{2\pi}{N_s}$ radians is drawn. This is illustrated in Figure A.1 for a machine with 12 slots and 5 pole pairs ($\tau = 1$). Every spoke now corresponds to a slot in the electrical machine. Logically, the spoke with number i corresponds to the slot with number i.
The third step is drawing the phase zones. Every phase is assigned two zones, a positive zone and a negative zone. Each phase zone spans $\frac{\pi}{m}$ radians. The shift between two phase zones equals the shift between their corresponding phases, as illustrated in Figure A.1 for a three-phase system. Consequently the time shift between the currents linked to the phases of subsequent phase zones is $\frac{1}{\omega_e}\frac{\pi}{m}$ seconds. The resulting diagram defines one conductor of each coil by linking the spokes, and thereby the slots, to the phases of the applied current system. The slot corresponding to the other conductor of the same coil is determined by the coil throw, which is calculated as:

$$y_q = \text{round}\left(\frac{N_s}{2p}\right) \tag{A.2}$$

The obtained distribution is repeated after $\frac{N_s}{\tau}$ slots.
The winding distribution obtained from the star-of-slots in Figure A.1 is shown in Figure A.2.

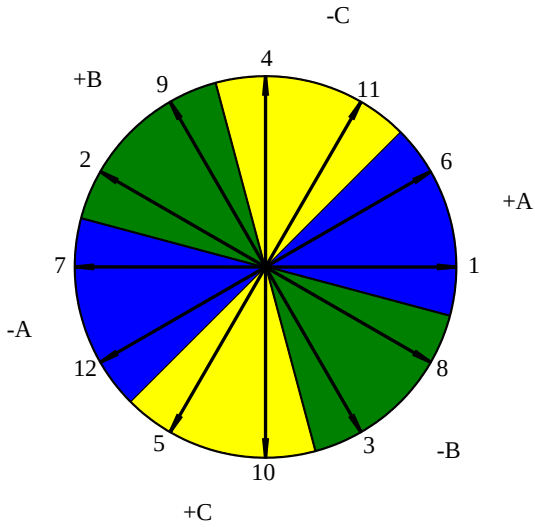

Figure A.1: Star of slots for a machine with $N_s = 12$ and $p = 5$

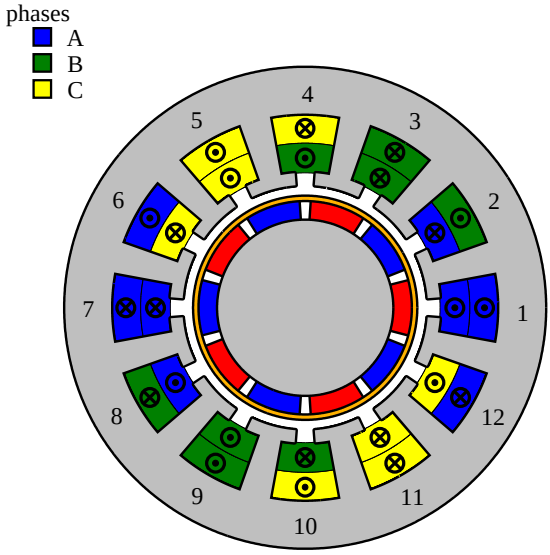

Figure A.2: Winding distribution of a machine with $N_s = 12$ and $p = 5$

A.2 Slot groups

In this section the term slot group is introduced as a number of subsequent slots so that, under synchronous operation, the mechanical shift between two slot groups

equals the time shift of their corresponding current densities. In other words, the time the rotor needs to rotate from one slot group to the next equals the time shift of the current densities related to those slot groups.
For simplicity reasons the slot groups are chosen so that each group is dominated by one phase, this is illustrated in Figure A.3.
In the following the mechanical shift and the time shift of subsequent slot groups are calculated to prove that they indeed correspond.

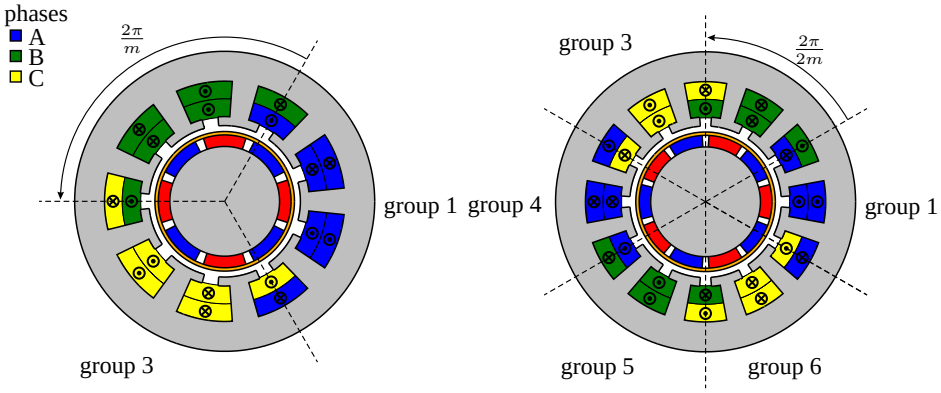

(a) Machine with $\frac{N_s}{\tau}$ odd (b) Machine with $\frac{N_s}{\tau}$ even

Figure A.3: Slot groups

A.2.1 Mechanical shift

First, the mechanical shift is regarded. If the number of slots per machine period is odd, every phase will dominate one slot group per machine period. Indeed, every phase should dominate an equal number of similar slot groups, otherwise the winding distribution can never be balanced. A phase dominating more than one slot group, on the other hand, would imply two coinciding spokes in the star of slots. This in turn would imply that all of the following spokes also coincide with another spoke, this can only happen if these spokes belong to another machine period. Therefore a machine with $\frac{N_s}{\tau}$ odd contains $m\tau$ slot groups. The number of slots per slot group (N_g) can then be calculated as:

$$N_g = \frac{N_s}{m\tau} \tag{A.3}$$

If $\frac{N_s}{\tau}$ is even, spoke $i + \frac{N_s}{2\tau}$ will be opposite to spoke i. Indeed, the rotation between these spokes is:

$$\frac{N_s}{2\tau} p \frac{2\pi}{N_s} = \frac{p}{\tau}\pi \tag{A.4}$$

Since $\frac{N_s}{\tau}$ is even and τ is the greatest common divider of N_s and p, $\frac{p}{\tau}$ has to be odd. This means that spokes i and $i + \frac{N_s}{2\tau}$ are indeed opposite.
Because of the fact that this is true for every spoke, every phase will dominate two similar groups of slots per machine period. One due to the spokes in its positive phase zone and one due to the spokes in its negative phase zone, this can be seen in Figure A.3(a). This implies that the number of slot groups is now $2m\tau$, the number of slots in every slot group is then:

$$N_g = \frac{N_s}{2m\tau} \tag{A.5}$$

The mechanical shift between similar slots of subsequent slot groups can now be calculated as:

$$\frac{N_s}{\upsilon m\tau}\frac{2\pi}{N_s} = \frac{2\pi}{\upsilon m\tau} \tag{A.6}$$

with $\upsilon = 1$ if $\frac{N_s}{\tau}$ is odd and $\upsilon = 2$ is $\frac{N_s}{\tau}$ is even.
The mechanical shift, found in (A.6), translates to a time shift when divided by the synchronous pulsation:

$$\frac{1}{\omega}\frac{2\pi}{\upsilon m\tau} = \frac{T_t}{\upsilon m\tau} \tag{A.7}$$

A.2.2 Time shift

Secondly, the time shift between subsequent slot groups will be computed. In the SoS, the angle between two subsequent slots is $p\frac{2\pi}{N_s}$ electrical radians. This implies that in the SoS the angle between similar slots of subsequent slot groups is:

$$\frac{N_s}{\upsilon m\tau}p\frac{2\pi}{N_s} = p\frac{2\pi}{\upsilon m\tau} \tag{A.8}$$

As shown in the above, the SoS consists of $2m$ phase zones with a mutual shift of $\frac{\pi}{m}$ radians. Knowing this, the number of phase zones between similar slots of subsequent slot groups can be calculated as:

$$\frac{p\frac{2\pi}{\upsilon m\tau}}{\frac{\pi}{m}} = \frac{2p}{\upsilon\tau} \tag{A.9}$$

The time shift between currents linked to consecutive phase zones in the SoS is $\frac{\pi}{m}$ electrical radians. Consequently the shift in electrical radians between the currents linked to similar slots of subsequent slot groups is:

$$\frac{2p}{\upsilon\tau}\frac{\pi}{m} \tag{A.10}$$

Which results in a time shift when divided by the electrical pulsation:

$$2p\frac{\pi}{\upsilon m\tau}\frac{1}{p\omega} = \frac{T_t}{\upsilon m\tau} \tag{A.11}$$

This indeed equals (A.7).
Practically this implies that the rotor will experience the same current density after $\frac{T_t}{m\tau}$ or $\frac{T_t}{2m\tau}$ seconds, depending on whether $\frac{N_s}{\tau}$ is odd or even. From the stator point of view it means that after $\frac{T_t}{m\tau}$ or $\frac{T_t}{2m\tau}$ seconds the armature reaction field will be identical but shifted over $\frac{2\pi}{m\tau}$ or $\frac{\pi}{m\tau}$ mechanical radians respectively.

Appendix B

Harmonic content of PMSMs

In Section 5.3, the computational time of Fourier-based models was reduced with the help of preliminary knowledge of the studied machine's harmonic content. Although the harmonic content of electric machines is a topic that has extensively been studied ever since such machines were first used, literature lacks a complete discussion of the harmonic content of synchronous machines. To be applicable for Section 5.3, such a discussion should account for higher time-harmonic orders and for every winding configuration that can be obtained with the star of slots. In the scope of this PhD a paper on harmonic content was published [139]. That study will be repeated here to support the work in Section 5.3. Note that an overview of the existing literature can be found in [139].
Section B.1 discusses the different sources of harmonic content. Based on that discussion, Section B.2 presents simple rules on which harmonic combinations are present in no-load, armature-reaction and load conditions.

B.1 Sources of harmonic content

A harmonic combination (n, k) can only be present in an electric machine if it is either introduced by the source terms or the machine's geometry. Both aspects are considered in this section.
Note that the following discussion is limited to unsaturated PMSMs that are synchronously operated, but can easily be broadened to other machine types and operation modes.

B.1.1 Permanent magnets

The magnets are a source of magnetic flux. They can, however, only introduce components of the magnetic field with a harmonic combination that is present in $\mathbf{B}_0$. For that reason it is important to understand which harmonic combinations are available in the distribution of the remanent magnetic flux density.
First of all, as already mentioned in Section 3.3.3, the synchronous rotation of the magnets implies that they can only introduce synchronous harmonic combinations, i.e. combinations for which $n = k$.
Secondly, as can be seen in Figure 3.6, the magnet distribution contains p identical parts along the ϕ-direction. These repetitions imply that the spatial period in the ϕ-direction is p times smaller than the mechanical spatial period. This smaller period is referred to as the fundamental spatial period and it equals $\frac{2\pi}{p}$ mechanical radians. To comply with the fundamental spatial period, $\mathbf{B}_0$ can only contain harmonic orders that are a multiple of p. Note that this demand requires p identical repetitions of the magnet distribution. If for example one of the magnets is demagnetised, it is no longer valid.
Finally, in most machines the spatial distribution of the remanent magnetic flux density is symmetrical in the ϕ-direction over half a fundamental period. This symmetry can only be maintained if, when referred to the fundamental spatial period, there are no even harmonic orders, i.e $\frac{k}{p}$ is odd. Indeed, as illustrated in Figure B.1, even harmonic orders do not show symmetry with respect to the middle of half a period. Note that the demand for odd spatial-harmonic orders is common but not absolute, one could build a machine with asymmetrical magnets.
As a conclusion it can be stated that the magnets will only introduce time-harmonic orders, n, wherefore $n \in h_m$. With h_m the set of time-harmonic orders for which $\mathbf{B}_{0,n,k} \neq \mathbf{0}$. In a healthy machine h_m will only contain multiples of p. Due to the assumption of synchronous operation, the magnets will only introduce harmonic combinations for which $n = k$. If the magnets are symmetrical over half a period, an extra constraint can be imposed; $\frac{k}{p}$ should then be odd.

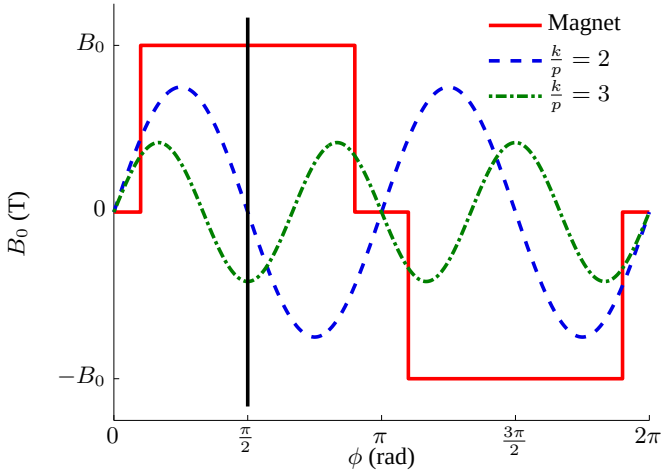

Figure B.1: Illustration of symmetry in the magnet distribution

B.1.2 Stator-current density

Like the magnets, the current density is a source of magnetic flux. But again, restrictions can be imposed on the induced harmonic combinations. In order to study these restrictions, the applied current and the spatial distribution of the windings through which these currents flow are regarded separately.

Current

The current is time-dependent and will determine which time-harmonic orders are introduced by the current density. The applied current system is a balanced system with an odd number of evenly distributed phases (m). This means that the rotation between neighboring phases is $\frac{2\pi}{m}$ electrical radians, as illustrated in Figure B.2 for a five-phase system.
The current, related to an arbitrary phase with number $i \in [1, m]$, can be written as a Fourier series over time:

$$I^{(i)} = \sum_{n=-\infty}^{\infty} I_n^{(i)} e^{-jn\left(\omega t-(i-1)\frac{2\pi}{m}\right)} \tag{B.1}$$

The current density in the machine can only introduce components of the magnetic field whose time-harmonic order n corresponds to a non-zero $I_n^{(i)}$. The following general consideration on the time-harmonic content of $I^{(i)}$ can be made.
For the sake of uniformity, the mechanical pulsation has been used in (B.1). However, the base pulsation of current $I^{(i)}$ is the electrical pulsation $p\omega$. This implies

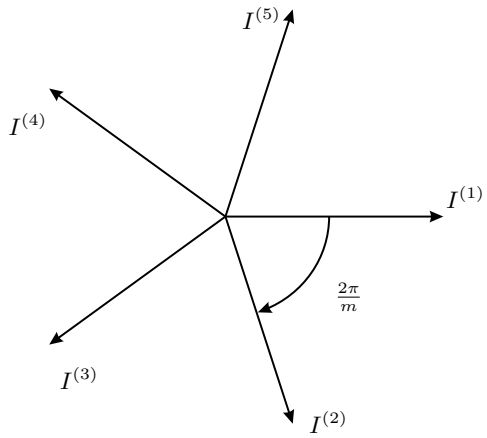

Figure B.2: Balanced five-phase current system

that only multiples of p are eligible for n.
The assumption that the applied system is balanced implies that the sum of the current phasors should always equal zero. When referred to the fundamental time period, this means that the current does not contain time-harmonic orders that are a multiple of m. This consideration results in $\frac{n}{p} \neq cm$, with c an integer.
The above considerations allow stating that the current density will only introduce harmonic combinations with time-harmonic orders that are multiples of p and wherefore $\frac{n}{p}$ is no multiple of m. More generally it can be stated that, if h_c contains the time-harmonic orders that are present in $I^{(i)}$, the current density will only introduce time-harmonic orders, wherefore $n \in h_c$.

Winding distribution

As opposed to the current, the distribution of the windings has a spatial dependency and will determine which spatial-harmonic orders are present. There are a great number of possibilities to distribute the windings around the stator surface. However, mostly the so called Star-Of-Slots (SOS) technique is used to assign the slots to one or more phases. The technique is introduced in Appendix A, important for the following is the definition of the machine's period (τ). This is the number of times the winding topology is repeated along the stator surface, it is calculated as:

$$\tau = \gcd(p, N_s) \tag{B.2}$$

where N_s is the amount of stator slots. In Appendix A the term *slot group* has been defined as a set of adjacent stator slots so that, at synchronous operation, the mechanical shift between similar slots of different slot groups corresponds to the time shift of the current densities linked to these slots. These slot groups are

illustrated in Figure A.3.
It was shown in Appendix A that, depending on whether $\frac{N_s}{\tau}$ is odd or even, the magnetic field will be identical but rotated over $\frac{2\pi}{m\tau}$ or $\frac{\pi}{m\tau}$ mechanical radians after $\frac{T_t}{m\tau}$ or $\frac{T_t}{2m\tau}$ seconds. This can be written mathematically for the magnetic vector potential:

$$A(r,\phi,t_0) = A\left(r,\phi+\frac{2\pi}{\upsilon m\tau},t_0+\frac{T_t}{\upsilon m\tau}\right) \tag{B.3}$$

where υ is 1 if $\frac{N_s}{\tau}$ is even and 2 if $\frac{N_s}{\tau}$ is odd. Note that (B.3) relates to the field of the entire machines, not to individual subdomains. These will be considered in Chapter 5.
The above time periodicity is not only valid for the complete function, it is also valid for every separate (n,k)-component of the magnetic field. Indeed, another harmonic component of the magnetic field can only have the same rotational speed if it has both a different time and a different spatial-harmonic order. This, in turn, would imply a different source term, $I_{n'}^{(i)}$.
It can thus be written that:

$$A_{n,k}(r)e^{j(k\phi-n\omega t_0)} = A_{n,k}(r)e^{j\left(k\left(\phi+\frac{2\pi}{\upsilon m\tau}\right)-n\omega\left(t_0+\frac{T_t}{\upsilon m\tau}\right)\right)} \tag{B.4}$$

Knowing that $\omega T_t = 2\pi$, the above can be simplified:

$$1 = e^{j(k-n)\frac{2\pi}{\upsilon m\tau}} \tag{B.5}$$

With c an integer, this results in:

$$k-n = c\upsilon m\tau \tag{B.6}$$

Equation (B.6) imposes a relation between the time- and spatial-harmonic orders. As a conclusion it can be stated that the current density will only introduce time-harmonic orders that are present in the applied currents, i.e. $n \in h_c$. Due to the distribution of the windings, the induced spatial-harmonic orders have to satisfy (B.6).

Machine geometry

Unlike the permanent magnets and the stator-current density, the machine's geometry is not a source of magnetic flux. Nevertheless, the geometry can introduce additional harmonic combinations. At no-load for example, harmonic combinations, different from the synchronous ones found in Section B.1.1, are present in the magnetic field.
The reason for these extra harmonic orders is a variation along ϕ of the magnetic permeance. This effect is best known as the slotting effect and is mostly associated with slotted machine topologies. The latter is because the amplitude of the

induced harmonic components depends on the difference in magnetic permeance, the greater this difference the greater the amplitude. In slotless machines, where the highly permeable teeth are replaced with non-magnetic teeth, the difference between the permeability of the copper windings and that of the synthetic teeth is very small. The slotting effect is then so small that most authors neglect it.
As mentioned, the source of the induced spatial-harmonic orders is a difference in magnetic permeance. The reason is that such differences introduce a time periodicity, similar to the one in (B.3). Indeed, under synchronous operation, the machine's rotor will have rotated over one slot pitch after a time of $\frac{T_t}{N_s}$ seconds. The rotor will then experience the same stator topology. Under no-load conditions, the magnetic field will then be equal but shifted over one slot pitch. This can be expressed mathematically in terms of the magnetic vector potential:

$$A(r,\phi,t_0) = A\left(r,\phi+\frac{2\pi}{N_s},t_0+\frac{T_t}{N_s}\right) \tag{B.7}$$

As explained in the above, this has to be true for every time- and spatial-harmonic combination separately:

$$A_{n,k}(r)e^{j(k\phi-n\omega t_0)} = A_{n,k}(r)e^{j\left(k\left(\phi+\frac{2\pi}{N_s}\right)-n\omega\left(t_0+\frac{T_t}{N_s}\right)\right)} \tag{B.8}$$

And again a relation between the spatial- and time-harmonic orders is found:

$$k-n = cN_s \tag{B.9}$$

Where c is an integer. The above-mentioned time periodicity is only introduced due to different magnetic permeances in the ϕ-direction, consequently changes in the r-direction do not introduce harmonic combinations.
Note that, concerning the armature reaction, the effect of the geometry is embedded in the winding distribution. Therefore the geometry will have no further effect on the harmonic combinations introduced due to the current distribution.
Finally, it should also be noted that differences in the magnetic permeance can also occur on the rotor. However, due to the synchronous rotation of the rotor, these differences do not affect the periodicity found in (B.7).
As a conclusion, it can be stated that, under no-load conditions, the machine's geometry will introduce harmonic combinations wherefore $k-n = cN_s$. However, in a slotless machine, the field components related to combinations for which $c \neq 0$ may be considered negligible.

B.2 Harmonic combinations

In Section B.1, the harmonic orders introduced due to the magnets, the current density and the geometry were discussed. Based on that discussion it can be concluded that, on the one hand, the source terms, being the permanent magnets and

the applied current density, determine which time-harmonic orders will be present. On the other hand, the distribution of the windings and the machine's geometry determine the present spatial-harmonic orders.
Practically, no-load, armature-reaction and load conditions are considered. This section discusses the harmonic combinations for each of these conditions based on the findings in the previous sections.

No load

Under no-load conditions, the currents in the slots equal zero. This means that the harmonic combinations found in Section B.1.2 will not be present. The magnets will introduce synchronous harmonic combinations $(n = k)$ that are present in the magnet distribution. For every present time-harmonic order n, the geometry will introduce spatial-harmonic orders that satisfy (B.9). The restriction on the harmonic combinations under no-load conditions can thus be summarized as:

$$\begin{cases} n \in h_m \\ k - n = cN_s \end{cases} \tag{B.10}$$

With c an integer and h_m the time-harmonic orders for which $B_{0,r,n,k} \neq 0$ or $B_{0,\phi,n,k} \neq 0$. In a healthy machine h_m can only contain time harmonics that are multiples of p. If the magnets are symmetrical over half a fundamental period, no time-harmonic orders wherefore $\frac{n}{p}$ is even are present.

Armature reaction

When $\mathbf{B}_0 = \mathbf{0}$, the permanent magnets will not introduce any harmonic combinations. The current density will only introduce the time-harmonic orders that are present in the applied current. The introduced spatial-harmonic orders are defined by the distribution of the current density (B.6). The restrictions on the harmonic combinations can then be summarized as:

$$\begin{cases} n \in h_c \\ k - n = c\upsilon m\tau \end{cases} \tag{B.11}$$

With c an integer and h_c the time-harmonic orders for which $I_n \neq 0$. h_c can only contain multiples of p and will not contain any time-harmonic orders for which $\frac{n}{p}$ is a multiple of m.

Load

The load situation is a superposition of the no-load and the armature-reaction situations. This implies that all the harmonic combinations that satisfy either (B.10) or (B.11) will be present in the magnetic field.

Bibliography

[1] A. Binder and T. Schneider, "High-speed inverter-fed AC drives," in *International Aegean Conference on Electrical Machines and Power Electronics, 2007. ACEMP '07*, Sep. 2007, pp. 9–16.

[2] J. Gieras and J. Saari, "Performance Calculation for a High-Speed Solid-Rotor Induction Motor," *IEEE Transactions on Industrial Electronics*, vol. 59, no. 6, pp. 2689–2700, Jun. 2012.

[3] J. Peirs, D. Reynaerts, and F. Verplaetsen, "Development of an axial microturbine for a portable gas turbine generator," *J. Micromech. Microeng.*, vol. 13, no. 4, p. S190, 2003.

[4] C. Zwyssig, S. Round, and J. Kolar, "An Ultrahigh-Speed, Low Power Electrical Drive System," *IEEE Transactions on Industrial Electronics*, vol. 55, no. 2, pp. 577–585, Feb. 2008.

[5] Capstoneturbine.com, "C30 :: Capstone Turbine Corporation (CPST)," 2017. [Online]. Available: https://www.capstoneturbine.com/products/c30

[6] Mohawkinnovative.com, "Mohawk Innovative Technology, Inc. - Motors," 2017. [Online]. Available: http://mohawkinnovative.com/oil-free-turbomachinery/motors/

[7] B.-H. Bae, S.-K. Sul, J.-H. Kwon, and J.-S. Byeon, "Implementation of sensorless vector control for super-high-speed PMSM of turbo-compressor," *IEEE Transactions on Industry Applications*, vol. 39, no. 3, pp. 811–818, May 2003.

[8] C. Zwyssig, J. W. Kolar, and S. D. Round, "Megaspeed Drive Systems: Pushing Beyond 1 Million r/min," *IEEE/ASME Transactions on Mechatronics*, vol. 14, no. 5, pp. 564–574, Oct. 2009.

[9] A. S. Nagorny, R. H. Jansen, and M. D. Kankam, "Experimental Performance Evaluation of a High Speed Permanent Magnet Synchronous Motor and Drive for a Flywheel Application at Different Frequencies," NASA, Tech. Rep., Dec. 2007.

[10] Calnetix.com, “Magnetic Bearings, Motor Generators, Power Electronics, Energy Efficiency, Savings, Consumption, Reduce Harmful Emissions, Medical, Food, Marine, Composite Rotor Sleeving Technology | calnetix.com,” 2017. [Online]. Available: https://www.calnetix.com/

[11] Eunda.ch, “e+a Elektromaschinen und Antriebe AG,” 2013. [Online]. Available: https://www.eunda.ch/en.html

[12] M. T. Caprio, V. Lelos, J. D. Herbst, and J. Upshaw, “Advanced Induction Motor Endring Design Features for High Speed Applications,” in *IEEE International Conference on Electric Machines and Drives, 2005.*, May 2005, pp. 993–998.

[13] Ate-system.de, “Micro drives - ATE Antriebstechnik und Entwicklungs GmbH _ EN.” [Online]. Available: http://www.ate-system.de/en/products/micro-drives.html

[14] M. Ahrens, U. Bikle, R. Gottkehaskamp, and H. Prenner, “Electrical design of high-speed induction motors of up to 15 MW and 20000 RPM,” in *2002 International Conference on Power Electronics, Machines and Drives (Conf. Publ. No. 487)*, Jun. 2002, pp. 381–386.

[15] M. Aoulkadi, A. Binder, and G. Joksimovic, “Additional losses in high-speed induction machine - removed rotor test,” in *2005 European Conference on Power Electronics and Applications*, Sep. 2005, pp. 10 pp.–P.10.

[16] I. Takahashi, T. Koganezawa, G. Su, and K. Oyama, “A super high speed PM motor drive system by a quasi-current source inverter,” in *Conference Record of the 1993 IEEE Industry Applications Conference Twenty-Eighth IAS Annual Meeting*, Oct. 1993, pp. 657–662 vol.1.

[17] J. Oyama, T. Higuchi, T. Abe, K. Shigematsu, and R. Moriguchi, “The Development of Small Size Ultra-High Speed Drive System,” in *2007 Power Conversion Conference - Nagoya*, Apr. 2007, pp. 1571–1576.

[18] J. R. Bumby, E. S. Spooner, J. Carter, H. Tennant, G. G. Mego, G. Dellora, W. Gstrein, H. Sutter, and J. Wagner, “Electrical machines for use in electrically assisted turbochargers,” in *Second International Conference on Power Electronics, Machines and Drives (PEMD 2004).*, vol. 1, Mar. 2004, pp. 344–349 Vol.1.

[19] C. Zwyssig, M. Duerr, D. Hassler, and J. W. Kolar, “An Ultra-High-Speed, 500000 rpm, 1 kW Electrical Drive System,” in *2007 Power Conversion Conference - Nagoya*, Apr. 2007, pp. 1577–1583.

[20] A. Binder, T. Schneider, and M. Klohr, "Fixation of buried and surface-mounted magnets in high-speed permanent-magnet synchronous machines," *IEEE Transactions on Industry Applications*, vol. 42, no. 4, pp. 1031–1037, Jul. 2006.

[21] O. Aglen and A. Andersson, "Thermal analysis of a high-speed generator," in *38th IAS Annual Meeting on Conference Record of the Industry Applications Conference, 2003.*, vol. 1, Oct. 2003, pp. 547–554 vol.1.

[22] J. Barta, C. Ondrusek, P. Losak, and R. Vlach, "Design of high-speed induction machine for the 6 kW, 120 000 rpm helium turbo-circulator," in *2016 XXII International Conference on Electrical Machines (ICEM)*, Sep. 2016, pp. 1552–1558.

[23] R. K. Jardan, P. Stumpf, Z. Varga, and I. Nagy, "Novel Solutions for High-Speed Self-Excited Induction Generators," *IEEE Transactions on Industrial Electronics*, vol. 63, no. 4, pp. 2124–2132, Apr. 2016.

[24] D. Zhao, M. Dou, B. Blunier, and A. Miraoui, "Control of an ultra high speed centrifugal compressor for the air management of fuel cell systems," in *2012 IEEE Industry Applications Society Annual Meeting*, Oct. 2012, pp. 1–8.

[25] T. Baumgartner, R. Burkart, and J. W. Kolar, "Analysis and design of an ultra-high-speed slotless self-bearing permanent-magnet motor," in *IECON 2012 - 38th Annual Conference on IEEE Industrial Electronics Society*, Oct. 2012, pp. 4477–4483.

[26] L. Xu, Y. Li, Z. Zheng, H. Ma, and K. Wang, "A Multi-Level Inverter for Ultra High Speed PM Motor Control Application," *Przeglad Elektrotechniczny*, vol. R. 88, nr 5b, pp. 11–16, 2012.

[27] N. Bianchi, S. Bolognani, and F. Luise, "Potentials and limits of high-speed PM motors," *IEEE Transactions on Industry Applications*, vol. 40, no. 6, pp. 1570–1578, Nov. 2004.

[28] H. Cho and S. Jang, "A Design Approach to Reduce Rotor Losses in High-Speed Permanent Magnet Machine for Turbo-Compressor," in *INTERMAG 2006 - IEEE International Magnetics Conference*, May 2006, pp. 209–209.

[29] C. Zwyssig and J. W. Kolar, "Design considerations and experimental results of a 100 W, 500 000 rpm electrical generator," *J. Micromech. Microeng.*, vol. 16, no. 9, p. S297, 2006.

[30] Y. Xia, J. Li, R. Qu, and H. Fang, "Comparison of two rotor topologies for high-speed permanent magnet synchronous machines," in *2016 XXII International Conference on Electrical Machines (ICEM)*, Sep. 2016, pp. 1419–1425.

[31] T. Wang, F. Wang, H. Bai, and J. Xing, "Optimization design of rotor structure for high speed permanent magnet machines," in *2007 International Conference on Electrical Machines and Systems (ICEMS)*, Oct. 2007, pp. 1438–1442.

[32] A. Borisavljevic, H. Polinder, and J. A. Ferreira, "On the Speed Limits of Permanent-Magnet Machines," *IEEE Transactions on Industrial Electronics*, vol. 57, no. 1, pp. 220–227, Jan. 2010.

[33] J. Saari, "Thermal Analysis of High-Speed Induction Machines," Text.Thesis.Doctoral, Helsinki University of Technology, Helsinki, 1998.

[34] R. M. Kennel, "Ultra high speed drive with permanent magnet synchronous motors and hardware based field oriented control," in *2007 International Aegean Conference on Electrical Machines and Power Electronics*, Sep. 2007, pp. 116–124.

[35] Z. Varga, R. K. Jardan, and I. Nagy, "Ultrahigh speed induction generators applied in Disperse Power Plants," in *2011 IEEE 33rd International Telecommunications Energy Conference (INTELEC)*, Oct. 2011, pp. 1–7.

[36] C.-W. Hung, "An ultra-high-speed motor driver with hybrid modulations," *Artif Life Robotics*, vol. 18, no. 1-2, pp. 70–75, Dec. 2013.

[37] S. Konaka, Y. Inoue, S. Morimoto, and M. Sanada, "Comparative study of control characteristics in ultra-high-speed PMSM drives," in *2014 IEEE 5th International Symposium on Sensorless Control for Electrical Drives*, May 2014, pp. 1–6.

[38] H. Zhou and F. Wang, "Comparative study on high speed induction machine with different rotor structures," in *2007 International Conference on Electrical Machines and Systems (ICEMS)*, Oct. 2007, pp. 1009–1012.

[39] A. Arkkio, T. Jokinen, and E. Lantto, "Induction and permanent-magnet synchronous machines for high-speed applications," in *2005 International Conference on Electrical Machines and Systems*, vol. 2, Sep. 2005, pp. 871–876 Vol. 2.

[40] A. S. Nagorny, N. V. Dravid, R. H. Jansen, and B. H. Kenny, "Design aspects of a high speed permanent magnet synchronous motor / generator for flywheel applications," in *IEEE International Conference on Electric Machines and Drives, 2005.*, May 2005, pp. 635–641.

[41] M. Shah and S.-B. Lee, "Rapid analytical optimization of eddy-current shield thickness for associated loss minimization in electrical Machines," *IEEE Transactions on Industry Applications*, vol. 42, no. 3, pp. 642–649, May 2006.

[42] F. Zhou, J. Shen, W. Fei, and R. Lin, "Study of Retaining Sleeve and Conductive Shield and Their Influence on Rotor Loss in High-Speed PM BLDC Motors," *IEEE Transactions on Magnetics*, vol. 42, no. 10, pp. 3398–3400, Oct. 2006.

[43] S. R. Holm, H. Polinder, and J. A. Ferreira, "Analytical Modeling of a Permanent-Magnet Synchronous Machine in a Flywheel," *IEEE Transactions on Magnetics*, vol. 43, no. 5, pp. 1955–1967, May 2007.

[44] M. Amrhein and P. Krein, "3-D Magnetic Equivalent Circuit Framework for Modeling Electromechanical Devices," *IEEE Transactions on Energy Conversion*, vol. 24, no. 2, pp. 397–405, Jun. 2009.

[45] J. Perho, "Reluctance network for analysing induction machines," Ph.D. dissertation, Helsinki University of Technology, Helsinki, Finland, 2002.

[46] A. Hemeida, P. Sergeant, and H. Vansompel, "Comparison of Methods for Permanent Magnet Eddy-Current Loss Computations With and Without Reaction Field Considerations in Axial Flux PMSM," *IEEE Transactions on Magnetics*, vol. 51, no. 9, pp. 1–11, Sep. 2015.

[47] B. van Ninhuijs, T. Motoasca, B. Gysen, and E. Lomonova, "Modeling of Spherical Magnet Arrays Using the Magnetic Charge Model," *IEEE Transactions on Magnetics*, vol. 49, no. 7, pp. 4109–4112, Jul. 2013.

[48] E. P. Furlani, "A three-dimensional field solution for axially-polarized multipole disks," *Journal of Magnetism and Magnetic Materials*, vol. 135, no. 2, pp. 205–214, Jul. 1994.

[49] D. van Casteren, J. Paulides, and E. Lomonova, "3-D Numerical Surface Charge Model Including Relative Permeability: The General Theory," *IEEE Transactions on Magnetics*, vol. 50, no. 11, pp. 1–4, Nov. 2014.

[50] B. L. J. Gysen, K. J. Meessen, J. J. H. Paulides, and E. A. Lomonova, "General Formulation of the Electromagnetic Field Distribution in Machines and Devices Using Fourier Analysis," *IEEE Transactions on Magnetics*, vol. 46, no. 1, pp. 39–52, Jan. 2010.

[51] P.-D. Pfister and Y. Perriard, "Slotless Permanent-Magnet Machines: General Analytical Magnetic Field Calculation," *IEEE Transactions on Magnetics*, vol. 47, no. 6, pp. 1739–1752, Jun. 2011.

[52] N. Boules, "Prediction of No-Load Flux Density Distribution in Permanent Magnet Machines," *IEEE Transactions on Industry Applications*, vol. IA-21, no. 3, pp. 633–643, May 1985.

[53] Z. Q. Zhu, D. Howe, E. Bolte, and B. Ackermann, "Instantaneous magnetic field distribution in brushless permanent magnet DC motors. I. Open-circuit field," *Magnetics, IEEE Transactions on*, vol. 29, no. 1, pp. 124–135, 1993.

[54] Z. Zhu and D. Howe, "Instantaneous magnetic field distribution in brushless permanent magnet DC motors. II. Armature-reaction field," *IEEE Transactions on Magnetics*, vol. 29, no. 1, pp. 136–142, Jan. 1993.

[55] ——, "Instantaneous magnetic field distribution in brushless permanent magnet DC motors. III. Effect of stator slotting," *IEEE Transactions on Magnetics*, vol. 29, no. 1, pp. 143–151, Jan. 1993.

[56] ——, "Instantaneous magnetic field distribution in permanent magnet brushless DC motors. IV. Magnetic field on load," *IEEE Transactions on Magnetics*, vol. 29, no. 1, pp. 152–158, Jan. 1993.

[57] Y. N. Zhilichev, "Three-dimensional analytic model of permanent magnet axial flux machine," *IEEE Transactions on Magnetics*, vol. 34, no. 6, pp. 3897–3901, Nov. 1998.

[58] K. Rasmussen, "Analytical prediction of magnetic field from surface mounted permanent magnet motor," in *Electric Machines and Drives, 1999. International Conference IEMD '99*, May 1999, pp. 34–36.

[59] D. Ishak, Z. Zhu, and D. Howe, "Comparison of PM brushless motors, having either all teeth or alternate teeth wound," *IEEE Transactions on Energy Conversion*, vol. 21, no. 1, pp. 95–103, Mar. 2006.

[60] D. Žarko, D. Ban, and T. Lipo, "Analytical Solution for Cogging Torque in Surface Permanent-Magnet Motors Using Conformal Mapping," *IEEE Transactions on Magnetics*, vol. 44, no. 1, pp. 52–65, Jan. 2008.

[61] F. Deng and T. Nehl, "Analytical modeling of eddy-current losses caused by pulse-width-modulation switching in permanent-magnet brushless direct-current motors," *IEEE Transactions on Magnetics*, vol. 34, no. 5, pp. 3728–3736, Sep. 1998.

[62] H. Toda, Z. Xia, J. Wang, K. Atallah, and D. Howe, "Rotor eddy-current loss in permanent magnet brushless machines," *IEEE Transactions on Magnetics*, vol. 40, no. 4, pp. 2104–2106, Jul. 2004.

[63] Z. Zhu, K. Ng, N. Schofield, and D. Howe, "Improved analytical modelling of rotor eddy current loss in brushless machines equipped with surface-mounted permanent magnets," *Electric Power Applications, IEE Proceedings* -, vol. 151, no. 6, pp. 641–650, Nov. 2004.

[64] Y. Amara, P. Reghem, and G. Barakat, "Analytical Prediction of Eddy-Current Loss in Armature Windings of Permanent Magnet Brushless AC Machines," *IEEE Transactions on Magnetics*, vol. 46, no. 8, pp. 3481–3484, Aug. 2010.

[65] T. Lubin, S. Mezani, and A. Rezzoug, "Two-Dimensional Analytical Calculation of Magnetic Field and Electromagnetic Torque for Surface-Inset Permanent-Magnet Motors," *IEEE Transactions on Magnetics*, vol. 48, no. 6, pp. 2080–2091, Jun. 2012.

[66] K. Boughrara, N. Takorabet, R. Ibtiouen, O. Touhami, and F. Dubas, "Analytical Analysis of Cage Rotor Induction Motors in Healthy, Defective and Broken Bars Conditions," *IEEE Transactions on Magnetics*, vol. PP, no. 99, pp. 1–1, 2014.

[67] M. Dhifli, H. Bali, Y. Laoubi, G. Verez, Y. Amara, and G. Barakat, "Modeling and prototyping of axial flux permanent magnet machine for small wind turbine," in *2014 International Conference on Electrical Sciences and Technologies in Maghreb (CISTEM)*, Nov. 2014, pp. 1–7.

[68] P.-D. Pfister, X. Yin, and Y. Fang, "Slotted Permanent-Magnet Machines: General Analytical Model of Magnetic Fields, Torque, Eddy Currents and Permanent Magnet Power Losses including the Diffusion Effect," *IEEE Transactions on Magnetics*, vol. 52, no. 5, pp. 1–13, 2016.

[69] F. Dubas and K. Boughrara, "New Scientific Contribution on the 2-D Subdomain Technique in Cartesian Coordinates: Taking into Account of Iron Parts," *Mathematical and Computational Applications*, vol. 22, no. 1, p. 17, Feb. 2017.

[70] S. R. Holm, "Modelling and optimization of a permanent-magnet machine in a flywheel," Ph.D. dissertation, Technical University Delft, Delft, The Netherlands, 2003.

[71] J. Azzouzi, G. Barakat, and B. Dakyo, "Quasi-3-D analytical modeling of the magnetic field of an axial flux permanent-magnet synchronous machine," *IEEE Transactions on Energy Conversion*, vol. 20, no. 4, pp. 746–752, Dec. 2005.

[72] H. Tiegna, A. Bellara, Y. Amara, and G. Barakat, "Analytical Modeling of the Open-Circuit Magnetic Field in Axial Flux Permanent-Magnet Machines With Semi-Closed Slots," *IEEE Transactions on Magnetics*, vol. 48, no. 3, pp. 1212–1226, Mar. 2012.

[73] A. Hemeida, B. Hannon, H. Vansompel, and P. Sergeant, "Comparison of Three Analytical Methods for the Precise Calculation of Cogging Torque

and Torque Ripple in Axial Flux PM Machines," *Mathematical Problems in Engineering*, vol. 2016, p. e2171547, Oct. 2016. [Online]. Available: http://www.hindawi.com/journals/mpe/2016/2171547/abs/

[74] M. Marinescu and N. Marinescu, "New concept of permanent magnet excitation for electrical machines: analytical and numerical computation," *IEEE Transactions on Magnetics*, vol. 28, no. 2, pp. 1390–1393, Mar. 1992.

[75] K. Atallah, Z. Q. Zhu, and D. Howe, "Armature reaction field and winding inductances of slotless permanent-magnet brushless machines," *IEEE Transactions on Magnetics*, vol. 34, no. 5, pp. 3737–3744, Sep. 1998.

[76] D. Ishak, Z. Zhu, and D. Howe, "Eddy-current loss in the rotor magnets of permanent-magnet brushless machines having a fractional number of slots per pole," *IEEE Transactions on Magnetics*, vol. 41, no. 9, pp. 2462–2469, Sep. 2005.

[77] J. Wang, G. Jewell, and D. Howe, "A general framework for the analysis and design of tubular linear permanent magnet machines," *IEEE Transactions on Magnetics*, vol. 35, no. 3, pp. 1986–2000, May 1999.

[78] N. Bianchi, "Analytical field computation of a tubular permanent-magnet linear motor," *IEEE Transactions on Magnetics*, vol. 36, no. 5, pp. 3798–3801, Sep. 2000.

[79] Y. Amara, J. Wang, and D. Howe, "Analytical prediction of eddy-current loss in modular tubular permanent-magnet machines," *IEEE Transactions on Energy Conversion*, vol. 20, no. 4, pp. 761–770, Dec. 2005.

[80] M.-G. Park, J.-Y. Choi, H.-J. Shin, K. Lee, and K. Hong, "Electromagnetic Analysis and Experimental Testing of a Tubular Linear Synchronous Machine With a Double-Sided Axially Magnetized Permanent Magnet Mover and Coreless Stator Windings by Using Semianalytical Techniques," *IEEE Transactions on Magnetics*, vol. 50, no. 11, pp. 1–4, Nov. 2014.

[81] M. Marković and Y. Perriard, "Analytical Solution for Rotor Eddy-Current Losses in a Slotless Permanent-Magnet Motor: The Case of Current Sheet Excitation," *IEEE Transactions on Magnetics*, vol. 44, no. 3, pp. 386–393, Mar. 2008.

[82] C. Custers, T. Overboom, J. Jansen, and E. Lomonova, "2-D Semianalytical Modeling of Eddy Currents in Segmented Structures," *IEEE Transactions on Magnetics*, vol. 51, no. 11, pp. 1–4, Nov. 2015.

[83] Z. Zhu, K. Ng, N. Schofield, and D. Howe, "Analytical prediction of rotor eddy current loss in brushless machines equipped with surface-mounted

permanent magnets. I. Magnetostatic field model," in *Proceedings of the Fifth International Conference on Electrical Machines and Systems, 2001. ICEMS 2001*, vol. 2, Aug. 2001, pp. 806–809.

[84] U. Kim and D. Lieu, "Magnetic field calculation in permanent magnet motors with rotor eccentricity: without slotting effect," *IEEE Transactions on Magnetics*, vol. 34, no. 4, pp. 2243–2252, Jul. 1998.

[85] B. Gysen, E. Lomonova, J. Paulides, and A. Vandenput, "Analytical and Numerical Techniques for Solving Laplace and Poisson Equations in a Tubular Permanent-Magnet Actuator: Part I. Semi-Analytical Framework," *IEEE Transactions on Magnetics*, vol. 44, no. 7, pp. 1751–1760, Jul. 2008.

[86] F. Dubas and C. Espanet, "Analytical Solution of the Magnetic Field in Permanent-Magnet Motors Taking Into Account Slotting Effect: No-Load Vector Potential and Flux Density Calculation," *IEEE Transactions on Magnetics*, vol. 45, no. 5, pp. 2097–2109, May 2009.

[87] K.-H. Shin, M.-G. Park, H.-W. Cho, and J.-Y. Choi, "Comparative Study of Armature Reaction Field Analysis for Tubular Linear Machine with Axially Magnetized Single-sided and Double-sided Permanent Magnet Based on Analytical Field Calculations," *J. Magn.*, vol. 20, no. 1, pp. 79–85, Mar. 2015.

[88] K. Atallah, D. Howe, P. Mellor, and D. Stone, "Rotor loss in permanent-magnet brushless AC machines," *IEEE Transactions on Industry Applications*, vol. 36, no. 6, pp. 1612–1618, Nov. 2000.

[89] X. Wang, Q. Li, S. Wang, and Q. Li, "Analytical calculation of air-gap magnetic field distribution and instantaneous characteristics of brushless DC motors," *IEEE Transactions on Energy Conversion*, vol. 18, no. 3, pp. 424–432, Sep. 2003.

[90] S. Jumayev, K. O. Boynov, J. J. H. Paulides, E. A. Lomonova, and J. Pyrhönen, "Slotless PM machines with Skewed Winding Shapes: 3d Electromagnetic Modeling," *IEEE Transactions on Magnetics*, vol. 52, no. 11, pp. 1–13, 2016.

[91] U. Kim and D. Lieu, "Effects of magnetically induced vibration force in brushless permanent-magnet motors," *IEEE Transactions on Magnetics*, vol. 41, no. 6, pp. 2164–2172, Jun. 2005.

[92] P. Kumar and P. Bauer, "Improved Analytical Model of a Permanent-Magnet Brushless DC Motor," *IEEE Transactions on Magnetics*, vol. 44, no. 10, pp. 2299–2309, Oct. 2008.

[93] D. Žarko, D. Ban, and T. Lipo, "Analytical calculation of magnetic field distribution in the slotted air gap of a surface permanent-magnet motor using complex relative air-gap permeance," *IEEE Transactions on Magnetics*, vol. 42, no. 7, pp. 1828–1837, Jul. 2006.

[94] K. Boughrara, B. Chikouche, R. Ibtiouen, D. Žarko, and O. Touhami, "Analytical Model of Slotted Air-Gap Surface Mounted Permanent-Magnet Synchronous Motor With Magnet Bars Magnetized in the Shifting Direction," *IEEE Transactions on Magnetics*, vol. 45, no. 2, pp. 747–758, Feb. 2009.

[95] A. Hanic, D. Žarko, and Z. Hanic, "A Novel Method for No-Load Magnetic Field Analysis of Saturated Surface Permanent-Magnet Machines Using Conformal Mapping and Magnetic Equivalent Circuits," *IEEE Transactions on Energy Conversion*, vol. 31, no. 2, pp. 1–10, 2016.

[96] K. Ramakrishnan, M. Curti, D. Žarko, G. Mastinu, J. Paulides, and E. Lomonova, "Comparative Analysis of Various Methods for Modelling Permanent Magnet Machines," *IET Electric Power Applications*, Jan. 2017.

[97] P. Arumugam, T. Hamiti, and C. Gerada, "Estimation of Eddy Current Loss in Semi-Closed Slot Vertical Conductor Permanent Magnet Synchronous Machines Considering Eddy Current Reaction Effect," *IEEE Transactions on Magnetics*, vol. 49, no. 10, pp. 5326–5335, Oct. 2013.

[98] B. Chikouche, K. Boughrara, and R. Ibtiouen, "Cogging Torque Minimization of Surface-Mounted Permanent Magnet Synchronous Machines Using Hybrid Magnet Shapes," *Progress In Electromagnetics Research B*, vol. 62, pp. 49–61, Jan. 2015.

[99] R. Sprangers, J. Paulides, B. Gysen, and E. Lomonova, "Towards Magnetic Saturation in Semi-Analytical Harmonic Modeling for Electric Machine Analysis," *IEEE Transactions on Magnetics*, vol. 2, no. 52, pp. 1–10, 2016.

[100] A. Zangwill, *Modern Electrodynamics*. Cambridge: Cambridge University Press, 2013.

[101] G. Rousseaux, "Forty years of Galilean Electromagnetism (1973-2013)," *Eur. Phys. J. Plus*, vol. 128, no. 8, pp. 1–14, Aug. 2013.

[102] R. C. Costen, *Four dimensional derivation of the electrodynamic jump conditions, tractions, and power transfer at a moving boundary*. Washington, D.C. : NASA, 1965.

[103] M. Kuczmann and A. Iványi, *The Finite Element Method in Magnetics*. Budapest: Akadéiai Kiadó, 2008.

[104] E. Kreyszig, *Advanced engineering mathematics*, 4th ed. New York: John Wiley & Sons, Ltd, 1979.

[105] A. Rahideh and T. Korakianitis, "Analytical Magnetic Field Distribution of Slotless Brushless Machines With Inset Permanent Magnets," *IEEE Transactions on Magnetics*, vol. 47, no. 6, pp. 1763–1774, Jun. 2011.

[106] K. Meessen, "Electromagnetic Fields and Interactions in 3d Cylindrical Structures: Modeling and Application," Ph.D. dissertation, Technical University Eindhoven, Eindhoven, The Netherlands, 2012.

[107] T. Lubin and a. rezzoug, "Improved 3-D Analytical Model for Axial-Flux Eddy-Current Couplings with Curvature Effects," *IEEE Transactions on Magnetics*, no. in press, 2017.

[108] N. Boules, "Two-Dimensional Field Analysis of Cylindrical Machines with Permanent Magnet Excitation," *IEEE Transactions on Industry Applications*, vol. IA-20, no. 5, pp. 1267–1277, Sep. 1984.

[109] B. Gysen, "Generalized Harmonic Modeling Technique for 2d Electromagnetic Problems Applied to the Design of a Direct-Drive Active Suspension System," Ph.D. dissertation, Technical University Eindhoven, Eindhoven, The Netherlands, 2011.

[110] D. Gerling and G. Dajaku, "Three-dimensional analytical calculation of induction machines with multilayer rotor structure in cylindrical coordinates," *Electr Eng*, vol. 86, no. 4, pp. 199–211, Nov. 2003.

[111] S. Jumayev, J. Paulides, K. Boynov, J. Pyrhönen, and E. Lomonova, "Three-Dimensional Analytical Model of Helical Winding PM Machines Including Rotor Eddy-Currents," *IEEE Transactions on Magnetics*, vol. 52, no. 5, pp. 1–8, 2016.

[112] B. Hannon, P. Sergeant, and L. Dupré, "2d Analytical Torque Study of Slotless and Slotted Stator Topologies at High-Speed Operation," in *Submitted to 11th International Conference on Modeling and Simulation of Electric Machines, Converters and Systems*, Valencia, Spain, 2014.

[113] Z. Liu and J. Li, "Analytical Solution of Air-Gap Field in Permanent-Magnet Motors Taking Into Account the Effect of Pole Transition Over Slots," *IEEE Transactions on Magnetics*, vol. 43, no. 10, pp. 3872–3883, Oct. 2007.

[114] Z. Zhu, D. Howe, and C. Chan, "Improved analytical model for predicting the magnetic field distribution in brushless permanent-magnet machines," *IEEE Transactions on Magnetics*, vol. 38, no. 1, pp. 229–238, Jan. 2002.

[115] Z. Xia, Z. Zhu, and D. Howe, "Analytical magnetic field analysis of Halbach magnetized permanent-magnet machines," *IEEE Transactions on Magnetics*, vol. 40, no. 4, pp. 1864–1872, Jul. 2004.

[116] T. Lubin, S. Mezani, and A. Rezzoug, "2-D Exact Analytical Model for Surface-Mounted Permanent-Magnet Motors With Semi-Closed Slots," *IEEE Transactions on Magnetics*, vol. 47, no. 2, pp. 479–492, Feb. 2011.

[117] B. Hannon, P. Sergeant, and L. Dupré, "2-D Analytical Subdomain Model of a Slotted PMSM With Shielding Cylinder," *IEEE Transactions on Magnetics*, vol. 50, no. 7, pp. 1–10, Jul. 2014.

[118] L. Wu, Z. Zhu, D. Staton, M. Popescu, and D. Hawkins, "Analytical Model for Predicting Magnet Loss of Surface-Mounted Permanent Magnet Machines Accounting for Slotting Effect and Load," *IEEE Transactions on Magnetics*, vol. 48, no. 1, pp. 107–117, Jan. 2012.

[119] K. Boughrara, T. Lubin, and R. Ibtiouen, "General Subdomain Model for Predicting Magnetic Field in Internal and External Rotor Multiphase Flux-Switching Machines Topologies," *IEEE Transactions on Magnetics*, vol. 49, no. 10, pp. 5310–5325, Oct. 2013.

[120] P. Arumugam, J. Dusek, S. Mezani, T. Hamiti, and C. Gerada, "Modeling and analysis of eddy current losses in permanent magnet machines with multi-stranded bundle conductors," *Mathematics and Computers in Simulation*, Oct. 2015.

[121] A. Dalal and P. Kumar, "Analytical Model for Permanent Magnet Motor with Slotting Effect, Armature Reaction and Ferromagnetic Material Property," *IEEE Transactions on Magnetics*, vol. 51, no. 12, pp. 1–10, 2015.

[122] K. Ramakrishnan, D. Žarko, A. Hanic, and G. Mastinu, "An Improved Method for Field Analysis of Surface Permanent MagnetMachines Using Schwarz-Christoffel Transformation," *IET Electric Power Applications*, vol. 11, no. 6, Feb. 2017.

[123] A. Bellara, Y. Amara, G. Barakat, and B. Dakyo, "Two-Dimensional Exact Analytical Solution of Armature Reaction Field in Slotted Surface Mounted PM Radial Flux Synchronous Machines," *IEEE Transactions on Magnetics*, vol. 45, no. 10, pp. 4534–4538, Oct. 2009.

[124] B. Hannon, P. Sergeant, and L. Dupré, "Voltage Sources in 2d Fourier-Based Analytical Models of Electric Machines," *Mathematical Problems in Engineering*, vol. 2015, p. e195410, Oct. 2015.

[125] M. Marković, M. Jufer, and Y. Perriard, "Determination of tooth cogging force in a hard-disk brushless DC motor," *IEEE Transactions on Magnetics*, vol. 41, no. 12, pp. 4421–4426, Dec. 2005.

[126] L. Liu and S. Yang, "A numerical conformal transformation for investigating slot effects of high speed brushless PM motors," in *Automation Congress, 2008. WAC 2008. World*, Sep. 2008, pp. 1–4.

[127] D. B. Ackermann and D. R. Sottek, "Analytical modeling of the cogging torque in permanent magnet motors," *Electrical Engineering*, vol. 78, no. 2, pp. 117–125, Mar. 1995.

[128] M. Marković, M. Jufer, and Y. Perriard, "Reducing the cogging torque in brushless DC motors by using conformal mappings," *IEEE Transactions on Magnetics*, vol. 40, no. 2, pp. 451–455, Mar. 2004.

[129] L. J. Wu, Z. Q. Zhu, D. Staton, M. Popescu, and D. Hawkins, "Comparison of analytical models for predicting cogging torque in surface-mounted PM machines," in *The XIX International Conference on Electrical Machines - ICEM 2010*, Sep. 2010, pp. 1–6.

[130] U. Kim and D. Lieu, "Magnetic field calculation in permanent magnet motors with rotor eccentricity: with slotting effect considered," *IEEE Transactions on Magnetics*, vol. 34, no. 4, pp. 2253–2266, Jul. 1998.

[131] Y. Li, Q. Lu, Z. Zhu, L. Wu, G. Li, and D. Wu, "Analytical Synthesis of Air-Gap Field Distribution in Permanent Magnet Machines With Rotor Eccentricity by Superposition Method," *IEEE Transactions on Magnetics*, vol. 51, no. 11, pp. 1–4, Nov. 2015.

[132] M. Merdzan, S. Jumayev, A. Borisavljevic, K. Boynov, J. Paulides, and E. Lomonova, "Electrical and Magnetic Model Coupling of Permanent Magnet Machines Based on the Harmonic Analysis," *IEEE Transactions on Magnetics*, vol. 51, no. 11, pp. 1–4, Nov. 2015.

[133] H. Bali, Y. Amara, G. Barakat, R. Ibtiouen, and M. Gabsi, "Analytical Modeling of Open Circuit Magnetic Field in Wound Field and Series Double Excitation Synchronous Machines," *IEEE Transactions on Magnetics*, vol. 46, no. 10, pp. 3802–3815, Oct. 2010.

[134] J. Wang, K. Atallah, R. Chin, W. Arshad, and H. Lendenmann, "Rotor Eddy-Current Loss in Permanent-Magnet Brushless AC Machines," *IEEE Transactions on Magnetics*, vol. 46, no. 7, pp. 2701–2707, Jul. 2010.

[135] A. Bellara, H. Bali, R. Belfkira, Y. Amara, and G. Barakat, "Analytical Prediction of Open-Circuit Eddy-Current Loss in Series Double Excitation Synchronous Machines," *IEEE Transactions on Magnetics*, vol. 47, no. 9, pp. 2261–2268, Sep. 2011.

[136] M. Marković and Y. Perriard, "An Analytical Determination of Eddy-Current Losses in a Configuration With a Rotating Permanent Magnet," *IEEE Transactions on Magnetics*, vol. 43, no. 8, pp. 3380–3386, Aug. 2007.

[137] ——, "An analytical solution for the torque and power of a solid-rotor induction motor," in *Electric Machines Drives Conference (IEMDC), 2011 IEEE International*, May 2011, pp. 1053–1057.

[138] S. Nair, J. Wang, R. Chin, L. Chen, and T. Sun, "Analytical Prediction of 3d Magnet Eddy Current Losses in Surface Mounted PM Machines Accounting Slotting Effect," *IEEE Transactions on Energy Conversion*, vol. 32, no. 2, pp. 1–9, 2016.

[139] B. Hannon, P. Sergeant, and L. Dupré, "Time- and Spatial-Harmonic Content in Synchronous Electrical Machines," *IEEE Transactions on Magnetics*, vol. 53, no. 3, pp. 1–11, 2016.

[140] S. Eriksson, H. Bernhoff, and M. Leijon, "A 225 kW Direct Driven PM Generator Adapted to a Vertical Axis Wind Turbine," *Advances in Power Electronics*, vol. 2011, p. e239061, Oct. 2011.

[141] J. Pyrhönen, J. Tapani, and V. Hrabovcová, *Design of Rotating Electrical Machines*. Chichester: John Wiley & Sons, Ltd, Jan. 2008.

[142] O. de la Barrière, S. Hlioui, H. Ben Ahmed, and M. Gabsi, "An analytical model for the computation of no-load eddy current losses in the rotor of a permanent magnet synchronous machine," *IEEE Transactions on Magnetics*, vol. 52, no. 6, pp. 1–14, 2013.

[143] S. Jumayev, M. Merdzan, K. Boynov, J. Paulides, J. Pyrhönen, and E. Lomonova, "The Effect of PWM on Rotor Eddy-Current Losses in High-Speed Permanent Magnet Machines," *IEEE Transactions on Magnetics*, vol. 51, no. 11, pp. 1–4, Nov. 2015.

[144] F. Dubas and A. Rahideh, "Two-Dimensional Analytical Permanent-Magnet Eddy-Current Loss Calculations in Slotless PMSM Equipped With Surface-Inset Magnets," *IEEE Transactions on Magnetics*, vol. 50, no. 3, pp. 54–73, Mar. 2014.

[145] J. Beurms, "Test bench for a high-speed permanent magnet machine," Master thesis, Ghent University, Ghent, Belgium, 2014.

[146] G. De Smaele and M. Verschelden, "Control of an electric machine with permanent magnets," Master thesis, Ghent University, Ghent, Belgium, 2015.

[147] N. Parmentier, "Control of a high-speed electrical machine with permanent magnets," Master thesis, Ghent University, Ghent, Belgium, 2016.

[148] M. Doclo, “Back-EMF Based Sensorless BLDC Control of a High-Speed Permanent Magnet Machine,” Master thesis, Ghent University, Ghent, Belgium, 2017.

[149] S. Wauters, “Control and efficiency determination of a high-speed permanent magnet synchronous motor,” Master thesis, Ghent University, Ghent, Belgium, 2017.

[150] I. Boldea and S. A. Nasar, *The Induction Machine Handbook*. CRC Press, Dec. 2010.

[151] N. Bianchi and M. Dai Pré, “Use of the star of slots in designing fractional-slot single-layer synchronous motors,” *Electric Power Applications, IEE Proceedings* -, vol. 153, no. 3, pp. 459–466, May 2006.

[152] L. Alberti and N. Bianchi, “Theory and Design of Fractional-Slot Multilayer Windings,” *IEEE Transactions on Industry Applications*, vol. 49, no. 2, pp. 841–849, Mar. 2013.